# Caesium and strontium sorption to sediment and clay minerals

Adam James Fuller

Submitted in accordance with the requirements for the degree of
Doctor of Philosophy

The University of Leeds
School of Earth and Environment

April 2014

The candidate confirms that the work submitted is his/her own, except where work which has formed part of jointly-authored publications has been included. The contribution of the candidate and the other authors to this work has been explicitly indicated below. The candidate confirms that appropriate credit has been given within the thesis where reference has been made to the work of others.

The work presented in Chapter 4 of this thesis has appeared as the following publication:

**Fuller, A. J.,** Shaw, S., Peacock, C. L., Trivedi, D., Small, J. S., Abrahamsen, L. G. & Burke, I. T. 2014. Ionic strength and pH dependent multi-site sorption of Cs onto a micaceous aquifer sediment. *Applied Geochemistry,* **40,** 32-42.

Candidate's contribution (A.J. Fuller) – Developed the concept, prepared the manuscript, conducted batch experiments, interpreted data, developed PHREEQC model; S. Shaw – Formed intial concept, adided in data intepretation, commented on the manuscript; C.L. Peacock – Commented on the manuscript, aided in model development; D. Trivedi - Trained candidate in PHREEQC modelling, commented on manuscript; J.S. Small – Helped with model development, commented on manuscript; L.G. Abrahamsen – Helped with model development, commented on manuscript; I.T. Burke – Formed intial concept, adided in data intepretation, commented on the manuscript

Work presented in Chapter 5 of this thesis forms a jointly authored paper currently in preparation.

Candidate's contribution – Initial concept, prepared manuscript, analysed data; S. Shaw – Initial concept, commented on the manuscript; M.B. Ward – Assisted with TEM imaging, commented on the manuscript; S. Haigh – Assisted with ChemiSTEM imaging and image/EDX anaylsis, commented on the manuscript; J.F.W Mosslemans – Interpretation and fitting of Cs EXAFS spectra; C.L. Peacock - Commented on the manuscript; S. Stackhouse – DFT modelling and wrote DFT modelling methods section, commented on the manuscript; A. Dent – Data collection Cs-EXAFS spectra; D.Trivedi - Commented on the manuscript; I.T. Burke – Initial concept, commented on the manuscript

Work presented in Chapter 6 of this thesis will form a jointly authored paper currently in preparation.

Candidate's contribution – Prepared the manuscript, conducted batch experiments, gathered and interpreted EXAFS data, performed PHREEQC modelling; S. Shaw – Initial concept, Commented on the manuscript, assisted with EXAFS fitting; C.L. Peacock – Commented on the manuscript, assisted with EXAFS fitting; D.Trivedi – Commented on the manuscript; I.T. Burke - Initial concept, Commented on the manuscript, assisted with EXAFS fitting

## Acknowledgments

Well, where to begin...? I have a very long list of people to thank for getting me to this point. Most important, I guess, are my supervisors: Ian Burke and Caroline Peacock in Leeds, Sam Saw in Manchester and Divyesh Trivedi at the NNL. They have been an invaluable source of knowledge, advice and support. The fact that as I write these words I can call myself a scientist is largely down to their influence over the years. I should also thank the EPSRC and the NNL for funding this little adventure of mine and the University of Leeds for letting my dwell in its ivory towers for a few years.

The work I present in this thesis is the culmination of a highly collaborative set of projects. This is reflected in the preceding pages, however I would like to again thank all my co-authors. Without their input this thesis would be a shadow of what it actually became. Particular thanks goes to Mike Ward whose company made the many hours on the TEM in a dark basement far more enjoyable. This is also a good point at which to thank all those who have provided me with technical support during this research. Firstly I thank Sam Allshorn who was essential to the smooth running of the Cohen labs for most of the time when I was working in them. I would also thank our beamline scientists for their support during our beamtimes: At Diamond Light Source; Silvia Ramos-Perez on B18 and Adam Freeman on I20 (LOLA); and at the ESRF Dipanjan Banerjee on BM26A (DUBBLE).

Beyond those who have directly inputted to the work in this thesis I have many people to thank for their support, encouragement and love which has proven invaluable to me over the years. Firstly, and most importantly, I would thank my parents, John and Susan, for their ceaseless support and encouragement. By exposing me to such a diversity of experiences from a young age they peaked my curiosity about the world and opened my eyes to the joys of science. I would also thank my brother, Matthew, who I am sure will play the essential role of any big brother and stop this achievement from going to my head.

It is certainly more than just family members who deserve thanks however. I would thank my office mates, especially Aislinn Boylan who had the dubious honour of being my go-to-gal for write up grumblings. I also have to mention the Catan trio, Andy Bray, Steffi Lutz and Pieter Bots. I might never have won (grrr!) but I always enjoyed our game nights (the red wine might have helped!) This is probably also a good time to mention Brendan Stokes, Tim Holland and Luca Flailabrese who were kind enough to let me beat them at Risk on regular occasions and gave me a nice break from the science world (ART!) I also promised that I would thank my Italian holiday compatriots, Stephen Pasquale, Brendan Stokes, but most especially Mike Pasquale. I could not have thought of a more fun group of guys to spend a great holiday with. It was the perfect antidote to 3rd year stress, so thanks.

Finally I would thank the many members of the Cohen Geochemistry group, and many others in the school, whose good humour and readiness to share a beer at the end of the week made my time in Leeds so enjoyable.

## Abstract

Radioactive caesium ($^{137}$Cs) and strontium ($^{90}$Sr) are two of the most important contaminant radionuclides present in many terrestrial environments, as a result of accidental and approved releases from anthropogenic nuclear activity. This thesis investigates the sorption of Cs and Sr onto the surfaces of common terrestrial minerals and a mixed phase sediment.

The key findings of the work were with regard to the effect of solution pH and ionic strength on changing the mechanism of Cs and Sr interaction with reactive mineral surfaces. Caesium was found to sorb to multiple sorption sites within the mixed phase sediment. The first of these was a Cs selective site at the edge of the illite interlayer, known as the frayed edge site. It was determined from electron microscopy and x-ray absorption spectroscopy that Cs was selectively incorporated and retained in the interlayer structure in inner-sphere complexes. Cs was also found to sorb to two other main sorption sites in competition with other cations. Therefore the concentrations of Cs sorbing to the mineral surfaces were greatly reduced in low pH or high ionic strength conditions. Solution pH and ionic strength also played a major role in Sr sorption. At intermediate pH Sr sorbed to the surface of illite, chlorite and goethite in outer-sphere complexes. Therefore the presence of competing ions in solution significantly reduced total Sr sorption. However, at very high pH, Sr was specifically adsorbed into inner-sphere surface complexes. This allowed significant concentrations of Sr to sorb to the mineral surface even in high ionic strength solutions.

The findings of this thesis mark a significant advance in understanding the fundamental processes governing the behaviour of $^{137}$Cs and $^{90}$Sr in the environment. Particularly it shows the importance of groundwater chemistry in governing sorption behaviour.

# Table of Contents

# Table of Figures

# Table of Tables

# Chapter 1 – Introduction

This introductory chapter presents the overall context of and rationale for the research. Particular attention is given to the development of nuclear power and the associated environmental impact. The overall aims and hypotheses which drove the research are then given. Finally an overview of the structure of the thesis is given, with specific details on the objectives and experimental approach employed in each of the data chapters.

## 1.1 Background context and Rationale

Since the discovery of the potential to use the fission of atomic nuclei as a source for energy, as well as a weapon, nuclear power has formed an important part of the global energy mix (Murray, 1993, Graetzer and Anderson, 1971). The first wave of nuclear power generation was centred in the nuclear armed states, chiefly the USA, UK and France (Hall, 1986, Lillington, 2004). At the early stages, a range of reactor technologies using both uranium and thorium fuel emerged. However over time the uranium powered boiling water reactor became dominant and the majority of nuclear reactors in the world today are of this type (Lillington, 2004).

A number of high profile accidents and a growing opposition to nuclear weapons during the cold war saw a decline in investment in nuclear power in many countries. However France and Japan continued to rely on it as they

had little fossil fuel resources (WNA, 2014). However, with the growing awareness of climate change in the past 30 years nuclear power has seen resurgence as a carbon free fuel. Today both China and India are investing heavily in both uranium and thorium fuelled nuclear power stations. The UK has also recently announced intentions to build a minimum of 5 new nuclear power stations, and many more may be on the horizon (NAMRC, NiA, 2013).

This thesis is concerned with the environmental legacy left from the first generation of nuclear power plants. Most notably it focuses on the mobility and long term fate of the important fission products, $^{137}Cs$ and $^{90}Sr$ in the environment. Both these radionuclides are produced in high yield as a result of nuclear fission reactions. Therefore they are common in radioactive wastes and are present in the environment as a result of both accidental and authorised releases (NDA, 2010, NCRP, 2007). Accidental releases have occurred locally at designated nuclear sites (such as at Sellafield and Hanford (McKenzie et al., 2011, Rotenberg et al., 2001)) and over much larger areas as a result of accidents (such as Fukushima (Kinoshita et al., 2011)).

Although not chemically toxic, both $^{137}Cs$ and $^{90}Sr$ present a serious risk to both human health and the wider environment due to their radioactive emissions. The beta and gamma radiation released as a result of their radioactive decay can seriously damage the cells of living organisms leading to cancers and in the most extreme cases, radiation poisoning (Hill et al.,

2001, Stamoulis et al., 1999). Therefore it is unsafe for humans to inhabit (for the long term) any areas of land which are highly radioactive (as a result of contamination). Both $^{137}Cs$ ($t_{1/2}$ = 30 years) and $^{90}Sr$ ($t_{1/2}$ = 29 years) are relatively long lived radionuclides, meaning that these contaminated areas may need to be abandoned for multiple generations.

Although it would be ideal to prevent the release of these radionuclides into the environment, their presence is a historical reality; so it is important to understand how these dangerous contaminants behave and interact with their surroundings. The mobility of $^{137}Cs$ and $^{90}Sr$ in the environment is chiefly controlled by interaction with charged surface sites in the subsurface, often referred to as sorption (Krauskopf and Bird, 1995). These charged (reactive) sites can occur on a range of surfaces, including clay minerals, hydroxides and organic components (including natural organic matter and bacteria cell walls) (Artinger et al., 2002, Sposito et al., 1999, Cornell and Schwertmann 2003). Two main types of surface charge commonly occur on minerals. Permanent charge sites occur (mainly on clay minerals) as a result of substitutions within the mineral structure. For example substitution of $Al^{3+}$ for $Si^{4+}$ within the illite structure yields a net negative charge for that unit cell of -1 (Sposito, 1989, Sposito, 1984, Sposito et al., 1999, Grim, 1968). If the exchange happens in reverse then a net positive surface charge can develop. These charges are permanent and do not change with solution composition. Conversely variable charge sites can occur at the broken edges of clays and hydroxide minerals (Cornell and Schwertmann 2003, Krauskopf and Bird, 1995). These form where the crystal is cleaved leaving

a dangling O or OH group. These hydroxyls carry a charge which is satisfied by ions from solution. These sites can become protonated or deprotonated, depending on the solution pH, this can change them from being positive to negative (Onoda Jr and De Bruyn, 1966). Hence they are known as variable charge sites.

This thesis focuses primarily on sorption to clay minerals as these are often the most important sorbing phase for Cs and Sr in temperate soils (Aldaba et al., 2010). However the sorption of Sr to iron oxides is also addressed. Understanding the fundamental sorption behaviour of these radionuclides over a wide range of environmental conditions is extremely important for predicting their long term behaviour. Without this fundamental understanding of the mineral surface interactions any predictive models would be unable to accurately predict the mobility of these contaminants in the subsurface environment.

## 1.2 Aims and hypotheses

The overall aim of this thesis was to understand the sorption processes governing the mobility of $Cs^{+}$ and $Sr^{2+}$ at the near surface. As part of this a number of specific hypotheses were tested:

1. The removal of Cs from solution in the subsurface is governed by cation exchange reactions with charged sites, primarily on clay minerals

2. The sorption behaviour of Cs to soil minerals is controlled by the ionic strength and pH of the background solution
3. There exists at the edge of an illite particle a partially expanded interlayer region, known as the frayed edge where Cs is preferentially adsorbed via cation exchange
4. Over greatly extended time periods Cs may be able to migrate from the frayed edge of the interlayer into the illite particle interlayer, where it becomes irreversibly trapped
5. Sr sorption at circumneutral pH is via simple cation exchange in competition with other ions in solution and is thus controlled by solution ionic strength
6. Under extremely high pH conditions Sr sorption to mineral surfaces is unaffected by solution ionic strength, due to a change in the sorption mechanism

## 1.3 Thesis structure and experimental approach

This thesis is structured to address the overall aim and test the stated hypotheses. It begins with an overview of the current state of the art in all areas pertaining to this work. Chapter 2 presents a detailed discussion of the UKs nuclear legacy, sorption theory and the chemistry and mineralogy of key elements and minerals discussed in this work.

Chapter 3 of the thesis focuses on the thermochemical background to the sorption processes investigated within the thesis. Specifically it focuses on

the concepts of entropy, enthalpy, and free energy change. The application of these principles to describing cation exchange and surface complexation reactions is then described in detail.

Chapter 4 then presents a detailed description of the materials and methods employed as part of the work. Detailed relevant background to the techniques utilised in this work is also given.

Chapter 5 is the first results chapter and presents an investigation of Cs sorption relevant to the Sellafield site in West Cumbria. It had two main objectives: Determine the effect of Cs solution concentration on its sorption to mixed phase sediment and investigate the effect of pH and ionic strength on Cs sorption to the mixed sediment. These objectives are addressed through a detailed experimental program using radioactive batch sorption experiments with a large concentration range of Cs ($10^{-11}$ – 1 mol $L^{-1}$). The experiments were conducted across a wide range of pH (2-10) and ionic strength ($10^{-9}$ – 1 mol $L^{-1}$) conditions. The results are then interpreted using a multi-site cation exchange model which was written in PHREEQC (Parkhurst and Appelo, 1999) and fitted to the experimental results.

Chapter 6 builds on this work and focuses on gaining an atomic scale understanding of the processes governing the long term sorption of Cs onto illite. Specifically two objectives were identified: Determine the sorption/desorption processes of Cs onto the Frayed Edge Sites of illite and investigate the long term fate of Cs sorbed to illite. Again a batch sorption

experiment was used but it was conducted for up to one year. To investigate the atomic scale changes to the crystallography and chemistry of the illite particles a range of techniques were used. Primarily the samples were characterised using Transmission Electron Microscopy (TEM) and their chemical composition was determined by Energy Dispersive X-ray (EDX) spectroscopy. Caesium's bonding environment was also determined by Extended X-ray Absorption Fine Structure Spectroscopy (EXAFS). Finally a theoretical interpretation of Cs's sorption environment was aided by Density Functional Theory (DFT) calculations.

Chapter 7 then focuses on sorption of Sr at hyper-alkaline pH. It addresses the following objective: Investigate the effect of pH and ionic strength on the sorption of Sr to illite, goethite, chlorite and a mixed sediment. To address this we carried out anaerobic batch sorption experiments. Sr was sorbed to the various minerals in backgrounds of NaCl and NaOH from $10^{-5}$ to 1 mol $L^{-1}$. The sorbed Sr concentrations were determined by ICP-AES. EXAFS was then used to investigate the different sorption environments of Sr to the various minerals under the different solution conditions. The changes in Sr sorption with pH are interpreted in light of the Sr solution speciation as determined from PHREEQC modelling.

Finally Chapter 8 presents the conclusions from this work together with an overall discussion of the results. The implications of this work for the management of radioactively contaminated land are also offered. Finally, some suggestions for further research are given.

## 1.4 References

Aldaba, D., Rigol, A. & Vidal, M. 2010. Diffusion experiments for estimating radiocesium and radiostrontium sorption in unsaturated soils from Spain: Comparison with batch sorption data. *Journal of Hazardous Materials,* 181**,** 1072-1079.

Artinger, R., Rabung, T., Kim, J. I., Sachs, S., Schmeide, K., Heise, K. H., Bernhard, G. & Nitsche, H. 2002. Humic colloid-borne migration of uranium in sand columns. *Journal of Contaminant Hydrology,* 58**,** 1-12.

Cornell, R. & Schwertmann , U. 2003. *The iron oxides: structure, properties, reactions, occurences and uses,* Weinheim, Wiliey-VCH.

Graetzer, H. G. & Anderson, D. L. 1971. *The Discovery of Nuclear Fission: A Documentary History,* London, Van Norstrand Reinhold Company.

Grim, R. E. 1968. *Clay Mineralogy,* New York, McGraw-Hill.

Hall, T. 1986. *Nuclear Politics,* Middlesex, Penguin Books.

Hill, M. D., Steeds, J. E. & Slade, N. J. 2001. Land Contamination: Technical Guidance on Special Sites: Nuclear Sites. Bristol: Environment Agency.

Kinoshita, N., Sueki, K., Sasa, K., Kitagawa, J.-i., Ikarashi, S., Nishimura, T., Wong, Y.-S., Satou, Y., Handa, K., Takahashi, T., Sato, M. & Yamagata, T. 2011. Assessment of individual radionuclide distributions from the Fukushima nuclear accident covering central-east Japan. *Proceedings of the National Academy of Sciences of the United States of America,* 108**,** 19526-19529.

Krauskopf, K. B. & Bird, D. K. 1995. *Introduction to Geochemistry,* New York, McGraw-Hill.

Lillington, J. 2004. *The Futute of Nuclear Power,* Oxford, Elsevier.

McKenzie, H. M., Coughlin, D., Laws, F. & Stampler, A. 2011. Groundwater Annual Report 2011. Sellafield Ltd.

Murray, R. L. 1993. *Nuclear Energy: An Introduction to the Concepts, Systems, and Applications of Nuclear Processes,* Oxford, Pergamon.

NAMRC. *UK new build plans* [Online]. Available: http://namrc.co.uk/intelligence/uk-new-build-plans/ [Accessed 13th February 2014].

NCRP 2007. Cesium-137 in the Environment - Radioecology and Approaches to Assessment and Management (Report No. 154). National Council on Radiation Protection and Measurements (NCRP).

NDA 2010. The 2010 UK Radioactive Waste Inventory.

NiA 2013. The Essential Guide for the Nuclear New Build Supply Chain. 2 ed.

Onoda Jr, G. Y. & De Bruyn, P. L. 1966. Proton adsorption at the ferric oxide/aqueous solution interface. I. A kinetic study of adsorption. *Surface Science,* 4**,** 48-63.

Parkhurst, D. L. & Appelo, C. A. J. 1999. *User's guide to PHREEQC (version 2),* Denver, US Geological Survey.

Rotenberg, P., Choi, S., Karthikeyan, K. G. & Chorover, J. 2001. Cesium and strontium sorption and mineral weathering in Hanford sediments at high pH. *Abstracts of Papers of the American Chemical Society,* 222**,** 68-GEOC.

Sposito, G. 1984. *The Surface Chemistry of Soils,* New York, Oxford University Press.

Sposito, G. 1989. *The Chemistry of Soils,* New York, Oxford University Press.

Sposito, G., Skipper, N. T., Sutton, R., Park, S.-h., Soper, A. K. & Greathouse, J. A. 1999. Surface Geochemistry of the Clay Minerals. *Proceedings of the National Academy of Sciences of the United States of America,* 96**,** 3358-3364.

Stamoulis, K. C., Assimakopoulos, P. A., Ioannides, K. G., Johnson, E. & Soucacos, P. N. 1999. Strontium-90 concentration measurements in human bones and teeth in Greece. *The Science of The Total Environment,* 229**,** 165-182.

WNA. 2014. *Nuclear Power in France* [Online]. Available: http://www.world-nuclear.org/info/Country-Profiles/Countries-A-F/France/ [Accessed 20th February 2014].

# Chapter 2 – Literature Review

This thesis is concerned with the surface sorption of Cs and Sr onto a mixed sediment and the main minerals present within that sediment. This chapter offers a background on these sorption processes. It begins with a detailed theoretical discussion of sorption theory focusing on both the solution and solid phase controls. A detailed description of the key minerals studied in this work is then offered. A specific discussion is then given of the key elements addressed in this work, Cs and Sr, focusing specifically on their environmental behaviour and sorption. This chapter is then completed by a summary of nuclear power in the UK, with a particular focus on land contamination at the Sellafield site to which a large portion of the work in this thesis pertains.

## 2.1 Sorption theory

Sorption is an overarching term which encompasses a group of related processes whereby a dissolved species is removed from solution and becomes associated with a mineral. These include: surface precipitation, where one mineral precipitates on the surface of another; absorption, whereby a mineral incorporates new ions into its structure through diffusion or co-precipitation; and adsorption where ions bind amorphously (through inner or outer-sphere bonds) to the mineral surface and do not precipitate a new mineral (Krauskopf and Bird, 1995).

### 2.1.1 Clay mineralogy and surface charge

In soils, clay minerals (sheet aluminosilicates with a particle size smaller than 2µm (Auerbach et al., 2004) possess the highest sorptive capacity (Grim, 1968). This is due to their large surface area and charge density (Langmuir, 1997). The surface charge of a mineral particle $\sigma_P$ is the sum of a number of different types of charge. The first of these is the permanent structural charge, $\sigma_O$ (Sposito, 1989). Clay minerals are formed from tetrahedral and octahedral sheets. These are groups of silica tetrahedra (or octahedra) covalently bonded together via a common oxygen (see Figure 2.1) (Auerbach et al., 2004). The tetrahedral and octahedral sheets then form into 1:1 (1 tetrahedral sheet, 1 octahedral sheet) or 2:1 layered structures (2 tetrahedral sheets, 1 octahedral sheet) (Sposito et al., 1999). Isomorphic substitution (commonly of $Al^{3+}$ for $Si^{4+}$) within the tetrahedral and octahedral sheets causes a net charge to develop ($\sigma_O$) (Auerbach et al., 2004).

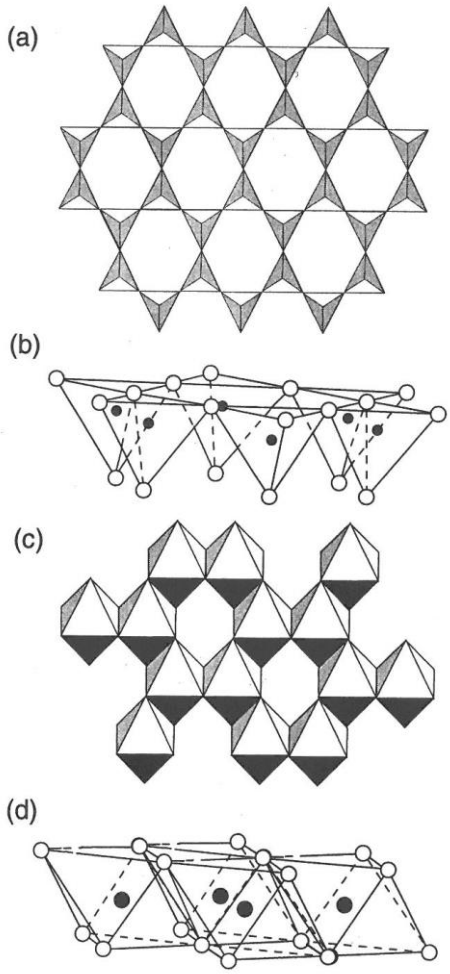


**Figure 2.1** A tetrahedral sheet viewed from the top (a) and side (b) and an octahedral sheet viewed from the top (c) and side (d), reproduced from (Auerbach et al., 2004)

The pH dependant charge, $\sigma_H$ is the relationship between the number of $H^+$ and $OH^-$ ions on the surface (Sposito, 1989). Generally at low pH surfaces have a positive charge and at high pH a negative charge (Krauskopf and Bird, 1995). The point of zero charge is the name given to the pH at which the net surface charge is zero (Krauskopf and Bird, 1995).

Finally the binding of charged ions in innersphere, $\sigma_{IS}$ and outersphere, $\sigma_{OS}$ complexes (discussed in section 1.1.2) affects the overall charge of the

surface (Sposito, 1989). Equation (2.1) summarises this relationship (Sposito, 1989).

$$\sigma_P = \sigma_O + \sigma_H + \sigma_{IS} + \sigma_{OS} \tag{2.1}$$

This overall surface charge is balanced by charged ions in the diffuse ion swarm so that the system remains electrically neutral (Krauskopf and Bird, 1995).

The portioning of charge balancing ions between the surface and solution is described by the electric double layer (Cornell and Schwertmann 2003). Briefly those atoms in close association with (adsorbed in inner-sphere complexes) contribute to the surface charge. Away from this region the electrical potential caused by the charged surface gradually decreases. This region of gradually decreasing charge is known as the Gouy-Chapman layer. Atoms in this region are able to move freely but are still influenced by the charged surface (Hiemstra and van Riemsdijk, 1996, Krauskopf and Bird, 1995). The thickness of the electric double layer is strongly influenced by the salinity of the solution in which the mineral sits. The greater concentration of ions in more saline waters mean the charge deficit is more readily balanced and the electric double layer is thinner than in solutions with lower ionic strength (Krauskopf and Bird, 1995). The mathematical description of this double layer is described in detail in chapter 3.

### 2.1.2 Sorption processes

The sorption of an ion to a surface occurs by three main processes namely inner sphere surface complexation, outer sphere surface complexation (or cation exchange) and attraction in the diffuse ion swarm (Sposito, 1989). Inner sphere surface complexes (Figure 2.2) occur when an ion bonds directly to the surface site through ionic or covalent bonding (Krauskopf and Bird, 1995). As it involves direct bonding it follows that ions held in inner sphere complexes are the most strongly sorbed. Due to the sharing of electrons in covalent bonds they can only occur between specific ions and surface sites and may be considered specific adsorption (Sposito, 1989).

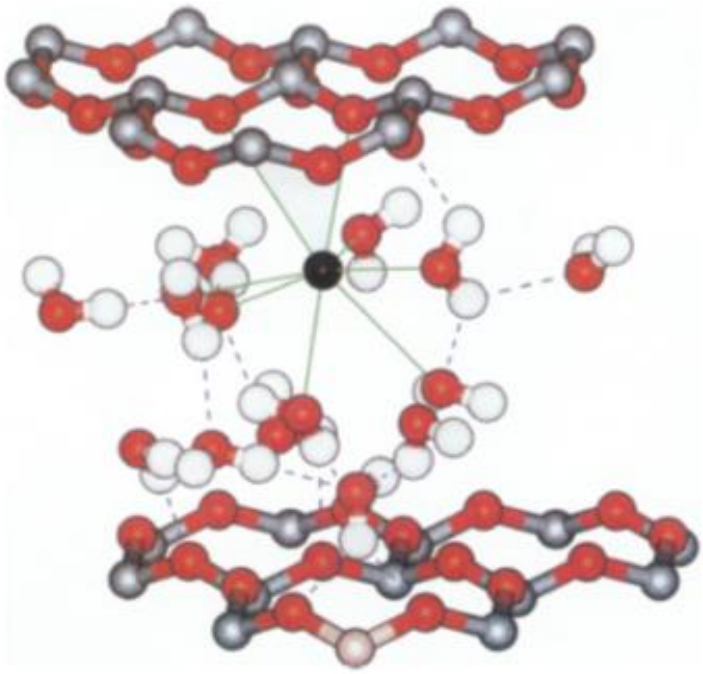

**Figure 2.2** Innersphere surface complex in the interlayer of a generic clay mineral surface, showing direct bonding between the adsorbed ion (black) and the surface oxygens on the upper surface layer (red circles). The target ion is shown with its waters of hydration present (red circles, O white circles, H). Reproduced from Sposito et al., (1999)

Outersphere surface complexes (Figure 2.3) occur when ions bond to water molecules which are then bonded to the surface through electrostatic attraction (Krauskopf and Bird, 1995). This form of bonding is non-specific and ions complexed in this way are considered readily exchangeable (Sposito, 1989).

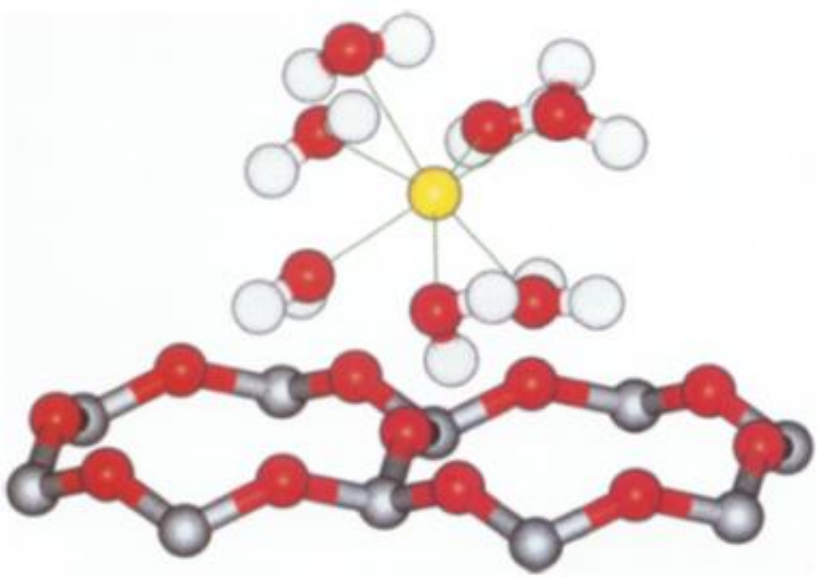

**Figure 2.3** An outersphere surface complex showing the target ion (yellow) surrounded by its waters of hydration and no direct chemical bonding between the ion and the surface oxygens (red circles), from Sposito et al. (1999)

### 2.1.3 The adsorption isotherm

The most important factor governing the amount of sorption is the concentration of the ion in solution. Thus increasing the solution concentration increases the sorbed concentration (Krauskopf and Bird, 1995). As with all chemical reactions sorption can be reversed (a process known as desorption) and the overall surface concentration is a product of these two processes occurring in dynamic equilibrium (Limousin et al.,

2007). Mathematically we can express the sorbed concentration, *Q* as a function of the solution concentration, *C*; solution volume, *V*; and the mass of the solid onto which sorption occurs, m (with $Q_0$ and $C_0$ being the initial sorbed and solution concentrations).

$$Q = \frac{V}{m}(C_0 - C) + Q_0 \tag{2.2}$$

Measurements of this relationship found experimentally under constant temperature, pressure and pH conditions are referred to as sorption isotherms (Krauskopf and Bird, 1995). Four main types have been found, they are referred to as the S, L, H and C isotherms because of their distinctive shape (Figure 2.4).

The S-curve show a shallow initial increase which steepens and then levels off. This is characteristic of a surface which shows low sorption at low solution concentrations but once a critical point has been reached the surface sorbs normally (Limousin et al., 2007). This critical point usually occurs once the surface has undergone some chemical alteration which allows it to effectively sorb the ion (Sposito, 1984). The L-curve show high initial adsorption with relatively little change in solution concentration followed by a levelling off either to a plateau or a shallow curve (Sposito, 1984, Limousin et al., 2007). The H-curve may be considered an exaggerated L-curve and is demonstrated by soils with extremely high affinity for the ion under investigation (Sposito, 1984, Limousin et al., 2007).

Finally the C-curve, which is the simplest isotherm and a graphical representation of the distribution coefficient, $K_d$ of the system (Limousin et al., 2007). It presupposes that the ratio of $Q$ / $C$ is an independent variable and remains constant for all values of C (Sposito, 1984).

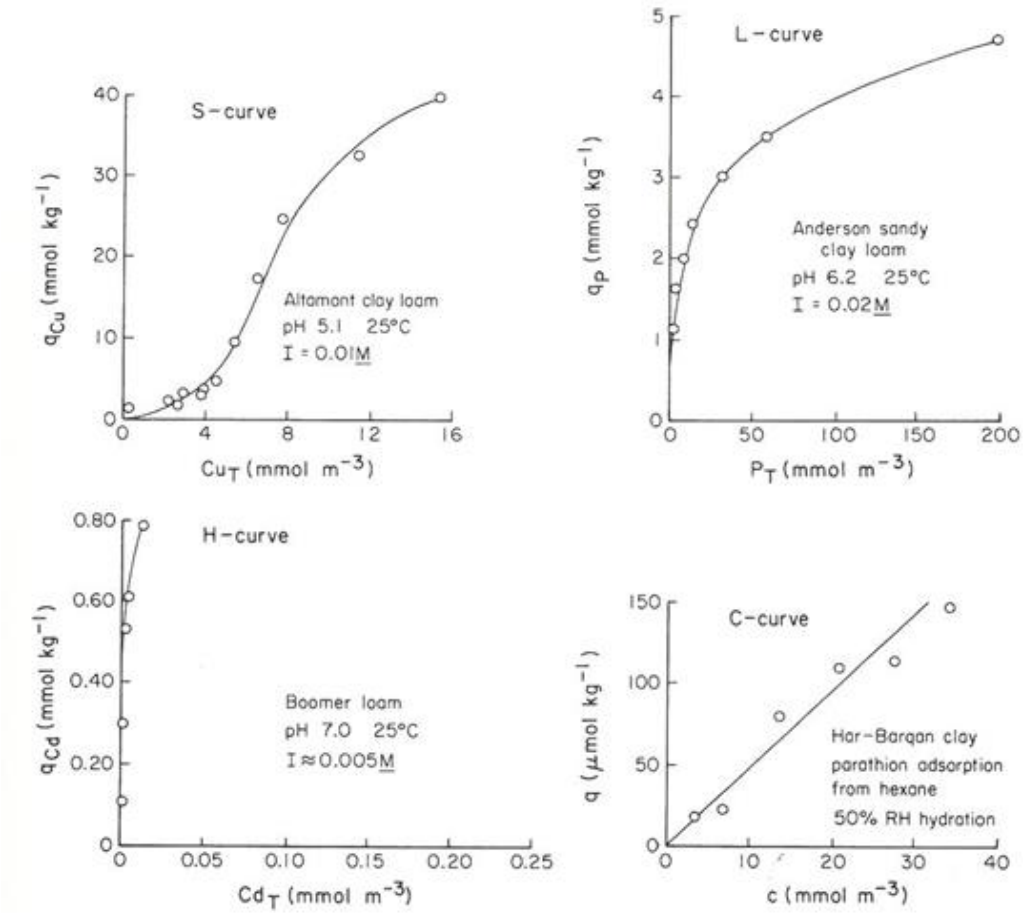


**Figure 2.4** The four main adsorption isotherms, S, L, H and C from Sposito (1984)

The normal relationship between solution and surface concentration (the L curve) can be modelled by the Freundlich and Langmuir equations (Appelo and Postma, 2005).

#### 2.1.3.1 The Freundlich isotherm

The Freundlich isotherm gives the simplest description of this relationship (Appelo and Postma, 2005) with *K* and *n* being reaction dependant coefficients.

$$Q = KC^n \tag{2.3}$$

Taking logs (eq 2.4) gives a straight line relationship with *Q* increasing linearly with *C* for any range of values (Limousin et al., 2007).

$$logQ = logK \times n\ logC \tag{2.4}$$

The Freundlich isotherm describes an idealised system and does not account for other limiting factors, such as number of surface sites (Appelo and Postma, 2005). Therefore it is only applicable at low *C* values where other factors are not of consequence (Sposito, 1984).

#### 2.1.3.2 The Langmuir isotherm

At higher solution concentrations the Langmuir isotherm must be used as it accounts for the maximum sorption of a surface where *Q* plateaus (Limousin et al., 2007). The Langmuir isotherm makes a number of assumptions: that sorption must reach a maximum; all surface sites behave the same; sites are independent of one another and sorption to one site does not affect sorption to its neighbour (Atkins and de Paula, 2006). The isotherm is described by the Langmuir equation (Limousin et al., 2007), where *K* is the equilibrium constant.

$$Q = Q_{max} \frac{KC}{1+KC} \tag{2.5}$$

## 2.2 Mineralogy of key minerals

### 2.2.1 Illite

The micaceous minerals are non-expanding layered dioctahedral or trioctahedral alumina-silicates (Fanning and Keramidas, 1977). Each layer is formed of a silica tetrahedra, an Aluminium octahedra and another silica tetrahedra (Grim, 1968). Isomorphic substitutions of $Al^{3+}$ for $Si^{4+}$ in the tetrahedral layer give an interlayer charge of -1 which is balanced by interlayer $K^{+}$ ions (Grim, 1968, Meunier and Velde, 2004, Velde, 1985). These form 10Å repeating units. An example of a unit cell is shown in Figure 2.5.

Illite, with the formula $(K,H_3O)(Al,Mg,Fe)_2(Si,Al)_4O_{10}[(OH)_2,(H_2O)]$ (Rosenberg, 2002), is a di-octahedral, non-expanding micaceous mineral (Srodon and Eberl, 1984) which was first identified from argillaceous rocks as having distinct optical and diffraction properties (Ross and Kerr, 1931). It was first named illite by Grim et al. (1937) although the definition as a distinct phase was initially contentious. However more recent advances in mineralogical characterisation have allowed illite to be defined as a distinct micaceous phase with a strict definition (Velde, 1985). Illite is differentiated

from mica as it often has lower levels of Al/Si substitution in the tetrahedral layer. This gives it a lower interlayer charge, typically 0.9 rather than 1. Because of this some of the interlayer sites are left vacant and may be filled with water rather than K (Meunier and Velde, 2004). This is why illite is sometimes referred to as K deficient or hydrated mica (Fanning and Keramidas, 1977). Interlayer $K^+$ ions can also be substituted for $Ca^{2+}$, $Mg^{2+}$ or $H^+$ (Grim, 1968). Isomorphic substitutions in the octahedral layer can also occur with $Mg^{2+}$ or $Fe^{2+}$ substituted for octahedral $Al^+$ causing a net negative charge (Grim, 1968).

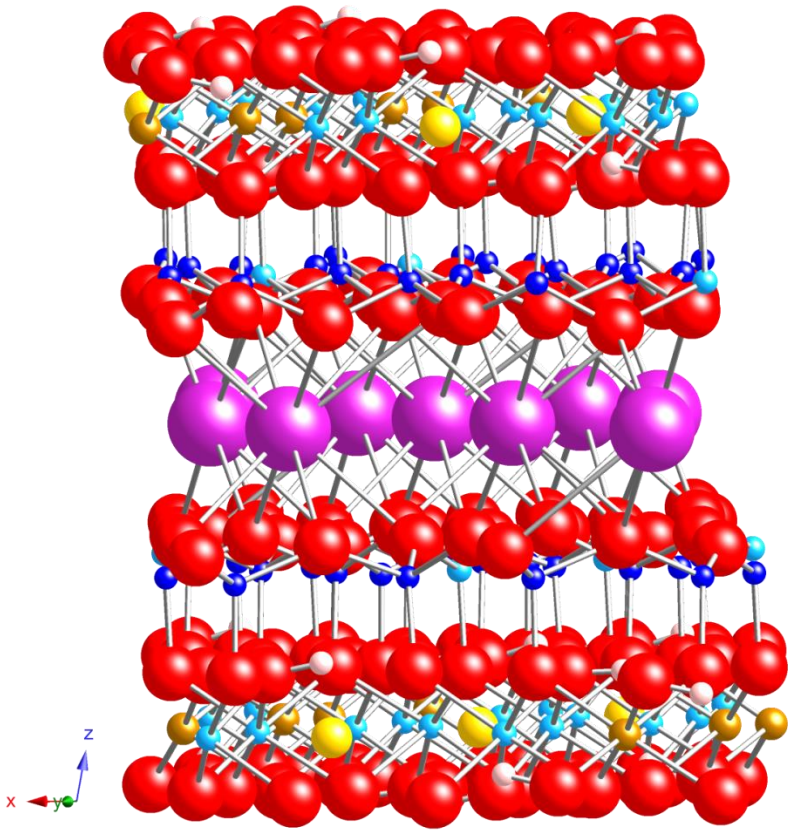


**Figure 2.5** Illite unit cell showing interlayer K ions (purple) surrounded by tetrahedrally and octahedrally coordinated Si (dark blue) and Al ions (light blue) with octahedrally substituted Fe (brown) and Mg (yellow)

#### 2.2.1.1 TEM observation of illite

The advent of transmission electron microscopy (TEM) has allowed detailed imaging of the nanoscale structure of illite and revealed in great detail the structural and chemical variation within the mineral (Kogure, 2002). At the most basic level TEM techniques can be important tools for characterisation of the macro and microstructure of illite minerals. Observation of layering and crystal thickness are important for characterising the mineralogical properties of samples (Dudek et al., 2002). Huggett (1982) used low resolution TEM and selected area electron diffraction (SAED) to observe the crystal nature of illite in sandstone, noting that particles consist of lath structures bound to a central core. Additionally a number of studies have focused on the formation of illite in diagenetic environments. Most illite in rocks is formed by diagenetic alteration of smectite minerals (Srodon et al., 1992). This is a complex process and leads to the formation of mixed layer illite/smectite phases (Elsass et al., 1997). The arrangement of these mixed layer minerals has been a major focus of research as illite/smectite mixed layering can be useful for identifying the origin and evolution of samples (Elsass et al., 1997, Veblen et al., 1990, Srodon et al., 1990, Srodon et al., 1992, Olives et al., 2000, Guthrie Jr and Reynolds Jr, 1998). Yates and Rosenberg (1996) and Yates and Rosenberg (1997) have shown that illite can also form from the dissolution of smectite phases at temperature in K rich solutions. Variation in illite formation environments and diagenetic processes can lead to a wide range of polytypes, namely $1M_d$, 1M (quite uncommon) and 2M (Grubb et al., 1991). These polytypes occur due to isomorphic substitutions in the TOT layers and crystallographic defects both

within layers and between interlayers (Chen and Wang, 2007, Chen et al., 2010, Guthrie Jr and Reynolds Jr, 1998).

Illite is a common clay mineral in soil environments where it weathers to smectite or vermiculite (Righi and Elsass, 1996). This process has been observed under TEM and it is thought to occur by expansion of the interlayer and removal of K ions (Sucha et al., 2001). This lowers the interlayer charge and can give rise to 'frayed edges' where the interlayer has expanded and other monovalent and divalent cations have entered the structure (Malla et al., 1993).

### 2.2.2 Chlorite

Chlorite is layed silicate mineral named for its greenish colour, 'chloros' means greenish-yellow in Greek (MacKenzie and Adams, 1994). It consists of mica-like layers with brucite-like interlayer hydroxide sheets, giving a 14Å basal spacing, Figure 2.6 (Weaver and Pollard, 1973, Velde, 1977, Barnhisel, 1977). Substitutions of $Al^{3+}$ for $Si^{4+}$, in the mica tetrahedra and $Fe^{2+}$ for $Al^{3+}$ in the mica octahedra yields a net -ve charge which is balanced by substitution of $Al^{3+}$ for $Mg^{2+}$ in the hydroxide interlayer (Weaver and Pollard, 1973, Grim, 1968). This charge balance holds the sheets together through electrostatic forces and is strong enough to prevent layer expansion. This lack of layer expansion causes the chlorite minerals to have a lower cation exchange capacity compared to 14 Å vermiculite or the smectite minerals (Grim, 1968, Barnhisel, 1977).

Chlorite is commonly associated with low-grade metamorphism and is also formed by sedimentation (Barnhisel, 1977, Velde, 1985) . It is found in temperate soils either directly inherited from parent material or from formation in the soil (Velde, 1977). Chlorite can form in acidic soils through weathering of micaceous minerals, such as biotite. As the biotite grains weather and their interlayers expand they are filled with Al and Mg ions yielding a chlorite structure. As a result these soil chlorites often have much higher levels of Al substitution in their interlayer hydroxide sheets than would be found in true chlorites (Velde, 1985).

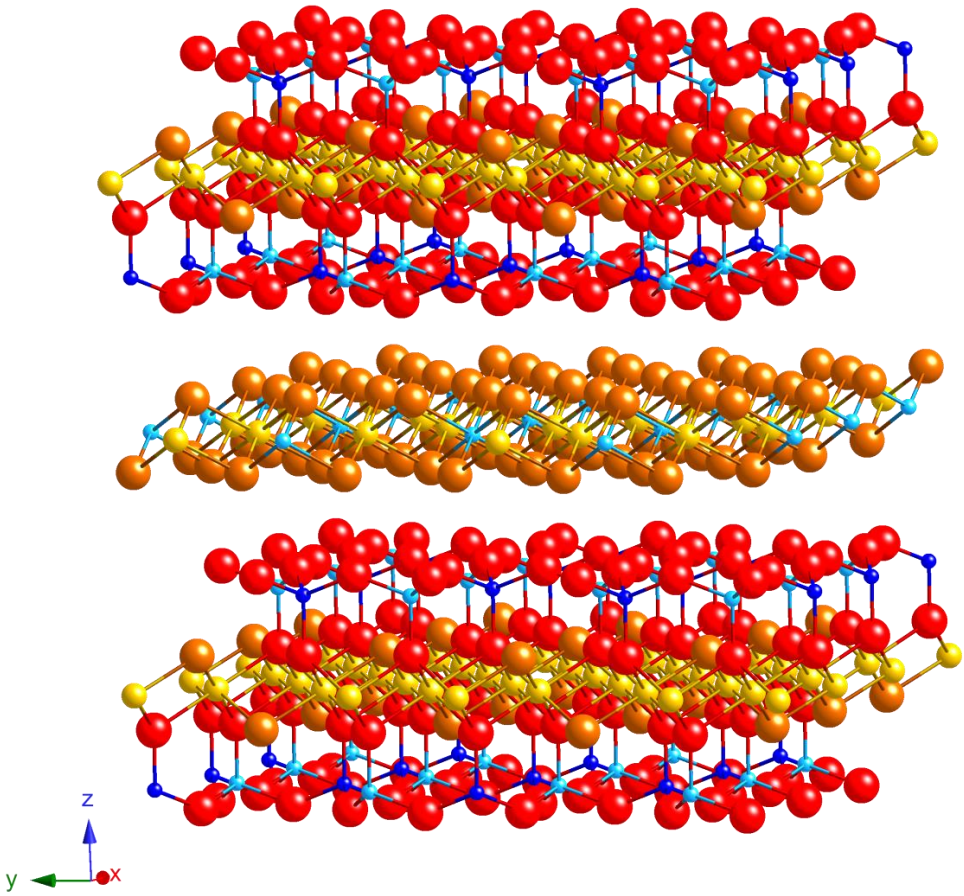


**Figure 2.6** The atomic structure of chlorite showing the aluminosilicate layers with oxygen (red), Mg (yellow), Si (dark blue) and Al (light blue) and the brucite like interlayer structure (comprised of Mg, Al and H (orange))

### 2.2.3 Goethite

Goethite is a common iron oxyhydroxide (FeOOH) which forms in the environment both directly from hydrothermal fluids and as a stable end member of the weathering of other iron oxides and hydroxides (Cornell and Schwertmann 2003, Schwertmann, 1971). As such it is found ubiquitously in the earth's crust and is also present on the surface of Mars, which together with other iron oxides give its distinctive red colour (Pollack et al., 1970a, Pollack et al., 1970b, Morris et al., 2008). Goethite has a relatively uniform structure with pairs of edge sharing iron octahedra which are bonded together through corner oxygens, (Figure 2.7). Substitutions can occur during formation, commonly Al for Fe, which can slightly alter the unit cell dimensions (Cornell and Schwertmann 2003).

The structural arrangement of goethite leaves reactive hydroxyl groups at the surface which can be involved in sorption reactions (Cornell and Schwertmann 2003). These hydroxyl groups act amphoterically becoming protonated at low pH and deprotonated at high pH. It is this amphoteric behaviour which controls the surface charge of goethtite (Onoda Jr and De Bruyn, 1966). At low pH the goethite has a positively charged surface and sorbs anionic species (Yates and Healy, 1975, Parfitt and Atkinson, 1976, Sigg and Stumm, 1981). At high pH the surface becomes negatively charged and cations can sorb (Doyurum Yusan and Akyil Erenturk, 2011, Missana et al., 2003, Sherman et al., 2008). The pH at which the surface has a neutral charge and the protonated and deprotonated OH groups are at equilibrium is known as the point of zero net proton charge (Cornell and Schwertmann 2003). This abundance of reactive sites and the often high

surface area to volume ratio of goethite makes it one of the most important phases controlling sorption of ions, including radionuclides, in soils.

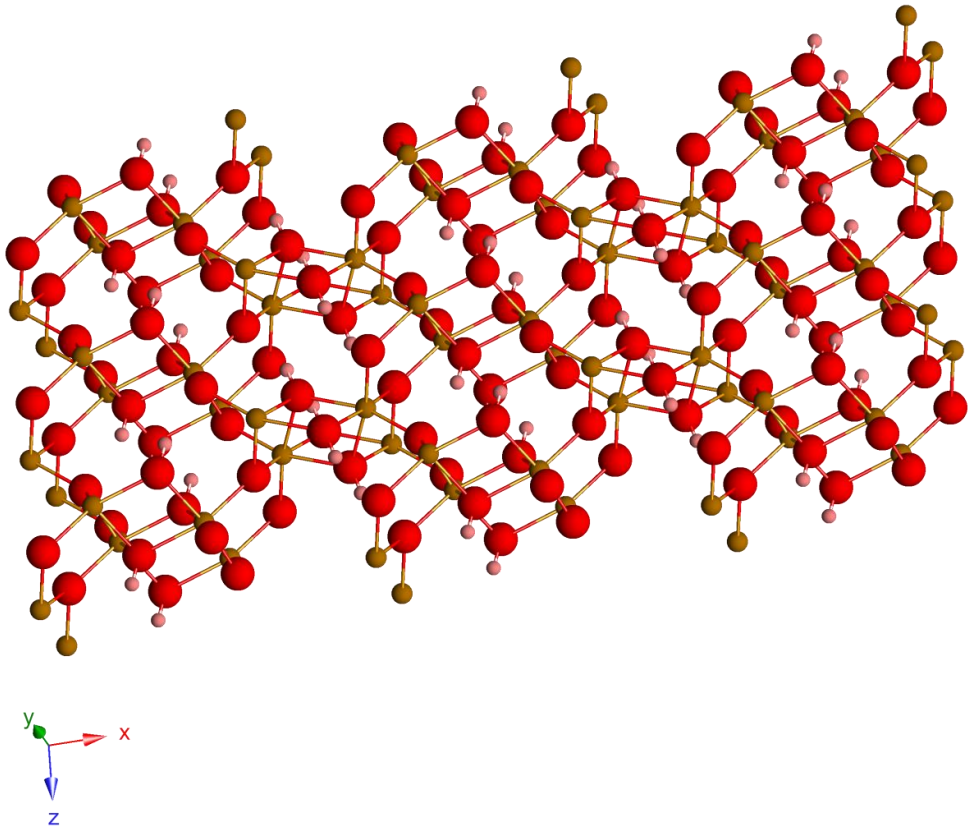


**Figure 2.7** Atomic structure of goethite showing iron (brown), oxygen (red) and hydrogen (small pink) atoms

## 2.3 Caesium in the environment

Caesium is a group 1 element with an atomic number of 55 (Mair and Snaith, 1994). It is the heaviest of the naturally occurring group 1 elements with a molecular mass of 132.91 (Bick et al., 2000, Masheim, 1968). Caesium is found ubiquitously in the environment, in rocks, minerals and waters. Although there are 40 known isotopes of Cs only the stable isotope, $^{133}$Cs, is naturally occurring (Macintyre, 1992). This is a rare earth element with $^{133}$Cs found at concentrations in igneous rocks and minerals between 1

and 5 ppm (Butler and Thompson, 1963, Cabell and Smales, 1957, Butler and Thompson, 1962). In aqueous solution it is present as the $Cs^+$ ion under all conditions of Eh and pH (Söderlund et al., 2011). The typical seawater $^{133}Cs$ concentration is ~0.002 ppm with groundwater concentrations varying widely (NCRP, 2007). However the majority of the Cs present in the environment is anthropogenically derived. Radioactive isotopes of Cs, notably $^{134}Cs$, $^{135}Cs$ and $^{137}Cs$ are generated from fission of U (and to a lesser extent Th and Pu) in nuclear reactors and atomic bombs. Although $^{134}Cs$ has a relatively high fission yield it has a relatively short half-life ($t_{1/2}$ = 2.1 yr) (NCRP, 2007). Conversely while $^{135}Cs$ is extremely long lived ($t_{1/2}$ = $2.3 \times 10^6$ yr) it has a low yield (NCRP, 2007). Due to its high yield and relatively long half-life $^{137}Cs$ is the dominant radioactive isotope present in the environment. It has a half-life of ~30 years (Brown et al., 1955) and it has a complex decay path with 95% decaying to a metastable form of $^{137m}Ba$ via $\beta$ emission. This subsequently decays to stable $^{137}Ba$ via emission of $\gamma$ rays. Roughly 5% of the $^{137}Cs$ undergoes direct $\beta$ decay to $^{137}Ba$ (Goodier et al., 1975). Figure 2.8 shows a diagrammatic representation of this decay series. The radioactive decay of $^{137}Cs$ makes it a major health hazard with the high energy $\gamma$ rays the main hazard. These generate a large external body dose which is hard to shield and can penetrate deep into the body (Hill et al., 2001). Ingestion of contaminated foodstuffs can also lead to a large body dose (Fry and Britcher, 1987). This external and internal radiation can have an adverse effect on health, especially increasing chance of cancers developing.

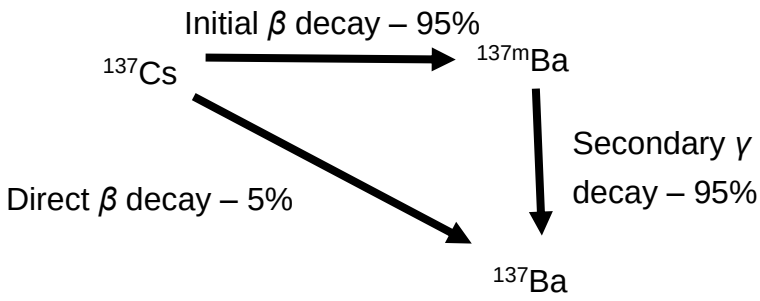


**Figure 2.8** The decay series of $^{137}Cs$

### 2.3.1 Sources

The radioactive Cs isotopes (predominantly $^{137}Cs$) are present at low concentrations ubiquitously in the environment. This diffuse contamination is derived from radioactive fallout from nuclear weapons testing and nuclear accidents as well as authorised atmospheric and oceanic releases from nuclear facilities. Nuclear weapon tests performed during the cold war period (1950s-1980s) represent the dominant source of $^{137}Cs$ in the environment and the main source of anthropogenic environmental radioactivity (UNSCEAR, 1993). Additionally large scale releases from civil power reactors have occurred as a result of nuclear accidents, which contaminated large areas of land. Most notable of these are the 1986 Chernobyl accident in the former USSR (now Ukraine), the 2011 Fukushima accident in Japan and the 1957 Windscale fire in Cumbria, UK (Beresford, 2006, Povinec, 2012, Dunster et al., 2007, UNSCEAR, 2000, Hodgson et al., 2004, Jacob et al., 2009, Walling and He, 1999).

In addition to this diffuse radioactivity, highly contaminated areas exist as a legacy of civil and military nuclear programmes. These include former R&D and weapons testing sites, such as Hanford and Oak Ridge in the USA. At

these sites releases of radioactive liqueurs to water courses and burial of radioactive material has left much of the soil contaminated to a greater or lesser degree with $^{137}Cs$ (Clapp and Watts, 1993, Ashwood, 1994, Cushing, 1992, Johnson et al., 1994). Most radioactively contaminated land in the UK is associated with civil power generation and reactor development, particularly at the Sellafield site.

### 2.3.2 Mobility of radiocaesium

There is disagreement in the literature regarding the vertical mobility of caesium within the soil profile. Caesium has been found to readily leach and move down the profile accumulating at depth in the mineral horizons (Copplestone et al., 1999, Ruhm et al., 1996). This is disputed by those who show the greatest concentration of $^{137}Cs$ at the top of the profile (Dolhanczuk-Srodka et al., 2006, Almgren and Isaksson, 2006). This variation is likely caused by soil physical and chemical properties (Dolhanczuk-Srodka et al., 2006). Where caesium is bound to the clays at the top of the soil it prevents its vertical migration down the profile (Arapis et al., 2003, Luksiene et al., 2006).

Spatial distribution of $^{137}Cs$ varies greatly depending on environmental conditions, principally soil properties (Plamboeck et al., 2006, Nylena and Grip, 1997, Owens and Walling, 1996, Luksiene et al., 2006, Panin et al., 2001). Finer textured soils show greater retention of $^{137}Cs$ (Akhmetov et al., 2004, Barisic et al., 1999) and the soil mineral phase is of more importance in retention of $^{137}Cs$ than organic matter (Hou et al., 2003). It has been

suggested that organic matter may even reduce sorption of $^{137}Cs$ to clay minerals (Shand et al., 1994) or increase its mobility through binding of $^{137}Cs$ to colloidal organic matter which is then highly mobile (Nakamaru et al., 2007). Although soil properties largely determine mobility, local hydrological conditions can have a great influence (Aslani et al., 2003). A final important influencing factor in determining $^{137}Cs$ mobility is bioturbation. Plant roots, micro-organisms (Rosen et al., 2009, Parekh et al., 2008) and earthworms (Müller-Lemans and van Dorp, 1996) have been shown to affect the distribution of $^{137}Cs$ (Tyler et al., 2001). All these factors are united by models of the mobility of $^{137}Cs$ within soils (Faroussi et al., 2007, Chamard et al., 1993)

### 2.3.3 Caesium sorption

Caesium sorption is a thermodynamically governed (Limousin et al., 2007, Cornell, 1993) cation exchange process (Poinssot et al., 1999, Cornell, 1993, Mollah and Ullah, 1998, He and Walling, 1996, Bostick et al., 2002). It shows complex kinetic behaviour with rapid initial sorption followed by a very gradual increase (Comans et al., 1991, Comans and Hockley, 1992). A soils mineralogy is a major control on its sorption properties (Liu et al., 2004, de Koning et al., 2007, Francis and Brinkley, 1976, Livens and Baxter, 1988) along with the Cs solution concentration (Torstenfelt et al., 1982).

The mineralogy of the soil is of primary importance in determining its sorptive capacity (Liu et al., 2004, de Koning et al., 2007, Francis and Brinkley, 1976). Sorption of Cs within soils is controlled by the mineral

fraction, and primarily by clays (He and Walling, 1996, Shenber and Eriksson, 1993, Cremers et al., 1988, Grutter et al., 1990, Chibowski and Zygmunt, 2002). Different clays, however, show different sorptive properties. Cs adsorbs on illite by inner-sphere complexation (Bostick et al., 2002) to the frayed edge sites where it is hard to exchange (Comans and Hockley, 1992, Hird et al., 1996). These sites are highly selective and will favour Cs over other cations (Cornell, 1993, Hird et al., 1996). Cs binds to the interlayer of both montmorillonite and vermiculite, in outer-sphere complexes in the former and inner-sphere in the latter (Bostick et al., 2002). On kaolinite Cs binds to smectite like interlayers (Kim et al., 1996a, Kim et al., 1996b). There is great variation in the literature regarding the relative sorptive capacity of different clays. Chorover et al (1999) found montmorillonite sorbed more Cs than illite. Nakao et al (2008) found vermiculite showed the most caesium sorption followed by montomorillonite while Bostick et al (2002) found the reverse. Kaolinite was found to sorb the least caesium (Kim et al., 1996b). This variation in sorptive behaviour is thought to be due to the differing cation exchange capacities of the minerals used (Nakao et al., 2008).

Caesium shows multisite sorption behaviour (Figure 2.9). Most authors propose a two site model with one high affinity site and one low affinity site (Liu et al., 2004, Man and Chu, 2004, Poinssot et al., 1999, Comans and Hockley, 1992) although Bradbury and Baeyens (2000) and Brouwer (1983) added a third (see Figure 2.9). The high affinity site has been identified as the frayed edge site (FES) of clays (primarily illite) (Poinssot et al., 1999,

Bradbury and Baeyens, 2000, Brouwer et al., 1983, Nakao et al., 2008, Davies and Shaw, 1993). This site accounts for around 0.02 – 0.08% of the total CEC of the soil (Zachara et al., 2002, Cremers et al., 1988). Caesium preferentially adsorbs to these sites through inner sphere surface complexation (Bostick et al., 2002, Nakao et al., 2008) due to its low hydration energy (Kim et al., 1996b). This process is thermodynamically favoured (Cornell, 1993) and caesium adsorbed to these sites is not readily exchangeable (Hird et al., 1996). Caesium also adsorbs by outer-sphere surface complexation and electrostatic attraction (Bostick et al., 2002) to low affinity planar sites on the surface of clays and in expanding interlayers (Poinssot et al., 1999) which account for around 99% of the CEC (Zachara et al., 2002). Caesium does not preferentially adsorb to these sites (Sawhney, 1972) and will only do so when the FES are saturated (de Koning et al., 2007, Bradbury and Baeyens, 2000, Kim et al., 1996b). The third, Type II site was proposed by Brouwer (1983) to be located at the edge of the frayed edge, where weakly hydrated monovalent ions (Cs, Rb, K) are favoured. They showed that the FES had a higher affinity for Cs than Rb or K, but that the Type II site did not differentiate.

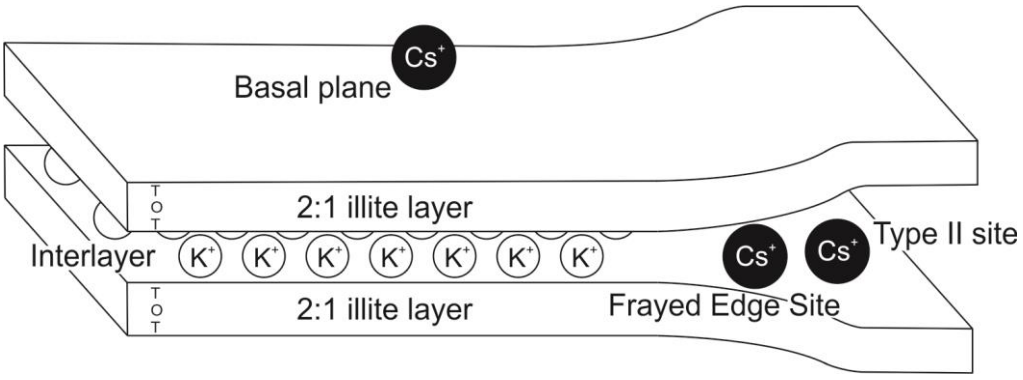


**Figure 2.9** Diagrammatic representation of multi-site Cs sorption to an illite particle

Caesium solution concentration affects the site, rate and amount of caesium sorbed (Torstenfelt et al., 1982, Man and Chu, 2004). At low concentrations, caesium is preferentially adsorbed to the high affinity FES where it is strongly bound (de Koning et al., 2007, Bradbury and Baeyens, 2000, Bostick et al., 2002, Chorover et al., 1999). As the solution concentration is increased the FES becomes saturated and excess caesium is bound to the non-specific planar sites (Bradbury and Baeyens, 2000, de Koning et al., 2007, Kim et al., 1996b).

## 2.4 Strontium in the environment

The alkali earth metal strontium (atomic number 38, atomic mass, 87.62) was discovered by Adair Crawford in 1790 (Macintyre, 1992, 1968, Murray, 1993). It is a silvery white metal and is highly reactive in water and readily oxidises in air. Strontium is found naturally as four isotopes, namely $^{84}Sr$, $^{86}Sr$, $^{87}Sr$ and $^{88}Sr$ in two main minerals, celestite ($SrSO_4$) and strontianite ($SrCO_3$) (Macintyre, 1992, 1968). The fission product $^{90}Sr$ (Wilson, 1996) is an important nuclear contaminant (Baes et al., 1986). It has a half-life of 29.1 years and decays to yttrium-90 via $\beta$ emission (EPA, 2010). Strontium is a particular concern to human health as it behaves the same as calcium entering bones and teeth where its emitted $\beta$ radiation can damage cells and cause cancers (Stamoulis et al., 1999). Sr is redox inactive and is present in the environment as the $Sr^{2+}$ cation under most solution conditions. However, at very high pH (>pH 13.5) Sr forms the $SrOH^+$ complex (Takeno, 2005).

### 2.4.1 Mobility

Radiostrontium shows greater environmental mobility than caesium or the actinides (Wilson, 1996, Froidevaux et al., 2010, Cross et al., 2002). This is likely because the majority of the $^{90}Sr$ is held in the easily extractable soil fraction and remains mobile rather than being strongly bound (Salbu et al., 1994, Chien et al., 2007). Studies of the vertical distribution of $^{90}Sr$ showed great variation between sites. Fernandez et al (2006) found the highest concentrations at 45-50 cm depth and predicted a vertical migration of around 1 cm $year^{-1}$. This movement speed is in agreement with Solecki (2007) although he found it to increase with depth. By contrast Lujaniene et al (2002) found little vertical movement with the majority being held in the top 3cm. Soil properties are important in determining the mobility of $^{90}Sr$ (Chawla et al., 2010, Chien et al., 2007) with texture a major determinant (Forsberg et al., 2000). Movement within the soil aqueous fraction (Amano et al., 1999, Mason et al., 2000, Askbrant et al., 1996) and interactions with organic matter (Agapkina et al., 1995, Lujaniene et al., 2002) also influence strontium's environmental mobility. Binding of strontium to colloids is also thought to increase its mobility (Tanaka and Ohnuki, 1996, Mason et al., 2000, Matsunaga et al., 2004). A number of studies have attempted to use this knowledge to model the movement and evolution of $^{90}Sr$ within the environment (Monte, 2010, Fernandez et al., 2006, Cigna et al., 2000, Chamard et al., 1993, Bulgakov and Konoplev, 2005).

### 2.4.2 Sorption & precipitation

The greater mobility of Sr in soil is chiefly due to its sorption behaviour. As Sr is a strongly hydrated divalent cation it primarily interacts with the

charged surfaces of soils by forming outer-sphere surfaces complexes (Axe et al., 1998, Carroll et al., 2008, Chen and Hayes, 1999, Parkman et al., 1998, Sahai et al., 2000, Chen et al., 2006). Sr held in these outer-sphere complexes is weakly sorbed and can be easily exchanged by other divalent cations (Solecki, 2005, Wang et al., 2004). Therefore Sr held in this way can be easily remobilised and continue to migrate in the environment. On clay minerals Sr principally forms these complexes on the permanent charge cation exchange sites on the clay's basal plane (Saunders and Toran, 1995, Bartl and Czurda, 1991, Konishi et al., 1988, Lee et al., 1997). As these sites hold a permanent structural charge, this sorption occurs largely independently of pH (Missana et al., 2008). It can be strongly influenced by cation competition, however, with strongly hydrated cations such as Ca and Mg effectively competing with Sr and reducing total sorption to clay minerals (Khan et al., 1995). In addition Sr also sorbs to $O^-$ and OH sites on a range on minerals including quartz and amorphous silica; iron oxides and at the broken edge of clays (Arafat et al., 2010, Balek et al., 1996, Carroll et al., 2008, Chen et al., 2006, Lu and Mason, 2001, Missana et al., 2008). Sorption of Sr to these sites is strongly controlled by pH as their charge is controlled by protonation and deprotonation processes. Sr readily sorbs at high pH, where the sites hold a negative charge, but remains in solution when the sites protonate and take on a positive charge, at low pH (Balek et al., 1996, Carroll et al., 2008, Fujikawa and Fukui, 1997, Li et al., 2007, Rahnemaie et al., 2006).

In addition to sorption processes the environmental behaviour of Sr is controlled by precipitation reactions. Under conditions of highly elevated pH atmospheric $CO_2$ equilibrates with the solution leading to an increase in dissolved carbonate ions. The carbonate complexes with any Sr ions present, which precipitates $SrCO_3$ on mineral surfaces (Sahai et al., 2000, Mell et al., 2006, Parkman et al., 1998). Calcium carbonates form, when Ca is present, with partial substitution of Sr for the Ca in their structure (Choi et al., 2006). In the absence of $CO_2$ dissolution of silicate minerals and reprecipitation of zeolites can incorporate aqueous Sr ions, although this takes a long time (Chorover et al., 2003, Wallace et al., 2013).

## 2.5 The UK's nuclear legacy

Nuclear power is an important energy source globally (Wilson, 1996) and as of 2008 13% of the UK's energy production came from nuclear reactors (DECC, 2009). The process of generating electricity from raw fuel is known as the nuclear fuel cycle (WNA, 2010). It has six main stages: briefly, mine and mill the ore, purify the ore, utilise the fuel in reactors, reprocess the fuel, reuse the reprocessed U and Pu and dispose of the waste (Wilson, 1996). All stages of the nuclear fuel cycle create waste which requires management and disposal (NEA and OECD, 2006). This comes in three main forms, low level waste (which has low activity), intermediate level waste (which can range from mildly to very radioactive) and high level waste (which is both highly radioactive and heat producing) (Openshaw et al., 1989). Historically the UK has opted for reprocessing and surface storage (McKenzie and

McCord, 2010), although plans are underway for a deep earth repository (DEFRA, 2008).

Rapid industrialisation within the nuclear industry has left a legacy of contaminated land on nuclear sites (Bell et al., 1997, Beresford, 2006, Joyce and Port, 1999). Many of the former generation of power plants are now undergoing decommissioning and remediation forms an important part of this process (Beresford, 2006). In the UK responsibility for this falls to the Nuclear Decommissioning Authority in collaboration with site managers (NDA, 2010a). Figure 2.10 gives an overview of NDA sites around the UK and the various contamination issues are summarised below. This thesis focuses specifically on the Sellafield site in West Cumbria which is discussed in more detail in section 2.6.

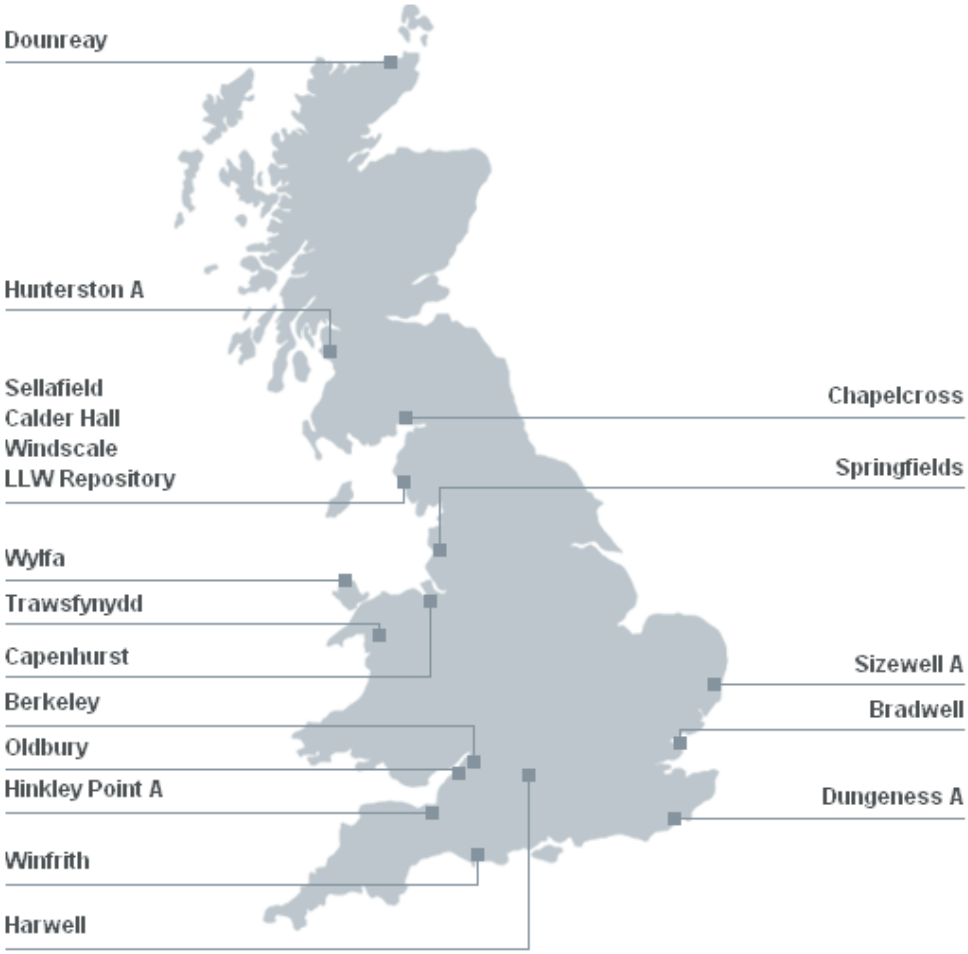


**Figure 2.10** Nuclear decommissioning authority owned sites (NDA, 2009a)

### 2.5.1 Dounreay

Until 1994 Dounreay operated three reactors and a fuel processing facility (NDA, 2013a). The site is managed by Dounreay Site Restoration Ltd under license. The site has is known to be contaminated with $^{137}Cs$, $^{90}Sr$ and some $^{234}U$ (Atherton, 2005) and $^{99}Tc$ (Begg et al., 2007). Contamination at Dounreay was caused by leaks, spills and airborne releases, but is at fairly low levels (Goss and Liddiard, 2007).

### 2.5.2 Hunterston A

The Hunterston A plant stopped producing in 1989 and is currently undergoing decommissioning (NDA, 2009e). A brief review of the literature shows no work has been done on contamination at the Hunterston A site suggesting it is not a major problem.

### 2.5.3 Chapelcross

Built initially to provide military grade Uranium and Plutonium as well as for power generation Chapelcross operated from 1959 – 2004 (NDA, 2009d, Stewart, 1959). There is little in the literature relating to land contamination at Chapelcross however a report by the Scottish Environmental Protection Agency reported tritium as present in the groundwater (SEPA, 2009).

### 2.5.4 Trawsfynydd

Trawsfynydd operated two reactors from 1965 to 1991 and commenced decommissioning in 1993 (Anonymous, 2010a). Although there are some radioactive soils on site it is considered to be at low levels and would not be formally classified as contaminated land (NDA, 2010c, Westall, 2007).

### 2.5.5 Capenhurst

Capenhurst housed a uranium enrichment plant which operated until 1982 (NDA, 2009c). It has been identified as a site for storage of urranium and will remain a nuclear licensed site (NDA, 2006c). Previous operations have caused little land contamination and the focus now must be on preventing contamination through future activities (HSI, 2004).

### 2.5.6 Berkeley

Berkeley was one of the UKs first nuclear power plants operating from 1962 until 1989 (NDA, 2009b). A contaminated land survey is currently being undertaken as part of the decommissioning process. (NDA, 2006a).

### 2.5.7 Hinkly Point A

Operating from 1965 to 1999 Hinkly Point A is surrounded by ecologically valuable land (MagnoxSouth, 2010b). Some low level contaminated soil is thought to be present on the site (NDA, 2010e) though a thorough contaminated land assessment could not be found.

### 2.5.8 Harwell

The Atomic Energy Research Establishment at Harwell was built in 1946 and carried out nuclear research with labs and test reactors until 1990 (UKAEA, 2003). A 2009 contaminated land survey found a number of areas of radioactive and non-radioactive contamination which need remediating (Crook, 2009, Hamblin and Ensor, 2004).

### 2.5.9 Dungeness A

The Magnox reactors at Dungeness A operated from 1965 till 2006 (MagnoxSouth, 2010a). At the site there is approx 1100 $m^3$ of radioactively contaminated soil as well an area contaminated with non-radioactive hydrocarbons (NDA, 2010d).

### 2.5.10 Sizewell A

Sizewell A operated 2 reactors from 1966 to 2006 (MagnoxSouth, 2010c). It is currently coming to the end of the defueling stage and about to begin decommissioning (NDA, 2009f, NDA, 2006d). Assessment of land contamination will occur during the care and maintenance phase which is yet to begin (NDA, 2006d).

### 2.5.11 Bradwell

The power plant at Bradwell operated from 1962 till 2002 (NDA, 2006b). It is known that there is some contaminated ground at Bradwell but it is yet to be fully investigated (MagnoxSouth, 2008).

### 2.5.12 Winfrith

Winfrith was built in 1957 and served as a research site until 1990. The site was occupied by nine separate reactors over its lifetime (Anonymous, 2010b). Although no contaminated land survey was found, publically available reports indicate that contaminated land is present (NDA, 2010b).

## 2.6 Sellafield site overview

The Sellafield site in West Cumbria, UK (aerial photo, Figure 2.11 and site map, Figure 2.12), is one of the largest and most complex nuclear sites in Western Europe. It is situated to the west of the Lake District National Park on the coast of the Irish Sea (see Figure 2.12 inset). Sellafield began operating as a nuclear licensed site in 1947 (NDA, 2013b). Initially, this

solely involved the operation of the Windscale piles which were used to generate plutonium for military uses (SellafieldLtd, 2010). It was this work conducted at Sellafield which led to the successful development of the UK's first atomic bomb (Bolter, 1996). As well as the military research, Sellafield also conducted extensive nuclear power research. This development of nuclear power generation culminated in 1956 with the opening of the Calder Hall nuclear power plant. This was the world's first nuclear reactor to generate commercial electricity and it remained in operation until 2003 (NDA, 2013b).

Additionally, the UK's nuclear waste is reprocessed and stored at Sellafield (McKenzie and McCord, 2010). This reprocessing is performed at the Thermal Oxide Reprocessing Plant (THORP) facility and the Magnox reprocessing plant for historic Magnox (magnesium oxide cladded) fuel (NDA, 2011, SellafieldLtd). Both of these reprocessing plants are located within the separations area where fuel awaiting reprocessing is also stored in ponds. It is this area where most of the historic leaks have occurred and most of the contamination is present. Originally the aim of this reprocessing was to obtain plutonium for use in the UK atomic weapons program (Bolter, 1996). As military demand for plutonium has reduced most of it was fed into production of mixed oxide fuels (MOX) (Bolter, 1996). However the UK's MOX plant was recently shut down as demand for MOX fuel has greatly reduced (Harvey, 2011). The UK does not currently have any reactors which are running on MOX. Therefore the majority of the MOX fuel was exported, chiefly to Japan (Harvey, 2011). This demand has ceased following the

closure of many of Japans nuclear plants as a result of the Fukushima disaster (Harvey, 2011). This closure of the MOX plant has left large stock piles of plutonium at Sellafield with no clear value or use. (Connor, 2011). This long history and mixed use makes the site a complex mix of both operating facilities and buildings at various stages of decommissioning (NDA, 2013b, SellafieldLtd, 2010).


**Figure 2.11** Satellite image of the Sellafield nuclear site ©2012 Digital Globe, GeoEye, Infoterra Ltd & Bluesky, TerraMetrics

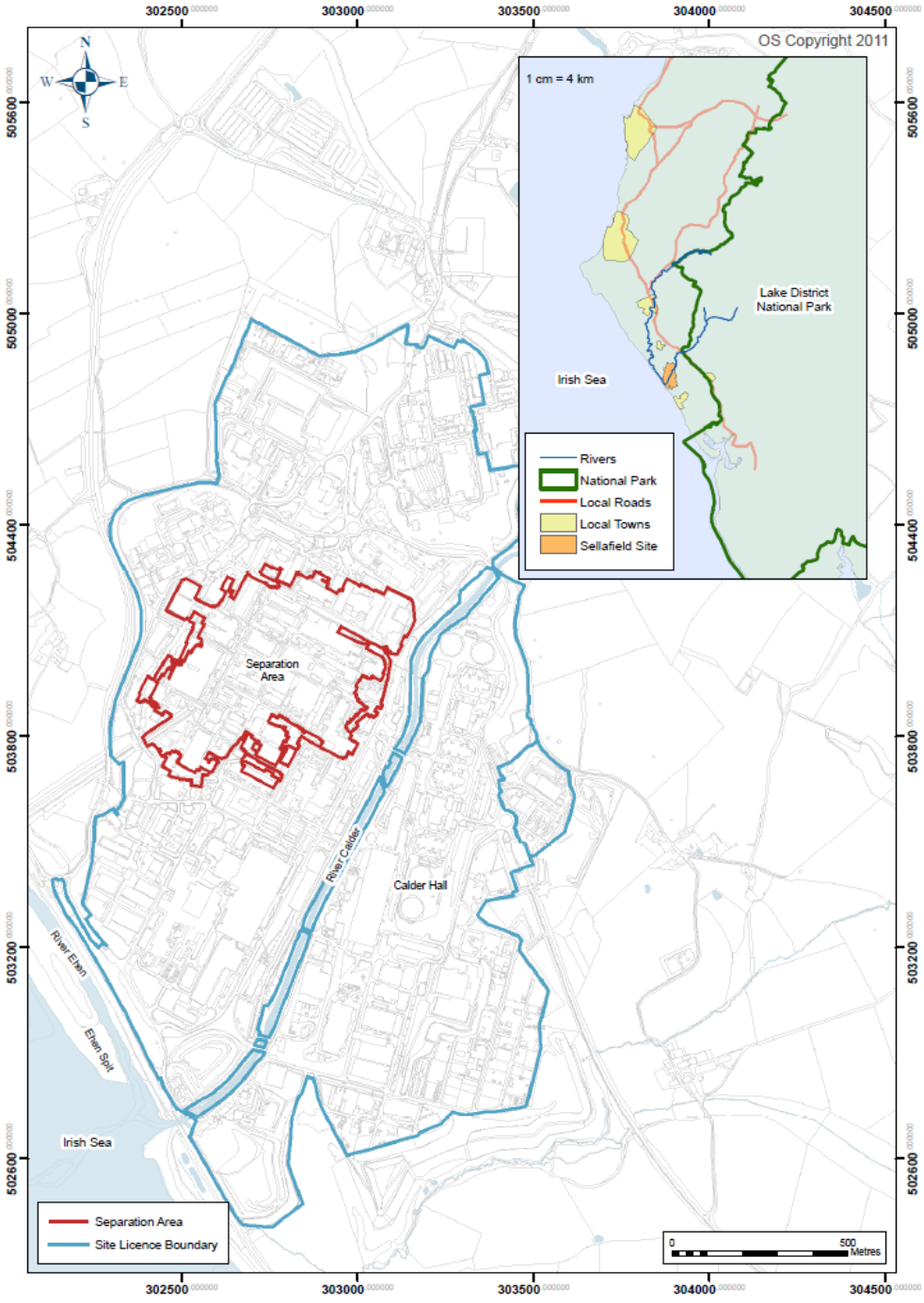


**Figure 2.12** Overview map of the Sellafield site. Site boundary fence is shown in blue and separation area boundary is shown in red. Inset shows the location of the Sellafield site with relation to the surrounding area. Reproduced from Sellafield 2011 groundwater report (McKenzie et al., 2011)

### 2.6.1 Geology

The geology of the Sellafield area has been extensively studied for a number of years owing to the planned construction of a geological repository for nuclear waste (Chaplow, 1996). The area has a complex geological and tectonic history. Borehole investigations on the site have uncovered a complex succession, shown in Figure 2.13 (Chaplow, 1996). The earliest stratum is the Borrowdale volcanic group (Chaplow, 1996, Michie, 1996). These were deposited as a result of volcanic activity during the late Ordovician and were then uplifted and extensively eroded (Chaplow, 1996, Michie, 1996). This is overlain by Carboniferous limestone (Chaplow, 1996). Permian sediments then occur, notably Brockham, and St Bees Evaporites (dolomite and anhydrite; Michie,1996) and St Bees Shale (Chaplow, 1996). This is overlain by Triassic sandstones namely the fluvial St Bees sandstone and the alluvial Calder sandstone (Michie, 1996). These are overlain by a thin layer of the Ormskirk sandstone which is much more extensive under the Irish Sea (Michie, 1996). Finally the surface layers comprise unconsolidated heterogeneous glacial drift deposits (Michie, 1996). These drift deposits have weathered to form the soils underlying Sellafield and most contaminant radionuclides are present in the drift deposits (although groundwater flow has also contaminated the underlying sandstones to a lesser degree). The quaternary drift deposits are described in more detail in the next section.

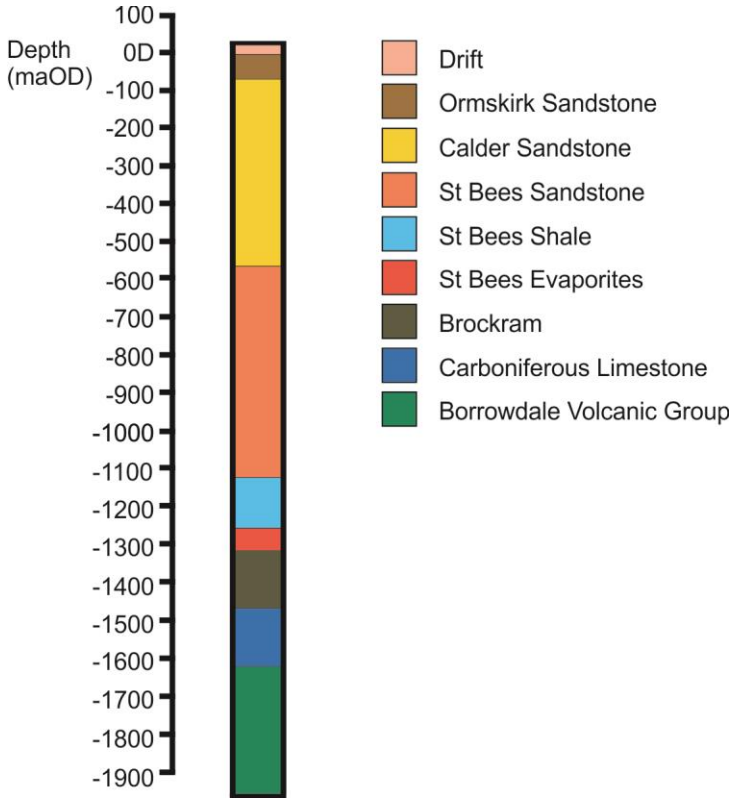


**Figure 2.13** Geological strata from a deep borehole on the Sellafield site, reproduced from Chaplow (1996)

### 2.6.2 Sediment mineralogy

Most of the radionuclide contamination at Sellafield is located in the surface layers of sediment. This material is characterised as heterogeneous quaternary drift deposits overlying the Triassic sandstone (see Figure 2.14). The deposits themselves are primarily alluvial sand and gravel deposits mixed with river terrace deposits and fluvio-glacial tills (Chaplow, 1996, Hunter, 2004). The deposits contain a number of clay lenses and sand channels which are important in controlling the groundwater flow across the site (McKenzie and McCord, 2010). As mineralogy is an important control on the mobility and sorption of radionuclides (especially $^{137}Cs$) these sediments have been extensively studied. The sediments have a very coarse texture with around 50 weight % gravel or course sand (> 2 mm) and around 40

weight % in the sand fraction (Randall et al., 2004). The bulk sediment is dominated by quartz (60 weight %), and feldspar (10 weight % albite; 10 weight % orthoclase) with about 18 weight % di-octahedral and tri-octahedral clay minerals (Randall et al., 2004). Very minor quantities (2 weight %) of haematite are also present (Randall et al., 2004). The clay sized fraction (<2 um) accounts for around 1-5% by weight and the remainder is silt and sand (Randall et al., 2004). As the sorption of radionuclides (especially Cs) is so strongly controlled by the clay fraction and detailed understanding of the mineralogy of the clay fraction is also important. The clay fraction of the drift deposits is dominated by mica and micaceous minerals (chiefly illite, being around 72 weight % (Randall et al., 2004, Dutton et al., 2009)). The remainder is a mix of chlorite (5 weight %), mixed chlorite-vermiculite (14 weight %), vermiculite (3 weight %) and kaolinite (6 weight %) (Randall et al., 2004).

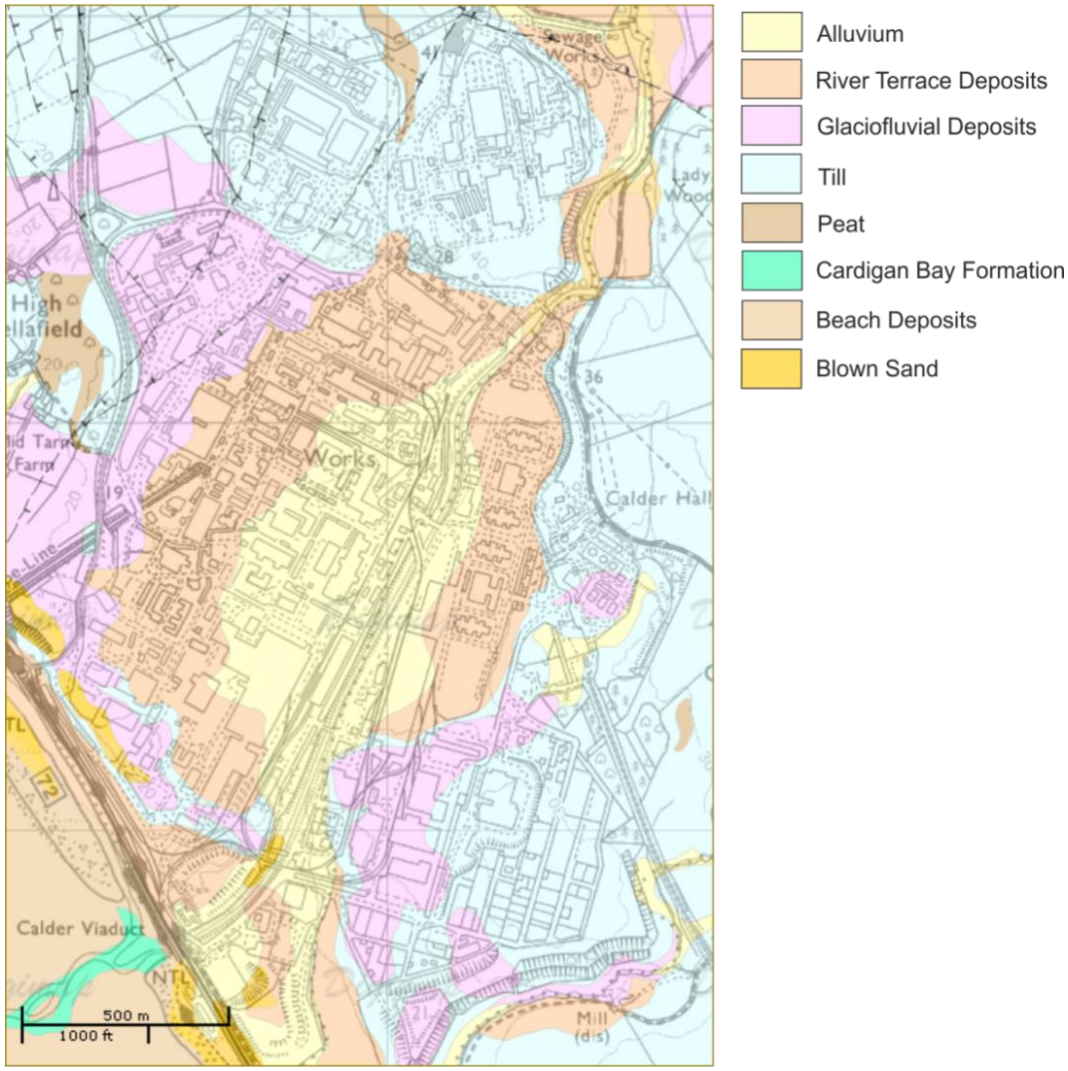


**Figure 2.14** Drift map of the Sellafield site (BGS, 2010)

### 2.6.3 Contamination on site

Various leaks and spills over the life of the facility have left a legacy of radioactive land and groundwater (Reeve and Eilbeck, 2009, McKenzie and McCord, 2010). The Sellafield Contaminated Land Study was begun in 2001 and has yielded information about this contamination (Hunter, 2004). Investigations by Hunter (2004) showed that the majority of contaminated soil present at Sellafield was contained within the separation area, that is "the area around the Magnox reprocessing plants and the older production plants in the centre of the site" (SellafieldLtd, 2010). The boundary of the

separation area is shown in Figure 2.12. Total volumes of contaminated soil on the site were estimated at 1.285 x$10^7$ $m^3$ and the main radioactive contaminants released were $^3$H, $^{137}$Cs, $^{99}$Tc and $^{90}$Sr (Dutton et al., 2009). A number of non-radioactive contaminants were also found on the site, notably Pb, Zn, PAHs, PCBs, TPHs, Cu and asbestos (Hunter, 2004).

As the dominant contaminant at Sellafield $^3$H is found in a large plume which extends from the separations area (the source of most of the leaks) towards the Irish sea (McKenzie et al., 2011). This plume follows the dominant groundwater path and reflects the high mobility of $^3$H in groundwater at Sellafield (Cruickshank, 2012). The behaviour of $^{137}$Cs on the site is thought to be complex. A number of leaks are known to be present at the site and $^{137}$Cs has been detected in groundwater at a number of boreholes (McKenzie and McCord, 2010, McKenzie and Armstrong-Pope, 2010, McKenzie et al., 2011). However concentrations are extremely low and the Cs is not rapidly migrating in the groundwater. This is different to $^{99}$Tc which has been shown to be highly mobile and has migrated across most of the site (Cruickshank, 2012). $^{90}$Sr is also more mobile and has been seen migrating from the initial point source leaks, it is now fairly homogenously distributed in groundwater across the site (Cruickshank, 2012).

Concentrations for both $^{90}$Sr and $^{99}$Tc in groundwater are also significantly higher than $^{137}$Cs (McKenzie et al., 2011). The low concentrations of $^{137}$Cs and the low rate of migration are explained by its strong sorption to the sediments underlying the site (Randall et al., 2004). Most of the $^{137}$Cs

contamination on the site is thought to be associated with the solid phase (Randall et al., 2004) . Therefore groundwater monitoring may not be a good measure of the potential level of $^{137}Cs$ contamination (and associated dose) close to the site of the leaks.

Remediation of this land and groundwater contamination forms an important part of the long term decommissioning plan for Sellafield (SellafieldLtd, 2011). The final financial liability of full decommissioning and remediation of the whole site is expected to be around £42bn (NDA, 2013b).

## 2.7 References

Agapkina, G. I., Tikhomirov, F. A., Shcheglov, A. I., Kracke, W. & Bunzl, K. 1995. Association of Chernobyl-derived Pu-239+240, Am-241, Sr-90 and Cs-137 with organic matter in the soil solution. *Journal of Environmental Radioactivity,* 29**,** 257-269.

Akhmetov, E. Z., Adymov, Z. I., Dzhezairov-Kakhramanov, V. & Yermatov, A. S. 2004. Characteristics of broken grounds at the former Azgir nuclear test site. *In:* ZAIDI, M. K. & MUSTAFAEV, I. (eds.) *Radiation Safety Problems in the Caspian Region.* Dordrecht: Springer.

Almgren, S. & Isaksson, M. 2006. Vertical migration studies of Cs-137 from nuclear weapons fallout and the Chernobyl accident. *Journal of Environmental Radioactivity,* 91**,** 90-102.

Amano, H., Matsunaga, T., Nagao, S., Hanzawa, Y., Watanabe, M., Ueno, T. & Onuma, Y. 1999. The transfer capability of long-lived Chernobyl radionuclides from surface soil to river water in dissolved forms. *Organic Geochemistry,* 30**,** 437-442.

Anonymous. 2010a. *Our sites: Trawsfynydd* [Online]. Magnox North. Available: http://www.magnoxnorthsites.com/about-us/our-sites/trawsfynydd [Accessed November 2010].

Anonymous. 2010b. *Winfrith Site introduction* [Online]. Research Site Restoration Ltd. Available: http://www.research-sites.com/winfrith-site-operations/site-introduction [Accessed November 2010].

Appelo, C. A. J. & Postma, D. 2005. *Geochemistry, groundwater and pollution,* Leiden, A.A. Balkema Publishers.

Arafat, H. A., Aase, S. B., Bakel, A. J., Bowers, D. L., Gelis, A. V., Regalbuto, M. C. & Vandegrift, G. F. 2010. The application of in situ formed mixed iron oxides in the removal of strontium and actinides from nuclear tank waste. *AIChE Journal,* 56**,** 3012-3020.

Arapis, G., Saitanis, C. & Salakou, G. 2003. Caesium-137 distribution in the soil in a semi-natural ecosystem in Greece. *In:* LEKKAS, T. D. (ed.) *Proceedings of the 8th International Conference on Environmental Science and Technology, Vol B, Poster Presentations.* Athens: Univ Aegean.

Ashwood, T. L. 1994. Eighth Annual Report on the ORNL Biological Monitoring and Abatement Program. Oak Ridge, Tennessee: Oak Ridge National Laboratory.

Askbrant, S., Melin, J., Sandalls, J., Rauret, G., Vallejo, R., Hinton, T., Cremers, A., Vandecastelle, C., Lewyckyj, N., Ivanov, Y. A., Firsakova, S. K., Arkhipov, N. P. & Alexakhin, R. M. 1996. Mobility of radionuclides in undisturbed and cultivated soils in Ukraine, Belarus and Russia six years after the Chernobyl fallout. *Journal of Environmental Radioactivity,* 31**,** 287-312.

Aslani, M. A. A., Aytas, S., Akyil, S., Yaprak, G., Yener, G. & Eral, M. 2003. Activity concentration of caesium-137 in agricultural soils. *Journal of Environmental Radioactivity,* 65**,** 131-145.

Atherton, N. 2005. 2004 Contaminated Land Report. Dounreay Site Restoration Ltd.

Atkins, P. & de Paula, J. 2006. *Atkins' Physical Chemistry,* Oxford, Oxford University Press.

Auerbach, S. M., Corrado, K. A. & Dutta, P. K. 2004. *Handbook of Layered Materials,* New York, Marcel Dekker, Inc.

Axe, L., Bunker, G. B., Anderson, P. R. & Tyson, T. A. 1998. An XAFS analysis of strontium at the hydrous ferric oxide surface. *Journal of Colloid and Interface Science,* 199**,** 44-52.

Baes, C. F., Garten, C. T., Taylor, F. G. & Witherspoon, J. P. 1986. Long-term environmental problems of radioactively contaminated land. *Environment International,* 12**,** 545-553.

Balek, V., Málek, Z., Šubrt, J. & Ždimera, A. 1996. Characterization of iron(III) oxide and oxide-hydroxide as Sr-sorbent. *Journal of Radioanalytical and Nuclear Chemistry,* 212**,** 321-331.

Barisic, D., Vertacnik, A. & Lulic, S. 1999. Caesium contamination and vertical distribution in undisturbed soils in Croatia. *Journal of Environmental Radioactivity,* 46**,** 361-374.

Barnhisel, R. B. 1977. Chlorites and Hydroxy Interlayered Vermiculite and Smectite. *In:* DIXON, J. B., WEED, S. B., KITTRICK, J. A., MILFORD, M. H. & WHITE, J. L. (eds.) *Minerals in Soil Environments.* Madison: Soil Science Society of America.

Bartl, U. & Czurda, K. A. 1991. Migration and retention phenomena of radionuclides in clay-barrier systems. *Applied Clay Science,* 6**,** 195-214.

Begg, J. D. C., Burke, I. T. & Morris, K. 2007. The behaviour of technetium during microbial reduction in amended soils from Dounreay, UK. *Science of the Total Environment,* 373**,** 297-304.

Bell, F. G., Lindsay, P. & Hytiris, N. 1997. Contaminated ground and contaminated estuary sediment illustrated by two case histories. *Environmental Geology,* 32**,** 191-202.

Beresford, N. A. 2006. Land contaminated by radioactive materials. *Soil Use and Management,* 21**,** 468-474.

BGS. 2010. *British Geological Survey Maps*, 1:50,000. NERC.

Bick, M., Prinz, H. & Steinmetz, A. 2000. Cesium and Cesium Compounds. *Ullmann's Encyclopedia of Industrial Chemistry.* Wiley-VCH Verlag GmbH & Co. KGaA.

Bolter, H. 1996. *Inside Sellafield,* London, Quartet Books Ltd.

Bostick, B. C., Vairavamurthy, M. A., Karthikeyan, K. G. & Chorover, J. 2002. Cesium adsorption on clay minerals: An EXAFS spectroscopic investigation. *Environmental Science & Technology,* 36**,** 2670-2676.

Bradbury, M. H. & Baeyens, B. 2000. A generalised sorption model for the concentration dependent uptake of caesium by argillaceous rocks. *Journal of Contaminant Hydrology,* 42**,** 141-163.

Brouwer, E., Baeyens, B., Maes, A. & Cremers, A. 1983. Cesium and Rubidium Ion Equilibrium in Illite Clay. *Journal of Physical Chemistry,* 87**,** 1213-1219.

Brown, F., Hall, G. R. & Walter, A. J. 1955. The half-life of Cs137. *Journal of Inorganic and Nuclear Chemistry,* 1**,** 241-247.

Bulgakov, A. A. & Konoplev, A. V. 2005. Modeling of long-term transformation of Sr-90 forms in soils. *Eurasian Soil Science,* 38**,** 727-733.

Butler, J. R. & Thompson, A. J. 1962. Different values for caesium in G-1. *Geochimica Et Cosmochimica Acta,* 26**,** 1349-1350.

Butler, J. R. & Thompson, A. J. 1963. Caesium in some alkali granites (Younger Granites) of Northern Nigeria. *Geochimica Et Cosmochimica Acta,* 27**,** 769-773.

Cabell, M. J. & Smales, A. A. 1957. The determination of rubidium and caesium in rocks, minerals and meteorites by neutron-activation analysis. *Analyst,* 82**,** 390-406.

Carroll, S. A., Roberts, S. K., Criscenti, L. J. & O'Day, P. A. 2008. Surface complexation model for strontium sorption to amorphous silica and goethite. *Geochemical Transactions,* 9.

Chamard, P., Velasco, R. H., Belli, M., Disilvestro, G., Ingrao, G. & Sansone, U. 1993. Cesium-137 and Sr-90 Distribution in a Soil-Profile. *Science of the Total Environment,* 136**,** 251-258.

Chaplow, R. 1996. The geology and hydrogeology of Sellafield: an overview. *Quarterly Journal of Engineering Geology and Hydrogeology,* 29**,** S1-12.

Chawla, F., Steinmann, P., Pfeifer, H. R. & Froidevaux, P. 2010. Atmospheric deposition and migration of artificial radionuclides in Alpine soils (Val Piora, Switzerland) compared to the distribution of selected major and trace elements. *Science of the Total Environment,* 408**,** 3292-3302.

Chen, C. C., Coleman, M. L. & Katz, L. E. 2006. Bridging the gap between macroscopic and spectroscopic studies of metal ion sorption at the oxide/water interface: Sr(II), Co(II), and Pb(II) sorption to quartz. *Environmental Science and Technology,* 40**,** 142-148.

Chen, C. C. & Hayes, K. F. 1999. X-ray absorption spectroscopy investigation of aqueous Co(II) and Sr(II) sorption at clay-water interfaces. *Geochimica Et Cosmochimica Acta,* 63**,** 3205-3215.

Chen, T. & Wang, H. J. 2007. Determination of layer stacking microstructures and intralayer transition of illite polytypes by high-resolution transmission electron microscopy (HRTEM). *American Mineralogist,* 92**,** 926-932.

Chen, T., Wang, H. J., Mason, R. & Chen, L. 2010. HRTEM investigation of intralayer and interlayer stacking defects and pyrophyllite interlayers in illite. *Mineralogical Magazine,* 74**,** 451-461.

Chibowski, S. & Zygmunt, J. 2002. The influence of the sorptive properties of organic soils on the migration rate of Cs-137. *Journal of Environmental Radioactivity,* 61**,** 213-223.

Chien, S. W. C., Wang, M. C., Chiu, C. L., Lin, Y. M. & Lai, S. Y. 2007. The contents and forms of solid-phase species of radioactive strontium and cesium in Taiwan soils. *Environmental Monitoring and Assessment,* 125**,** 29-39.

Choi, S., O'Day, P. A., Rivera, N. A., Mueller, K. T., Vairavamurthy, M. A., Seraphin, S. & Chorover, J. 2006. Strontium speciation during reaction of kaolinite with simulated tank-waste leachate: Bulk and

microfocused EXAFS analysis. *Environmental Science & Technology,* 40**,** 2608-2614.

Chorover, J., Choi, S., Amistadi, M. K., Karthikeyan, K. G., Crosson, G. & Mueller, K. T. 2003. Linking cesium and strontium uptake to kaolinite weathering in simulated tank waste leachate. *Environmental Science and Technology,* 37**,** 2200-2208.

Chorover, J., DiChiaro, M. J. & Chadwick, O. A. 1999. Structural charge and cesium retention in a chronosequence of tephritic soils. *Soil Science Society of America Journal,* 63**,** 169-177.

Cigna, A. A., Romero, L., Monte, L., Karavaeva, Y. N., Molchanova, I. V. & Trapeznikov, A. 2000. Sr-90 profile in soil samples from the East Urals Radioactive Trail (EURT): a quantitative approach. *Journal of Environmental Radioactivity,* 49**,** 85-96.

Clapp, R. B. & Watts, J. A. 1993. Second Annual Report of the Environmental Restoration Monitoring and Assessment Program at Oak Ridge National Laboratory. Oak Ridge, Tennessee: Oak Ridge National Laboratory.

Comans, R. N. J., Haller, M. & Depreter, P. 1991. Sorption of cesium on illite: None-equilibrium behaviour and reversibility. *Geochimica Et Cosmochimica Acta,* 55**,** 433-440.

Comans, R. N. J. & Hockley, D. E. 1992. Kinetics of cesium sorption on illite. *Geochimica Et Cosmochimica Acta,* 56**,** 1157-1164.

Connor, S. 2011. Closure of Mox plant leaves nuclear waste headache for Cumbria *The Independant*.

Copplestone, D., Johnson, M. S., Jones, S. R., Toal, M. E. & Jackson, D. 1999. Radionuclide behaviour and transport in a coniferous woodland ecosystem: vegetation, invertebrates and wood mice, Apodemus sylvaticus. *Science of the Total Environment,* 239**,** 95-109.

Cornell, R. 1993. Adsorption of cesium on minerals: A review. *Journal of Radioanalytical and Nuclear Chemistry,* 171**,** 483-500.

Cornell, R. & Schwertmann , U. 2003. *The iron oxides: structure, properties, reactions, occurences and uses,* Weinheim, Wiliey-VCH.

Cremers, A., Elsen, A., Depreter, P. & Maes, A. 1988. Quantitative analysis of radiocaesium retention in soils. *Nature,* 335**,** 247-249.

Crook, M. 2009. Harwell Land Quality Report. Research Sites Restoration Ltd.

Cross, M. A., Smith, J. T., Saxen, R. & Timms, D. 2002. An analysis of the environmental mobility of radiostrontium from weapons testing and Chernobyl in Finnish river catchments. *Journal of Environmental Radioactivity,* 60**,** 149-163.

Cruickshank, J. 2012. Findings of the Sellafield Contaminated Land & Groundwater Management Project and the Next Steps for the Land Quality Programme. Sellafield Ltd.

Cushing, C. E. 1992. Hanford Site National Environmental Policy Act (NEPA) Characterization. Richland, Washington.

Davies, K. S. & Shaw, G. 1993. Fixation of Cs-137 by soils in sediments in the Esk Estuary, Cumbria, UK. *Science of the Total Environment,* 132**,** 71-92.

de Koning, A., Konoplev, A. V. & Comans, R. N. J. 2007. Measuring the specific caesium sorption capacity of soils, sediments and clay minerals. *Applied Geochemistry,* 22**,** 219-229.

DECC 2009. UK Energy in Brief 2009. Department of Energy and Climate Change.

DEFRA 2008. Managing Radioactive Waste Safely: A Framework for Implementing Geological Disposal.

Dolhanczuk-Srodka, A., Majcherczyk, T., Smuda, M., Ziembik, Z. & Waclawek, M. 2006. Spatial Cs-137 distribution in forest soil. *Nukleonika,* 51**,** S69-S79.

Doyurum Yusan, S. & Akyil Erenturk, S. 2011. Sorption behaviors of uranium (VI) ions on α-FeOOH. *Desalination,* 269**,** 58-66.

Dudek, T., Środoón, J., Eberl, D. D., Elsass, F. & Uhlik, P. 2002. Thickness distribution of illite crystals in shales. I: X-ray diffraction vs. high-resolution transmission electron microscopy measurements. *Clays and Clay Minerals,* 50**,** 562-577.

Dunster, H. J., Howells, H. & Templeton, W. L. 2007. District surveys following the windscale incident, October 1957. *Journal of Radiological Protection,* 27**,** 217-230.

Dutton, M. V., Foster, C. & Trivedi, D. 2009. Characterisation of Soils from B38 Site Investigation within the Sellafield Separation Area. NNL Commercial.

Elsass, F., Srodon, J. & Robert, M. 1997. Illite-smectite alteration and accompanying reactions in a Pennsylvanian underclay studied by TEM. *Clays and Clay Minerals,* 45**,** 390-403.

EPA. 2010. *Strontium* [Online]. US Environmental Protection Agency. Available: http://www.epa.gov/radiation/radionuclides/strontium.html [Accessed December 2010].

Fanning, D. S. & Keramidas, V. Z. 1977. Micas. *In:* DIXON, J. B., WEED, S. B., KITTRICK, J. A., MILFORD, M. H. & WHITE, J. L. (eds.) *Minerals in Soil Environments.* Madison: Soil Science Society of America.

Faroussi, S., Belali, S., Fahli, A., Fakhi, S., Khomsi, M. & Laachir, S. 2007. (CS)-C-137 profile modelling by means of a model applicable to different types of undisturbed soils. *Comptes Rendus Geoscience,* 339**,** 143-149.

Fernandez, J. M., Piault, E., Macouillard, D. & Juncos, C. 2006. Forty years of Sr-90 in situ migration: importance of soil characterization in modeling transport phenomena. *Journal of Environmental Radioactivity,* 87**,** 209-226.

Forsberg, S., Rosen, K., Fernandez, V. & Juhan, H. 2000. Migration of Cs-137 and Sr-90 in undisturbed soil profiles under controlled and close-to-real conditions. *Journal of Environmental Radioactivity,* 50**,** 235-252.

Francis, C. W. & Brinkley, F. S. 1976. Preferential adsorption of $^{137}$Cs to micaceous minerals in contaminated freshwater sediment. *Nature,* 260**,** 511-513.

Froidevaux, P., Steinmann, P. & Pourcelot, L. 2010. Long-Term and Long-Range Migration of Radioactive Fallout in a Karst System. *Environmental Science & Technology,* 44**,** 8479-8484.

Fry, F. A. & Britcher, A. 1987. Doses from Chernobyl Radiocesium. *Lancet,* 2**,** 160-161.

Fujikawa, Y. & Fukui, M. 1997. Radionuclide sorption to rocks and minerals: Effects of pH and inorganic anions .1. Sorption of cesium, cobalt, strontium and manganese. *Radiochimica Acta,* 76**,** 153-162.

Goodier, I. W., Makepeace, J. L. & Stuart, L. E. H. 1975. The decay scheme of caesium 137. *The International Journal of Applied Radiation and Isotopes,* 26**,** 490-492.

Goss, O. E. & Liddiard, M. 2007. Management of particles detected on the Dounreay site. *Journal of Radiological Protection,* 27**,** A89-A96.

Grim, R. E. 1968. *Clay Mineralogy,* New York, McGraw-Hill.

Grim, R. E., Bray, R. H. & Bradley, W. F. 1937. The mica in argillaceous sediments. *American Mineralogist,* 22**,** 813-829.

Grubb, S. M. B., Peacor, D. R. & Wei-Teh, J. 1991. Transmission electron microscope observations of illite polytypism. *Clays & Clay Minerals,* 39**,** 540-550.

Grutter, A., Vongunten, H. R., Kohler, M. & Rossler, E. 1990. Sorption, Desorption and exchange of cesium on glaciofluvial deposits. *Radiochimica Acta,* 50**,** 177-184.

Guthrie Jr, G. D. & Reynolds Jr, R. C. 1998. A coherent TEM- and XRD-description of mixed-layer illite/smectite. *Canadian Mineralogist,* 36**,** 1421-1434.

Hamblin, C. & Ensor, B. 2004. Decommissioning of a liquid effluent treatment R&D facility. *Proceedings of the Institution of Mechanical Engineers Part E-Journal of Process Mechanical Engineering,* 218**,** 169-174.

Hampel, C. A. 1968. Strontium. *In:* HAMPEL, C. A. (ed.) *The Encyclopedia of the Chemical Elements.* Reinhold Book Corporation.

Harvey, F. 2011. Sellafield Mox nuclear fuel plant to close. *The Guardian*.

He, Q. & Walling, D. E. 1996. Interpreting particle size effects in the adsorption of Cs-137 and unsupported Pb-210 by mineral soils and sediments. *Journal of Environmental Radioactivity,* 30**,** 117-137.

Hiemstra, T. & van Riemsdijk, W. H. 1996. A Surface Structural Approach to Ion Adsorption: The Charge Distribution (CD) Model. *Journal of Colloid and Interface Science,* 179**,** 488-508.

Hill, M. D., Steeds, J. E. & Slade, N. J. 2001. Land Contamination: Technical Guidance on Special Sites: Nuclear Sites. Bristol: Environment Agency.

Hird, A. B., Rimmer, D. L. & Livens, F. R. 1996. Factors affecting the sorption and fixation of caesium in acid organic soil. *European Journal of Soil Science,* 47**,** 97-104.

Hodgson, S. A., Ham, G. J., Youngman, M. J., Etherington, G. & Stradling, G. N. 2004. A review of measurements of radionuclides in members of the public in the UK. *Journal of Radiological Protection,* 24**,** 369-389.

Hou, X. L., Fogh, C. L., Kucera, J., Andersson, K. G., Dahlgaard, H. & Nielsen, S. P. 2003. Iodine-129 and Caesium-137 in Chernobyl contaminated soil and their chemical fractionation. *Science of the Total Environment,* 308**,** 97-109.

HSI 2004. Urenco (Capenhurst) Ltd's strategy for decommissioning its nuclear licensed site. HM Nuclear Installations Inspectorate.

Huggett, J. M. 1982. On the nature of fibrous illite as observed by electron microscopy. *Clay Minerals,* 17**,** 433-441.

Hunter, J. 2004. SCLS Phase 1 - Conceptual Model of Contamination Below Ground at Sellafield. BNFL.

Jacob, P., Fesenko, S., Bogdevitch, I., Kashparov, V., Sanzharova, N., Grebenshikova, N., Isamov, N., Lazarev, N., Panov, A., Ulanovsky, A., Zhuchenko, Y. & Zhurba, M. 2009. Rural areas affected by the Chernobyl accident: Radiation exposure and remediation strategies. *Science of the Total Environment,* 408**,** 14-25.

Johnson, A. R., Markes, B. M., Schmidt, J. W., Shah, A. N., Weiss, S. G. & Wilson, K. J. 1994. Historical Records of Radioactive Contamination in Biota at the 200 Areas of the Hanford Site. Springfield, Virginia.

Joyce, M. J. & Port, S. N. 1999. Environmental Impact of the Nuclear Fuel Cycle. *In:* HESTER, R. E. & HARRISON, R. M. (eds.) *Environmental Impact of Power Generation.* Cambridge, UK: Royal Society of Chemistry.

Khan, S. A., Riaz ur, R. & Khan, M. A. 1995. Sorption of strontium on bentonite. *Waste Management,* 15**,** 641-650.

Kim, Y., Cygan, R. T. & Kirkpatrick, R. J. 1996a. Cs-133 NMR and XPS investigation of cesium adsorbed on clay minerals and related phases. *Geochimica Et Cosmochimica Acta,* 60**,** 1041-1052.

Kim, Y., Kirkpatrick, R. J. & Cygan, R. T. 1996b. Cs-133 NMR study of cesium on the surfaces of kaolinite and illite. *Geochimica Et Cosmochimica Acta,* 60**,** 4059-4074.

Kogure, T. 2002. Investigations of Micas Using Advanced Transmission Electron Microscopy. *In:* MOTTANA, A., PAOLO SASSI, F., THOMPSON JR, J. B. & GUGGENHEIM, S. (eds.) *Micas: Crystal Chemistry and Metamorphic Petrology.* Mineralogical Society of America.

Konishi, M., Yamamoto, K., Yanagi, T. & Okajima, Y. 1988. Sorption behavior of cesium, strontium and americium ions on clay materials. *Journal of Nuclear Science and Technology,* 25**,** 929-933.

Krauskopf, K. B. & Bird, D. K. 1995. *Introduction to Geochemistry,* New York, McGraw-Hill.

Langmuir, D. 1997. *Aqueous Environmental Geochemistry,* New Jersey, Prentice Hall.

Lee, J. O., Lee, K. J. & Cho, W. J. 1997. Sorption and diffusion of I-125 and Sr-90 in a mixture of bentonite and crushed granite backfill of a radioactive waste repository. *Radiochimica Acta,* 76**,** 143-151.

Li, S., Ni, S. J., Zhang, C. J., Ding, M. G. & Wu, H. J. 2007. Sorption kinetics of strontium in soil. *He-Huaxue yu Fangshe Huaxue/Journal of Nuclear and Radiochemistry,* 29**,** 90-95.

Limousin, G., Gaudet, J. P., Charlet, L., Szenknect, S., Barthes, V. & Krimissa, M. 2007. Sorption isotherms: A review on physical bases, modeling and measurement. *Applied Geochemistry,* 22**,** 249-275.

Liu, C. X., Zachara, J. M. & Smith, S. C. 2004. A cation exchange model to describe Cs+ sorption at high ionic strength in subsurface sediments at Hanford site, USA. *Journal of Contaminant Hydrology,* 68**,** 217-238.

Livens, F. R. & Baxter, M. S. 1988. Chemical Associations of Artificial Radionuclides in Cumbrian Soils. *Journal of Environmental Radioactivity,* 7**,** 75-86.

Lu, N. P. & Mason, C. F. V. 2001. Sorption-desorption behavior of strontium-85 onto montmorillonite and silica colloids. *Applied Geochemistry,* 16**,** 1653-1662.

Lujaniene, G., Plukis, A., Kimtys, E., Remeikis, V., Jankunaite, D. & Ogorodnikov, B. I. 2002. Study of Cs-137, Sr-90, Pu-239,Pu-240, Pu-238 and Am-241 behavior in the Chernobyl soil. *Journal of Radioanalytical and Nuclear Chemistry,* 251**,** 59-68.

Luksiene, B., Druteikiene, R., Gvozdaite, R. & Gudelis, A. 2006. Comparative analysis of Pu-239, Cs-137, Pb-210 and K-40 spatial distributions in the top soil layer at the Baltic coast. *Journal of Environmental Radioactivity,* 87**,** 305-314.

Macintyre, J. E. 1992. *Dictionary of Inorganic Compounds,* New York, Chapman and Hall.

MacKenzie, W. S. & Adams, A. E. 1994. *A Colour Atlas of Rocks and Minerals in Thin Section,* London, Mansion Publishing.

MagnoxSouth 2008. Bradwell Reactor Site: Environmental Management Plan. MagnoxSouth.

MagnoxSouth. 2010a. *Dungeness A: Facts and Figures* [Online]. Available: http://www.magnoxsouthsites.com/about-us/our-sites/dungeness-a/facts-and-figures [Accessed November 2010].

MagnoxSouth. 2010b. *Hinkley Point A: Facts and Figures* [Online]. Available: http://www.magnoxsouthsites.com/about-us/our-sites/hinkley-point-a/facts-and-figures [Accessed November 2010].

MagnoxSouth. 2010c. *Sizewell A: Facts and Figures* [Online]. Available: http://www.magnoxsouthsites.com/about-us/our-sites/sizewell-a/facts-and-figures [Accessed November 2010].

Mair, F. S. & Snaith, R. 1994. Alkali Metals, Inorganic Chemistry. *In:* KING, R. B. (ed.) *Encyclopedia of Inorganic Chemistry.* John Wiley and Sons.

Malla, P. B., Robert, M., Douglas, L. A., Tessier, D. & Komarneni, S. 1993. Charge heterogeneity and nanostructure of 2/1 layer silicates by High Resolution Transmission Electron-Microsocopy. *Clays and Clay Minerals,* 41**,** 412-422.

Man, C. K. & Chu, P. Y. 2004. Experimental and modeling studies of radiocesium retention in soils. *Journal of Radioanalytical and Nuclear Chemistry,* 262**,** 339-344.

Masheim, C. E. 1968. Cesium. *In:* HAMPEL, C. A. (ed.) *The Encyclopedia of the Chemical Elements.* Reinhold Book Corporation.

Mason, C. F. V., Lu, N. & Conca, J. 2000. Radioactive strontium- and caesium-contaminated sites: Characterisation, transport, and remedial options. *In:* HECKER, S. S., MASON, C. F. V., KADYRZHANOV, K. K. & KISLITSIN, S. B. (eds.) *Nuclear Physical Methods in Radioecological Investigations of Nuclear Test Sites.* Dordrecht: Springer.

Matsunaga, T., Nagao, S., Ueno, T., Takeda, S., Amano, H. & Tkachenko, Y. 2004. Association of dissolved radionuclides released by the Chernobyl accident with colloidal materials in surface water. *Applied Geochemistry,* 19**,** 1581-1599.

McKenzie, H. & Armstrong-Pope, N. 2010. Groundwater Annual Report 2010. Sellafield Ltd.

McKenzie, H. & McCord, J. 2010. Groundwater Annual Report, 2009. Sellafield Ltd.

McKenzie, H. M., Coughlin, D., Laws, F. & Stampler, A. 2011. Groundwater Annual Report 2011. Sellafield Ltd.

Mell, P., Megyeri, J., Riess, L., Máthé, Z., Csicsák, J. & Lázár, K. 2006. Sorption of Co, Cs, Sr and I onto argillaceous rock as studied by radiotracers. *Journal of Radioanalytical and Nuclear Chemistry,* 268**,** 405-410.

Meunier, A. & Velde, V. 2004. *Illite,* Berlin, Springer-Verlag.

Michie, U. 1996. The geological framework of the Sellafield area and its relationship to hydrogeology. *Quarterly Journal of Engineering Geology and Hydrogeology,* 29**,** S13-27.

Missana, T., Garcia-Gutierrez, M. & Alonso, U. 2008. Sorption of strontium onto illite/smectite mixed clays. *Physics and Chemistry of the Earth,* 33**,** S156-S162.

Missana, T., García-Gutiérrez, M. & Maffiotte, C. 2003. Experimental and modeling study of the uranium (VI) sorption on goethite. *Journal of Colloid and Interface Science,* 260**,** 291-301.

Mollah, A. S. & Ullah, S. M. 1998. Determination of distribution coefficient of Cs-137 and Sr-90 in soil from AERE, Savar. *Waste Management,* 18**,** 287-291.

Monte, L. 2010. Modelling multiple dispersion of radionuclides through the environment. *Journal of Environmental Radioactivity,* 101**,** 134-139.

Morris, R. V., Klingelhöfer, G., Schröer, C., Fleischer, I., Ming, D. W., Yen, A. S., Gellert, R., Arvidson, R. E., Rodionov, D. S., Crumpler, L. S., Clark, B. C., Cohen, B. A., McCoy, T. J., Mittlefehldt, D. W., Schmidt,

M. E., De Souza, P. A. & Squyres, S. W. 2008. Iron mineralogy and aqueous alteration from Husband Hill through Home Plate at Gusev Crater, Mars: Results from the Mössbauer instrument on the Spirit Mars Exploration Rover. *Journal of Geophysical Research E: Planets,* 113.

Müller-Lemans, H. & van Dorp, F. 1996. Bioturbation as a mechanism for radionuclide transport in soil: Relevance of earthworms. *Journal of Environmental Radioactivity,* 31**,** 7-20.

Murray, T. 1993. Elementary Scots: The discovery of Strontium. *Scottish Medical Journal,* 38**,** 188-189.

Nakamaru, Y., Ishikawa, N., Tagami, K. & Uchida, S. 2007. Role of soil organic matter in the mobility of radiocesium in agricultural soils common in Japan. *Colloids and Surfaces a-Physicochemical and Engineering Aspects,* 306**,** 111-117.

Nakao, A., Thiry, Y., Funakawa, S. & Kosaki, T. 2008. Characterization of the frayed edge site of micaceous minerals in soil clays influenced by different pedogenetic conditions in Japan and northern Thailand. *Soil Science & Plant Nutrition,* 54**,** 479-489.

NCRP 2007. Cesium-137 in the Environment - Radioecology and Approaches to Assessment and Management (Report No. 154). National Council on Radiation Protection and Measurements (NCRP).

NDA 2006a. Berkeley Site Summary: Lifetime Plan. Nuclear Decommissioning Authority.

NDA 2006b. Bradwell Site Summary: Lifetime Plan. Nuclear Decommissioning Authority.

NDA 2006c. Capenhurst Site Summary: Lifetime Plan. Nuclear Decommissioning Authorty.

NDA 2006d. Sizewell A Site Summary: Lifetime Plan. Nuclear Decommissioning Authority.

NDA. 2009a. *Our Sites* [Online]. Available: http://www.nda.gov.uk/sites/ [Accessed January 2011].

NDA. 2009b. *Our Sites: Berkeley* [Online]. Nuclear Decommissioning Authority. Available: http://www.nda.gov.uk/sites/berkeley/ [Accessed November 2010].

NDA. 2009c. *Our Sites: Capenhurst* [Online]. Nuclear Decommissioning Authority. Available: http://www.nda.gov.uk/sites/capenhurst/ [Accessed November 2010].

NDA. 2009d. *Our Sites: Chapelcross* [Online]. Nuclear Decommissioning Authority. Available: http://www.nda.gov.uk/sites/chapelcross/ [Accessed November 2010].

NDA. 2009e. *Our Sites: Hunterston A* [Online]. Nuclear Decommissioning Authority. Available: http://www.nda.gov.uk/sites/hunterstona/ [Accessed November 2010].

NDA. 2009f. *Our Sites: Sizewell A* [Online]. Available: http://www.nda.gov.uk/sites/sizewella/ [Accessed November 2010].

NDA 2010a. Corporate Brochure: Dealing with the Past. Protecting the Future. Nuclear Decommissioning Authority.

NDA 2010b. Research Sites Restoration Ltd: Lifetime Plan Baseline, Winfrith Site Summary. Nuclear Decommissioning Authority.

NDA 2010c. Strategic Environmental Assessment, Site Specific Baseline Trawsfynydd. Nuclear Decommissioning Authority.

NDA 2010d. Strategic Environmental Assessment, Site Specific Baseline: Dungeness A. Nuclear Decommissioing Authority.

NDA 2010e. Strategic Environmental Assessment, Site Specific Baseline: Hinkley Point A. Nuclear Decommissioning Authority.

NDA 2011. Oxide Fuels: Credible Options.

NDA. 2013a. *Our Sites: Dounreay* [Online]. Available: http://www.nda.gov.uk/sites/dounreay/ [Accessed November 2010].

NDA. 2013b. *Our Sites: Sellafield* [Online]. Nuclear Decommissioning Authority. Available: http://www.nda.gov.uk/sites/sellafield/ [Accessed February 2014].

NEA & OECD 2006. *Advanced nuclear fuel cycles and radioactive waste management*, OECD.

Nylena, T. & Grip, H. 1997. The origin and dynamics of Cs-137 discharge from a coniferous forest catchment. *Journal of Hydrology,* 192**,** 338-354.

Olives, J., Amouric, M. & Perbost, R. 2000. Mixed layering of illite-smectite: Results from high-resolution transmission electron microscopy and lattice-energy calculations. *Clays and Clay Minerals,* 48**,** 282-289.

Onoda Jr, G. Y. & De Bruyn, P. L. 1966. Proton adsorption at the ferric oxide/aqueous solution interface. I. A kinetic study of adsorption. *Surface Science,* 4**,** 48-63.

Openshaw, S., Carver, S. & Fernie, J. 1989. *Britain's Nuclear Waste: Siting and Safety,* London, Belhaven Press.

Owens, P. N. & Walling, D. E. 1996. Spatial variability of caesium-137 inventories at reference sites: An example from two contrasting sites in England and Zimbabwe. *Applied Radiation and Isotopes,* 47**,** 699-707.

Panin, A. V., Walling, D. E. & Golosov, V. N. 2001. The role of soil erosion and fluvial processes in the post-fallout redistribution of Chernobyl-derived caesium-137: a case study of the Lapki catchment, Central Russia. *Geomorphology,* 40**,** 185-204.

Parekh, N. R., Poskitt, J. M., Dodd, B. A., Potter, E. D. & Sanchez, A. 2008. Soil microorganisms determine the sorption of radionuclides within organic soil systems. *Journal of Environmental Radioactivity,* 99**,** 841-852.

Parfitt, R. L. & Atkinson, R. J. 1976. Phosphate adsorption on goethite (α-FeOOOH). *Nature,* 264**,** 740-742.

Parkman, R. H., Charnock, J. M., Livens, F. R. & Vaughan, D. J. 1998. A study of the interaction of strontium ions in aqueous solution with the surfaces of calcite and kaolinite. *Geochimica Et Cosmochimica Acta,* 62**,** 1481-1492.

Plamboeck, A. H., Nylen, T. & Agren, G. 2006. Comparative estimations of Cs-137 distribution in a boreal forest in northern Sweden using a traditional sampling approach and a portable NaI detector. *Journal of Environmental Radioactivity,* 90**,** 100-109.

Poinssot, C., Baeyens, B. & Bradbury, M. H. 1999. Experimental and modelling studies of caesium sorption on illite. *Geochimica Et Cosmochimica Acta,* 63**,** 3217-3227.

Pollack, J. B., Pitman, D., Khare, B. N. & Sagan, C. 1970a. Goethite on Mars. A laboratory study of physically and chemically bound water in ferric oxides. *J Geophys Res,* 75**,** 7480-7490.

Pollack, J. B., Wilson, R. N. & Goles, G. G. 1970b. Re- examination of the stability of goethite on Mars. *J Geophys Res,* 75**,** 7491-7500.

Povinec, P. P. 2012. Preface – Fukushima II. *Journal of Environmental Radioactivity,* 114**,** 1.

Rahnemaie, R., Hiemstra, T. & van Riemsdijk, W. H. 2006. Inner- and outer-sphere complexation of ions at the goethite–solution interface. *Journal of Colloid and Interface Science,* 297**,** 379-388.

Randall, M. G., Brydie, J., Graham, J. & Small, J. S. 2004. SCLS Phase 1: The Geochemistry of the Sellafield Site. BNFL Commercial.

Reeve, P. & Eilbeck, K. Contaminated land and groundwater management at Sellafield, a large operational site with significant legacy and contaminated land challenges. 11th International Conference on Environmental Remediation and Radioactive Waste Management, ICEM'07, September 2, 2007 - September 6, 2007, 2009 Bruges, Belgium. American Society of Mechanical Engineers, 431-437.

Righi, D. & Elsass, F. 1996. Characterization of soil clay minerals: Decomposition of X-ray diffraction diagrams and high-resolution electron microscopy. *Clays and Clay Minerals,* 44**,** 791-800.

Rosen, K., Vinichuk, M. & Johanson, K. J. 2009. Cs-137 in a raised bog in central Sweden. *Journal of Environmental Radioactivity,* 100**,** 534-539.

Rosenberg, P. E. 2002. The nature, formation, and stability of end-member illite: A hypothesis. *American Mineralogist,* 87**,** 103-107.

Ross, C. S. & Kerr, P. F. 1931. The clay minerals and their identity. *Journal of Sedimentary Research,* 1**,** 55-65.

Ruhm, W., Kammerer, L., Hiersche, L. & Wirth, E. 1996. Migration of Cs-137 and Cs-134 in different forest soil layers. *Journal of Environmental Radioactivity,* 33**,** 63-75.

Sahai, N., Carroll, S. A., Roberts, S. & O'Day, P. A. 2000. X-ray absorption spectroscopy of strontium(II) coordination. II. Sorption and precipitation at kaolinite, amorphous silica, and goethite surfaces. *Journal of Colloid and Interface Science,* 222**,** 198-212.

Salbu, B., Oughton, D. H., Ratnikov, A. V., Zhigareva, T. L., Kruglov, S. V., Petrov, K. V., Grebenshakikova, N. V., Firsakova, S. K., Astasheva, N. P., Loshchilov, N. A., Hove, K. & Strand, P. 1994. THE MOBILITY OF CS-137 AND SR-90 IN AGRICULTURAL SOILS IN THE UKRAINE, BELARUS, AND RUSSIA, 1991. *Health Physics,* 67**,** 518-528.

Saunders, J. A. & Toran, L. E. 1995. Modeling of radionuclide and heavy metal sorption around low- and high-pH waste disposal sites at Oak Ridge, Tennessee. *Applied Geochemistry,* 10**,** 673-684.

Sawhney, B. L. 1972. Selective Sorption and Fixation of Cations by Clay-Minerals - Review. *Clays and Clay Minerals,* 20**,** 93-100.

Schwertmann, U. 1971. Transformation of hematite to goethite in soils [4]. *Nature,* 232**,** 624-625.

SellafieldLtd. *Magnox Reprocessing* [Online]. Available: http://www.sellafieldsites.com/solution/spent-fuel-management/magnox-reprocessing/ [Accessed 30 January 2014].

SellafieldLtd. 2010. *Introduction to Sellafield* [Online]. Available: http://www.sellafieldsites.com/land/pages/introduction.html [Accessed November 2010].

SellafieldLtd 2011. Sellafield Plan.

SEPA 2009. Report by the Scottish Environmental Protection Agency for the Chapelcross Site Stakeholder group on tritium levels in the local Chapelcross environment. Scottish Environmental Protection Agency.

Shand, C. A., Cheshire, M. V., Smith, S., Vidal, M. & Rauret, G. 1994. Distribution of Radiocesium in Organic Soils. *Journal of Environmental Radioactivity,* 23**,** 285-302.

Shenber, M. A. & Eriksson, A. 1993. Exchangeability of Cesium in Various Soils. *Science of the Total Environment,* 138**,** 271-279.

Sherman, D. M., Peacock, C. L. & Hubbard, C. G. 2008. Surface complexation of U(VI) on goethite (α-FeOOH). *Geochimica Et Cosmochimica Acta,* 72**,** 298-310.

Sigg, L. & Stumm, W. 1981. The interaction of anions and weak acids with the hydrous goethite (α-FeOOH) surface. *Colloids and Surfaces,* 2**,** 101-117.

Söderlund, M., Lusa, M., Lehto, J., Hakanen, M., Vaaramaa, K. & Lahdenperä, A.-M. 2011. Sorption of Iodine, Chlorine, Technetium, and Cesium in Soil. Eurajoki, Finland: Posiva.

Solecki, J. 2005. Investigation of Sr-85 adsorption on selected soils of different horizons. *Journal of Environmental Radioactivity,* 82**,** 303-320.

Solecki, J. 2007. Studies of Sr-90 concentration and migration in the soils of the Leczna-Wodawa Lake District. *Journal of Radioanalytical and Nuclear Chemistry,* 274**,** 27-38.

Sposito, G. 1984. *The Surface Chemistry of Soils,* New York, Oxford University Press.

Sposito, G. 1989. *The Chemistry of Soils,* New York, Oxford University Press.

Sposito, G., Skipper, N. T., Sutton, R., Park, S.-h., Soper, A. K. & Greathouse, J. A. 1999. Surface Geochemistry of the Clay Minerals. *Proceedings of the National Academy of Sciences of the United States of America,* 96**,** 3358-3364.

Srodon, J., Andreoli, C., Elsass, F. & Robert, M. 1990. Direct high-resolution transmission electron microscopic measurement of expandability of mixed-layer illite/smectite in bentonite rock. *Clays & Clay Minerals,* 38**,** 373-379.

Srodon, J. & Eberl, D. D. 1984. ILLITE. *Reviews in Mineralogy,* 13**,** 495-544.

Srodon, J., Elsass, F., McHardy, W. J. & Morgan, D. J. 1992. Chemistry of illite-smectite inferred from TEM measurements of fundamental particles. *Clay Minerals,* 27**,** 137-158.

Stamoulis, K. C., Assimakopoulos, P. A., Ioannides, K. G., Johnson, E. & Soucacos, P. N. 1999. Strontium-90 concentration measurements in human bones and teeth in Greece. *The Science of The Total Environment,* 229**,** 165-182.

Stewart, J. C. C. 1959. The Chapelcross Nuclear Power Station. *Nature,* 183**,** 1361-1363.

Sucha, V., Srodon, J., Clauer, N., Elsass, F., Eberl, D. D., Kraus, I. & Madejova, J. 2001. Weathering of smectite and illite-smectite under temperate climatic conditions. *Clay Minerals,* 36**,** 403-419.

Takeno, N. 2005. Atlas of Eh-pH diagrams: Intercomparison of thermodynamics databases. National Institute of Advanced Industrial Science and Technology.

Tanaka, T. & Ohnuki, T. 1996. Colloidal migration behavior of radionuclides sorbed on mobile fine soil particles through a sand layer. *Journal of Nuclear Science and Technology,* 33**,** 62-68.

Torstenfelt, B., Andersson, K. & Allard, B. 1982. Sorption of Strontium and Cesium on Rocks and Minerals. *Chemical Geology,* 36**,** 123-137.

Tyler, A. N., Carter, S., Davidson, D. A., Long, D. J. & Tipping, R. 2001. The extent and significance of bioturbation on Cs-137 distributions in upland soils. *Catena,* 43**,** 81-99.

UKAEA 2003. Evolution of UKAEA Harwell. UKAEA.

UNSCEAR 1993. United Nations Scientific Committee on the Effects of Atomic Radiation: Sources and Effects of Ionizing Radiation. New York.

UNSCEAR 2000. United Nations Scientific Committee on the Effects of Atomic Radiation: Sources and Effects of Ionizing Radiation. New York.

Veblen, D. R., Guthrie Jr, G. D. & Livi, K. J. T. 1990. High-resolution transmission electron microscopy and electron diffraction of mixed-layer illite/smectite: experimental results. *Clays & Clay Minerals,* 38**,** 1-13.

Velde, B. 1977. *Clays and clay minerals in natural and synthetic systems,* Amsterdam, Elsevier.

Velde, B. 1985. *Clay Minerals: A Physio-Chemical Explanation of their Occurrence,* Amsterdam, Elsevier.

Wallace, S. H., Shaw, S., Morris, K., Small, J. S. & Burke, I. T. 2013. Alteration of sediments by hyperalkaline k-rich cement leachate: Implications for strontium adsorption and incorporation. *Environmental Science and Technology,* 47**,** 3694-3700.

Walling, D. E. & He, Q. 1999. Improved Models for Estimating Soil Erosion Rates from Cesium-137 Measurements. *J. Environ. Qual.,* 28**,** 611-622.

Wang, X., Chen, Y. & Wu, Y. 2004. Sorption and desorption of radiostrontium on powdered bentonite: Effect of pH and fulvic acid. *Journal of Radioanalytical and Nuclear Chemistry,* 261**,** 497-500.

Weaver, C. E. & Pollard, L. D. 1973. *The chemistry of clay minerals,* Amsterdam, Elsevier.

Westall, W. A. 2007. Trawsfynydd decommissioning site End State Development Report. British Nuclear Group.

Wilson, P. D. 1996. *The Nuclear Fuel Cycle: From Ore to Wastes,* Oxford, Oxford University Press.

WNA. 2010. *The Nuclear Fuel Cycle* [Online]. World Nuclear Association. Available: http://www.world-nuclear.org/info/inf03.html [Accessed November 2010].

Yates, D. E. & Healy, T. W. 1975. Mechanism of anion adsorption at the ferric and chromic oxide/water interfaces. *Journal of Colloid and Interface Science,* 52**,** 222-228.

Yates, D. M. & Rosenberg, P. E. 1996. Formation and stability of endmember illite .1. Solution equilibration experiments at 100-250 degrees C and P-v,P-soln. *Geochimica Et Cosmochimica Acta,* 60**,** 1873-1883.

Yates, D. M. & Rosenberg, P. E. 1997. Formation and stability of endmember illite .2. Solid equilibration experiments at 100 to 250 degrees C and P-v,P-soln. *Geochimica Et Cosmochimica Acta,* 61**,** 3135-3144.

Zachara, J. M., Smith, S. C., Liu, C. X., McKinley, J. P., Serne, R. J. & Gassman, P. L. 2002. Sorption of Cs+ to micaceous subsurface sediments from the Hanford site, USA. *Geochimica Et Cosmochimica Acta,* 66**,** 193-211.

# Chapter 3 – Thermodynamics of the mineral-water interface

The work presented in this thesis focuses primarily on the interaction of charged ions with the surfaces of minerals, a process known as sorption. As with all chemical reactions, sorption reactions are governed by the laws of thermodynamics. It is these mathematical laws which underpin geochemical models of solid-solution reactions, such as the cation exchange model presented in chapter 5 of this thesis. A detailed treatise of these thermochemical principles relevant to geochemical systems is therefore of great value and is presented here. The fundamental concepts of enthalpy, $H$; entropy, $S$; Gibbs free energy, $G$; chemical potential, $\mu$ and equilibrium are described in detail and then applied to sorption reactions at the mineral-solution interface. The contents of this chapter are greatly indebted to Langmuir (1997). Note that the concepts of activity and the activity coefficient are discussed in detail in section 4.2.3 and are not considered here. Adsorption isotherms have been previously addressed in chapter 2.

## 3.1 Basic concepts – systems, phases and components

The most fundamental concept within thermodynamics is that of the system. A system, briefly, is a group of phases (either solids, liquids, gasses, or any combination of the three) which has a defined boundary. There is no limit on the scale of a system, it can be a collection of atoms, a whole rock or an entire planet. The only unifying concept is that it must have boundaries, outside of which are its surroundings. The boundaries of a system can be

either open or closed, thus a system is classified as either open or closed. An open system is one which is free to exchange both matter and energy with its surroundings, such as a lake which can gain matter ($H_2O$) through precipitation and energy through heating (often resulting in the loss of $H_2O$ due to evaporation). Conversely a closed system cannot exchange matter with its surroundings, however it can still exchange energy. For example a sealed steel drum can successfully contain spent nuclear fuel whilst still allowing the transfer of energy and dissipation of residual heat into the surroundings. Of particular importance with regard to natural systems is that a system can be open to one substance and closed to another. Consider a land-fill site surrounded by a semi-permeable membrane, it may be open with regard to air and water but closed to organic molecules and other contaminants. Additionally a system can be isolated. An isolated system cannot exchange either matter or energy with its surroundings.

The definition of a phase was just hinted at, but it is an important concept and deserves full explanation. Thermodynamically a phase is a homogenous part of a system possessing distinct and consistent physical and chemical characteristics. A pure mineral may be considered a phase, as may an ice crystal.

Phases are formed from components, which are the basic chemical units within the system. Components may be specific atoms, such as O and H or oxides, such $Al_2O_3$. Components may be thought of as the building blocks of phases. It should be noted that in geochemical modelling codes phases are

often referred to as master species and this is nomenclature followed in chapter 5.

The number of components and phases that can exist in a given system is governed by the Gibbs phase rule:

$$F = C - P + 2 \tag{3.1}$$

In most systems $P \geq C$ where $F$ is the number of degrees of freedom. When the pressure and temperature of the system is fixed the system loses two degrees of freedom and therefore $F = C - P$. Selecting the correct number and identity of components with regard to the desired phases is an important part of geochemical modelling.

## 3.2 Enthalpy and Entropy

All of the calculations and predictions made by thermodynamics with regard to the likelihood and direction of spontaneous change are underpinned by the dual concepts of system enthalpy, *H* and entropy, *S*. As such they warrant a detailed discussion.

Enthalpy is most formally defined as the heat content (internal energy) of a substance, *U*, at constant pressure, *P* and volume, *V* as expressed in equation 3.2

$$H = U + PV \tag{3.2}$$

However it is not possible to directly measure the absolute enthalpy of any substance. Instead the enthalpy of formation, $\Delta H_f^o$, of a substance from its component parts is reported at standard temperature and pressure. Standard temperature and pressure means 298.15K (25°C) and 1 bar and all thermodynamic quantities measured under these conditions are denoted by the ° sign. For all elements in their most stable form $\Delta H_f^o = 0$. All the less stable forms of the element are thus denoted as such by their non-zero values of $\Delta H_f^o$.

All chemical reactions have an associated reaction enthalpy, $\Delta H_r^o$. This defines the heat transferred to its surroundings by system undergoing a reaction. Values of $\Delta H_r^o$ are reported at constant pressure (1 bar in standard conditions) but not at constant temperature or volume. This is because the reaction can result in a change in values of temperature and volume within the system. Specifically a reaction with a negative $\Delta H_r^o$ produces heat (which increases system temperature), or is exothermic. Conversely an endothermic reaction with a positive $\Delta H_r^o$ consumes system heat and leads to a reduction in system temperature. Similarly some reactions may lead to an increase or decrease in the overall volume of the system. Due to this the direction of a reaction can be affected be changing the temperature and/or pressure of the reacting system. The nature of this affect is given by Le Chatelier's principle. This briefly states that after a change in temperature or

pressure in a system at equilibrium, the system will adjust itself to nullify the change. This same principle also applies to reactions at equilibrium (where none of the reactants and turning into products, or vice versa) and they will also adjust themselves the nullify any change in the activity of one (or more) reactants or products. Thus when a system undergoes an exothermic reaction it becomes out of thermal equilibrium with its surroundings and heat is transferred from the system into the surroundings until equilibrium is restored. The reverse disequilibrium occurs after an endothermic reaction and the system gains heat from its surroundings.

Entropy is a measure of the degree of randomness, or disorder within a phase. In all cases a phase has minimum entropy at 0 K. The change in entropy, Δ*S* of any reversible process is defined as the heat absorbed by the system as a result of the process, *Q*, divided by the absolute temperature of the system, *T*. These values are usually measured under standard conditions of temperature and pressure, thus:

$$\Delta S^\circ = \frac{Q}{T} \tag{3.3}$$

In this case the standard conditions indicate that the change in entropy was measured as a result of raising the temperature of the phase from 0 K (where as previously stated entropy is at a minimum) to 298.15 K at a constant pressure (usually 1 bar). These entropy values can be measured for any given final temperature, which is usually denoted as a subscript (e.g.

$S^{o}_{298}$).These values of absolute entropy are determined via the following relationship:

$$dS = \left(\frac{Cp}{T}\right) dT \tag{3.4}$$

where *C*p is the heat capacity or the calories required to raise the temperature of 1 mole of a substance by 1 K. Importantly values of absolute entropy cannot be calculated for dissolved species, and instead the difference in entropy, Δ*S*, is calculated relative to $H^{+}_{(aq)}$ (for which $S_T = 0$).

## 3.3 Gibbs free energy and the equilibrium constant

The Gibbs free energy of a given substance, $G_i = H_i - TS_i$, (with units kJ / mol). However, as with entropy it is not possible to measure absolute values of *G*. Therefore the change in Gibbs energy of a reaction at constant temperature and pressure, $\Delta G^{o}_{r}$ is determined as.

$$\Delta G^{o}_{r} = \Delta H^{o}_{r} - T\Delta S^{o}_{r} \tag{3.5}$$

Within any reaction there is a direct relationship between $\Delta G^{o}_{r}$ and the equilibrium constant, $K_{eq.}$ Take the generic reaction

$$aA + bB \leftrightarrow cC + dD \tag{3.6}$$

where A and B are the reactants and C and D are the products. The lower case letters represent the number of moles of the respective substances. Each of these constituents within the reaction have their own Gibbs free energy determined, for example for a mole of A:

$$aG_A = a\Delta G_A^o + RT\ ln[A]^a \tag{3.7}$$

Here $\Delta G_A^o$ is the standard molar Gibbs free energy of reactant A, or the Gibbs energy when solution activity [A] = 1 and *R* is the gas constant.

The change in Gibbs free energy of the reaction, $\Delta G_r$ is determined the total Gibbs free energy of the products minus the reactants or

$$\Delta G_r = cG_C + dG_D - aG_A - bG_B \tag{3.8}$$

By substituting equation 3.7 into equation 3.8 for each of the reacting species we obtain

$$\Delta G_r = [cG_C + dG_D - aG_A - bG_{B]}] + RT\ ln[C]^c + RT\ ln[D]^d - RT\ ln[A]^a - RT\ ln[B]^b \tag{3.9}$$

Collecting all of the respective terms together yields

$$\Delta G_r = \Delta G_r^o - RT\ ln\frac{[C]^c[D]^d}{[A]^a[B]^b}$$

(3.10)

When the system is at equilibrium the ratio of activities of the products and reactants is the equilibrium constant, $K_{eq}$ therefore equation 3.10 can be expressed as

$$\Delta G_r = \Delta G_r^o - RT\ lnK_{eq}$$

(3.11)

This is the fundamental relationship between Gibbs free energy and the equilibrium constant. It can also be expressed in terms of the reaction quotient, $Q$ giving

$$\Delta G_r = \Delta G_r^o + RT\ \ln[Q]$$

(3.12)

And these two formulations can be combined to give

$$\Delta G_r = \Delta G_r^o - RT\ ln\frac{Q}{K_{eq}}$$

(3.13)

From this we can determine the direction of spontaneous change of a chemical reaction. Specifically where $Q = K_{eq}$ and $\Delta G_r = 0$ the system is at equilibrium. Where $Q < K_{eq}$ and $\Delta G_r < 0$ the reaction proceeds to the right. Where $Q > K_{eq}$ and $\Delta G_r > 0$ the reaction is reversed and proceeds from right to left. The larger the value (either positive or negative) of $\Delta G_r$ the larger the likelihood of it occurring spontaneously (in either direction).

The values of $\Delta G_r^o$ can be computed from tabulated values of the Gibbs free energy of formation of each of the reaction species. Here

$$\Delta G_r^o = c\Delta G_f^o(C) + d\Delta G_f^o(D) - a\Delta G_f^o(A) - b\Delta G_f^o(B) \tag{3.14}$$

Importantly the direction of the reaction is determined by $\Delta G_r$, not $\Delta G_r^o$. Only when the system contains pure phases does $\Delta G_r = \Delta G_r^o$. This equity does not hold true for well mixed species in solution, or mixed gases.

## 3.4 Chemical potential

The likelihood and direction of a reaction happening spontaneously can be determined from the chemical potential, $\mu$. The chemical potential is equal to the Gibbs free energy of 1 mole of a substance. Therefore equation 3.11 can be rewritten as

$$\mu_i = \mu_i^o + RT\ ln\ a_i \tag{3.15}$$

where $\mu_i^o$ is the standard state chemical potential of the component ($i$) and $a$ is the activity of the component. When a component is at equilibrium its value of $\mu$ is equal in all phases. However if component is in disequilibrium then it will tend to spontaneously migrate from phases with a higher chemical potential to phases where $\mu$ is lower.

## 3.5 Sorption reactions

Within this thesis, thermodynamic principals have been applied to model sorption reactions at the surfaces of minerals. Sorption involves the removal of an ion from solution and its binding onto a reactive site on a mineral surface. The different processes of sorption have been previously discussed in chapter 2. Here the underlying mathematical formulation of these sorption reactions and their relationship to the thermochemical laws previously discussed is considered in detail. Specifically the processes of cation exchange and surface complexation are considered.

### 3.5.1 Cation exchange

Sorption onto minerals with a permanent structural charge (e.g. clays) is well captured by simple cation exchange. These cation exchange reactions are governed by the laws of mass action and have an associated equilibrium constant.

Consider the generic cation exchange of monovalent species A and B onto site X.

$$A + BX \leftrightarrow AX + B \tag{3.16}$$

The equilibrium exchange coefficient for this reaction is given by the law of mass action

$$K = \frac{[B][AX]}{[BX][A]} \tag{3.17}$$

It was previously shown, in equation 3.11, that the equilibrium coefficient of a chemical reaction is directly related to the Gibbs free energy of that reaction. This same law holds true for exchange reactions at mineral surfaces. This relationship has two important implications for modelling cation exchange.

Firstly we saw that when the system was out of equilibrium the relationship of reactants and products was captured by the reaction quotient, $Q$. Just as ratio of $Q$ to $K_{eq}$ could tell us about the direction of spontaneous change of a reaction it can also be used to determine the spontaneous sorption or desorption of a species based on its activity in solution and on the reactive surface site.

Beginning with the generic reaction but with specific molar concentrations of the reacting species. At equilibrium, assuming all the ions, and sites are monovalent the system has the following relationship.

$$1A + 1BX \leftrightarrow 1AX + 1B \tag{3.18}$$

Taking these concentrations gives the exchange coefficient for the reaction at equilibrium as

$$K = \frac{1 \times 1}{1 \times 1} = 1 \tag{3.19}$$

However if the concentration of A in solution is increased to 2 then the reaction becomes out of equilibrium as so

$$2A + 1BX \leftrightarrow 1AX + 1B \tag{3.20}$$

Working this through gives a reaction quotient, Q of

$$[Q] = \frac{1 \times 1}{2 \times 1} = \frac{1}{2} = 0.5 \tag{3.21}$$

As stated above, where $Q < K$ the reaction is out of equilibrium and proceeds to the right, causing more of A to sorb to the sorption site and more of B to desorb into solution until equilibrium is re-established.

Secondly, and importantly, the values of K for a specific exchange reaction do not have to be one. Thus a system can be at equilibrium when the activity of A and B in solution and their concentrations on the solid are not equal. This is a fundamental principle underlying the multi-element cation exchange modelling performed in chapter 5 of this thesis. Within minerals the Gibbs free energy of a sorption reaction, $\Delta G_r$, for a specific ion on a specific mineral can be extremely low (negative many thousands of kJ $mol^{-1}$). From equation 3.11 it can be determined that that $\Delta G_r \alpha -K_{eq}$ (Gerstner et al., 1994). Therefore when a cation exchange reaction has a very negative Gibbs energy (a large driving force for spontaneous change) it conversely has a very large positive value of $K_{eq}$. Equation 3.17 shows that a large

value of $K$ for a sorption reaction means that the system is at equilibrium when the concentration of the ion on the solid is much higher than its aqueous activity. This governed the selection of equilibrium coefficients in chapter 5 (there called $K_c$ values). There large $K_c$ values for certain elements mean that the activity of that element (e.g. Cs) at equilibrium was far higher on the solid that it was in solution. This captures the lower $\Delta G_r$ for certain elements on certain sorption sites, therein referred to as 'preferential sorption'. The specific formulation of the model and calibration of these $K_c$ values is discussed detail in chapters 4 and 5.

### 3.5.2 Surface complexation

Although all the modelling done within this thesis is based on simple cation exchange a brief discussion of surface complexation, or electrostatic adsorption models was deemed valuable. It is therefore included here for completeness.

Cation exchange models are often sufficient and appropriate for modelling sorption processes for ions onto surface sites with a permanent charge (such as clays). However they greatly simplify the sorption process as they fail to account for pH variable surface charge (due to protonation and deprotonation of surface sites) and the electrostatic properties of the system. Therefore in systems where pH variable surface charges dominate and the surface properties can be accurately measured, surface complexation models often offer a more accurate and holistic description of ion sorption. These models are often applied to single mineral systems with variable

surface charge, especially to the (hydr)oxide minerals. However it is often difficult to obtain reliable date about the surface charge and surface site density in mixed phase systems (such as soils) and clays. Therefore it is often not possible to apply electrostatic surface complexation models to these systems and they are best described by simple cation exchange models (Kulik, 2009). This was the primary reason for choosing to model the mixed sediment in chapter 5 in this way.

All surface complexation models begin with the same method of determining the protonation and de-protonation (and therefore the charge) of surface sites. The charge of the surface reactive oxygens are governed by the following protonation and deprotonation reactions (specific adsorption/desorption of $H^+$ ions), where *S* represents the surface:

$$SOH + H^+ \leftrightarrow SOH_2^+ \tag{3.22}$$

and

$$SOH \leftrightarrow SO^- + H^+ \tag{3.23}$$

From this mass action expressions can be used to determine the intrinsic equilibrium coefficients $K^{int}$. These intrinsic constants are determined from the system under investigation rather than from strict thermodynamic measurements of each component. Therefore they are intrinsic to the model and not inherent thermodynamic quantities (Sposito, 2004). For the reactions described above the $K^{int}$ values are determined as

$$\frac{1}{K_{a1}^{int}} = \frac{(SOH_2^+)}{(SOH)(H^+)}$$

(3.24)

$$K_{a2}^{int} = \frac{(SO^-)(H^+)}{(SOH)}$$

(3.25)

Importantly the concentration of hydrogen ions at the surface cannot be directly measured and is instead estimated from the total concentration of $H^+$ in the system. This estimation is made via the addition of the Boltzmann factor giving

$$(H_{sur}^+) = (H_{tot}^+)\exp(-\frac{\psi_o F}{RT})$$

(3.26)

Where *F* is Faraday's constant and $\psi_o$ is the potential at the surface. The Boltzmann constant in this case modifies the $H^+$ concentration in a similar way to the activity coefficient in aqueous reactions. Thus the mass action equations above can be rewritten to incorporate this constant to give

$$\frac{1}{K_{a1}^{int}} = \frac{(SOH_2^+)}{(SOH)(H^+)\ exp(-\psi_o F/RT)}$$

(3.27)

$$K_{a2}^{int} = \frac{(SO^-)(H^+)\ exp(-\psi_o F/RT)}{(SOH)}$$

(3.28)

In addition to these protonation and deprotonation reactions the overall surface charge is controlled by and adsorption and desorption of both cationic and anionic solution species. These species may adsorb into inner-

sphere surface complexes at the zero plane (directly on the surface via ligand exchange) as occurred with $H^+$. Additionally however, surface species may form outer-sphere surface complexes via electrostatic attraction to balance the charge of the surface. The constant capacitance and diffuse layer models do not account for the charge partitioning of these inner-sphere and outer-sphere complexes. However the triple layer model differentiates between those ions present in inner-sphere complexes at the zero plane and those held in outer-sphere complexes in the so called Stern layer. Below, the sorption reactions for monovalent and divalent cations (denoted as $M^{+/2+}$) and anions ( as $L^-$) at the charge surface are shown (Sposito, 2004, Sherman, 2009). In this case outer-sphere complexes are denoted via the ⋯ symbol and inner-sphere complexes are represented as in equations 3.22 and 3.23.

$$SOH + M^+ \leftrightarrow SOM + H^+ \tag{3.29}$$

$$2SOH + M^{2+} \leftrightarrow (SO)_2M + 2H^+ \tag{3.30}$$

$$SO^- + M^+ \leftrightarrow SO^- \cdots M^+ \tag{3.31}$$

$$SOH + M^+ + H_2O \leftrightarrow SO^- \cdots MOH^- + 2H^+ \tag{3.32}$$

$$SOH_2^+ + L^- \leftrightarrow SL + H_2O \tag{3.33}$$

$$SOH_2^+ + L^- \leftrightarrow SOH_2^+ \cdots L^- \tag{3.34}$$

In all these cases the sorption reactions have an associated $K^{int}$ value as determined by the law off mass action with the Boltzmann constant correction. For example the sorption of the monovalent and divalent cations (equation 3.29 and 3.30) gives

$$K^{int} = \frac{(SOM)(H^+)\ exp(-\psi_o F/RT)}{(SOH)(M^+)\ exp(-\psi_o F/RT)} \tag{3.35}$$

$$K^{int} = \frac{(SO)_2M)(H^+)^2\ exp(-\psi_o F/RT)}{(SOH)^2(M^{2+})\ exp(-\psi_o F/RT)} \tag{3.36}$$

### 3.5.3 The diffuse double layer

Although the interaction of ions at the zero plane, or directly at the ion surface are well constrained the changes in ion concentration, charge and potential away from the surface is complex. The bulk surface charge $\sigma_o$ is balanced in solution by charged ions in the diffuse double layer, giving a diffuse layer charge, $\sigma_d$. In all cases the system must remain electrically neutral, such that $\sigma_o + \sigma_d = 0$. The diffuse layer is not uniform and there is a gradual decrease in the electrical potential as distance from the surface, $x$, increases and as such a the activity of charge balancing counter ions, $a_i$ gradually reduces (Appelo and Postma, 2005). Given infinite dilution, so where $x = \infty$, both $\psi = 0$ and $a_i = 0$.

The charge in the diffuse layer, $\sigma_d$ at any given distance is given by the Gouy-Chapman equation

$$\sigma_d = \sqrt{(8(RT\varepsilon)a_{i,\infty})}\,\sinh(\frac{F\psi_o}{2RT}) \tag{3.37}$$

where $\epsilon$ is the dielectric constant and $a_{i,\infty}$ is the ion activity at infinite distance. The charge at a specific point within the diffuse layer is determined from the activity of the counter ions at the point according to Boltzmann's law

$$\frac{a_{i.a}}{a_{i,b}} = \frac{exp\ (-z_i F\psi_a/RT)}{exp(-z_i F\psi_b/RT)} \tag{3.38}$$

where *a* and *b* are the positions of interest and $z_i$ is the electrolyte charge number.

This formulation of the diffuse layer assumes a gradual decrease in the $\sigma_d$ away from the surface zero plane. As such it assumes that all adsorbed ions are present at the zero plane and therefore present in inner-sphere complexes. As a consequence the surface charge $\sigma_o$ is located only at the surface itself. However, in many systems, counter ions may be held in outer-sphere complexes where they contribute to the surface charge, $\sigma_o$ whilst being spatially present in the diffuse layer. To account for this the concept of the Stern layer (and the triple layer model) was introduced. This is a region of constant capacitance in the diffuse layer close to the surface. When this layer is included the value of $\sigma_o$ can be determined as

$$\sigma_o = C_s(\psi_o - \psi_b) \tag{3.39}$$

where $C_s$ is the Stern layer constant capacitance term and $\psi_o$ and $\psi_b$ are the potential of the surface and the stern layer respectively. The diffuse layer charge is then determined by the Gouy-Chapman equation (3.37).

In systems with high ionic strength and low surface potential this region of constant capacitance is modelled to extend out to infinity away from the surface. In this way the diffuse layer approximation is simplified and the double or triple layer behaviour is not accounted for. These constant capacitance models are strongly affected by ionic strength and may be difficult to apply to other systems, other than the one investigated experimentally.

## 3.6 References

Appelo, C. A. J. & Postma, D. 2005. *Geochemistry, groundwater and pollution,* Leiden, A.A. Balkema Publishers.

Gerstner, J. A., Bell, J. A. & Cramer, S. M. 1994. Gibbs free energy of adsorption for biomolecules in ion-exchange systems. *Biophysical Chemistry,* 52**,** 97-106.

Kulik, D. A. 2009. Thermodynamic Concepts in Modeling Sorption at the Mineral-Water Interface. *In:* OELKERS, E. H. & SCHOTT, J. (eds.) *Thermodynamics and Kinetics of Water-Rock Interaction.*

Langmuir, D. 1997. *Aqueous Environmental Geochemistry,* New Jersey, Prentice Hall.

Sherman, D. M. 2009. Surface complexation modeling: Mineral fluid equilbria at the molecular scale. *Reviews in Mineralogy and Geochemistry.*

Sposito, G. 2004. *The Surface Chemistry of Natural Particles,* Oxford, UK, Oxford University Press.

# Chapter 4 – Materials and Methods

This chapter offers a detailed overview of the materials and the experimental methods used in this thesis. In each case a detailed theoretical background to each technique is provided. Specific details of the application of each technique in this work are then given.

## 4.1 Materials

### 4.1.1 Sediment samples

Sediment Samples were collected by S. H. Wallace and I. T. Burke (Wallace, 2012) in August 2009 from near the village of Calder Bridge in West Cumbria, UK in the fluvial valley formed by the River Calder where a section of the glacial till geological unit is exposed (54°26.3'N, 3°28.2'W). These sediments form part of the same quaternary deposits that underlie the UK Sellafield site. The overall mineralogical composition is similar to samples recovered from Sellafield cores (McMillan et al., 2000). However, it only represents one textural member present at the site, which ranges from clay-rich horizons to course gravels (Dutton et al., 2009). It is also not contaminated with radioactive substances. A shallow pit was dug down into the sediment with a trowel and representative samples removed. They were initially passed through a 1 cm sieve and stored in HDPE plastic containers for transport back to the lab. The samples were then oven dried at 40°C and stored in HDPE plastic containers. Before use the dried sediment was sieved through a 1 mm sieve to remove large stones, gravel and organic

detritus. This material was used for experiments reported in chapters 4 and 6.

### 4.1.2 Illite

A sample of Illite from the Silver Hills of Montanna, USA was obtained from the Clay Minerals Society Source Clay Repository. This is a well characterised clay mineral standard with the formula $(Mg_{0.09}\ Ca_{0.06}\ K_{1.37})\ [Al_{2.69}\ Fe(III)_{0.76}\ Fe(II)_{0.06}\ Mntr\ Mg_{0.43}\ Ti_{0.06}]\ [Si_{6.77}\ Al_{1.23}]O_{20}(OH)_4$. It is identified by the Clay Minerals Society as Illite IMT-1 standard. The sample was finely crushed by hand with a pestle and mortar until it passed through a 63µm sieve. The crushed sample was then stored in a plastic sample bag. The sample composition was confirmed as illite by x-ray diffraction. The illite was used for experiments in chapters 5 and 6.

### 4.1.3 Chlorite

A sample of chlorite from Madison, North Carolina, USA was purchased from Ward's Science, Rochester, NY. The sample was finely crushed in a ball mill to pass through a 63µm sieve. The crushed sample was then stored in a plastic sample bag prior to use. X-ray diffraction confirmed the sample to be of the chlorite group, most closely matching clinochlore, $(Mg, Fe)_5\ (Si_3\ Al)\ O_{10}\ (OH)_8$. This material was used for the Sr sorption experiments in chapter 6.

### 4.1.4 Goethite

Samples of goethite was synthesised in the lab following the procedure of Schwertmann and Cornell (2000). To make roughly 9 g of goethite: 180 ml of 5 mol $L^{-1}$ KOH was mixed with 100 ml of 1 mol $L^{-1}$ $Fe(NO_3)_3$ and diluted into 2 L with deionised water in a polypropylene beaker. The flask was then sealed with cling film and placed in a 70°C oven for roughly 2 weeks. The synthesised goethite solid sank to the bottom of the beaker. Therefore at the end of the synthesis period the remaining solution was removed and discarded. To remove any excess salts the solid was then re-suspended in deionised water and decanted into centrifuge tubes. The suspension was then centrifuged at 8000 g for 10 minutes to achieve solid/solution separation and the supernatant was discarded. This washing procedure was then repeated three times. The wet goethite paste was then oven dried at 40°C. Once dry the goethite was lightly crushed in a pestle and mortar to pass through a 63µm sieve. The formation and purity of the goethite was confirmed by x-ray diffraction. The synthesised goethite was utilised in experiments reported in chapter 6.

## 4.2 Methods

### 4.2.1 Laboratory experimental methods

#### 4.2.1.1 Batch sorption of Cs to sediment

Batch sorption experiments were performed to investigate the sorption of caesium to the sediments, the results of which are presented in chapter 4. Two types of sorption experiments were performed: concentration variable isotherm experiments where the pH was kept constant and the concentration of $Cs^+$ varied across a range from $1x10^{-9}$ to $1x10^{-1}$ mol $L^{-1}$ and pH sorption edge experiments where a fixed $Cs^+$ concentration was used, and the pH varied across the range 2-10. Both sets of experiments were conducted using three background solution matrices, namely starting solutions of deionised water (DIW), 1 mol $L^{-1}$ NaCl and 1 mol $L^{-1}$ KCl to probe the effect of cationic competition.

The full range of experimental conditions is shown in Table 4.1, and the specific procedure for setting up each experiment is described below. All experiments were performed in triplicate with a sediment-free control sample to determine if any sorption to the tubes was occurring.

**Table 4.1** Experimental parameters for Cs sorption to the Sellafield sediment

| Experiment | pH | Initial Cs concentration mol $L^{-1}$ | Background solution |
|---|---|---|---|
| Isotherms | 6.8 ± 0.2 | 1 $x10^{-9}$; 1 $x10^{-4}$; 1 $x10^{-1}$ | Deionised water<br>1 mol $L^{-1}$ NaCl<br>1 mol $L^{-1}$ KCl |
| pH sorption edges | 2.0 – 10.0 | 1 $x10^{-11}$ | Deionised water<br>1 mol $L^{-1}$ NaCl<br>1 mol $L^{-1}$ KCl |
| | | 1 $x10^{-4}$ | Deionised water<br>1 mol $L^{-1}$ NaCl<br>1 mol $L^{-1}$ KCl |
| | | 1 $x10^{-1}$ | Deionised water<br>1 mol $L^{-1}$ NaCl<br>1 mol $L^{-1}$ KCl |

The solution composition of the system was varied depending on the requirements of the experiment. For all experiments samples of < 1 mm sieved sediment were pre-saturated with deionised water. Samples were then suspended in the particular experimental solution, containing the desired amount of inactive CsCl, in 50 mL polypropylene Oak Ridge tubes at a solid solution ratio of 100 g $L^{-1}$. Specifically 2.00 ± 0.05 g of the sediment was suspended in 20 ml of solution. Immediately following suspension the samples were spiked with a radiotracer of $^{137}Cs^{+}$ at a specific activity of 30 Bq $mL^{-1}$ (equivalent to $7x10^{-11}$ mol $L^{-1}$). This was added as a 60 µL aliquot taken from a 10,000 Bq $mL^{-1}$ working stock which was diluted into the 20 mL samples to give a final concentration of 30 Bq $mL^{-1}$. Samples were then placed in a beta shielded box and agitated for 48 hours on an orbital shaker at 140 rpm at room temperature (20 ± 1°C). The pH of the solution was

measured before and immediately after addition to the sediment and adjusted by drop-wise (10 µL aliquots) titration with 1 mol $L^{-1}$ HCl and NaOH to overcome the sediments buffering capacity and ensure minimal pH drift during the 48 hour equilibration period (when pH was not monitored). The soil naturally buffered to around pH 5, so it was necessary to add large volumes (up to 100µL) to the high pH samples. This had a minimal effect on the total solid: solution ratio and was within the error caused by variation in the total mass of sediment used in each repeat  The pH was recorded using an Orion model 420A bench top pH meter and glass bulb electrode calibrated to pH 4, 7 and 10 using standard buffer solutions. Following the sorption period tubes were centrifuged for 10 minutes at 6,000*g*. A 1 mL representative sample of the supernatant was then transferred to a liquid scintillation vial containing 10 mL of Ecoscint A solution. Final solution activity (Bq $mL^{-1}$) was then measured by liquid scintillation counting on a Packard Tri-Carb 2100TR liquid scintillation counter with a counting window of 0 – 280 keV and 10 minute counting period (further explained in section 3.2.1). Percentage sorption and distribution coefficient, $K_d$ values were then calculated using the methodology of Khan et al. (1995) shown in Wallace et al. (2012).

For the isotherm experiments, the effect of $Cs^+$ solution concentration on sorption was investigated using CsCl solutions at a range of concentrations between $1x10^{-9}$ mol $L^{-1}$ and 1 mol $L^{-1}$. Isotherms were performed at circumneutral pH (6.8 ± 0.2); achieved by adjustment with HCl or NaOH (as described above). The sorption behaviour was analysed using a tracer spike

of $^{137}Cs^{+}$ (30 Bq $mL^{-1}$ or 7.0 x $10^{-11}$ mol $L^{-1}$) and the aqueous activity measured by liquid scintillation counting (see above).

For the pH sorption edge experiments, the effect of pH upon the sorption of $Cs^{+}$ was determined by dropwise adjusting the initial experimental suspensions with 1mol $L^{-1}$ HCl and 1 mol $L^{1}$ NaOH to give a range of pH from 2-10. Samples were pH checked at the beginning of the analysis, and after adjustment. The final pH values at the end of a 48 hour sorption period are then reported. For the pH experiments three concentrations of $Cs^{+}$ were chosen. These were selected based on the different regimes of $Cs^{+}$ sorption behaviour displayed in the isotherm experiments and were 7 x $10^{-11}$ mol $L^{-1}$ added as a 30Bq $mL^{-1}$ tracer spike of $^{137}Cs^{+}$ and 1 x $10^{-4}$ mol $L^{-1}$ and 1 x $10^{-1}$ mol $L^{-1}$ added as CsCl (with a radioactive tracer spike to allow analysis by liquid scintillation counting).

#### 4.2.1.2 Batch sorption of Cs to illite

For the atomic scale investigation of Cs sorption to illite presented in chapter 5, two distinct experimental systems were established. A system to test the short term sorption/desorption of Cs on weathered illite and a long term Cs-illite sorption system.

For the short term system 0.1 g samples of the crushed illite were weathered by suspension in a 0.1 mol $L^{-1}$ CaCl solution at a solid solution ratio of 1:50 in 10ml polypropylene Oak-Ridge centrifuge tubes. The samples were then thoroughly shaken by hand and stored in the dark. The weathering reaction

was allowed to continue for one week and the tubes were shaken daily. The tubes were then sampled as described below. A small sub-sample of the dried Ca-illite was prepared for TEM (see TEM imaging section 3.2.4) and the remainder was re-suspended in 1.0 mol $L^{-1}$ CsCl at the same solid: solution ratio for 1 month and shaken weekly. This Cs-exchanged Ca-illite was then sampled following the same procedure as the long term Cs sorption experiments (see below). Again a small sub-sample was taken for TEM analysis. The remainder was then re-suspended at the same solid: solution ratio in 0.1 mol $L^{-1}$ CaCl for 1 week and shaken daily. This was then sampled for TEM analysis.

For the long term experiments fresh samples of the crushed illite were also suspended in a 1 mol $L^{-1}$ CsCl solution at a solid solution ratio of 0.1g 5 $mL^{-1}$ (equivalent 0.02 g $mL^{-1}$) in 10 mL polypropylene Oak-Ridge centrifuge tubes. The tube caps were sealed with Parafilm to prevent any evaporation which would change the solid solution ratio. Following preparation the samples were shaken by hand to thoroughly mix and homogenise them. They were then stored in the dark at room temperature (20 ± 1°C) and shaken by hand once a week to ensure uniform wetting. This long term experiment was sampled at 4, 7 and 12 months according to the method below.

The tubes were destructively sampled using the following method. First, the tubes were centrifuged at 6,000 g for 10 minutes to achieve solid-solution separation. The solution was then decanted and for samples exposed to Cs the sediment washed in 0.1 mol $L^{-1}$ NaCl to remove any outer-sphere

sorbed Cs on the basal plane sites. This was important as the work focused on Cs sorption into the illite interlayers. These sites represent a small fraction of illite's total cation exchange capacity. To ensure that data from the energy dispersive x-ray (EDX) and extended x-ray absorption (EXAFS) spectroscopies was interpretable in terms of interlayer Cs it was important that other cation exchange sites did not dominate the signal. Washing with Na removed the Cs from these sites (but not from the interlayer, where Cs is strongly retained). This provides confidence in the interpretation of the spectroscopic data. For the Ca-exchanged samples the NaCl step was skipped to avoid Na exchanging with Ca and invalidating the experiment. The sample was then washed 3 times with deionised water to remove any excess salts. The washing procedure was as follows. The Oak-Ridge centrifuge tube containing the illite was filled with the washing solution (NaCl / deionised water) and thoroughly shaken by hand for ~30 seconds to fully suspend the illite. The resulting suspension was then centrifuged for 10 minutes at 6,000*g* to separate the solid from the washing solution. The washing solution was then decanted and the procedure repeated. After the final wash the illite was re-suspended in deionised water and the suspension was decanted into a weighing boat. The illite was then dried overnight in the weighing boat in an oven set to 40°C. The sample flocculated together when it was dried, so it was lightly crushed before being prepared for the TEM.

#### 4.2.1.3 Anaerobic Sr batch sorption experiments

Finally a series of Sr sorption experiments were performed at high pH and changes in $Sr^{2+}$ solid speciation analysed using EXAFS. The results of this work are presented in chapter 6. As Sr is known to readily precipitate as

$SrCO_3$ at high pH great care was taken to exclude carbonate from the system. Solutions of degassed ($CO_2$ and $O_2$ free) NaCl and NaOH at concentrations ranging from $10^{-5}$ to 1 mol $L^{-1}$ were prepared in glass Schott bottles. For this deionsed water was degassed for 30 minutes $L^{-1}$ by bubbling with $N_2$ whilst constantly stirring at 90°C on a hot plate. Following the initial degassing period the relevant mass of NaOH or NaCl was added to the deionised water while degassing continued. Additionally, 2.5 $x10^{-4}$ mol $L^{-1}$ of Ca (as $CaCl_2.2H_2O$) was added to all solutions to precipitate any carbonate which was not removed as $CO_2$ by the degassing procedure. The solutions were then degassed for another 30 minutes $L^{-1}$ before being transferred to a coy cabinet anaerobic chamber (with average $CO_2$ concentrations <40ppm). Both a 0.005 mol $L^{-1}$ and a 0.02 mol $L^{-1}$ solution of Sr (as $SrCl_2.6H_2O$) were also prepared by the same degassing procedure but Ca was not added.

All sample handling was then performed inside the anaerobic chamber. The minerals were suspended in NaOH and NaCl at a solid solution ratio of 0.8 g 35 $ml^{-1}$ in 40 ml Oak-Ridge centrifuge tubes. Solutions were filtered through a 0.45µm filter before addition to the solids. This was to ensure removal of any $CaCO_3$ which may have precipitated during the solution preparation. The samples were then spiked with a hundred fold dilution of the 0.005 mol $L^{-1}$ $SrCl_2.6H_2O$ solution (0.35 ml) to yield 3.9 $x10^{-4}$ mol $L^{-1}$ in the following samples: Illite, all NaCl samples; chlorite all NaCl samples, $10^{-3}$ mol $L^{-1}$ NaOH and $10^{-5}$ mol $L^{-1}$ NaOH; goethite, all NaCl samples and $10^{-5}$ mol $L^{-1}$ NaOH; sediment $10^{-5}$ mol $L^{-1}$ NaOH and $10^{-1}$ mol $L^{-1}$ NaOH. All other

samples contained a hundred fold dilution of the 0.02 mol $L^{-1}$ $SrCl_2.6H_2O$ solution to yield 1.1 $x10^{-3}$ mol $L^{-1}$ of Sr in solution. Samples were then sealed and equilibrated for 48 hours on a rotary shaker. During equilibration samples remained in the $CO_2$ free atmosphere to prevent any carbonate formation. Following the equilibration period the samples were transferred unopened from the chamber to a -80°C freezer and frozen to suspend the sorption reaction. They were then transported to the synchrotron (either DLS or ESRF; Sr-EXAFS data was collected during three separate beamtimes, see details below) in a $N_2$ purged air tight kilner jar to minimise $CO_2$ and with ice packs to prevent defrosting. During the beamtime all samples were stored in a freezer and defrosted as needed prior to sample preparation.

Before mounting the samples in holders for EXAFS the tubes were centrifuged and the supernatant was decanted. The pH of the supernatant was immediately measured and the aqueous sample refrozen for transport back to Leeds and preparation for ICP-AES analysis (see ICP-AES section, below). The wet paste was then mounted in a Perspex sample holder and sealed with Kapton tape. The sample was then immediately frozen by immersion in liquid nitrogen. To minimise exposure to atmospheric $CO_2$ during mounting the material was kept under a constant flow of $N_2$ until it was re-frozen by submersion in liquid $N_2$ and transferred to the on-line cryostat for analysis.

## 4.2.2 Analytical methods

### 4.2.2.1 Liquid scintillation counting

Analysis of the sorption of $^{137}Cs$ in the active batch reactions was performed by liquid scintillation counting on a Packard Tri-Carb 2100TR liquid scintillation counter. The liquid scintillation counter measures the radioactivity of a sample by measuring the emission of α (a helium nucleus) and/or β (an electron or positron) particles during radioactive decay (Neame and Homewood, 1974). The process relies on the fact that these emitted α and β particles ionise the surrounding matter when they interact with it. The liquid sample to be measured is dispersed in a scintillation cocktail in a transparent scintillation vial. A number of scintillation solutions are available and as results can vary between them it is important to consistently use the same one. All analyses in this thesis were made using Ecoscint A. The vials are then lowered into the measuring well of the machine. The measuring well sits between two photomultiplier tubes. The whole measuring well is shielded by lead lining to reduce any effect of background radiation, (where cosmic particles can excite the scintillation cocktail and give a false reading). When the radionuclides decay the emitted particles ionise solvent molecules in the scintillation cocktail which upon ionisation emit a photon. This photon is then detected by the photomultiplier tubes which converts them to electron pulses which are counted by the scintillation counter (Neame and Homewood, 1974).

Different radionuclides emit particles in different energy ranges, and these in turn result in scintillations of different energies. These act as a finger print for

different radionuclides. Therefore to measure the concentration of a given radionuclide the system can be windowed so the photomultiplier tubes only accept scintillations in the energy range for the desired radionuclide (Neame and Homewood, 1974). This removes the contribution of any activity outside of the energy range and so reduces the background, improving the result. In this work concentrations of $^{137}Cs$ were measured by windowing the detector between 0 – 280 keV, which was within the observed energy range of $^{137}Cs$ β emissions (NCRP, 1978). This yielded a counting efficiency of around 95% and was deemed acceptable.

The scintillation counter outputs either a total count in a given time period, or more commonly a count rate (counts $min^{-1}$). To convert from the detected counts to activity of the sample the efficiency of the system and the background count rate must be measured. The efficiency is determined by measuring a calibration curve over the range of concentrations in the final samples to be measured. The background is then determined by measuring the counts from a blank vial, containing only scintillation cocktail. The radioactivity of the sample is measured in Bq, or disintegrations (emission of a decay particle) per second. All of these factors are accounted for when converting from the measured counts per minute to the activity (Bq). Initially the background counts are subtracted. This background subtracted count is then converted to activity using the following formula.

$$activity = \left(\frac{count\ rate}{efficieny}\right)/60 \tag{4.1}$$

This gives the final activity of the radionuclide in solution. To determine sorption to the solid phases in the batch experiments this final measured activity ($A_e$) was subtracted from the initial added activity ($A_i$) and the difference represented the sorbed fraction. This was then recast in % sorption and $K_d$ terms (equation 3.2 (Khan et al., 1995)).

$$K_d = \frac{A_i - A_e}{A_e} \times \frac{V}{W} \tag{4.2}$$

where $V$ is the volume of solution (ml) and $W$ is the mass of sediment (g).

#### 4.2.2.2 Solution analysis by ICP-AES

As the Sr batch experiments were performed with the stable isotope ($^{88}Sr$), Sr sorption was determined by measurement on an inductively coupled plasma atomic emission spectrometer (ICP-AES, also known as an optical emission spectrometer or OES). The ICP-AES relies on a fundamental physical property of metals, namely that when metal atoms are raised to higher energy states they emit electromagnetic radiation (much of it visible) when they return to their ground state (Mendham et al., 2000). Every metal emits a unique spectrum of light, known as emission lines, which can be used as a finger print to identify the presence of that metal in a mixed solution. The relative intensity of the emissions at the specific wavelengths for those atoms can also be used to quantify the concentration of that metal in solution (Mendham et al., 2000). This is done by comparing the emissions to those from a standard of known concentration. The ICP-AES itself

operates with a flame of ionised plasma (usually ionised argon gas). The liquid sample is then nebulised and suspended in a stream of argon which is blown into the burning plasma. This excites the atoms which then emit their light which is captured by a photo-multiplier tube and converted into an electrical current, the voltage of which relates to the intensity of the emissions, and thus the concentration in solution (Mendham et al., 2000). Modern multi-element ICP-AES machines use a diffraction grating which diffracts the emissions from different elements into different photo-multiplier tubes, in an array (Mendham et al., 2000). This allows the concentrations of a range of elements to be determined simultaneously and greatly reduces time needed for measurement.

ICP-AES was utilised in chapter 6 to analyse concentrations of aqueous Sr after equilibration with the minerals. The frozen solutions were defrosted in the anaerobic chamber and diluted into 10% $HNO_3$ to acidify them. Dilution was necessary due to the high ionic strength of the background electrolyte. The concentration of Sr in the diluted solutions was then measured and the final aqueous concentration in the sample calculated.

### 4.2.3 PHREEQC cation exchange modelling and model development

For chapter 3 of this work a multi-site cation exchange model was constructed in PHREEQCv2 to perform geochemical modelling of $Cs^+$ sorption to the micaceous sediment (Parkhurst and Appelo, 1999). The full PHREEQC modelling input data is provided in appendix 2. The model was based initially on the model of Bradbury and Baeyens (2000). The modelling

aim was twofold: Firstly to test the validity of the generic Bradbury and Baeyens (2000) model under scenarios of $Cs^+$ contamination relevant to the UK Sellafield nuclear site, and secondly to refine the model in light of experimental results (see Ch. 5) to provide a specific description and prediction of $Cs^+$ sorption at Sellafield. The generic $K_c$ values (selectivity coefficients) proposed by Bradbury and Baeyens (2000) for $Cs^+$ sorption to argillaceous rocks in the presence of competing $Na^+$ and $K^+$ ions have been used in previous models of $Cs^+$ sorption at Sellafield (Randall et al., 2004). These models are used to predict likely sorption and migration of $Cs^+$ in the subsurface as part of safety case evaluations. Therefore it is extremely important to assess whether the generic Bradbury and Baeyens model accurately predicts $Cs^+$ sorption onto Sellafield-like sediments, and to refine the model in light of experimental investigation to improve the accuracy of future predictive modelling.

In the generic Bradbury and Baeyens (2000) model, and in the refined version, all aqueous phases are assumed to be in thermodynamic equilibrium. The behaviour of aqueous species *i* is governed by its activity, $a_i$, activity coefficient, $\gamma_i$, molality, $m_i$, and number of moles in solution, $n_i$ where

$$a_i = \gamma_i m_i \tag{4.3}$$

and

$$n_i = m_i W_{aq} \tag{4.4}$$

where $W_{aq}$ is the mass of aqueous water in solution.

Additionally the activity of each species is related to the chemical potential, $\mu$, of that species via equation 4.5

$$\mu_i = \mu_i^o + RT\ ln\ a_i\ = \mu_i^o + RTln\ \gamma_i + RT\ ln\ m_i \tag{4.5}$$

where $R$ is the gas constant, and $T$ is the absolute temperature of the system.

When at equilibrium the relationship between all the aqueous species in a chemical reaction is related via a mass-action equation 4.6.

$$K_i = \ a_i \prod_{m}^{M_{aq}} a_m^{-c_{m.i}} \tag{4.6}$$

where $K_i$ is the temperature-dependent equilibrium constant, $c_{m,i}$ is the stoichiometric coefficient of master species $m$ in species $i$, and $M_{aq}$ is the total number of aqueous master species. Activity coefficients, $\gamma$, of the aqueous species are defined with the extended Debye-Hückel equation

$$log\gamma_i\ = \ - \frac{Az_i^2\sqrt{\mu}}{1 + Ba_i^o\sqrt{\mu}} + \ b_i\mu \tag{4.7}$$

or the Davies equation

$$log\gamma_i = Az_i^2 \left( \frac{\sqrt{\mu}}{1 + \sqrt{\mu}} - 0.3\mu \right) \tag{4.8}$$

where $z_i$ is the ionic charge of aqueous species $i$, $\mu$ is the ionic strength of the solution and $A$ and $B$ are temperature dependant constants.

Aqueous activity coefficients calculated using the extended Debye-Hückel equation are only valid for solutions of ionic strength ≤ 0.1 mol $L^{-1}$ for monovalent ions (Langmuir, 1997). At concentrations above this the Davies (valid up to 0.7 mol $L^{-1}$) or Pitzer (valid at ionic strength up to 6 mol $L^{-1}$) equations must be used (Langmuir, 1997). As some of the experimental work done here is performed at ionic strength of 1 mol $L^{-1}$ (and above) the Pitzer equation was used to calculate the $\gamma$ for these scenarios.

$$\begin{aligned} ln\gamma_M = -z_M^2 A^{\Phi} \left( \frac{I^{0.5}}{1 + bI^{0.5}} + \frac{2}{b} \ln(1 + bI^{0.5}) \right) + \sum_a m_a \left(2B_{Ma} + ZC_{Ma}\right) \\ + \sum_c m_c (2\Phi_{Mc} + \sum_a m_a \Psi_{Mca}) + \sum_a \sum_{<a`} m_a m_{a`} \Psi_{Maa`} \\ + |z_M| \sum_c \sum_a m_c m_a C_{ca} + \ldots \end{aligned} \tag{4.9}$$

Here the activity coefficient, $\gamma_M$, for the generic cation (called M) is determined as a function of ion specific parameters $B_M$, $C_M$, $\Phi_M$, and $\Psi_M$ determined from thermodynamic properties of the aqueous species of the

specified ion. Additionally $z_i$ is the charge of the ion and $m_i$ is its solution molality. Finally $A^{\Phi}$ and $b$ are modified forms of the Debye-Hückel constants (see equation 4.7).

All the sorption processes within the PHREEQC model are presented as binary cation exchange reactions, according to the Gains-Thomas convention. In the Gains-Thomas approach cation exchange is generically represented as

$$\mathrm{m}_1\text{-site} + \mathrm{m}_2 \leftrightarrow \mathrm{m}_2\text{-site} + \mathrm{m}_1 \tag{4.10}$$

where $m_1$ and $m_2$ are two distinct species (e.g. $Na^+$ and $Cs^+$, respectively) and the site is a specific cation exchange site in the sediment. Chemical species exchange in thermodynamic equilibrium with the sorption site, determined by a Gaines and Thomas (1953) mass action equation with an associated selectivity coefficient, $K_c$. Taking the example of $Cs^+$ for $Na^+$ exchange this gives

$$^{Cs}_{Na}Kc = \frac{N_{Cs}}{N_{Na}} . \frac{\alpha_{Na}}{\alpha_{Cs}} \tag{4.11}$$

where $\alpha_i$ is the aqueous activity of the solution species i and $N_m$ is the occupancy of the site with the given species, m, defined by

$$N_m = \Gamma_m / Q \tag{4.12}$$

where $\Gamma$ is the concentration of the sorbed species (mol $L^{-1}$) on the site and $Q$ is the total site capacity (mol $L^{-1}$).

In the model there are several specific sites available for cation exchange and a cation's affinity for each type of site is described by the relevant $K_c$ value. In the above example, a higher $K_c$ for any given site indicates that this site has a higher affinity for Cs and would sorb it more readily from solution compared to a site with a lower $K_c$. All the $K_c$ values are normalised against Na (with ${}^{Na}_{Na}K_c$ being 1), thus they describe the selectivity of each site for the sorbing ion relative to Na. The ${}^{Cs}_{K}K_c$ can be determined from ${}^{Cs}_{Na}K_c$ and ${}^{K}_{Na}K_c$ using the relationship

$$ {}^{Cs}_{K}Kc = \frac{{}^{Cs}_{Na}Kc}{{}^{K}_{Na}Kc} \tag{4.13} $$

In the model, $K_c$ values are entered as log $K_c$, and are referred to as such throughout.

Additionally, PHREEQC was utilised in chapter 6 to model the speciation of the alkali earth ions as a function of pH. In all cases a simple model was used with 45 ppm of the relevant element (Ca, Sr, Ba, Ra) at a pH range of 9-14. No other solid or solution phases were included. The activity of the different species was then determined using the extended Debye-Hückel equation (4.7). For Ca, Sr and Ba the modelling was performed using the PHREEQC thermodynamic database. However no thermodynamic data for

Ra is provided in this database so Ra modelling was performed using the HATCHES18 database (Bond et al., 1997).

### 4.2.4 Transmission electron microscopy

According to the de Broglie principle a beam of moving electrons behaves with wave like properties, as does a beam of moving photons. Therefore just as a beam of photons passing through a series of lenses and apertures is used to magnify a sample in a light microscope the same principle applies in an electron microscope. The first electron microscope was developed by Max Knoll and Ernst Ruska in 1934 and the same basic design principles continue in modern instruments (De Graef, 2003). An electron microscope consists of four basic components: an electron gun, to generate the electron beam; a series of focusing and magnifying lenses; the specimen, held in a mount; and various detectors for imaging or spectroscopy (McLaren, 1991, De Graef, 2003, Thomas and Goringe, 1979). An overview of this arrangement is shown in Figure 4.1 and each component will be discussed in more detail.

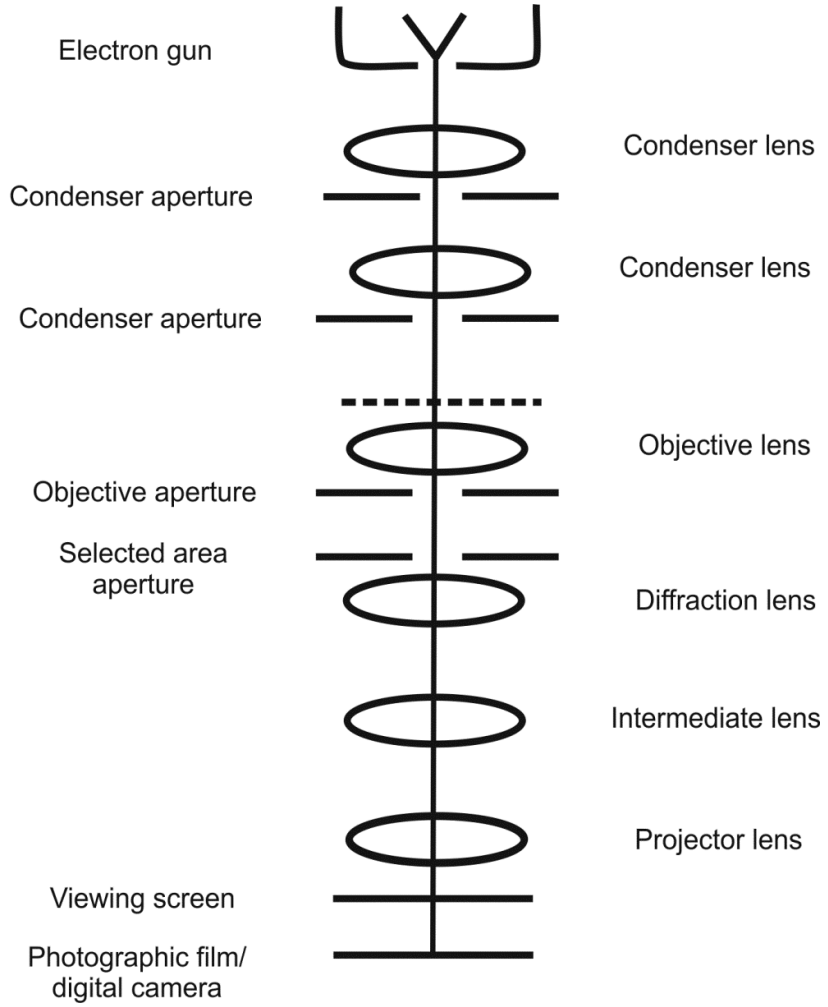


**Figure 4.1** Diagrammatic overview of a generic TEM, from McLaren (1991)

The electron gun acts in the same way as the lamp in a light microscope. Just as the lamp is required to produce a ray of photons of uniform wavelength the electron gun produces a beam of electrons of (ideally) uniform energy (Reimer and Kohl, 2010, De Graef, 2003, Thomas and Goringe, 1979, Von Heimendahl, 1980). Three main types of electron guns are employed in electron microscopy however they all share a basic arrangement of a cathode from which the electrons are emitted and an anode which accelerates them (Brydson, 2011). The first of these is the thermionic emission gun. It works by heating (to 1700-1900K) the cathode, a

thin metal (usually tungsten) wire, by passing a high current through it (De Graef, 2003). This wire then emits electrons which are focused and accelerated by the Wernholt anode which is much more negative than the cathode (Reimer and Kohl, 2010). The second class of gun is the Field Emission Gun which uses a tungsten or zirconium tip which acts as the cathode and emits electrons at room temperature. A series of anodes are then used to accelerate the emitted electrons (Brydson, 2011, Reimer and Kohl, 2010). Finally, if the tip is heated to aid emission then it is known as a Schottky electron gun (Brydson, 2011, Reimer and Kohl, 2010). Most modern (and all high resolution) TEMs use Schottky or Field Emission Guns as they provide a brighter and more spatially and temporally uniform electron beam than thermionic emission (Reimer and Kohl, 2010). The voltage of the emission is an important controlling factor in the resolution and magnification of the microscope. A simple rule of thumb is that microscopes with higher accelerating voltages will be able to resolve higher resolution images at higher magnification (Reimer and Kohl, 2010).

After leaving the electron gun the accelerated beam of electrons is focused and magnified by a series of lenses and apertures (McLaren, 1991, Fultz and Howe). Modern instruments use electromagnetic lenses. These are simply circular electromagnets, the centre through which the electron beam passes (Brydson, 2011). The focus and direction of the electron beam can then be altered by manipulating the lens current and the resulting magnetic field (Von Heimendahl, 1980). There are three main groups of lenses within the microscope. The condenser lenses are located above the specimen and

focus the generated electron beam onto the part of the specimen to be imaged (McLaren, 1991, Von Heimendahl, 1980, Thomas and Goringe, 1979). The beam then passes through the specimen, which is almost transparent to electrons (Von Heimendahl, 1980). The electrons are then scattered by elastic (diffraction without energy loss) and inelastic (electrons lose energy and are absorbed) scattering (Thomas and Goringe, 1979). The resulting image is then magnified and focused by the objective lens and objective aperture (Von Heimendahl, 1980, Fultz and Howe, 2002). For conventional transmission electron microscopy (CTEM) imaging, the beam is focused by the imaging lenses onto the viewing screen, or the imaging system (photographic plate or video camera) (Von Heimendahl, 1980, McLaren, 1991, Reimer and Kohl, 2010).

The practical magnification and resolution of any TEM is primarily limited by lens aberrations (Fultz and Howe, 2002, Von Heimendahl, 1980). Three main types of aberration occur due to different reasons and are corrected for by different methods. Astigmatism in lenses causes imaged points to become stretched and appear as small lines in the final image (Von Heimendahl, 1980). These are corrected using astimgmater which are fitted to all modern electron microscopes (Heidenreich, 1964). Chromatic aberration is caused by variation in the refractive indices of different wavelength electron beams (Von Heimendahl, 1980). This heterogeneity in the electron beam is caused by variation in their energy (Spence, 2003). It is most easily corrected using field emission guns, which have more uniform electron energy. In High Resolution TEM (HRTEM) spherical aberrations are

the main limit on resolution (Fultz and Howe, 2002). This occurs as electrons that travel through edges of the lenses are refracted more strongly (and to a greater angle) than those which pass through the central axis (Spence, 2003, SuperSTEM). In more recent years TEMs with spherical aberration correction have become more common. A number of approaches have been taken but they all involve the use of an aberration corrector which monitors the aberration and calculates the appropriate negative aberration which is then combined with the original beam to give a final aberration free image, with much higher resolution (SuperSTEM, Brydson, 2011). This correction of lens aberration and use of high energy electron guns has allowed modern microscopes to resolve to subatomic resolutions (better than 0.1nm) (SuperSTEM). In addition to CTEM the microscope can also be operated in scanning mode (STEM). In CTEM the whole area to be imaged is simultaneously exposed to the beam and the image is taken simultaneously (Brydson, 2011). In STEM mode the beam is focused to a much narrower point by the condenser aperture; this is then scanned across the sample building up the image one pixel at a time (Brydson, 2011, Fultz and Howe, 2002).

In addition to imaging techniques modern TEMs are also capable of a wide range of spectroscopic and analytical electron microscopy techniques. These can be performed in both CTEM and STEM microscopes. Electron Energy Loss Spectroscopy (EELS) allows elemental analysis of a solids composition by measuring the loss of energy from the electrons passing through the sample (Fultz and Howe, 2002, Reimer and Kohl, 2010). Similar

atomic information can be obtained by energy dispersive x-ray (EDX) spectroscopy. This relies on the fact that when the sample is bombarded by electrons, there is an energy transfer from the electron to the atoms within the specimen. This causes a rearrangements of the shell configuration of the electrons which results in the emission of x-rays (Brydson, 2011, McLaren, 1991). STEM EDX can be used to build atomic maps of a specimen for detailed quantitative analysis of crystal microstructure (Reimer and Kohl, 2010).

The final most important component of the TEM system is the specimen itself. Correct and careful preparation of the specimen is one of the most important determining factors in the quality of TEM images obtained. Specimens must be mounted on grids, which can be made from a range of materials, although carbon coated copper grids are most common (Reimer and Kohl, 2010, Von Heimendahl, 1980). When preparing the specimen the most important consideration is the thickness (McLaren, 1991). In order to allow penetration by electrons, samples should generally be very thin (<200nm for TEM and <50nm for HRTEM) although TEMs with higher accelerating voltages can tolerate thicker samples (in some cases up to 1μm) (McLaren, 1991, Reimer and Kohl, 2010). Thin samples can be prepared by a number of different chemical or mechanical techniques including microtoming and ion beam milling (Von Heimendahl, 1980, McLaren, 1991). The specimen is then inserted in holders into the microscope through an airlock(De Graef, 2003).

Extensive TEM work was conducted as part of chapter 5 of this thesis. Samples were mounted on carbon coated copper grids before imaging. A representative subsample was suspended in isopropyl alcohol and sonicated for around 5 minutes. A few drops of the suspension were then transferred onto the grid using a glass Pasteur pipette. This gave homogenous coverage of the grid with crystallites present at many different orientations. Bright field TEM imaging and spot EDX analysis of the Ca/Cs-illite system was performed using a Tecnai TF20 FEGTEM with an operating voltage of 200keV and at room temperature (293K). Damage experiments were also performed using the Tecnai TF20 FEGTEM at both room temperature (293K) and using a liquid nitrogen cryostat (80K). Ultra-high resolution STEM images and EDX maps were obtained using a FEI Titan G2 S/TEM at room temperature and with an operating voltage of 200keV, with a beam current of 0.1 nA, a convergence angle of 18 mrad and a HAADF inner angle of 54 mrad.

The image processing for this work was performed using Gatan DigitalMicograph. To determine the change in illite layer thickness associated with Cs interlayer incorporation the layer thickness was measured for both the starting illite material (with K in the interlayer) and 12 month Cs substituted illite. From this a range of measurements were taken. This gave a range of values from which a mean and mode could be determined. The mean layer thickness and the standard deviation within the measurements were then determined. A Mann Whitney U test was also performed to determine the statistical validity of this difference.

To take these measurements, intensity profiles of the HAADF images were produced which showed the relative amplitude across the illite crystal. In these cross sections peaks and troughs represented the aluminosilicate T-O-T layers and interlayers of the illite structure. The peak to peak or trough to trough difference between multiple peaks/troughs was measured and from this and average peak distance was determined. The average distance between the peaks then correlates to the average layer spacing in that transect. This process was repeated many times for interlayers in the 0 and 12 month illite samples.

The EDX data from the DIW control and Ca/Cs system was processed using INCA. For the long term system background subtracted EDX spectra were extracted from the elemental maps using Bruker ESPRIT software. The atomic percentage of the different elements within the spectra were then determined via a standardless Cliff-Lorimer analysis.

### 4.2.5 Density Functional Theory Calculations

Density functional theory is a quantum chemistry technique for estimating the electron structure of many body systems (groups of atoms). This involves solving the time-independent non-relativistic Schrödinger equation for many body systems. At its most basic level the theory relies on functionals (functions of functions) which estimate the spatial density of the electrons in the ground state atomic orbitals (Koch and Holthausen, 2000). The validity of density functional theory calculations is confirmed by the Hohenberg-Kohn theorems (Hohenberg and Kohn, 1964) which prove the

relationship between the ground state energy and ground state density. The most prevalent form of density functional theory is the Kohn-Sham approach (Kohn and Sham, 1965). Here the electrons are modelled as non-interacting bodies moving in an estimated potential (Koch and Holthausen, 2000). This potential is estimated using either the local density approximation (LDA) or the generalised gradient approximation (GGA). The modelling presented in this work offers both approaches.

The structural arrangement of illite, specifically the d-spacing, was modelled using density functional theory as part of chapter 6 of this work. Density functional theory calculations were performed using the projector-augmented-wave implementation (Blöchl, 1994, Kresse and Joubert, 1999) of the VASP code (Kresse and Furthmüller, 1996b, Kresse and Furthmüller, 1996a). The illite models comprised 83 atoms, with the chemical composition: $(M_3)[Al_5\ Fe(III)_2\ Mg][Si_{14}\ Al_2]O_{40}(OH)_8$, (where M = K or Cs), in order to match the sample used in the experiments as closely as possible. Isomorphic substitutions in the tetrahedral layer were placed far apart, in line with the observations of Militzer et al. (2011). Changing the arrangement of isomorphic substitution caused variations in d-spacing of about 0.01 Å.

The models were optimized with a kinetic energy cut-off for the plane-wave expansion of 800 eV and Brillouin-zone sampling restricted to the Γ-point. These settings ensured that calculated d-spacings were converged to within about 0.01 Å. The potentials were generated using the electronic configurations: $2p^6 3s^2$ for magnesium, $3d^7 4s^1$ for iron, $5s^2 5p^6 6s^1$ for

caesium, $3s^2 3p^1$ for aluminium, $1s^1$ for hydrogen, $3s^2 3p^2$ for silicon, and $2s^2 2p^4$ for oxygen. The calculations were spin polarised with iron modelled in a high-spin state.

All calculations were performed using both the local density approximation (LDA) (Perdew and Zunger, 1981) and PBE formulation of the generalized gradient approximation (GGA) (Perdew et al., 1996).The d-spacings predicted using the LDA and GGA differ by about 0.5 Å. This is in accord with the well-known fact that the LDA underestimates lattice parameters, while the GGA overestimates. Predicted changes in d-spacing, when going from K to Cs, however, are in much better agreement, as the effect of over- or under-binding cancels.

### 4.2.6 X-Ray Absorption Spectroscopy

For this work the coordination environment of Sr surface complexes was probed using Sr K-edge EXAFS, collected at both the B18 and I20 beam lines at the Diamond Light Source, Harwell, UK and BM26A (DUBBLE) at the European Synchrotron Radiation Facility (ESRF), Grenoble, France. Additionally Cs K-edge EXAFS data was collected at beamline B18 at the Diamond Light Source. The real achievable energy resolution of any beamline typically varies from ~0.1 eV to ~0.6 eV. This can make it difficult to compare XANES analysis from different beamlines as the spectra are collected at fundamentally different resolutions (variation in the calibration energy of the E0 position also occurs, but is easier to correct for using common standards). However in EXAFS analysis points are commonly

collected 3-5 eV apart (or rebinned to be so). Therefore the data analysed tends to be at similar resolution from all beamlines with the only significant difference being the signal/noise ratio. A brief overview of synchrotron radiation, EXAFS data collection and modelling is provided here with particular reference to Diamond and ESRF.

#### 4.2.6.1 The synchrotron and synchrotron radiation

Synchrotron radiation is a special type of electromagnetic radiation produced when charged particles travelling near the speed of light undergo centrifugal acceleration (Duke, 2000). The emitted radiation can cover a wide range of wavelengths, determined by the energy of the particles being accelerated (Kunz, 1979). Lower energy particles (in the 100-500MeV range) typically emit synchrotron radiation in the visible to near ultra-violet range. However, higher energy electrons (many GeVs) can emit synchrotron light up to hard x-rays (Kunz, 1979). This means that synchrotron light can be used for a wide range of analytical and spectroscopic techniques. Both Diamond and the ESRF can operate in the x-ray range, Diamond being a medium energy synchrotron (3GeV) (DiamondLightSource, 2009) and the ESRF a high energy source (6 GeV) (ESRF, 2013).

To produce this synchrotron light, synchrotrons are constructed. Synchrotrons consist of a few basic components, namely the electron source and accelerator, the storage ring and the beam lines (Margaritondo, 1998). Figure 4.2 shows a schematic overview of a synchrotron (Diamond) with the different components identified. Although synchrotron light can be

generated by the acceleration of either electrons or positrons, electrons are far easier to generate and so are much more commonly used (Kunz, 1979). The electrons are typically produced by thermionic emission from an electron gun (this is discussed in more detail in section 3.2.4). They are then collected into packets and accelerated initially by a linear accelerator up to a few hundred MeV before entering an accelerating synchrotron where they are sped up to relativistic speeds before the packets of electrons enter the storage ring (Ebashi et al., 1991). The storage ring is a synchrotron, but rather than being designed to accelerate the electrons it simply imparts enough energy to them to keep them at a constant relativistic speed and guides them through a circular path where they are accelerated centrifugally to generate synchrotron light (Margaritondo, 1998). The key component of the synchrotron is the bending magnets. These are large multi-polar electromagnets which serve the purpose of accelerating the electrons around a curved path (Kunz, 1979). This ensures that the electron beam follows a closed path, and it is at these bends that the electrons emit their synchrotron light. Coupled to the bending magnets are a series of focusing and defocusing lenses which ensure the beam maintains a stable and constant path around the ring. A number of radio-frequency cavities are also placed around the ring where an electromagnetic field imparts energy to the packets of electrons, to replace energy that was lost upon emission of synchrotron radiation and ensure the energy of the beam remains constant. If these cavities were not present the packets of electrons would quickly lose their energy and would have to be constantly replaced from the electron source. By having these cavities, the same packets of electrons can circulate the beam for many hours emitting synchrotron light (Margaritondo,

1998). In addition to bending magnets, many modern synchrotrons also include insertion devices, either wigglers or undulators. These are placed in the straight sections between bending magnets and consist of a set of permanent magnets which cause the beam of electrons to wiggle or undulate. These repeated accelerations of the electrons cause them to emit synchrotron radiation. The insertion devices can be purpose designed to give synchrotron radiation with unique characteristics not possible from bending magnets. Because of this the synchrotron radiation from insertion devices is often used for specialist applications where the radiation needs to have special properties of coherence or wavelength (Margaritondo, 1998, Ebashi et al., 1991). The whole storage ring arrangement is kept at an extremely low vacuum as the charged electrons are instantly destroyed when they come into contact with matter (Margaritondo, 1998). However, even at the low vacuums achieved some gas particles are present and collisions gradually reduce the total number of electron packets in the storage ring (the current). Because of this the ring must intermittently be topped up by adding new packets of electrons. This can be done either as a continuous trickle without interrupting the beam and the generation of synchrotron radiation (this is case at Diamond) or by injecting a large number of electrons in one go, which can disrupt synchrotron radiation generation (as occurs at ESRF).

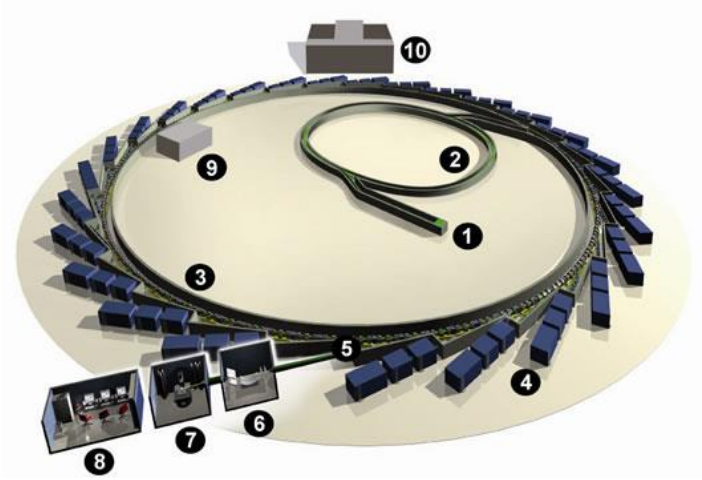


**Figure 4.2** Schematic diagram of the Diamond Light Source Synchrotron highlighting the key components. (1) The linear accelerator; (2) Booster Synchrotron (3)Storage ring; (4) Beam lines, comprised of (5) the front end (6) the optics hutch (7) experimental hutch and (8) control room; (9) a radio-frequency cavity; and (10) Diamond house, where offices are located. Schematic copied from (DiamondLightSource, 2009).

Once the synchrotron radiation has been produced it is utilised in beamlines. These are the ‘arms’ of the synchrotron which sprout out from the central storage ring at each of the bending magnets and insertion devices. The beamlines consists of a range of optical equipment which prepares the radiation for the intended end use. Most important of these with regard to x-ray absorption spectroscopy (XAS) is the monochromator. The monochromator (a solid silicon crystal for x-ray radiation) allows the selection of a specific energy of synchrotron radiation, by excluding all other energies (Kunz, 1979). For XAS this allows the beamline to be tuned to use x-rays of the given energy to probe the absorption edge of the given electron shell of the atom being studied. The x-rays are then focused and collimated by a collection of mirrors and lenses (Margaritondo, 1998). The final x-rays of extremely high optical quality are then used to probe the sample.

#### 4.2.6.2 Extended X-ray Absorption Fine Structure Spectroscopy

When the focused and monochromated x-ray beam interacts with the sample it is absorbed by the electron with the absorption energy equal to the energy of the incident x-ray beam. When the core electron absorbs the incident x-ray photon it becomes excited and rises to a higher energy level. This is an unstable state and it returns to its stable core energy by emission of a photo-electron of energy equal to the incident electron energy – the core electrons binding energy (Newville, 2004). These photo-electron waves radiate out from the central atom and are reflected by the nuclei of surrounding atoms with the wavelength of the reflected wave a product of the inter-atomic distances (Margaritondo, 1998). As these incident and reflected waves superimpose on one another they give the final measured wave. The high energy region (at energies well above the absorption edge) gives the EXAFS data as it is these higher energy photo-electrons which are emitted into the sample and reflected by the local atoms. Those photo-electrons emitted at energies just above the absorption edge yield information on the oxidation state of the central atom, these make up the XANES (x-ray absorption near edge spectroscopy) signal (Newville, 2004). In samples with significant concentrations of the atom of interest the resultant signal can be detected by transmission detectors which measure the change in the transmitted x-ray beam as a result of the absorption processes. In more dilute samples fluorescence detectors can measure the emitted (or fluoresced) photo-electron (Margaritondo, 1998).

The measured signal is then deconvoluted, normalised and mathematically processed to yield information on the interatomic distances and coordination

environment. In this work both Cs and Sr K-edge EXAFS were performed, the Cs EXAFS are presented in chapter 6 and the Sr EXAFS in chapter 7.

Cs K-edge (35985 keV) spectra were gathered on beamline B18 at the Diamond Light Source, Didcot, UK. The beam had a typical operating voltage of 3GeV and a stable beam current of 300 mA for the duration of the experiment. Before use the beam was vertically collimated by a Si mirror. The requisite beam energy range (35800 – 36800 keV) was then selected using a double crystal Si monochromator. A double torroidal mirror was then used to focus the monochromated beam onto the sample to give a final spot size of 200 x 250 µm. The 10 mg sub-sample was mounted into Perspex holders with Kapton tape windows. During data collection the sample was held in an Oxford Instruments cryostat at 80 K to enhance data quality and reduce the chance of radiation damage. Cs K-edge spectra were then gathered in fluorescence mode using a 9 element Ge solid state detector. To improve the signal to noise ratio a total of 144 5-minute scans were gathered and averaged using Athena. The default background subtraction provided by Athena was accepted and this final data was used for fitting.

The EXAFS data was analysed using Artemis (Ravel and Newville, 2005) running Feff 6.0 (Rehr and Albers, 2000). The initial model used was constructed using data from the molecular dynamics simulation. Similar length paths were grouped together, such that the initial model of O neighbours used was 2 at 3.04 Å, 4 at 3.12 Å and 6 at 3.40 Å with 12 Si atoms at 3.94 Å. Differentiating between Si and Al in EXAFS is difficult,

hence this last shell accounts for the signal due to both Si and Al scatterers. The inter-atomic distance and Debye-Waller factor for each shell, E0 and $S_0^2$ were refined in R-space using a range of 1.9 - 3.9 Å in R-space, keeping the number of atoms in each shell constant. To reduce the number of variables the Debye-Waller factors for the first two O shells were fixed to be the same value. The fit was made to the k, $k^2$ and $k^3$-weighted Fourier transforms using a range 2.5 -11 $Å^{-1}$ in k-space simultaneously. Once the best fit had been achieved each shell was removed in turn to check its significance. No reasonable fit could be achieved with only 3 shells of atoms.

The Sr EXAFS data presented here were gathered from three distinct beamline sessions. Spectral data for the chlorite samples with $10^{-5}$, $10^{-2}$ and $10^{-1}$ mol $L^{-1}$ NaOH and the sediment exposed to $10^{-1}$ mol $L^{-1}$ NaOH were gathered at beamline B18 at the Diamond Light Source. Here the incident beam has a typical operating voltage of 3 GeV and a current of 300 mA. The x-rays at B18 are generated from a bending magnet source. The beam is vertically collimated by a Si mirror before passing through a double crystal Si monochromator. It was then focused onto the sample to give a spot size of 200 x 250 µm. The Sr K edge (16105 keV) EXAFS spectra were gathered from fluorescence x-rays using a 9 element Ge solid state detector. The sample was held at 80K in a liquid nitrogen cryostat during data collection to improve the signal to noise ratio. The EXAFS data for samples of chlorite, goethite, sediment and illite in a 1 mol $L^{-1}$ NaOH background and the Chlorite sample in $10^{-5}$ mol $L^{-1}$ NaOH were gathered at the Dutch Belgian Beamline (DUBBLE) at the European Synchrotron Radiation Facility

(ESRF). This has an incident beam voltage of 6.04 GeV and a current of 200 mA. DUBBLE uses a bending magnet source which is vertically collimated by a Si mirror. The correct beam energy is then selected using a double crystal Si monochromator. The final incident beam has a spot size of 400 x 350 µm. Again at the ESRF a 9 element Ge detector was used to gather Sr K-edge fluoresce spectra. Data collection was also performed at 80 K in a liquid nitrogen cooled cryostat. Finally Sr K-edge EXAFS data from samples of Illite in $10^{-3}$ and $10^{-1}$ mol L NaOH and Goethite in $10^{-5}$, $10^{-3}$ and $10^{-1}$ mol L NaOH were gathered at beamline I20 at the Diamond light source. Here the x-ray source is derived from a wiggler style insertion device. The energy of the collimated beam is then selected by a unique 4 crystal monochromator which yields a beam with very high energy stability. The monochromated beam is then focused to give a final spot size of 400 x 350 µm. Sr K-edge fluorescence spectra were gathered using a 64 element solid state Ge detector and samples were held in a liquid nitrogen cryostat.

The scans were summed and averaged using Athena v 0.8.056 (Ravel and Newville, 2005) to maximise the signal/noise ratio. The background subtraction of the Sr EXAFS was then performed using PySpline v1.1 (Tenderholt et al., 2007). The EXAFS spectra were then fitted in k-space using DLexcurv v1.0 (Tomic et al., 2005) following full curved wave theory (Gunman et al., 1984). Ab initio calculations of the phaseshifts were performed using the Hedin-Lundqvist potentials and assuming the von-Barth ground states for all atoms (Binsted, 1998). Shell-by-shell fitting was then performed by estimating initial parameters for shells of backscattering atoms

and then interactively refining these parameters. Specifically fits were determined by refining the atom identity, number of atoms (± 25%), interatomic distances (± 0.02 Å in the first shell and ± 0.05 Å in subsequent shells), Fermi energy and Debye-Waller factor ($2\sigma^2$, ± 25%). This procedure was performed initially with a single shell and subsequent shells of surrounding atoms were added. Additional shells were then accepted where they improved the overall fit quality by greater than 5% (determined by reduction of the least squared residual, R-factor).

## 4.3 References

Binsted, N. 1998. *EXCURV98: CLRC Daresbury Laboratory computer program,* Warrington, CLRC Daresbury.

Blöchl, P. E. 1994. Projector augmented-wave method. *Physical Review B,* 50**,** 17963-17979

Bond, K. A., Heath, T. G. & Tweed, C. J. 1997. HATCHES: A Reference Thermodynamic Database for Chemical Equilibrium Studies. NDA.

Bradbury, M. H. & Baeyens, B. 2000. A generalised sorption model for the concentration dependent uptake of caesium by argillaceous rocks. *Journal of Contaminant Hydrology,* 42**,** 141-163.

Brydson, R. 2011. *Abberation-Corrected Analytical Transmission Electron Microscopy,* Chichester, UK, Wiley.

De Graef, M. 2003. *Introduction to Conventional Transmission Electron Microsopy,* Cambridge, Cambridge University Press.

DiamondLightSource. 2009. *The Diamond Machine* [Online]. Available: http://www.diamond.ac.uk/Home/Technology/Components/storagering.html [Accessed 8 October 2013.

Duke, P. J. 2000. *Synchrotron Radiation: Production and Properties,* Oxford, Oxford University Press.

Dutton, M. V., Foster, C. & Trivedi, D. 2009. Characterisation of Soils from B38 Site Investigation within the Sellafield Separation Area. NNL Commercial.

Ebashi, S., Koch, M. & Rubenstein, E. 1991. *Handbook on Synchrotron Radiation,* Amsterdam, North Holland.

ESRF. 2013. *What is a synchrotron?* [Online]. Available: http://www.esrf.eu/about/synchrotron-science/synchrotron [Accessed 8 October 2013.

Fultz, B. & Howe, J. M. 2002. *Transmission Electron Microscopy and Diffractometry of Materials,* Berlin, Springer.

Gaines, G. L. & Thomas, H. C. 1953. Adsorption Xtudies on Clay Minerals 2: A Formulation of the Thermodynamics of Exchange Adsorption. *Journal of Chemical Physics,* 21**,** 714-718.

Gunman, S. J., Binsted, N. & Ross, I. 1984. A rapid, exact curved-wave theory for EXAFS calculations. *Journal of Physics C: Solid State Physics,* 17**,** 143-151.

Heidenreich, R. D. 1964. *Fundamentals of Transmission Electron Microscopy,* New York, Wiley Interscience.

Hohenberg, P. & Kohn, W. 1964. Inhomogeneous electron gas. *Physical Review,* 136**,** B864-B871.

Khan, S. A., RiazurRehman & Khan, M. A. 1995. Sorption of strontium on bentonite. *Waste Management,* 15**,** 641-650.

Koch, W. & Holthausen, M. C. 2000. *A Chemist's Guide to Density Functional Theory,* Weinheim, Wiley-VCH.

Kohn, W. & Sham, L. J. 1965. Self-consistent equations including exchange and correlation effects. *Physical Review,* 140**,** A1133-A1138.

Kresse, G. & Furthmüller, J. 1996a. Efficiency of ab-initio total energy calculations for metals and semiconductors using a plane-wave basis set. *Computational Materials Science,* 6**,** 15-50.

Kresse, G. & Furthmüller, J. 1996b. Efficient iterative schemes for ab initio total-energy calculations using a plane-wave basis set. *Physical Review B,* 54**,** 11169-11186.

Kresse, G. & Joubert, D. 1999. From ultrasoft pseudopotentials to the projector augmented-wave method. *Physical Review B,* 59**,** 1758-1775.

Kunz, C. 1979. *Synchrotron Radiation: Techniques and Applications,* Berlin, Springer-Verlag.

Langmuir, D. 1997. *Aqueous Environmental Geochemistry,* New Jersey, Prentice Hall.

Margaritondo, G. 1998. *Introduction to Synchrotron Radiation,* Oxford, Oxford University Press.

McLaren, A. C. 1991. *Transmission electron microscopy of minerals and rocks,* Cambridge, Cambridge University Press.

McMillan, A. A., Heathcote, J. A., Klinck, B. A., Shepley, M. G., Jackson, C. P. & Degnan, P. J. 2000. Hydrogeological characterization of the onshore Quaternary sediments at Sellafield using the concept of domains. *Quarterly Journal of Engineering Geology & Hydrogeology,* 33**,** 301-323.

Mendham, J., Denney, R. C., Barnes, J. D. & Thomas, M. 2000. *Vogel's Textbook of Quantitative Chemical Analysis: Sixth Edition,* Harlow, UK, Prentice Hall.

Militzer, B., Wenk, H. R., Stackhouse, S. & Stixrude, L. 2011. First-principles calculation of the elastic moduli of sheet silicates and their application to shale anisotropy. *American Mineralogist,* 96**,** 125-137.

NCRP 1978. A Handbook of Radioactivity Mesurement Procedures. Washington DC.

Neame, K. D. & Homewood, C. A. 1974. *Introduction to liquid scintillation counting,* London, Butterworth & Co.

Newville, M. 2004. Fundamentals of EXAFS. Chicago: Consortium for Advanced Radiation Sources.

Parkhurst, D. L. & Appelo, C. A. J. 1999. *User's guide to PHREEQC (version 2),* Denver, US Geological Survey.

Perdew, J. P., Burke, K. & Ernzerhof, M. 1996. Generalized gradient approximation made simple. *Physical Review Letters,* 77**,** 3865-3868.

Perdew, J. P. & Zunger, A. 1981. Self-interaction correction to density-functional approximations for many electron systems. *Physical Review A,* 23.

Randall, M. G., Brydie, J., Graham, J. & Small, J. S. 2004. SCLS Phase 1: The Geochemistry of the Sellafield Site. BNFL Commercial.

Ravel, B. & Newville, M. 2005. ATHENA, ARTEMIS, HEPHAESTUS: data analysis for X-ray absorption spectroscopy using IFEFFIT. *Journal of Synchrotron Radiation,* 12**,** 537-541.

Rehr, J. J. & Albers, R. C. 2000. Theoretical approaches to x-ray absorption fine structure. *Reviews of Modern Physics,* 72**,** 621-654.

Reimer, L. & Kohl, H. 2010. *Transmission Electron Microscopy: Physics of Image Formation,* New York, Springer.

Schwertmann , U. & Cornell, R. M. 2000. *Iron Oxides in the Laboratory: Preparation and Characterisation,* Weinheim, Wiley-VCH.

Spence, J. C. 2003. *High Resolution Tranmssion Electron Microscopy,* Oxford, Oxford University Press.

SuperSTEM. *Introduction to Spherical Aberration Correction in Electron Microscopes* [Online]. Available: http://www.superstem.org/cs-correction [Accessed April 2013].

Tenderholt, A., Hedman, B. & Hodgson, K. O. 2007. Pyspline: A modern, cross-platform program for the processing of raw averaged XAS edge and EXAFS data. *AIP Conference Proceedings,* 882**,** 105-107.

Thomas, G. & Goringe, M. J. 1979. *Transmission Electron Microscopy of Materials,* New York, Wiley Interscience.

Tomic, S., Searle, B. G., Wander, A., Harrison, N. M., Dent, A., Mosselmans, J. F. W. & Inglesfield, J. E. 2005. New Tools for the Analysis of EXAFS: The DL_EXCURV Package. *CCLRC Technical Report DL-TR-2005-00.*

Von Heimendahl, M. 1980. *Electron Microscopy of Materials: An Introduction,* New York, Academic Press.

Wallace, S. H. 2012. *Investigation of strontium-90 beahviour in contaminated land.* PhD Thesis, The University of Leeds.

Wallace, S. H., Shaw, S., Morris, K., Small, J. S., Fuller, A. J. & Burke, I. T. 2012. Effect of groundwater pH and ionic strength on strontium sorption in aquifer sediments: Implications for 90Sr mobility at contaminated nuclear sites. *Applied Geochemistry,* 27**,** 1482-1491.

# Chapter 5 – Ionic strength and pH dependent multi-site sorption of Cs onto a micaceous aquifer sediment

This first experimental chapter presents results of an investigation into Cs sorption under conditions relevant to the Sellafield site in West Cumbria. This chapter is based on a paper published in Applied Geochemistry (Fuller et al., 2014)

## 5.1 Introduction

Fallout from nuclear weapons testing and reactor accidents (e.g. Chernobyl, Ukraine; Fukushima, Japan and Three Mile Island, USA) have left many areas of land around the world contaminated with radionuclides (chiefly $^{137}Cs^{+}$) (Bandstra et al., 2012, Beresford, 2006). Additionally, legacy wastes from civil power generation are held in storage ponds at a number of nuclear facilities internationally, e.g. Sellafield, UK and Hanford, USA (Babad et al., 1993, McKenzie and Armstrong-Pope, 2010). Accidental and approved releases from these storage facilities have led to contamination of the subsurface (e.g. soils and sediments) and groundwater environments (Reeve and Eilbeck, 2009, McKenzie and Armstrong-Pope, 2010, Chorover et al., 2008). Particular focus has been on the isotopes of caesium, notably $^{137}Cs$ ($t_{1/2}$ = 30 years), which occurs as $^{137}Cs^{+}$ in all environmental situations (Söderlund et al., 2011). As a high yield fission product $^{137}Cs^{+}$ is relatively abundant in nuclear waste (NDA, 2010). It is a high energy gamma emitter, which is not easily shielded by soils and structures (Hill et al., 2001). This makes it one of the main sources of external radiation dose at contaminated

sites. Predicting the transport and remediation of $Cs^+$ contamination at these sites is a major environmental challenge and many studies have reported its environmental behaviour (Beresford, 2006, Shand et al., 1994, Livens and Baxter, 1988). However, developing detailed models of $Cs^+$ transport requires site specific knowledge of its sorption behaviour, including the effect of changing geochemical conditions (e.g. pH and ionic strength).

It is well established that sorption to clay minerals governs the mobility of $Cs^+$ in the subsurface environment (Shenber and Eriksson, 1993, Aldaba et al., 2010). Studies into the sorption behaviour of $Cs^+$ in soils and sediments have traditionally used solution based experimental approaches (mainly batch experiments) to probe these processes (Sawhney, 1972, Eberl, 1980). In soils $Cs^+$ chiefly sorbs to the surfaces of clay minerals in the fine (< 2 μm) fraction (He and Walling, 1996). This is due to their large surface area and high density of charged surface sites (Langmuir, 1997). Like other monovalent cations, $Cs^+$ sorbs principally on clay minerals by charge compensating cation exchange (Beresford, 2006, Bouzidi et al., 2010, Cornell, 1993, Hird et al., 1995). Although $Cs^+$ will interact with all the charged surfaces in a soil or sediment, it has been shown repeatedly that $Cs^+$ sorbs preferentially to some sites before others (Livens and Loveland, 1988, de Koning et al., 2007, Francis and Brinkley, 1976).

$Cs^+$ selectively sorbs to 2:1 aluminosilicate clays of the mica group, specifically illite $(K,Ca,Mg)\,(Al,Mg,Fe)_2\,(Si,Al)_4\,O_{10}\,[(OH)_2,(H_2O)]$, through charge compensating cation exchange (Chorover et al., 2008, Cremers et

al., 1988, Sawhney, 1972). Illite is a common constituent of many temperate mineral soils (Meunier and Velde, 2004) such as those found at contaminated nuclear sites. Grutter et al. (1986) also noted that Cs can selectively sorb to (illite like) collapsed vermiculate interlayer defects in chlorite. Therefore many studies have focused on the sorption of $Cs^+$ to illite or illitic soils and sediments (de Koning et al., 2007, Poinssot et al., 1999, Sawhney, 1972). It is important to be able to accurately predict the likely behaviour of contaminants under all potential circumstances. As sorption of cations is known to be controlled by the ionic strength and pH of the system (Krauskopf and Bird, 1995, Sposito, 1989, Sposito, 1984) it is important to understand the sorption behaviour of $Cs^+$ under a range of geochemical conditions.

Isotherm investigations of $Cs^+$ sorption have shown that its uptake onto illitic sediments changes non-linearly with concentration (Campbell and Davies, 1995). Jacobs and Tamura (1960) were the first to propose a multi-site sorption process to account for this non-linearity. They suggested a small number of high affinity sites where $Cs^+$ preferentially sorbs, and a large number of non-specific exchange sites. Subsequent authors have used competitive sorption and retention studies to develop this theory. Currently the high affinity sorption sites are thought to be Frayed Edge Sites (FES), which sorb and retain $Cs^+$ in preference to other cations (Chorover et al., 2008, Hird et al., 1996, Dyer et al., 2000, Davies and Shaw, 1993). As sorption of $Cs^+$ to iron oxides and organic matter is known to be negligible (Campbell and Davies, 1995, Hou et al., 2003), the low affinity sites are

commonly assigned to the basal plane of clay minerals. The FES are defined by Nakao et al. (2008) as a partially expanded wedge zone at the edge of the clay interlayer with a basal spacing of 10-14 Å. The FES forms as the mica-illite undergoes weathering of the interlayer which expands from the edge inwards (Jackson et al., 1952, Jackson, 1968). $Cs^+$ ions are thought to sorb in this wedge through cation exchange with structural interlayer $K^+$ ions at the edge of the particle (Chorover et al., 1999, Sawhney, 1965, Kim et al., 1996). As $Cs^+$ is a weakly hydrated cation it is able to readily shed its hydration shell and form inner-sphere complexes with oxygen atoms from the illite tetrahedral layers (Cornell, 1993, Sawhney, 1972, Kim et al., 1996). These sites are inaccessible to more strongly hydrated monovalent and divalent cations (e.g. Na, Ca) so they selectively sorb $Cs^+$ from solution (Cremers et al., 1988, Francis and Brinkley, 1976, Staunton, 1994, de Koning and Comans, 2004).

Many authors have tried to use isotherms to elucidate the properties of the FES but the value of this approach is limited because they offer no direct mechanistic explanation for the site or Cs sorption behaviour. However, the introduction of geochemical modelling codes has allowed the complexities of the sorption process to be more effectively explained. A number of different geochemical speciation codes exist including Geochemists workbench (Bethke and Yeakel, 2013), MINSORB (Bradbury and Baeyens, 1997) and PHREEQC (Parkhurst and Appelo, 1999). These vary in both their mathematical formulation of activity coefficients and their programming language and structure. Most investigators have modelled $Cs^+$ sorption

isotherms for either pure illite systems (Poinssot et al., 1999) or bulk sediments containing mica/illite (Liu et al., 2004, Steefel et al., 2003, Zachara et al., 2002). The sorption of $Cs^+$ in these systems is modelled as a multi-site cation exchange process. Selectivity coefficients ($K_c$ values) are used to assign one site with high $Cs^+$ affinity and one generic site. More recently authors have proposed splitting the high affinity site in two to give a FES and “Type II” sorption site (Bradbury and Baeyens, 2000, Steefel et al., 2003). Experimental evidence for this was obtained by Brouwer et al., (1983) who showed the high affinity site could be divided into a $Cs^+$ selective site and a $Cs^+/Rb^+$ selective site. The FES are thought to be located right at the edge of the interlayer, with the Type II site further out in the wedge where the interlayer is slightly expanded (Bradbury and Baeyens, 2000, Brouwer et al., 1983). Although much work has been done on competitive sorption of $Cs^+$ in the presence of a variety of other cations (de Koning et al., 2007, Sawhney, 1970) there is limited knowledge of the effect of pH on $Cs^+$ uptake by sediments. All previous investigations where pH was varied have been done at trace $Cs^+$ concentrations where $H^+$ is not expected to compete for the specific FES, and $Cs^+$ will be selectively sorbed (Giannakopoulou et al., 2007, de Koning et al., 2007, Chorover et al., 1999). Although it is likely that on the non-specific sites $H^+$ will compete with $Cs^+$, this effect has not previously been investigated experimentally. Poinssot et al., (1999) observed some pH dependence at low $Cs^+$ concentrations, where sorption to the FES dominates, and they explained this as either mineral dissolution or $H^+$ cation exchange.

This study focuses on the Sellafield site, located in West Cumbria, UK on the Irish Sea coast and to the west of the Lake District National Park. The facility is located on heterogeneous glacial drift deposits which overlie a complex succession of Triassic sandstone, Carboniferous limestone and Ordovician volcanics (Chaplow, 1996). The deposits themselves are course sediments, with the sand or gravel fraction comprising 90% by weight, and around 1-5% clay sized particles (Randall et al., 2004). The mineralogy is dominated by quartz (65%) and K-feldspar (12%), with the remaining comprised of iron oxides and aluminosilicate clay minerals, dominantly illite (around 70% of the <2µm fraction) (Dutton et al., 2009, Randall et al., 2004). The site has a complex mix of radioactive and non-radioactive contaminants present as a result of its long history of civil and military nuclear development and waste reprocessing (McKenzie and Armstrong-Pope, 2010). It is reported to be one of the most radioactively contaminated sites in Europe (McKie, 2009) and provides a good test case for understanding the behaviour of radionuclides in the subsurface environment.

This chapter presents a study of the sorption behaviour of $Cs^+$ at a range of concentrations on a micaceous sediment representative of that underlying the Sellafield site. The first objective of the work was to experimentally describe $Cs^+$ sorption across a wide range of $Cs^+$ solution concentrations. Batch sorption experiments were used to determine the effect of varying pH and competing ions on the concentration dependent sorption process. This data was then interpreted using a fitted multi-site cation exchange model. The implications of these results for the management of contaminated land

at Sellafield are then discussed in detail. However, the results are likely to be broadly applicable to sites with similar mineralogy to Sellafield (especially if illite is present).

## 5.2 Materials and Methods

### 5.2.1 Sediment collection and storage

Experiments reported here were performed on sediment collected in August 2009 from the Calder Valley, Cumbria. This is close to the Sellafield site, on the same glacial till geological unit as that underlying the site. After collection, the sediment was oven dried at 40°C and stored in a HDPE plastic container (Wallace et al., 2012, Law et al., 2010).

### 5.2.2 Sorption experiments

In this work two types of experiments were performed: concentration variable isotherm experiments where the pH was kept constant and the concentration of $Cs^+$ varied across a range from $1.0 \times 10^{-9}$ to $1.0 \times 10^{-1}$ mol $L^{-1}$ and pH sorption edge experiments where a fixed $Cs^+$ concentration was used, and the pH varied across the range 2-10. Both sets of experiments were conducted using three background solution matrices, namely starting solutions of deionised water (DIW), 1.0 mol $L^{-1}$ NaCl and 1.0 mol $L^{-1}$ KCl to probe the effect of cationic competition. An initial set of competing ion experiments were performed to determine the most appropriate concentrations of $K^+$ and $Na^+$ to use as a background matrix to maximise any competing ion effect. It was determined that both $Na^+$ and $K^+$ should be

included in the background matrix at a concentration of 1.0 mol $L^{-1}$ to ensure an easily measurable competing ion effect was observed (Figure 5.1).

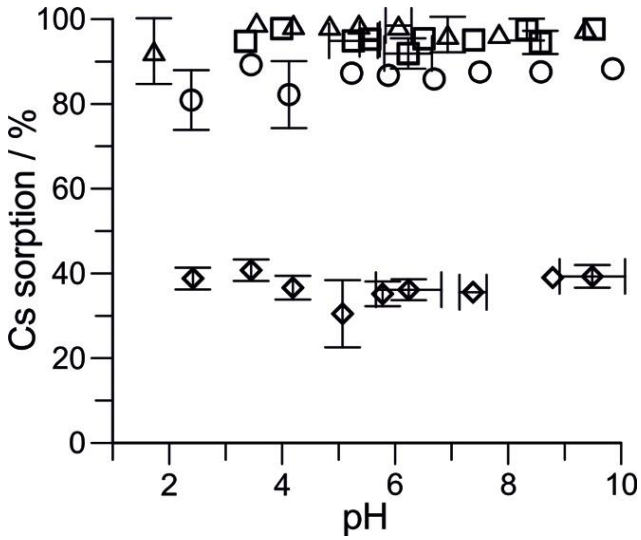


**Figure 5.1** Competitive sorption of $10^{-9}$ mol $L^{-1}$ Cs from a background solution of 1 mol $L^{-1}$ KCl (diamonds), 0.1 mol $L^{-1}$ KCl (circles), 0.01 mol $L^{-1}$ KCl (triangles) and 1 mol $L^{-1}$ NaCl (squares). Data points represent the average of a triplicate sample. Error bars are shown on those points where the error (standard deviation) was greater than or equel to the size of the symbol

The full range of experimental conditions is shown in Table 5.1, and the specific procedure for setting up each experiment is described below. All experiments were performed in triplicate with a sediment-free control sample to determine if any sorption to the tubes was occurring. Results from the blank experiments showed that there was no sorption of $Cs^+$ to the tubes under any of the experimental conditions (data not shown). Therefore all $Cs^+$ sorption was attributed to the sediment.

**Table 5.1** Experimental parameters

| Experiment | pH | Initial Cs concentration mol $L^{-1}$ | Background solution |
|---|---|---|---|
| Isotherms | 6.8 ± 0.2 | 1 $x10^{-9}$; 1 $x10^{-4}$; 1 $x10^{-1}$ | Deionised water<br>1 mol $L^{-1}$ NaCl<br>1 mol $L^{-1}$ KCl |
| pH sorption edges | 2.0 – 10.0 | 1 $x10^{-11}$ | Deionised water<br>1 mol $L^{-1}$ NaCl<br>1 mol $L^{-1}$ KCl |
| | | 1 $x10^{-4}$ | Deionised water<br>1 mol $L^{-1}$ NaCl<br>1 mol $L^{-1}$ KCl |
| | | 1 $x10^{-1}$ | Deionised water<br>1 mol $L^{-1}$ NaCl<br>1 mol $L^{-1}$ KCl |

The solution composition of the system was varied depending on the requirements of the experiment. For all experiments samples of < 1.0 mm sieved sediment were pre-wetted with deionised water. Samples were then suspended in the particular experimental solution, containing the desired amount of inactive CsCl, in 50 mL polypropylene Oak Ridge tubes at a solid solution ratio of 100 g $L^{-1}$. Following suspension the samples were spiked with a radiotracer of $^{137}Cs^{+}$ at a specific activity of 30 Bq $mL^{-1}$ (equivalent to 7.0 x $10^{-11}$ mol $L^{-1}$). Samples were then agitated for 48 hours on an orbital shaker at 140 rpm at room temperature (20 ± 1°C). Comans et al. (1991) and Poinssot et al. (1999) showed that $Cs^{+}$ sorption is kinetically moderated, involving a rapid initial cation exchange process, followed by a period of slow incorporation into the clay structure (Comans and Hockley, 1992). This work focuses solely on the cation exchange process so a 48 hours sorption period was chosen to allow pseudo-equilibrium to be reached and for cation

exchange processes to reach completion. The pH of the solution was measured before and immediately after addition to the sediment and adjusted with 1.0 mol $L^{-1}$ HCl and NaOH to overcome the sediments buffering capacity and ensure minimal pH drift during the 48 hour equilibration period (when pH was not monitored). Final experimental pH was recorded after 48 hours and this value was reported in the results. The pH was recorded using an Orion model 420A bench top pH meter and glass bulb electrode calibrated to pH 4, 7 and 10 using standard buffer solutions. Following the sorption period tubes were centrifuged for 10 minutes at 6,000*g*. A 1 mL representative sample of the supernatant was then transferred to a liquid scintillation vial containing 10 mL of Ecoscint A solution. Final solution activity (Bq $mL^{-1}$) was then measured by liquid scintillation counting on a Packard Tri-Carb 2100TR liquid scintillation counter with a counting window of 0 – 280 keV and 10 minute counting period. Percentage $Cs^+$ sorption and distribution coefficient, $K_d$, values were then calculated using the methodology of Khan et al. (1995) shown in Wallace et al. (2012). The final concentration of other ions (i.e. non $Cs^+$) in the system was not measured.

For the isotherm experiments, the effect of $Cs^+$ solution concentration on sorption was investigated using CsCl solutions at a range of concentrations between $1.0 \times 10^{-9}$ mol $L^{-1}$ and $1.0 \times 10^{-1}$ mol $L^{-1}$. Isotherms were performed at circumneutral pH (6.8 ± 0.2); achieved by adjustment with HCl or NaOH (as described above). The sorption behaviour was analysed using a tracer

spike of $^{137}Cs^{+}$ (30 Bq $mL^{-1}$ or 7.0 x $10^{-11}$ mol $L^{-1}$) and the aqueous activity measured by liquid scintillation counting.

For the pH sorption edge experiments, the effect of pH upon the sorption of $Cs^{+}$ was determined by adjusting the initial experimental suspensions with 1.0 mol $L^{-1}$ HCl and 1.0 mol $L^{1}$ NaOH to give a pH range from 2-10. Samples were pH checked at the beginning of the analysis, and after adjustment to overcome the sediments buffering capacity. The final pH values at the end of a 48 hour sorption period are then reported. For the pH experiments three concentrations of $Cs^{+}$ were chosen. These were selected based on the different regimes of $Cs^{+}$ sorption behaviour displayed in the isotherm experiments and were 7.0 x $10^{-11}$ mol $L^{-1}$ added as a 30 Bq $mL^{-1}$ tracer spike of $^{137}Cs^{+}$ and 1.0 x $10^{-4}$ mol $L^{-1}$ and 1.0 x $10^{-1}$ mol $L^{-1}$ added as CsCl (with a radioactive tracer spike to allow analysis by liquid scintillation counting).

### 5.2.3 Modelling

A multi-site cation exchange model was constructed in PHREEQCv2 to perform geochemical modelling of $Cs^{+}$ sorption to the micaceous sediment (Parkhurst and Appelo, 1999). The full PHREEQC modelling input data is provided in the supporting information. The model was based initially on the model of Bradbury and Baeyens (2000). The modelling aim was twofold: Firstly to test the validity of the generic Bradbury and Baeyens (2000) model under scenarios of $Cs^{+}$ contamination relevant to Sellafield, and secondly to refine the model in light of our experimental results to provide a specific

description and prediction of $Cs^+$ sorption at Sellafield. The generic $K_c$ values (selectivity coefficients) proposed by Bradbury and Baeyens (2000) for $Cs^+$ sorption to argillaceous rocks in the presence of competing $Na^+$ and $K^+$ ions have been used in previous models of $Cs^+$ sorption at Sellafield (Randall et al., 2004). These models are used to predict likely sorption and migration of $Cs^+$ in the subsurface as part of safety case evaluations. Therefore it is extremely important to assess whether the generic Bradbury and Baeyens model accurately predicts $Cs^+$ sorption onto Sellafield-like sediments, and to refine the model in light of our experimental investigation to improve the accuracy of future predictive modelling. As experiments were performed across a large ionic strength range the aqueous activity coefficients, γ, were calculated accordingly. At ionic strengths ≤ 0.1 mol $L^{-1}$ the extended Debye-Hückel equation was used, with the wateq4f.dat thermodynamic database (Ball and Nordstrom, 1991). However in the systems with a total ionic strength > 0.1 mol $L^{-1}$ the Pitzer equations were used, with the Pitzer.dat database (Plummer et al., 1988). In the generic Bradbury and Baeyens (2000) model, and in our refined version, all aqueous phases are assumed to be in thermodynamic equilibrium. The behaviour of aqueous species *i* is governed by its activity, $a_i$, activity coefficient, $\gamma_i$, molality, $m_i$, and number of moles in solution, $n_i$ where $a_i = \gamma_i m_i$ and $n_i = m_i W_{aq}$ where $W_{aq}$ is the mass of aqueous water in solution.

### 5.2.4 Binary cation exchange

The following section is heavily indebted to Bradbury and Baeyens (2000) whose model this work is based on, and refined from. All the sorption processes within the PHREEQC model are presented as binary cation

exchange reactions, according to the Gains-Thomas convention. In the Gains-Thomas approach cation exchange is generically represented as $m_1$-site + $m_2 \leftrightarrow m_2$-site + $m_1$, where $m_1$ and $m_2$ are two distinct species (e.g. $Na^+$ and $Cs^+$, respectively) and the site is a specific cation exchange site in the sediment. Chemical species exchange in thermodynamic equilibrium with the sorption site, determined by a Gaines and Thomas (1953) mass action equation with an associated selectivity coefficient, $K_c$. Taking the example of $Cs^+$ for $Na^+$ exchange this gives ${}^{Cs}_{Na}K_c = N_{Cs}/N_{Na} \,.\, \alpha_{Na}/\alpha_{Cs}$ where $\alpha_i$ is the aqueous activity of the solution species i and $N_m$ is the occupancy of the site with the given species, m, defined by $N_m = \Gamma_m/Q$ where Γ is the concentration of the sorbed species (mol $L^{-1}$) on the site and $Q$ is the total site capacity (mol $L^{-1}$).

In the model there are several specific sites available for cation exchange and a cation's affinity for each type of site is described by the relevant $K_c$ value. In the above example, a higher $K_c$ for any given site indicates that this site has a higher affinity for Cs and would sorb it more readily from solution compared to a site with a lower $K_c$. All the $K_c$ values are normalised against Na (with ${}^{Na}_{Na}K_c$ being 1), thus they describe the selectivity of each site for the sorbing ion relative to Na. The ${}^{Cs}_{K}K_c$ can be determined from ${}^{Cs}_{Na}K_c$ and ${}^{K}_{Na}K_c$ using the relationship ${}^{Cs}_{K}K_c = {}^{Cs}_{Na}K_c \,/\, {}^{K}_{Na}K_c$. In the model, $K_c$ values are entered as log $K_c$, and are referred to as such throughout.

## 5.3 Results and Discussion

### 5.3.1 Sediment characterisation

The sediment was previously characterised by Wallace et al. (2012) and Law et al. (2010), a brief summary is given here. It had a sandy texture containing 94% sand, 5% silt and 1% clay sized particles. Quartz dominated the bulk with minor muscovite, chlorite, albite and microcline also identified by x-ray diffraction (XRD). XRD analysis of the separated clay sized fraction showed it contained quartz, K- feldspar, iron oxides and aluminosilicate clays, namely illite and chlorite (clinochlore). Additionally, scanning electron microscopy (SEM) observations by Wallace et al. (2012) showed that many of the quartz grains were coated with aluminosilicate clay minerals, suggesting that the surfaces available for reaction within the sediment are likely to be dominated by clay minerals, including illite. Also, Dutton et al. (2009) showed that the same coatings were present on quartz grains in sediment taken from below the Sellafield site. The total cation exchange capacity (CEC) of the sediment, as determined by sorption of copper triethylenetetramine, was 8.2 ± 5.1 meq $100g^{-1}$ and it had a BET surface area of 3.4 ± 0.6 $m^2$ $g^{-1}$.

### 5.3.2 Cs concentration dependence

To allow maximum clarity for interpretation, the experimental and modelling results are presented in this work in terms of percentage sorption of the initial solution concentration. However, the isotherms (presented in Figure 5.2) are also presented in terms of equilibrium solution and solid concentrations in Figure 5.3.

For those experiments with no competing ion (Figure 5.2 a) near total sorption of $Cs^+$ (99.4 ± 0.2 %) was observed at very low $Cs^+$ concentrations ($1.0 \times 10^{-7}$ mol $L^{-1}$). This translates to a $K_d$ of 1471 ± 268 L $kg^{-1}$. A slight decrease in sorption was determined above this concentration. At $1 \times 10^{-5}$ mol $L^{-1}$ $Cs^+$, sorption was reduced by ~1 % to 98.4 ± 0.9 % which gives a $K_d$ of 695 ± 373 L $kg^{-1}$, a reduction of around 800 $K_d$ units. There was no further significant change in $Cs^+$ sorption until $1.0 \times 10^{-3}$ mol $L^{-1}$ where % sorption was reduced to 93.7 ± 1.9 % with a corresponding $K_d$ of 159 ± 45 L $kg^{-1}$. Further reduction in sorption was seen above this $Cs^+$ concentration with values of 46.2 ± 1.2 % at $1.0 \times 10^{-2}$ mol $L^{-1}$ and 8.3 ± 6.6 % at $1 \times 10^{-1}$ mol $L^{-1}$. This reflected a reduction in sorption of 85.4 % over two orders of magnitude of change in $Cs^+$ aqueous concentration.

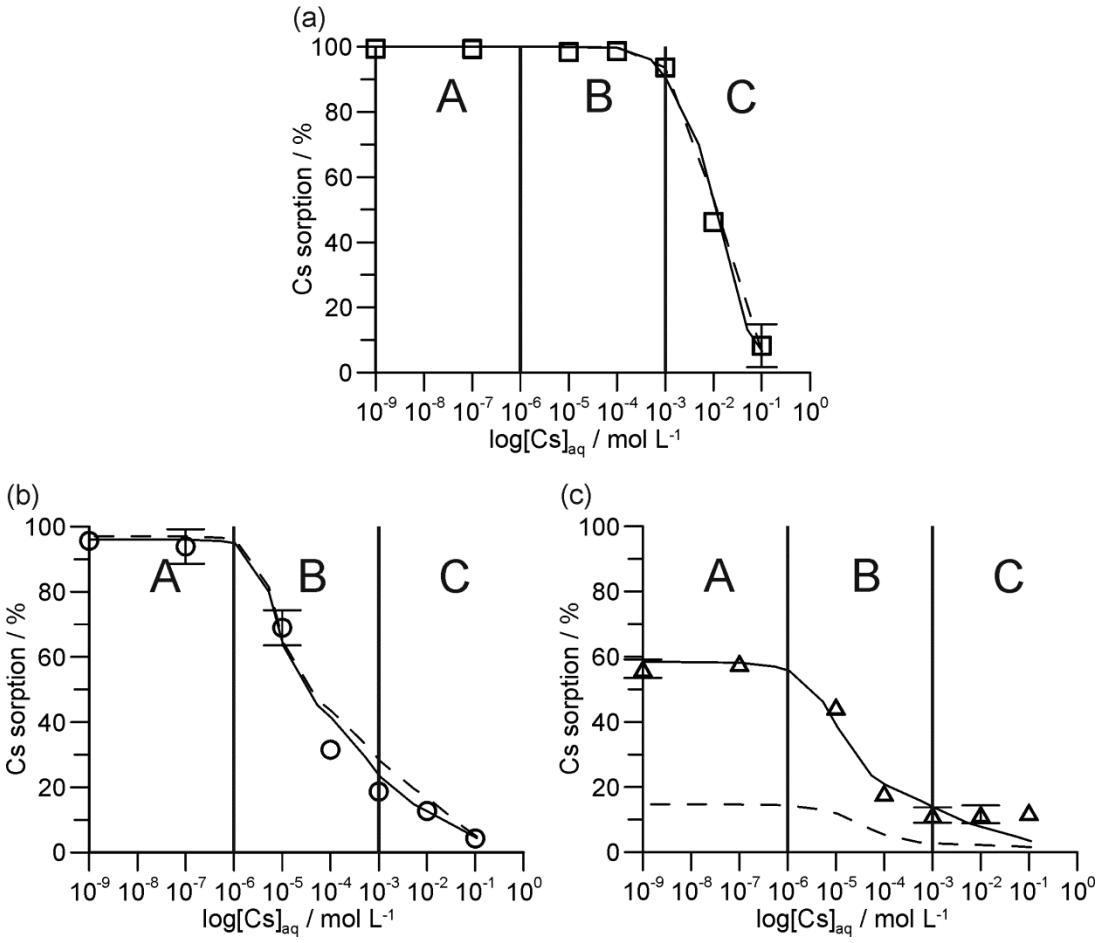


**Figure 5.2** Sorption isotherm showing sorption of $^{137}Cs$ ions from a solution of CsCl at a range of concentrations; from 1 x $10^{-9}$ to 1 mol L-1 and at a solid solution ratio of 100 g $L^{-1}$. Cs was present in a background of (a) deionised water, (b) 1 mol $L^{-1}$ Na (as NaCl) and (c) 1 mol $L^{-1}$ K (as KCl). Solid line represents modelling results using the new fitted values. Dotted line represents modelling prediction using generic values from Bradbury and Baeyens (2000). Vertical bars and reigons labelled A, B and C differentiate the concentration ranges with different Cs sorption behaviours, see section 3.2 main text. All data was collected at circumneutral pH. Data points represent the average of a triplicate sample. Error bars are shown on those points where the error (standard deviation) was greater than or equal to the size of the symbol

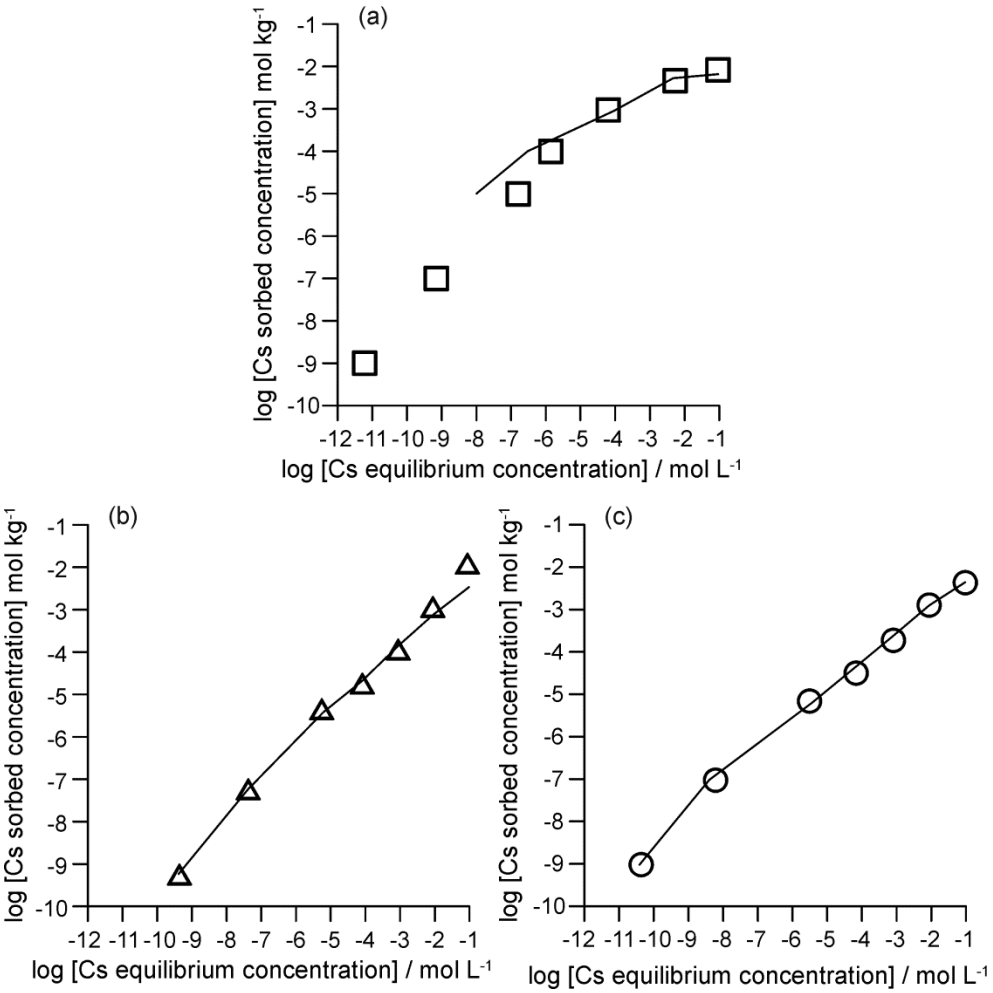


**Figure 5.3** Cs sorption isotherms in a background of (a) deionised water, (b) 1 mol $L^{-1}$ Na (as NaCl) and (c) 1 mol $L^{-1}$ K (as KCl). Data points indicate measured experimental results (averages of three replicates) and solid line is the model output. Error bars are not shown as they were smaller than the symbol

When the concentration dependent sorption experiments were repeated in a background of 1.0 mol $L^{-1}$ Na, markedly different results were observed (Figure 5.2b). Again at the very low concentrations (1.0 x $10^{-7}$ mol $L^{-1}$) near total Cs sorption occurred (95.9 ± 2.3 %, with a $K_d$ of 256 ± 156 L $kg^{-1}$). However, above this concentration there was a reduction in sorption. At $10^{-5}$ mol $L^{-1}$ $Cs^+$ only 71.1 ± 5.0 % ($K_d$: 25 ± 5 L $kg^{-1}$) of the $Cs^+$ is sorbed. This was a reduction of ~25%, compared to the same concentration of $Cs^+$ with

no competing ion. There was a steady reduction in percentage sorption as $Cs^+$ concentration was increased reaching a minimum value of 10.8 ± 1.0 % at a $Cs^+$ concentration of 1.0 x $10^{-1}$ mol $L^{-1}$.

In a background of 1.0 mol $L^{-1}$ $K^+$ (Figure 5.2 c) the $Cs^+$ sorption behaviour showed a similar trend with maximum sorption between 1.0 X $10^{-9}$ and 1.0 x $10^{-7}$ mol $L^{-1}$. At 1.0 x $10^{-7}$ mol $L^{-1}$ 57.3 ± 1.0% of the $Cs^+$ sorbed with a $K_d$ of 13 ± 1 L $kg^{-1}$. This then decreased to 43.7 ± 0.1 % at 1.0 x $10^{-5}$ mol $L^{-1}$ ($K_d$ 8 ± 0 L $kg^{-1}$). A further reduction was then observed at 1.0 x $10^{-3}$ mol $L^{-1}$ where 10.0 ± 2.4 % of the $Cs^+$ was sorbed. Above an aqueous $Cs^+$ concentration of 1.0 x $10^{-3}$ mol $L^{-1}$ there was no significant reduction in sorption.

Three clear regions are visible within the results (differentiated by solid vertical lines on Figure 5.2). At aqueous $Cs^+$ concentrations < 1.0 x $10^{-6}$ mol $L^{-1}$ (region A) there is near total sorption in the DIW system, and the system with competing $Na^+$ ions. However, in the $K^+$ competitive system only around 60% of the $Cs^+$ sorbs. This is followed by a region (B) of slightly reduced sorption between 1.0 x $10^{-6}$ and 1 x $10^{-3}$ mol $L^{-1}$ in the DIW system. There is a more significant reduction in $Cs^+$ sorption in the $Na^+$ and in the $K^+$ systems. Finally, in the DIW system there is a region (C) of rapidly reduced sorption percentages between 1.0 x $10^{-3}$ and 1.0 x $10^{-1}$ mol $L^{-1}$ above which the sediment reaches sorption saturation. This region of rapidly reducing sorption is also seen in the $Na^+$ system, although the total percentage reduction is lower than the DIW system. However in the $K^+$ system the

sediment had already reached a minimum sorption by 1.0 x $10^{-3}$ mol $L^{-1}$ and no further change in sorption was determined at higher $Cs^+$ concentrations.

### 5.3.3 pH dependency

The effect of pH on the sorption of $Cs^+$ was investigated at three concentrations of $Cs^+$, chosen to access each of the dominant sorption regions identified from the isotherms. At each of these concentrations 3 distinct pH sorption behaviours were observed as shown by Figure 5.4 (a-c). At the trace concentrations (1.0 x $10^{-11}$ mol $L^{-1}$) near total (99 ± 1 %) sorption of $Cs^+$ was seen at all pH values. Here the pH had no discernible effect upon the sorption of $Cs^+$. As $Cs^+$ concentration was increased, however, to 1.0 x $10^{-4}$ mol $L^{-1}$ a strong amphoteric effect emerged. A clear sorption edge occurred between pH 2 and 5. At pH 2, 7.0 ± 1.5 % of the $Cs^+$ was sorbed. This increases to 61.6 ± 2.9 % at pH 3.4 and 99.3 ± 0.3 % at pH 5.2. Sorption then remained constant as pH was increased before dropping slightly to 96.9 ± 1.5 % sorption at pH 8.8. Finally, at the saturating concentration of 1 x $10^{-1}$ mol $L^{-1}$ around 10 – 15% of the $Cs^+$ was sorbed at all pH values and any amphoteric behaviour was masked. Although Poinssot et al. (1999) suggested illite dissolution as a potential cause of reduced Cs sorption at low pH, they also noted that the rate of dissolution meant that only 0.1% of the illite had dissolved over a 7 day period at pH 3, which is insignificant. The experiments presented here were only run for 48 hours so dissolution is likely to be much less than 0.1% of the total illite/clay fraction. Therefore $H^+$ competition is most likely the dominant process

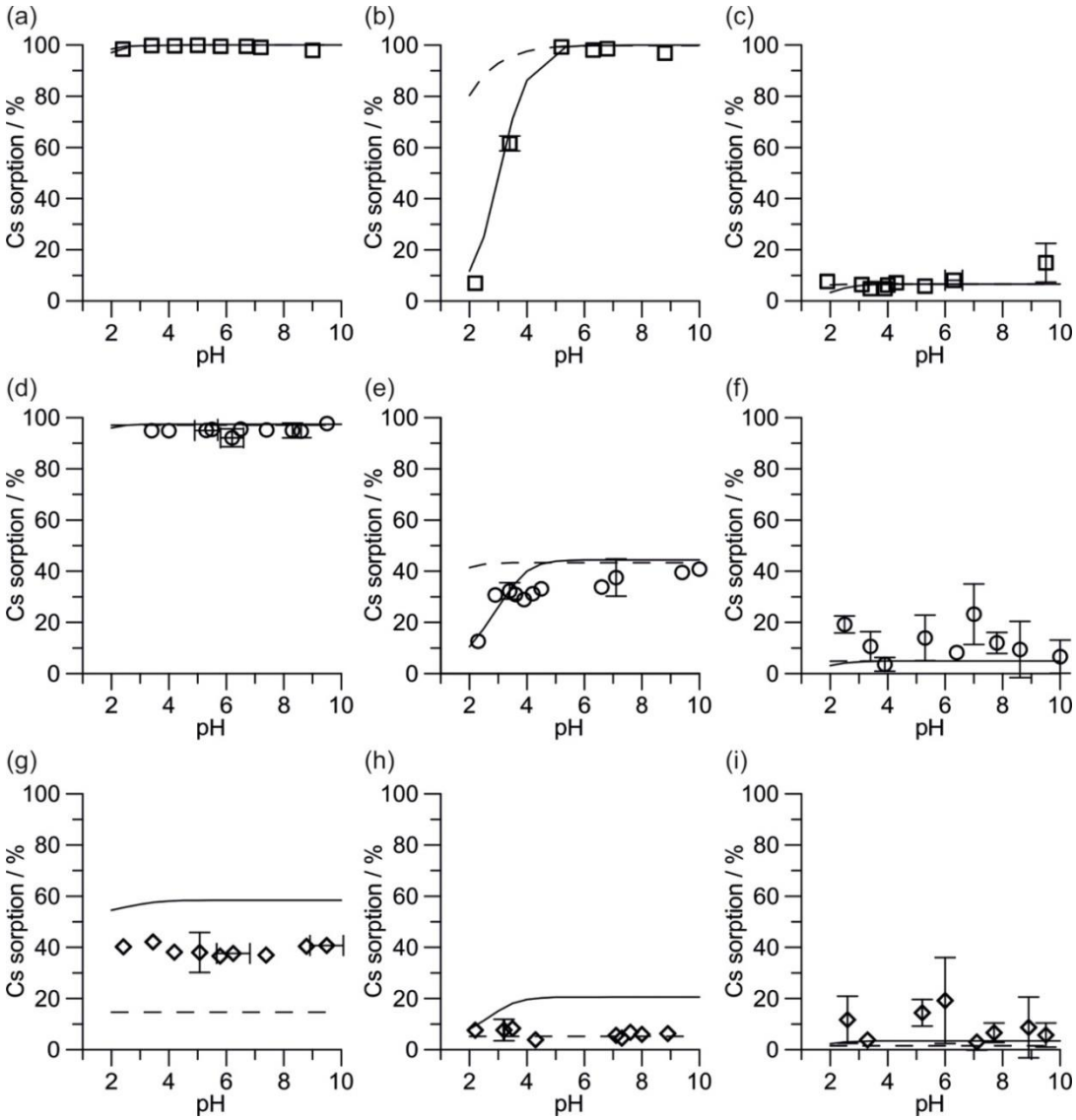


**Figure 5.4** Concentration dependent Cs sorption across a pH range in a background of competing K and Na. Each figure shows a different solution condition: (a) $10^{-11}$ mol $L^{-1}$ Cs in deionised water; (b) $10^{-4}$ mol $L^{-1}$ Cs in dionised water; (c) $10^{-1}$ mol $L^{-1}$ Cs in deionised water; (d)$10^{-11}$ mol $L^{-1}$ Cs in 1 mol $L^{-1}$ Na; (e)$10^{-4}$ mol $L^{-1}$ Cs in 1 mol $L^{-1}$ Na; (f) $10^{-1}$ mol $L^{-1}$ Cs in 1 mol $L^{-1}$ Na; (g) $10^{-11}$ mol $L^{-1}$ Cs in 1 mol $L^{-1}$ K; (h) $10^{-4}$ mol $L^{-1}$ Cs in 1 mol $L^{-1}$ K and (i) $10^{-1}$ mol $L^{-1}$ Cs in 1 mol $L^{-1}$ K. All data points represent averages of triplicate samples. For clarity errror bars are not shown where they were smaller than the size of the symbol. Results of modelling using fitted parameters (solid line) and generic parameters from Bradbury and Baeyens (2000) (dashed line) are also shown

To investigate the interplay between $H^+$, $Na^+$ and $K^+$ competition with Cs, pH dependent sorption experiments were also performed in a background of 1.0 mol $L^{-1}$ $Na^+$ and $K^+$. Results from pH dependent sorption experiments performed in 1.0 mol $L^{-1}$ $Na^+$ are shown in Figure 5.4 d-f. At low concentrations of $Cs^+$ ($1.0 \times 10^{-11}$ mol $L^{-1}$ of measured $^{137}Cs$, Figure 5.4 d) near total sorption (95 ± 2 %) of $Cs^+$ was determined across the entire pH range with no pH dependency. This is the same as the result for experiments with no competing ions (Figure 5.4 a). At an elevated concentration ($1.0 \times 10^{-4}$ mol $L^{-1}$, Figure 5.4 e) the sorption mainly occurred independently of pH, although a reduction in the sorbed $Cs^+$ was measured at pH 2, to 12.6 ± 1.1 % compared to an average of 33.0 ± 7.0% of the $Cs^+$ being sorbed across the rest of the pH range (3-10). At highly elevated concentrations of $Cs^+$ ($10^{-1}$ mol $L^{-1}$) an average of 17.0 ± 6.0 % of the $Cs^+$ was sorbed by the sediment and this process occurred independently of pH, likely due to the higher ratio of $Cs^+$ to $H^+$ ions.

In the $K^+$ dominated system (with 1.0 mol $L^{-1}$ K, Figure 5.4 g-i) $Cs^+$ sorbed independently of pH at all concentrations. Here at the lowest concentration of $Cs^+$ ($1.0 \times 10^{-11}$ mol $L^{-1}$ Figure 5.4 g) an average of 37.0 ± 3.0 % of the $Cs^+$ was sorbed across the pH range. As the concentration of Cs was increased to $1.0 \times 10^{-4}$ mol $L^{-1}$ (Figure 5.4 h) the percentage of $Cs^+$ sorbed was reduced to an average of 11.0 ± 1.0 % across the pH range. Here pH had no effect on $Cs^+$ sorption. At the highest $Cs^+$ concentration ($1.0 \times 10^{-1}$ mol $L^{-1}$) an average of 19.0 ± 6.0 % of the $Cs^+$ was sorbed across the pH range, with no pH effect. This was higher than at $1.0 \times 10^{-4}$ mol $L^{-1}$; however

there are large errors on a number of the data points. This is likely due to heterogeneity of the sediment and the extremely high salinity of the system (1.0 mol $L^{-1}$ $K^+$ and 1.0 x $10^{-1}$ mol $L^{-1}$ $Cs^+$). Again at this high $Cs^+$ concentration there was no apparent pH dependency.

### 5.3.4 Cation Exchange Modelling

To interpret the sorption behaviour of the $Cs^+$ in this system a three site cation exchange model was employed. The model was based on the generic model of Bradbury and Baeyens (2000) and refined as discussed below. In both the Bradbury and Baeyens (2000) model and this refinement of it there are three specific site types for the Cs sorption: Frayed Edge Sites (FES, located right at the edge of the interlayer), Type II sites (located on the edges of the clay particles) and Planar sites (located on the basal plane). Each site is assigned a site concentration (termed site capacity) in mol $L^{-1}$ and for each site there is a log $K_c$ for the exchange onto the site of $K^+$ for $Na^+$ (log ${}^{K}_{Na}K_c$ ) and $Cs^+$ for $Na^+$ (log ${}^{Cs}_{Na}K_c$) (where log ${}^{Na}_{Na}K_c$ is 0). Another selectivity constant describing $H^+$ exchange for $Na^+$ (log ${}^{H}_{Na}K_c$) was also used in the model. All $H^+$ selectivity coefficients (FES, Type II and Planar sites) were initially set to equal 1. In the modelling, site capacities and log $K_c$ values were the adjustable parameters used to fit the model to the data.

**Table 5.2** Modelling exchange log $K_C$ values normalised against $Na^+$. *From Poinssot et al. (1999)

| Source | Exchange species | FES | Type II | Planar |
|---|---|---|---|---|
| Bradbury and Baeyens (2000) | $K^+$ | 2.4 | 2.1 | 1.1 |
| | $Cs^+$ | 7.0 | 3.6 | 1.6 |
| This paper | $K^+$ | 1.5 | 0.6 | 0.5 |
| | $H^+$ | 1.8* | 3.6 | 2.5 |
| | $Cs^+$ | 7.0 | 3.6 | 1.6 |

Initially all the experimental data sets were individually modelled using the generic site capacities for the three sites and $K_c$ values for $K^+$ and $Cs^+$ exchange provided by Bradbury and Baeyens (2000). These are listed in Table 5.2. On inspection of the initial unrefined fits it was determined that both the total estimated CEC and the site ratios were incorrect. Initially the modelling was done using the average CEC value given by Wallace, et al (2012) and the site ratios determined by Bradbury and Baeyens (2000). These were 0.25% FES (2.05 $x10^{-5}$ mol $L^{-1}$), 20% Type II (1.64 $x10^{-3}$ mol $L^{-1}$) and 79.75% Planar (6.48 $x10^{-3}$ mol $L^{-1}$), with a total given CEC of 8.2 $x10^{-3}$ mol $kg^{-1}$. The CEC was converted from meq 100 $g^{-1}$ as measured to mol $L^{-1}$; as experiments were performed with a solid:solution ratio of 1:10 and Cs is a monovalent ion, this gave a direct conversion of 1 meq 100 $g^{-1}$ = $1x10^{-3}$ mol $L^{-1}$. When these site capacities were used it was seen that the Na-competitive isotherm overestimated Cs sorption at all concentrations, but especially at low concentrations (where sorption to the FES and Type II sites dominated).To correct this, the CEC of each site was iteratively adjusted, when keeping all other values constant. This gave new site concentrations of 0.05% FES (4.0 x $10^{-6}$ mol $L^{-1}$), 2% Type II (1.6 x $10^{-4}$ mol $L^{-1}$) and 97.95% Planar (6.5 x $10^{-3}$ mol $L^{-1}$), giving a total CEC of 6.66 x $10^{-3}$ mol $L^{-1}$ (which is

still within error of the original measured CEC of 8.2 $\pm$ 5.1 x $10^{-3}$ mol $L^{-1}$). Bradbury and Baeyens (2000) determined their site capacity ratios based on Opalinus clay, which contains around 10% illite. As the sediments used in this study contain a far lower percentage of clay minerals (and therefore less illite), this likely explains the lower concentration of the FES and Type II sites, which are located on the clay minerals. The sediments also contain comparatively more minerals with planar sites which accounts for the relatively higher percentage of these sites in our system. It should be noted that these new site ratios were close to those used by Steefel et al. (2003) when modelling mixed sediments (rather than a clay rock). The model was then re-run with the new CEC values and the log $K_c$ values of Bradbury and Baeyens (2000) and these fits are shown on all figures as dashed lines. From the modelling above it was determined that at all concentrations $Cs^+$ sorption was significantly underestimated in the 1 mol $L^{-1}$ $K^+$ background (dashed line, Figure 5.2 c). To correct this, the $K^+$ affinity was reduced by iterating the log ${}^{K}_{Na}K_c$ values while maintaining all other values as constant, until a good fit was obtained (solid line Figure 5.2 c). These new values are shown in Table 5.2.

From the pH matrix results (Figure 5.4), it was found that the model was significantly underestimating the effect of pH at intermediate $Cs^+$ concentrations (dashed lines Figure 5.4 b and e). Therefore the competitive effect of $H^+$ with $Cs^+$ (represented by log ${}^{H}_{Cs}K_c$ values) was deemed to be too low. The log ${}^{H}_{Cs}K_c$ values were determined by the relationship between the log ${}^{H}_{Na}K_c$ and the log ${}^{Cs}_{Na}K_c$ values as described in section 5.2.4. As the log

$^{Cs}_{Na}K_c$ had previously been fixed in the model adjustment of the log $^{H}_{Na}K_c$ was used to increase the modelled pH dependency of Cs sorption in the system and improve the models fit to the experimental data. To do this the log $^{H}_{Na}K_c$ value for the FES (1.8) was taken from Poinssot et al. (1999). For the Type II and Planar sites no literature values were available. As the focus was on determining the $Cs^+/H^+$ competition of the system the log $^{H}_{Na}K_c$ values were initially set as equal to log $^{Cs}_{Na}K_c$ values. As previously, the values were then sequentially iterated until the best fit to the experimental data was obtained. From this it was determined that further refinement of only the planar sites value was required to give a good fit for the pH behaviour seen in the experimental data (Figure 5.4). The initial Bradbury and Baeyens (2000) and final adjusted values for all parameters are show in Table 5.2 and the final fits are shown as solid lines in all figures. The final model overestimated Cs sorption in the pH varied system with a high K background (Figure 5.4 g and h). This is an artefact of the fact that $^{K}_{Na}K_c$ was refined from the isotherm experiments (Figure 5.2 c). In that system 60% of the $Cs^+$ was sorbed at low concentrations to the FES, at neutral pH. Therefore the model predicts 60% sorption of $Cs^+$ across the pH range at low concentrations (Figure 5.4 g). However the experimental results presented in Figure 5.4 g show that only 40% of the Cs was sorbed at pH 7 (and across the pH range). Therefore the model overestimates $Cs^+$ sorption in this system, when compared to the experiment. The difference between percentage sorption reported from the two experiments is likely due to variation in the illite concentration between the two sub-samples of sediment. At these low concentrations the $Cs^+$ would be sorbing to the FES and Type II sites with strong competition from the

background $K^+$ ions. The relative concentration of these sites in the sediment is extremely low and they are exclusively located on the clay minerals. Therefore a small variation in the total mass of clay minerals (especially illite) between the two sub-samples could give a large variation in the total concentration of FES and Type II sites. In the K rich system a large fraction of these sites would also be occupied by $K^+$ rather than $Cs^+$ ions. Therefore the effect on total $Cs^+$ sorption percentage would be very sensitive to small changes in clay content. This variability between sediment subsamples is therefore the most likely explanation of the models overestimation of $Cs^+$ sorption in Figure 5.4 g and h. This also presents a major constraint on the accuracy of modelling predictions in environmental scenarios.

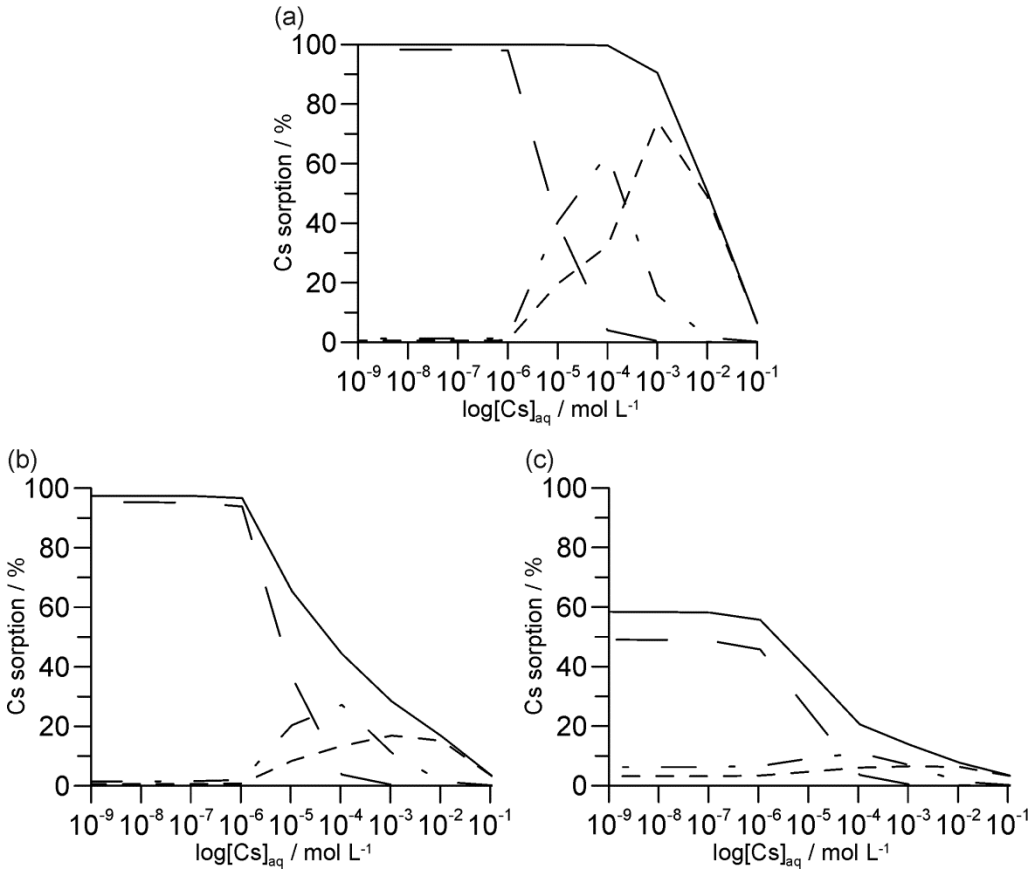


**Figure 5.5** Modelled sorption isotherms showing relative contributions of the three sorption sites in a background of (a) DIW, (b) 1 mol $L^{-1}$ $Na^{+}$ and (c) 1 mol $L^{-1}$ $K^{+}$. The long dashed line represents the FES, the dotted and dashed line represents the Type II site and the short dashed line indicates the contributions from the Planar sites. The solid line represents the cumulative total soption

It was previously identified from the experimental results (Figure 5.2) that there are three regions of distinct $Cs^{+}$ sorption behaviour, governed by the solution concentration. The cation exchange modelling shows that these three sorption regions related to the dominance of the three separate cation exchange sites within the sediment. Figure 5.5 shows that at low concentrations, where sorption was only reduced by $K^{+}$ competition, $Cs^{+}$ was sorbed almost exclusively onto the FES. However when Cs was present at concentrations above $10^{-6}$ mol $L^{-1}$, Na effectively reduced $Cs^{+}$ sorption.

The model shows that this was due to saturation of the FES and that sorption to the Type II sites dominated, where both $Na^+$ and $K^+$ could effectively compete with $Cs^+$. Finally above $10^{-3}$ mol $L^{-1}$ Cs, the Planar sites dominated sorption before becoming quickly saturated, which accounts for the reduction in sorption in the DIW system.

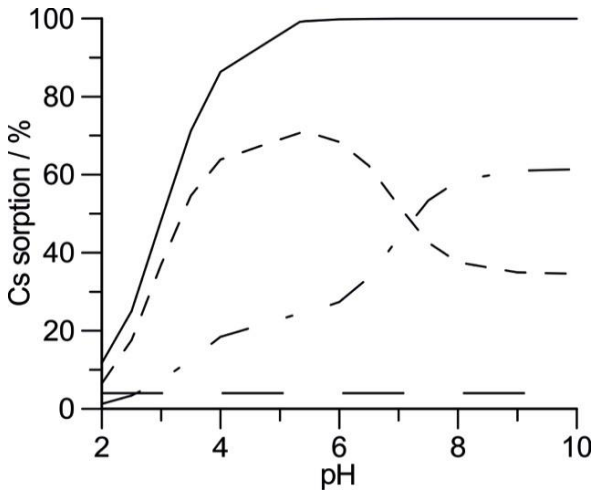


**Figure 5.6** Modelling of $10^{-4}$ mol $L^{-1}$ Cs in a DIW background (see figure 3b). Showing relative contribution of the the three sorption sites. The long dashed line represents the FES, the dotted and dashed line represents the Type II site and the short dashed line indicates the contributions from the Planar sites. The sum of these three sites, the total soprtion, is shown by the solid line

Finally, the relative contribution of the different sites to the pH dependent sorption is shown in Figure 5.6. This represents the relative contribution of each site for sorption of 1.0 x $10^{-4}$ mol $L^{-1}$ $Cs^+$ in a DIW background, which was the system with the strongest pH dependency (experimental data, Figure 5.4 b). Due to the relatively high concentration of $Cs^+$ in this system the FES are saturated and contribute to < 5% of total sorption. Therefore the Type II and Planar sites control sorption in this system. It can be seen from

the results that at low pH the Planar sites dominated the total sorption, however once the sorption edge reaches its maximum the Type II sites dominate at > pH 7. This was due to the relative balance of the $H^+$ and $Cs^+$ $K_c$ values of each site (see Table 5.2). The Type II sites have a higher Cs affinity than the Planar sites, but are far more amphoteric. Therefore at low pH the $H^+$ out-competed $Cs^+$ on the Type II sites and instead the $Cs^+$ sorbed to the Planar sites, which although they have a lower $Cs^+$ affinity also have a low $H^+$ affinity. However at neutral pH and above $H^+$ ions cease to affect $Cs^+$ sorption and therefore the larger ${}^{Cs}_{Na}K_c$ of the Type II sites relative to the Planar sites, means that more $Cs^+$ ions sorbed to the Type II sites and it became the dominant control on $Cs^+$ sorption, as was seen in the DIW isotherm experiments conducted at neutral pH (Figure 5.5 a).

### 5.3.5 Implications for $^{137}Cs^+$ mobility

The experimental results and modelling outlined in this study have important implications for the potential mobility of $^{137}Cs^+$ at contaminated nuclear sites such as Sellafield. It has long been known that a trace amount of $Cs^+$ will selectively and irreversibly sorb to the illitic FES (Comans et al., 1991, Hird et al., 1996, Cornell, 1993). However, results presented here show that once the FES are saturated $Cs^+$ sorption to the Type II and Planar sites occurs in competition with other cations and is strongly controlled by pH and ionic strength. The current models (e.g. Bradbury and Baeyens (2000)) do not predict the likely impact of $H^+$ competition on the sorption of $Cs^+$ and greatly overestimate $Cs^+$ uptake. The experimental results show during a leak of acidic liquor with high $Cs^+$ concentration, $Cs^+$ sorption to the sediment will be

lower than previously predicted by existing models. Therefore it is recommended that future modelling of this type of scenario at Sellafield use the new selectivity values presented here (Table 5.2), as they more accurately describe a leak of this nature and may give a more realistic description of likely $Cs^+$ migration in acidic liquors. It should be noted however that the modelling results here are calibrated for the experimental conditions, specifically the sediment particle size and experiment solid:solution ratio. In applying the new model to site specific reactive transport scenarios it is important to account for variation in these parameters. Hydrological parameters such as sediment density and porosity should also be considered. This chapter presents a simple cation exchange model, rather than a reactive transport model so these hydrological factors are not considered.

The fact that $H^+$ competes with $Cs^+$ for the Type II and Planar sites is an important new finding with implications for management and modelling of $Cs^+$ sorption and migration from acidic leaks. However the results also show that in alkaline leaks, which are much more common at Sellafield (Wallace et al., 2012; Thorpe et al., 2012), all the $Cs^+$ present will sorb to the clay fraction, even if the FES are saturated. It should also be noted that the ability of $K^+$ and $Na^+$ to compete with $Cs^+$ is an important controlling factor on $Cs^+$ sorption potential. We have shown that at high concentrations (1.0 mol $L^{-1}$) $K^+$ can significantly reduce sorption of $Cs^+$ to the FES. Where the FES is saturated both $Na^+$ and $K^+$ can also significantly reduce the sorption of $Cs^+$ to the less specific Planar and Type II sites. This is especially noticeable in

the high ionic strength solutions tested here. Therefore in highly alkaline liquors, rich in NaOH and KOH (such as young cement leachates), or salty solutions, rich in NaCl and KCl (such as seawater), Cs sorption may be significantly reduced by cationic competition.

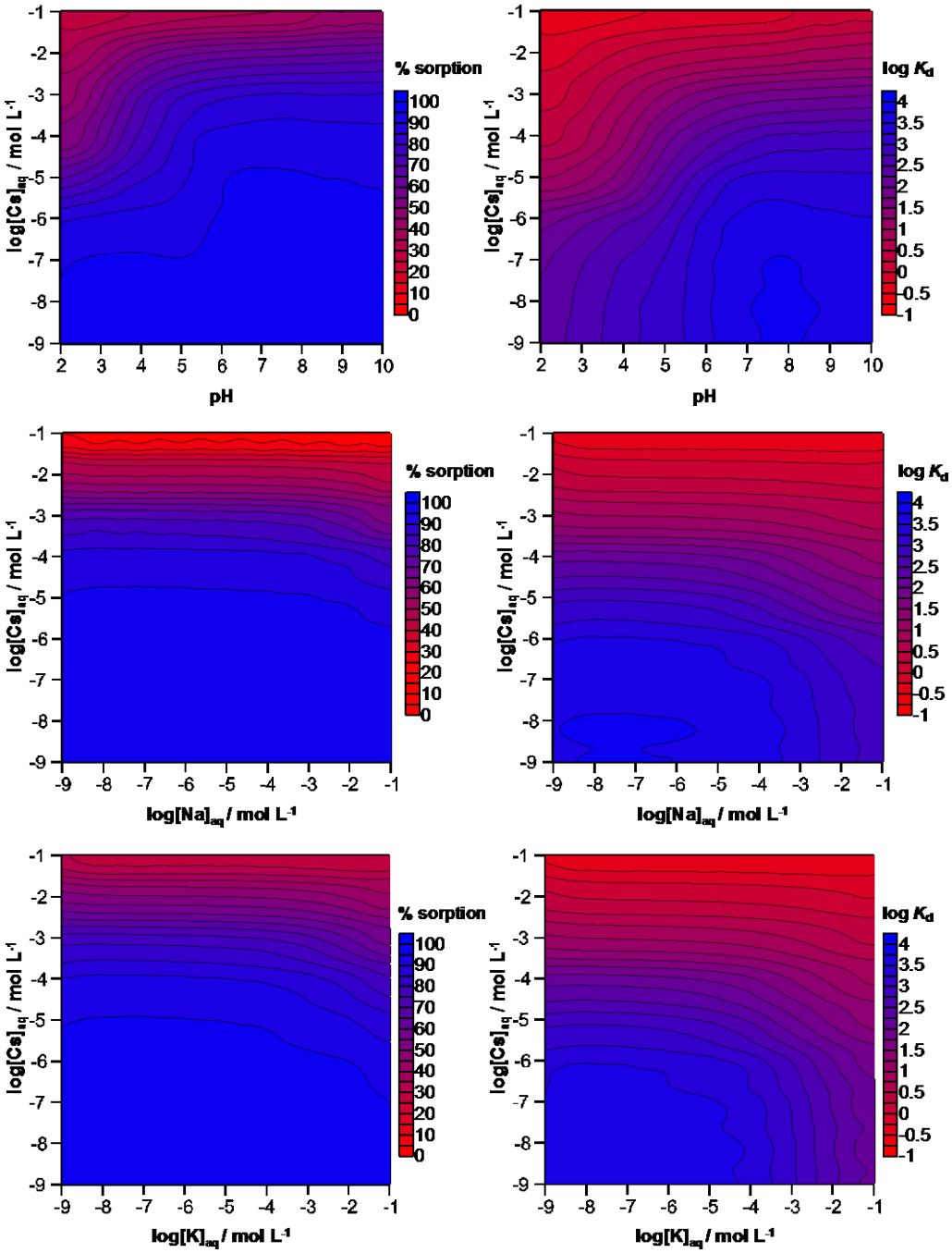


**Figure 5.7** Modelled dependency of $Cs^+$ sorption on concentrations of $H^+$, $Na^+$ and $K^+$. All figures are plotted on log/log axis for clarity. Results are shown in both % sorption and log Kd space for ease of reference with blue representing high sorption and red low

To summarise all of the findings of this work the refined cation exchange model was used to predict the sorption of $Cs^+$ under a wide range of solution conditions and contour plots were constructed (Figure 5.7). The concentration of $Cs^+$ is the most important parameter controlling its sorption behaviour. Therefore the effect of pH, $Na^+$ and $K^+$ concentrations were modelled with relation to increasing $Cs^+$ concentration. These results are expressed in both $K_d$ and percentage sorption terms for ease of reference. The results of this modelling clearly show that $Cs^+$ sorption is governed by the concentration of different ions in solution, as previously described. The system where pH was varied (Figure 5.7 a and b) shows two regions where pH has little effect on sorption. More than 90% of the $Cs^+$ sorbs across the whole pH range at very low $Cs^+$ concentrations (<1.0 x $10^{-7}$ mol $L^{-1}$). Sorption is also pH independent at very high $Cs^+$ concentrations (>1.0 x $10^{-2}$ mol $L^{-1}$), however <10% of the $Cs^+$ sorbs. The pH of the system has the greatest effect at intermediate $Cs^+$ concentrations, with a clear sorption edge between pH 3 and 5 most visible at $Cs^+$ concentrations between 1.0 x $10^{-2}$ and 1.0 x $10^{-6}$ mol $L^{-1}$. $Na^+$ has a less clear impact of $Cs^+$ sorption than pH. Figure 5.7 c and d show that $Cs^+$ sorption in the $Na^+$ background system is largely governed by the $Cs^+$ concentration (and therefore saturation of the sediments CEC). When expressed in $K_d$ terms (Figure 5.7 d) it is clearer that when $Na^+$ is present at concentrations > 1.0 x $10^{-3}$ mol $L^{-1}$ it competes with $Cs^+$ and reduces total sorption. This is most noticeable at $Cs^+$ concentration between 1.0 x $10^{-6}$ and 1.0 x $10^{-3}$ mol $L^{-1}$. Finally $K^+$ effectively competes with $Cs^+$ at all concentrations when present at concentrations > 1.0 x $10^{-4}$ mol $L^{-1}$ (Figure 5.7 e and f). This competition effect is masked above $Cs^+$ concentration of $10^{-2}$ mol $L^{-1}$ where the sediments sorption capacity is

saturated and <10% of the total $Cs^+$ sorbs. These modelling outputs give a strong prediction of likely $Cs^+$ sorption under a wide range of measureable conditions. Therefore it is essential when predicting the potential mobility of $Cs^+$ from leaks at Sellafield, and other nuclear sites, with similar near surface mineralogy (illite present), that the groundwater conditions and the chemistry of the leak solution are known.

The Nuclear Decommissioning Authority's inventory of waste at Sellafield (SellafieldLtd, 2009, NDA, 2007) shows that $Cs^+$ is present at high concentrations in a number of wastes on the sites. Notably at around 1 $x10^{-5}$ mol $L^{-1}$ in both the Magnox cladding waste and Magnox fuel pond sludge, which are known to have leaked to ground (McKenzie et al., 2011, Wallace et al., 2012). Other high level liquid wastes contain up to 2 x $10^{-2}$ mol $L^{-1}$ of $Cs^+$ (NDA, 2007; leaks from this source are currently not reported or suspected), which is in the sorption regime where both the FES and Type II sites would be saturated. Therefore this new modelling predicts that if the wastes containing $Cs^+$ at these very high concentrations were to leak then sorption is likely to be significantly reduced in groundwater with either low pH (e.g. an acid leak) or high ionic strength (e.g. seawater intrusion). However they also show that the $Cs^+$ could be effectively immobilised by either buffering the pH of the system to > pH5 or reducing the ionic strength. Therefore it is important that any $Cs^+$ bearing solutions are treated to neutralise their pH and reduce their ionic strength.

## 5.4 Conclusion

Here it has been shown through experimentation and cation exchange modelling that $Cs^+$ sorption to a micaceous aquifer sediment representative of those at the Sellafield site was predominantly controlled by $Cs^+$ solution concentration. At intermediate and high $Cs^+$ solution concentrations (> $10^{-6}$ mol $L^{-1}$) the pH and ionic strength of the system are of great importance due to the multi-site nature of the $Cs^+$ sorption to these sediments. The Frayed Edge Sites (FES) selectively sorb $Cs^+$ in preference to other solution cations, but are quickly saturated. Once they become saturated, excess $Cs^+$ sorbs to the non-specific Type II and Planar sites where other cations can effectively compete and reduce total $Cs^+$ sorption. Under most leak scenario conditions $Cs^+$ concentrations would be low enough that the FES are far from saturation. Therefore in these circumstances most of the $Cs^+$ will sorb to the FES regardless of solution conditions. However, under the scenario of an acidic leak with high $Cs^+$ concentrations present, a significant amount of the $Cs^+$ may migrate further than predicted by existing models because these do not account for $H^+$ competition.

## 5.5 References

Aldaba, D., Rigol, A. & Vidal, M. 2010. Diffusion experiments for estimating radiocesium and radiostrontium sorption in unsaturated soils from Spain: Comparison with batch sorption data. *Journal of Hazardous Materials,* 181**,** 1072-1079.

Babad, H., Cash, R. J., Deichman, J. L. & Johnson, G. D. 1993. High-priority Hanford Site radioactive waste storage tank safety issues: An overview. *Journal of Hazardous Materials,* 35**,** 427-441.

Ball, J. W. & Nordstrom, D. K. 1991. User's manual for WATEQ4F with revised thermodynamic database and test cases for calculating speciation of major, trace and redox elements in natural waters.

Bandstra, M. S., Vetter, K., Chivers, D. H., Aucott, T., Bates, C., Coffer, A., Curtis, J., Hogan, D., Iyengar, A., Looker, Q., Miller, J., Negut, V., Plimley, B., Satterlee, N., Supic, L. & Yee, B. Measurements of Fukushima fallout by the Berkeley Radiological Air and Water Monitoring project. 2012. 18-24.

Beresford, N. A. 2006. Land contaminated by radioactive materials. *Soil Use and Management,* 21**,** 468-474.

Bethke, C. M. & Yeakel, S. 2013. The Geochemists Workbench: Reference Manual.

Bouzidi, A., Souahi, F. & Hanini, S. 2010. Sorption behavior of cesium on Ain Oussera soil under different physicochemical conditions. *Journal of Hazardous Materials,* 184**,** 640-646.

Bradbury, M. H. & Baeyens, B. 1997. A mechanistic description of Ni and Zn sorption on Na-montmorillonite Part II: modelling. *Journal of Contaminant Hydrology,* 27**,** 223-248.

Bradbury, M. H. & Baeyens, B. 2000. A generalised sorption model for the concentration dependent uptake of caesium by argillaceous rocks. *Journal of Contaminant Hydrology,* 42**,** 141-163.

Brouwer, E., Baeyens, B., Maes, A. & Cremers, A. 1983. Cesium and Rubidium Ion Equilibrium in Illite Clay. *Journal of Physical Chemistry,* 87**,** 1213-1219.

Campbell, L. S. & Davies, B. E. 1995. Soil sorption of caesium modelled by the Langmuir and Freundlich isotherm equations. *Applied Geochemistry,* 10**,** 715-723.

Chaplow, R. 1996. The geology and hydrogeology of Sellafield: an overview. *Quarterly Journal of Engineering Geology and Hydrogeology,* 29**,** S1-12.

Chorover, J., Choi, S., Rotenberg, P., Serne, R. J., Rivera, N., Strepka, C., Thompson, A., Mueller, K. T. & O'Day, P. A. 2008. Silicon control of strontium and cesium partitioning in hydroxide-weathered sediments. *Geochimica Et Cosmochimica Acta,* 72**,** 2024-2047.

Chorover, J., DiChiaro, M. J. & Chadwick, O. A. 1999. Structural charge and cesium retention in a chronosequence of tephritic soils. *Soil Science Society of America Journal,* 63**,** 169-177.

Comans, R. N. J., Haller, M. & Depreter, P. 1991. Sorption of cesium on illite: None-equilibrium behaviour and reversibility. *Geochimica Et Cosmochimica Acta,* 55**,** 433-440.

Comans, R. N. J. & Hockley, D. E. 1992. Kinetics of cesium sorption on illite. *Geochimica Et Cosmochimica Acta,* 56**,** 1157-1164.

Cornell, R. 1993. Adsorption of cesium on minerals: A review. *Journal of Radioanalytical and Nuclear Chemistry,* 171**,** 483-500.

Cremers, A., Elsen, A., Depreter, P. & Maes, A. 1988. Quantitative analysis of radiocaesium retention in soils. *Nature,* 335**,** 247-249.

Davies, K. S. & Shaw, G. 1993. Fixation of Cs-137 by soils in sediments in the Esk Estuary, Cumbria, UK. *Science of the Total Environment,* 132**,** 71-92.

de Koning, A. & Comans, R. N. J. 2004. Reversibility of radiocaesium sorption on illite. *Geochimica Et Cosmochimica Acta,* 68**,** 2815-2823.

de Koning, A., Konoplev, A. V. & Comans, R. N. J. 2007. Measuring the specific caesium sorption capacity of soils, sediments and clay minerals. *Applied Geochemistry,* 22**,** 219-229.

Dutton, M. V., Foster, C. & Trivedi, D. 2009. Characterisation of Soils from B38 Site Investigation within the Sellafield Separation Area. NNL Commercial.

Dyer, A., Chow, J. K. K. & Umar, I. M. 2000. The uptake of caesium and strontium radioisotopes onto clays. *Journal of Materials Chemistry,* 10**,** 2734-2740.

Eberl, D. D. 1980. Alkali cation selectivity and fixation by clay minerals. *Clays and Clay Minerals,* 28**,** 161-172.

Francis, C. W. & Brinkley, F. S. 1976. Preferential adsorption of $^{137}$Cs to micaceous minerals in contaminated freshwater sediment. *Nature,* 260**,** 511-513.

Fuller, A. J., Shaw, S., Peacock, C. L., Trivedi, D., Small, J. S., Abrahamsen, L. G. & Burke, I. T. 2014. Ionic strength and pH dependent multi-site sorption of Cs onto a micaceous aquifer sediment. *Applied Geochemistry,* 40**,** 32-42.

Gaines, G. L. & Thomas, H. C. 1953. Adsorption Xtudies on Clay Minerals 2: A Formulation of the Thermodynamics of Exchange Adsorption. *Journal of Chemical Physics,* 21**,** 714-718.

Giannakopoulou, F., Haidouti, C., Chronopoulou, A. & Gasparatos, D. 2007. Sorption behavior of cesium on various soils under different pH levels. *Journal of Hazardous Materials,* 149**,** 553-556.

Grutter, A., Von Gunten, H. R. & Rossler, E. 1986. Sorption, desorption, and isotope exchange of cesium (10-9 - 10-3 M) on chlorite. *Clays & Clay Minerals,* 34**,** 677-680.

He, Q. & Walling, D. E. 1996. Interpreting particle size effects in the adsorption of Cs-137 and unsupported Pb-210 by mineral soils and sediments. *Journal of Environmental Radioactivity,* 30**,** 117-137.

Hill, M. D., Steeds, J. E. & Slade, N. J. 2001. Land Contamination: Technical Guidance on Special Sites: Nuclear Sites. Bristol: Environment Agency.

Hird, A. B., Rimmer, D. L. & Livens, F. R. 1995. Total Caesium-Fixing Potentials of Acid Organic Soils. *Journal of Environmental Radioactivity,* 26**,** 103-118.

Hird, A. B., Rimmer, D. L. & Livens, F. R. 1996. Factors affecting the sorption and fixation of caesium in acid organic soil. *European Journal of Soil Science,* 47**,** 97-104.

Hou, X. L., Fogh, C. L., Kucera, J., Andersson, K. G., Dahlgaard, H. & Nielsen, S. P. 2003. Iodine-129 and Caesium-137 in Chernobyl contaminated soil and their chemical fractionation. *Science of the Total Environment,* 308**,** 97-109.

Jackson, M. L. 1968. Weathering of Primary and Seondary Minerals in Soils. *9th International Congress of Soil Science.* Adelaide, Australia: The International Society of Soil Science and Angus & Robertson Ltd.

Jackson, M. L., Hseung, Y., Corey, R. B., Evans, E. J. & Heuvel, R. C. V. 1952. Weathering Sequence of Clay-size Minerals in Soils and Sediments: II. Chemical Weathering of Layer Silicates. *Soil Science Society of America Proceedings,* 16**,** 3-6.

Jacobs, D. G. & Tamura, T. 1960. The Mechanism of Ion Fixation using Radio-isotope Techniques. *7th Internation Congress of Soil Science.* Madison, Wisconsin, USA: The International Society of Soil Science.

Khan, S. A., RiazurRehman & Khan, M. A. 1995. Sorption of strontium on bentonite. *Waste Management,* 15**,** 641-650.

Kim, Y., Kirkpatrick, R. J. & Cygan, R. T. 1996. Cs-133 NMR study of cesium on the surfaces of kaolinite and illite. *Geochimica Et Cosmochimica Acta,* 60**,** 4059-4074.

Krauskopf, K. B. & Bird, D. K. 1995. *Introduction to Geochemistry,* New York, McGraw-Hill.

Langmuir, D. 1997. *Aqueous Environmental Geochemistry,* New Jersey, Prentice Hall.

Law, G. T. W., Geissler, A., Boothman, C., Burke, I. T., Livens, F. R., Lloyd, J. R. & Morris, K. 2010. Role of Nitrate in Conditioning Aquifer Sediments for Technetium Bioreduction. *Environmental Science & Technology,* 44**,** 150-155.

Liu, C. X., Zachara, J. M. & Smith, S. C. 2004. A cation exchange model to describe Cs+ sorption at high ionic strength in subsurface sediments at Hanford site, USA. *Journal of Contaminant Hydrology,* 68**,** 217-238.

Livens, F. R. & Baxter, M. S. 1988. Chemical Associations of Artificial Radionuclides in Cumbrian Soils. *Journal of Environmental Radioactivity,* 7**,** 75-86.

Livens, F. R. & Loveland, P. J. 1988. The influence of soil properties on the environmental mobility of caesium in Cumbria. *Soil Use and Management,* 4**,** 69-75.

McKenzie, H. & Armstrong-Pope, N. 2010. Groundwater Annual Report 2010. Sellafield Ltd.

McKenzie, H. M., Coughlin, D., Laws, F. & Stampler, A. 2011. Groundwater Annual Report 2011. Sellafield Ltd.

McKie, R. 2009. *Sellafield: the most hazardous place in Europe* [Online]. Available: http://www.theguardian.com/environment/2009/apr/19/sellafield-nuclear-plant-cumbria-hazards [Accessed 31st July 2013].

Meunier, A. & Velde, V. 2004. *Illite,* Berlin, Springer-Verlag.

Nakao, A., Thiry, Y., Funakawa, S. & Kosaki, T. 2008. Characterization of the frayed edge site of micaceous minerals in soil clays influenced by different pedogenetic conditions in Japan and northern Thailand. *Soil Science & Plant Nutrition,* 54**,** 479-489.

NDA 2007. Sellafield High Level Liquid Waste Inventory 2D02.

NDA 2010. The 2010 UK Radioactive Waste Inventory.

Parkhurst, D. L. & Appelo, C. A. J. 1999. *User's guide to PHREEQC (version 2),* Denver, US Geological Survey.

Plummer, L. N., Parkhurst, D. L., Fleming, G. W. & Dunkle, S. A. 1988. A computer program incorporating Pitzer's equation for calculation of geochemical reactions in brines. *Water-Resources Investigations Report, 88-4153.* Virginia: USGS.

Poinssot, C., Baeyens, B. & Bradbury, M. H. 1999. Experimental and modelling studies of caesium sorption on illite. *Geochimica Et Cosmochimica Acta,* 63**,** 3217-3227.

Randall, M. G., Brydie, J., Graham, J. & Small, J. S. 2004. SCLS Phase 1: The Geochemistry of the Sellafield Site. BNFL Commercial.

Reeve, P. & Eilbeck, K. Contaminated land and groundwater management at Sellafield, a large operational site with significant legacy and contaminated land challenges. 11th International Conference on Environmental Remediation and Radioactive Waste Management, ICEM'07, September 2, 2007 - September 6, 2007, 2009 Bruges, Belgium. American Society of Mechanical Engineers, 431-437.

Sawhney, B. L. 1965. Sorption of cesium from dilute solutions. *Soil Science Society of America Proceedings,* 29**,** 25-28.

Sawhney, B. L. 1970. Potassium and Cesium Ion Selectivity in Relation to Clay Mineral Structure. *Clays and Clay Minerals,* 18**,** 47-&.

Sawhney, B. L. 1972. Selective Sorption and Fixation of Cations by Clay-Minerals - Review. *Clays and Clay Minerals,* 20**,** 93-100.

SellafieldLtd 2009. Generic Basics for Inventory Challenge - Legacy Alkaline Sludge Systems. Cumbria, UK: Sellafield Ltd.

Shand, C. A., Cheshire, M. V., Smith, S., Vidal, M. & Rauret, G. 1994. Distribution of Radiocesium in Organic Soils. *Journal of Environmental Radioactivity,* 23**,** 285-302.

Shenber, M. A. & Eriksson, A. 1993. Sorption Behavior of Cesium in Various Soils. *Journal of Environmental Radioactivity,* 19**,** 41-51.

Söderlund, M., Lusa, M., Lehto, J., Hakanen, M., Vaaramaa, K. & Lahdenperä, A.-M. 2011. Sorption of Iodine, Chlorine, Technetium, and Cesium in Soil. Eurajoki, Finland: Posiva.

Sposito, G. 1984. *The Surface Chemistry of Soils,* New York, Oxford University Press.

Sposito, G. 1989. *The Chemistry of Soils,* New York, Oxford University Press.

Staunton, S. 1994. Adsorption of radiocaesium on various soils: interpretation and consequences of the effects of soil: solution ratio and solution composition on the distribution coefficient. *European Journal of Soil Science,* 45**,** 409-418.

Steefel, C. I., Carroll, S., Zhao, P. & Roberts, S. 2003. Cesium migration in Hanford sediment: a multisite cation exchange model based on laboratory transport experiments. *Journal of Contaminant Hydrology,* 67**,** 219-246.

Wallace, S. H., Shaw, S., Morris, K., Small, J. S., Fuller, A. J. & Burke, I. T. 2012. Effect of groundwater pH and ionic strength on strontium sorption in aquifer sediments: Implications for 90Sr mobility at contaminated nuclear sites. *Applied Geochemistry,* 27**,** 1482-1491.

Zachara, J. M., Smith, S. C., Liu, C. X., McKinley, J. P., Serne, R. J. & Gassman, P. L. 2002. Sorption of Cs+ to micaceous subsurface sediments from the Hanford site, USA. *Geochimica Et Cosmochimica Acta,* 66**,** 193-211.

# Chapter 6 – Caesium incorporation and retention in illite clay interlayers

This second experimental chapter presents aberration corrected (scanning) transmission electron microscopy performed to investigate the incorporation of Cs into the interlayer of illite. The atomistic imaging is supported by extended x-ray absorption fine structure spectroscopy and density functional theory modelling.

## 6.1 Introduction

The ubiquity of $^{137}$Cs in nuclear waste means it is one of the most common radionuclides released into the environment by human action. Once released, the relatively long half-life ($t_{1/2}$ = 30 years) and large dose rate of $^{137}$Cs means it can cause a long term radiation risk. The nuclear accidents at Chernobyl, and more recently at Fukushima, demonstrated this most acutely. In both these cases radiocaesium is the key contributor to radioactive dose and the reason for maintaining the exclusion zone (Kinoshita et al., 2011, Jacob et al., 2009). Additionally $^{137}$Cs is a common contaminant at nuclear sites, such as Hanford and Sellafield, due to historic releases. A detailed scientific understanding of Cs behaviour is extremely important for the long term management of these sites.

Caesium preferentially sorbs to layered clay minerals in soils and sediments, particularly illite, where it is strongly retained, even under conditions of high

ionic strength or extreme pH (Fuller et al., 2014, de Koning and Comans, 2004, Sawhney, 1972, Sawhney, 1965, Bradbury and Baeyens, 2000, Steefel et al., 2003, Cornell, 1993, Jacobs and Tamura, 1960, Hird et al., 1996). The illite structure consists of 2:1 layers with two Si/Al tetrahedral layers and a central octahedral layer (Si/Al/Fe/Mg) which are bound together by interlayer cations. Illite commonly has K in its interlayer site which yields an overall layer spacing of 1.00 nm. However other monovalent and divalent cations are able to exchange with the K ions and distort the structure. Most commonly illite weathers to vermiculite via the exchange of K ions for Ca (Jackson et al., 1952). As Ca is strongly hydrated it retains its waters of hydration in the interlayer causing an expansion of the illite layer to 1.40 nm (Jackson, 1968, Jackson et al., 1952). This Ca weathering yields a partially expanded wedge zone between the hydrated and dehydrated interlayers, commonly called the frayed edge (Nakao et al., 2008). Cs is proposed to preferentially sorb to this site via dehydration and inner-sphere incorporation (Kim et al., 1996, Cornell, 1993). Sawhney (1966) and Poinssot et al. (1999) showed this sorption to illite was controlled by kinetics, taking more than a year to reach sorption equilibrium. Comans and Hockley (1992) and Comans et al. (1991) speculate that this occurs via a two stage sorption process with both rapid cation exchange onto frayed edge sites and a much slower mechanism, potentially involving the illite interlayers.

A number of recent microscopic studies have confirmed that Cs is able to readily incorporate into the interlayer space of both expanding and non-expanding alumninosilicate clays (McKinley et al., 2004, Kogure et al., 2012,

Okumura et al., 2014, Tamura et al., 2014). In this paper we aim to confirm that this previously observed incorporation mechanism can also occur on illite and enhance understanding of the coordination environment of Cs in aluminosilicate interlayers.

To this end we studied the incorporation of caesium into illite over one year at the atomistic scale using aberration corrected (scanning) transmission electron microscopy ((S)TEM), Energy Dispersive X-ray Spectroscopy (EDX) and extended x-ray absorption fine structure spectroscopy (EXAFS), coupled with density functional theory (DFT) modelling.

## 6.2 Methods

### 6.2.1 Sample preparation

Samples of Illite IMT-1, $(Mg_{0.09}\ Ca_{0.06}\ K_{1.37})\ [Al_{2.69}\ Fe(III)_{0.76}\ Fe(II)_{0.06}\ Mn_{tr}\ Mg_{0.43}\ Ti_{0.06}]\ [Si_{6.77}\ Al_{1.23}]O_{20}(OH)_4$ were purchased from the Clay Minerals Society Source Clay Repository and finely crushed (<63µm) with a pestle and mortar. Two distinct experimental systems were established, a system to test the short term sorption/desorption of Cs on weathered illite and a long term Cs-illite sorption system.

For the short term system 0.1g samples of the crushed illite were weathered by suspension in a 0.1 mol $L^{-1}$ CaCl solution at a solid solution ratio of 1:50 in 10ml polypropylene Oak-Ridge centrifuge tubes. The weathering reaction

was allowed to continue for one week and the tubes were shaken daily. The tubes were then sampled according to the sampling procedure section. A small sub-sample of the dried Ca-illite was prepared for TEM (see TEM imaging section 6.2.3) and the remainder was re-suspended in 1.0 mol $L^{-1}$ CsCl at the same solid: solution ratio for 1 month and shaken weekly. This Cs-exchanged Ca-illite was then sampled following the same procedure outlined in the sampling procedure section. Again a small sub-sample was taken for TEM analysis. The remainder was then re-suspended at the same solid: solution ratio in 0.1M CaCl for 1 week and shaken daily to determine the exchangeability of the sorbed Cs. This was then sampled for TEM analysis.

For the long term experiments fresh samples of the crushed illite were suspended in a 1 mol $L^{-1}$ CsCl solution at a solid solution ratio of 0.1g $5ml^{-1}$ in 10ml polypropylene Oak-Ridge centrifuge tubes. As the proposed incorporation mechanism was thought to be extremely slow this high concentration of Cs was chosen to accelerate the kinetics. The tube caps were sealed with Parafilm to prevent any evaporation which would change the solid solution ratio. Following preparation the samples were shaken by hand to thoroughly mix and homogenise them. They were then stored in the dark at room temperature (20 ± 1°C) and shaken by hand once a week to ensure uniform wetting. This long term experiment was sampled at 4, 7 and 12 months according to the method below.

### 6.2.2 Sampling procedure

The tubes were destructively sampled using the following method. First, the tubes were centrifuged at 6,000 *g* for 10 minutes to achieve solid-solution separation. The solution was then decanted and for samples exposed to Cs the sediment washed in 0.1M NaCl to remove any outer-sphere sorbed Cs on the basal plane sites. For the Ca-exchanged samples the NaCl step was skipped to avoid Na exchanging with Ca and invalidating the experiment. The sample was then washed 3 times with deionised water to remove any excess salts. The washing procedure was as follows. The oak-ridge centrifuge tube containing the illite was filled with the washing solution (NaCl/deionised water) and thoroughly shaken by hand for up to 30 seconds to fully suspend the illite. The resulting suspension was then centrifuged for 10 minutes at 6,000 *g* to separate the solid from the washing solution. The washing solution was then decanted and the procedure repeated. After the final wash the illite was re-suspended in deionised water and the suspension was decanted into a weighing boat. The illite was then dried overnight in the weighing boat in an oven set to 40°C. The sample flocculated together when it was dried, so it was lightly crushed before being preparing for the TEM.

### 6.2.3 S/TEM imaging

Samples were mounted on carbon coated copper grids before imaging. A representative subsample was suspended in isopropyl alcohol and sonicated for around 5 minutes. A few drops of the suspension were then transferred onto the grid using a glass Pasteur pipette. This gave homogenous coverage of the grid with crystallites present at many different orientations. Bright field TEM imaging and spot EDX analysis of the Ca/Cs-

illite system was performed using a Tecnai TF20 FEGTEM with an operating voltage of 200keV and at room temperature (293K). Damage experiments were also performed using the Tecnai TF20 FEGTEM at both room temperature (293K) and using a liquid nitrogen cryostat (80K). Ultra-high resolution bright and dark field STEM images and EDX maps were obtained using a FEI Titan G2 S/TEM at room temperature and with an operating voltage of 200keV, with a beam current of 0.1 nA, a convergence angle of 18 mrad and a HAADF inner angle of 54 mrad.

### 6.2.4 TEM image and EDX analysis

The image processing for this work was performed using Gatan DigitalMicograph. The average change in d-spacing between those illite samples with and without Cs present in the interlayer was determined. To achieve this, cross sections of the HAADF images were produced which showed the relative intensities. In these cross sections peaks and troughs represented the aluminosilicate layers and interlayers of the illite structure. The peak to peak or trough to trough difference between multiple peaks/troughs was measured and from this an average peak distance was determined. The average distance between the peaks then correlates to the average d-spacing for the interlayers in that transect. This process was repeated many times for interlayers in the 0 and 12 month illite samples. This gave a range of values from which a mean and mode could be determined. The average change in d-spacing between K filled (0 month) and Cs filled (12 month) interlayers was then determined. A Mann Whitney U test was performed to determine the statistical validity of this difference.

The EDX data from the Ca/Cs system was processed using INCA. For the long term system background subtracted EDX spectra were extracted from the elemental maps using Bruker ESPRIT software. The atomic percentage of the different elements within the spectra were then determined via a standardless Cliff-Lorimer analysis.

### 6.2.5 Density Functional Theory Calculations

Density functional theory calculations were performed using the projector-augmented-wave implementation (Blöchl, 1994, Kresse and Joubert, 1999) of the VASP code (Kresse and Furthmüller, 1996b, Kresse and Furthmüller, 1996a). The illite models comprised 83 atoms, with the chemical composition: $(M_3)[Al_5\ Fe(III)_2\ Mg][Si_{14}\ Al_2]O_{40}(OH)_8$, (where M = K or Cs), in order to match the sample used in the experiments as well as possible. Isomorphic substitutions in the tetrahedral layer were placed far apart, in line with the observations of Militzer et al. (2011). Changing the arrangement of isomorphic substitution caused variations in d-spacing of about 0.01 Å.

The models were optimized with a kinetic energy cut-off for the plane-wave expansion of 800 eV and Brillouin-zone sampling restricted to the Γ-point. These settings ensured that calculated d-spacings were converged to within about 0.01 Å. The potentials were generated using the electronic configurations: $2p^6 3s^2$ for magnesium, $3d^7 4s^1$ for iron, $5s^2 5p^6 6s^1$ for caesium, $3s^2 3p^1$ for aluminium, $1s^1$ for hydrogen, $3s^2 3p^2$ for silicon, and $2s^2 2p^4$ for oxygen. The calculations were spin polarised with iron modelled in a high-spin state.

All calculations were performed using both the local density approximation (LDA)(Perdew and Zunger, 1981) and PBE formulation of the generalized gradient approximation (GGA) (Perdew et al., 1996).The d-spacings predicted using the LDA and GGA differ by about 0.5 Å. This is in accord with the well-known fact that the LDA underestimates lattice parameters, while the GGA overestimates. Predicted changes in d-spacing, when going from K to Cs, however, are in much better agreement, as the effect of over- or under-binding cancels.

### 6.2.6 EXAFS

The illite which had been exposed to Cs for 12 months was analysed by XAS. Cs K-edge (35985 keV) spectra were gathered on beamline B18 at the Diamond Light Source, Didcot, UK. The beam had a typical operating voltage of 3 GeV and a stable beam current of 300mA during the duration of the experiment. Before use the beam was vertically collimated by a Si mirror. The requisite beam energy range (35800 – 36800 keV) was then selected using a double crystal Si monochromator. A double torroidal mirror was then used to focus the monochromated beam onto the sample to give a final spot size of 200 x 250 µm. The 10 mg sub-sample was mounted into Perspex holders with Kapton tape windows. During data collection the sample was held in an Oxford Instruments cryostat at 80 K to enhance data quality and reduce the chance of radiation damage. Cs K-edge spectra were then gathered in fluorescence mode using a 9 element Ge solid state detector. To improve the signal to noise ratio a total of 144 5-minute scans

were gathered and averaged using Athena (Ravel and Newville, 2005). The default background subtraction provided by Athena was accepted and this final data was used for fitting.

The EXAFS data was analysed using Artemis (Ravel and Newville, 2005) running Feff6.0 (Rehr and Albers, 2000). The initial model used was constructed using data from the density functional theory (DFT) calculations. Similar length paths were grouped together, such that the initial model of O neighbours used was 2 at 3.04 Å, 4 at 3.12 Å and 6 at 3.40 Å with 12 Si atoms at 3.94 Å. Differentiating between Si and Al in EXAFS is difficult; hence this last shell accounts for the signal due to both Si and Al scatterers. The inter-atomic distance and Debye-Waller factor for each shell, E0 and $S_0^2$ were refined in R-space using a range of 1.9 - 3.9 Å in R-space, keeping the number of atoms in each shell constant. To reduce the number of variables the Debye-Waller factors for the first two O shells were fixed to be the same value The fit was made to the k, $k^2$ and $k^3$-weighted Fourier transforms using a range 2.5 -11 $Å^{-1}$ in k-space simultaneously. Once the best fit had been achieved each shell was removed in turn to check its significance. No reasonable fit could be achieved with only 3 shells of atoms. The Debye-Waller factors for the third O shell and the Si-Al shell are somewhat large, because they represent the average of individual scattering paths covering a wide spread of distances (ca 0.25 and 0.14Å respectively).

## 6.3 Results and Discussion

### 6.3.1 Negative control sample: Illite suspended in deionised water for 4 months

A large section of this work relies on the assumption that all compositional changes result from the presence of the ions in solution and there is negligible release of K from the illite interlayer due to equilibration with aqueous solution (deionised water). Additionally it is assumed that any release did not cause a change in the layer thickness. To confirm this assumption and disprove the null hypothesis the starting illite material was equilibrated with deionised water for 4 months. The samples were then imaged to determine any change in layer spacing and analysed by energy dispersive x-ray (EDX) spectroscopy to quantify any loss of K. Figure 6.1 shows the two EDX spectra from the starting illite material and from the sample exposed to deionised water for 4 months. The data was normalised on the silicon peak to determine the K/Si ratio for both systems. The starting illite material had a K/Si ratio of 0.19 and the K/Si ratio of illite after equilibration with deionised water was also 0.19. This confirms that any loss of K into solution was negligible and cannot account for the large reduction in K seen in data from both our Ca and Cs exposed systems. When the crystal structure of the illite material suspended in deionised water was imaged no evidence was found of edge fraying or expansion (Figure 6.2). Therefore the expansion seen in the Ca and Cs systems must be due to the sorption of hydrated Ca or Cs ions rather than just a loss of K.

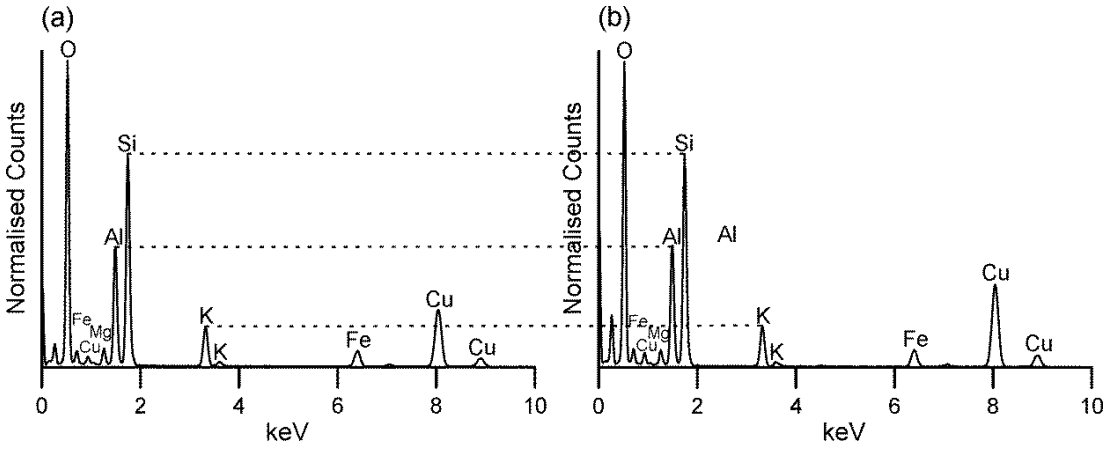


**Figure 6.1** Energy dispersive x-ray spectra of (a) the starting illite material and (b) illite suspended in deionised water for 4 months. Spectra are normalised to the Si peak and show no difference in concentrations of Al or K. The Cu peak at 8 keV is from the support grid and unrelated to the sample's composition

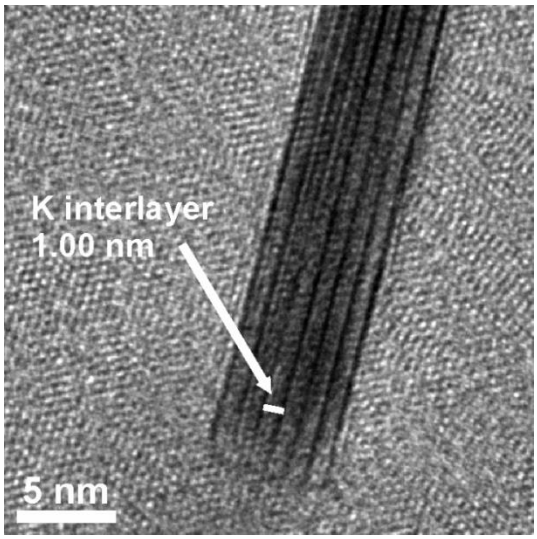


**Figure 6.2** Starting illite material suspended in deionised water for 4 months shows no expansion of the interlayer structure

### 6.3.2 Damage of illite by the TEM electron beam

When materials are exposed to an electron beam for a sufficient period of time they become damaged by the processes of radiolysis (or ionisation damage) and atom knock-on (Champness, 2001). Radiolysis dominates in insulating materials or semi-conductors (such as organics and silicate minerals) whilst conductive metals are resilliant to radiolysis and primarily damage via knock-on effects (Egerton, 2013). Radiolysis occurs when the beams high energy electrons collide with lower energy electrons orbiting the specimens atoms. The resulting transfer of energy raises the orbital electrons to higher energy levels and leaves a core hole (Egerton, 2013). In conductive materials (such as metals) electrons quickly migrate to fill this hole and the atomic bonds remain in tact (Egerton, 2013). In insulating materials this ionisation disrupts atomic bonds and causes the material to become amorphous (Champness, 2001, Agar et al., 1974). Knock-on occurs when one of the beam's high energy electrons collides with the nucleus of a specimen atom (Egerton et al., 2010). The high energy electrons displace the atoms and they can then migrate within the sample (often clumping together) or be lost into the void (Champness, 2001, Cosslett, 1969).

Materials vary widely in their resistance to damage because of their conductivity, elemental composition and the strength of inter-atomic bonds. Clay minerals are easily damaged by radiolysis and knock-on effects (Kogure, 2002, Chi et al., 1998). Clays often become damaged after very short expousre time (<10 seconds) when imaged at high resolution, meaning images must be acquired very rapidly (Chen et al., 1997, Chen and Hayes, 1999).

Electron beam induced sample damage is more serious an issue for high resolution work due to higher current densitites at the specimen. A TEM imaging and EDX time series was performed in order to better understand this damage process. Most TEM is performed at room temperature but imaging below room temperature has been proposed as a mechanism to reduce radiation damage (Cosslett, 1969). Therefore the imaging and EDX time series was repeated both at room temperature (Figure 6.3) and at -190°C (Figure 6.4). Cooling made little difference to the morphology observed during damage of the sample over 10 minutes, with both samples losing their crystallinity and becoming amorphous. However, the loss of K during imaging was slower at cooler temperatures. This is likely to be the result of the reduced kinetic energy of the atoms at lower temperatures slowing their diffusion, meaning they migrated outside of the field of view more slowly and therefore continued to be detected by EDX even when the sample was amorphous. The samples retained their crystallinity at this fluence rate for around one minute. But by two minutes significant damage was visible and by three minutes the samples were largely amorphous. It is not clear from these results whether damage is dominated by radiolysis or knock-on but it is likely that both processes are contributing. STEM imaging on the Titan was found to cause similar changes in the morphology of the samples but no systematic studies was undertaken for this imaging mode. Although beam induced radiation damage compromised the resolution of both the STEM images and the EDX spectrum images it did not prevent significant new findings being obtained to answer the projects hypothesis.

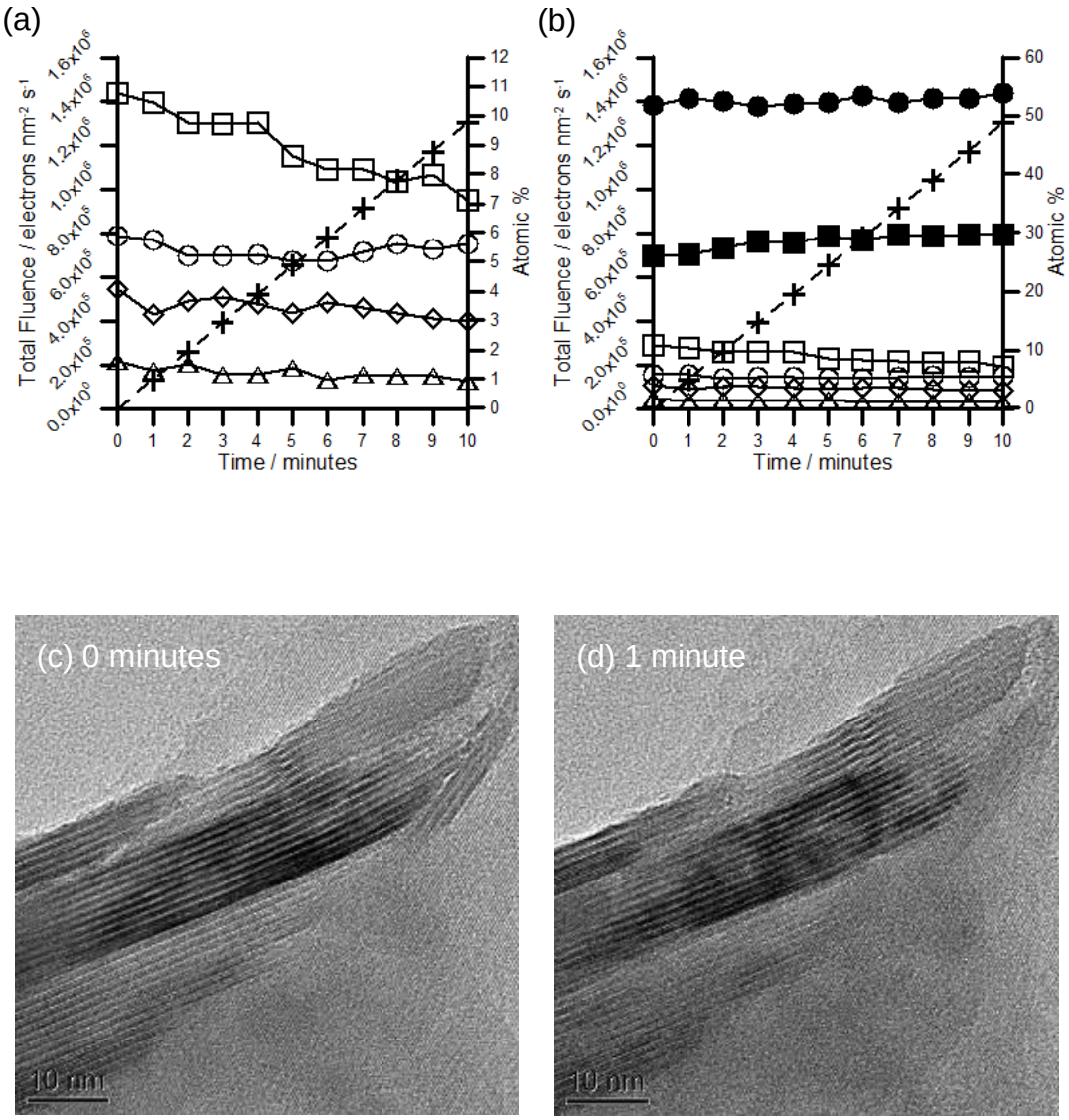
(a)
(b)
Total Fluence / electrons nm-2 s-1
Atomic %
Time / minutes
(c) 0 minutes
(d) 1 minute
10 nm
10 nm

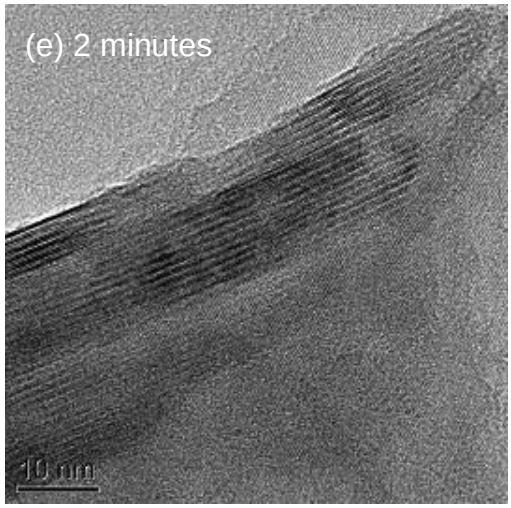
(e) 2 minutes
10 nm

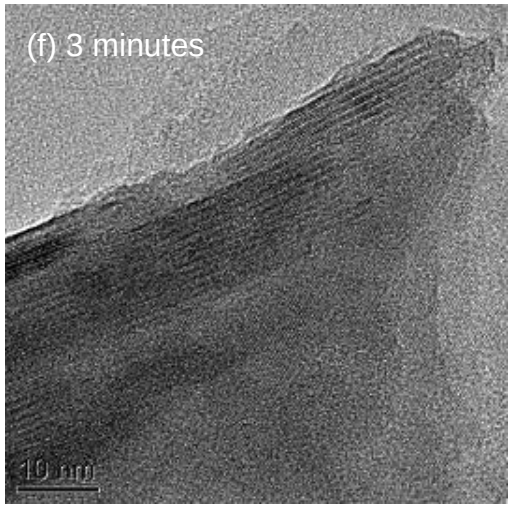
(f) 3 minutes
10 nm

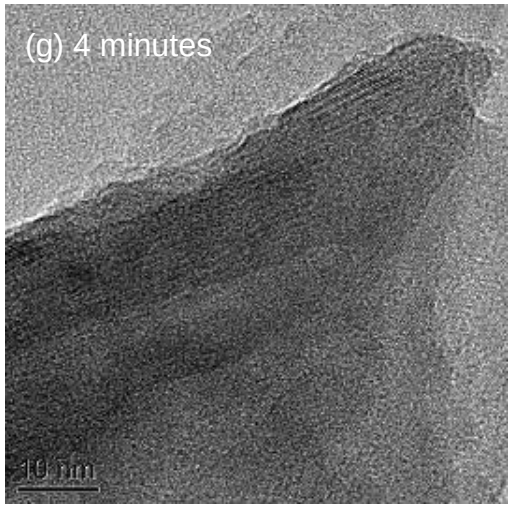
(g) 4 minutes
10 nm

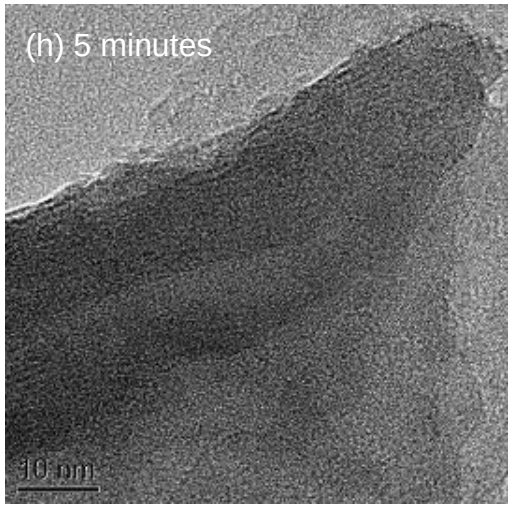
(h) 5 minutes
10 nm

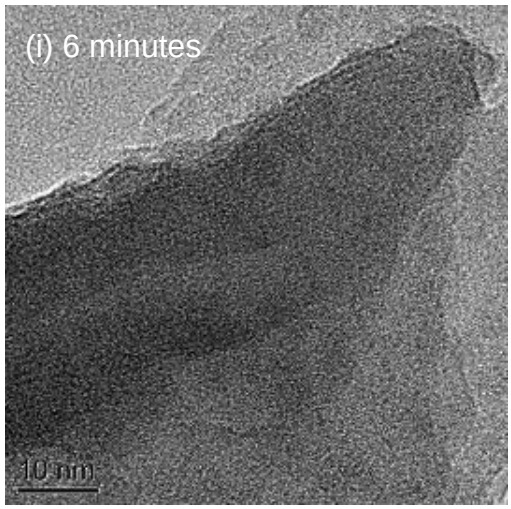
(i) 6 minutes
10 nm

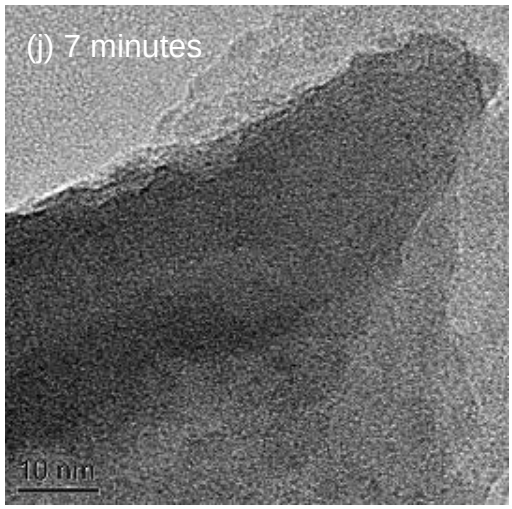
(j) 7 minutes
10 nm

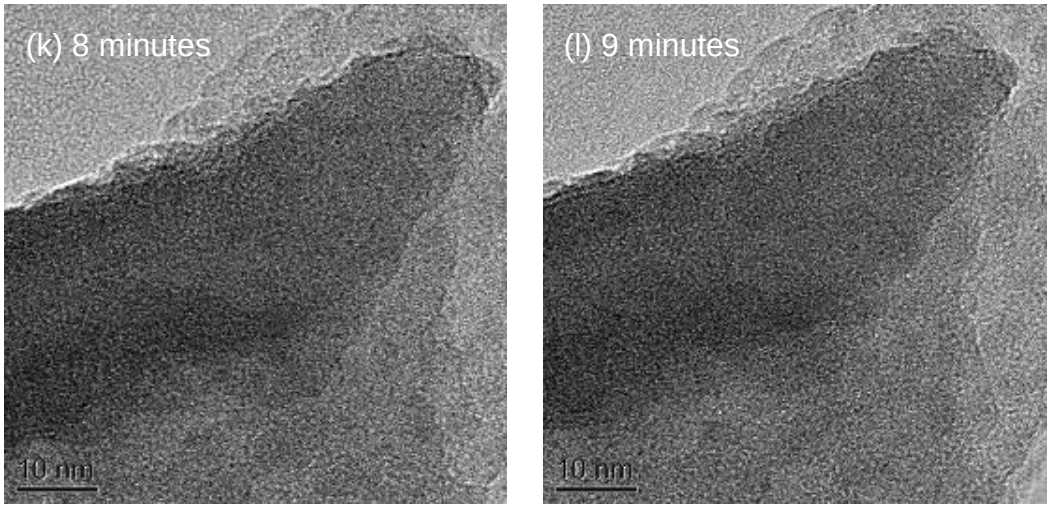


**Figure 6.3** Time series of illite damage by the electron beam when imaged at 20°C. The graph (a) shows the reduction in relative atomic % of key atoms in the sample as a product of increasing electron fluence. Symbols show % of Si (solid circles) Al (solid squares), K (hollow squares), Fe (hollow circles), Mg (hollow diamonds) and Cs (hollow traingles). Graph (b) shows an expanded region of graph (a) with Si and Al removed. Image (c) shows the sample at the beginning of the imaging period and images (d-l) were taken every minute for a further 9 minutes to show loss of sample crystallinity

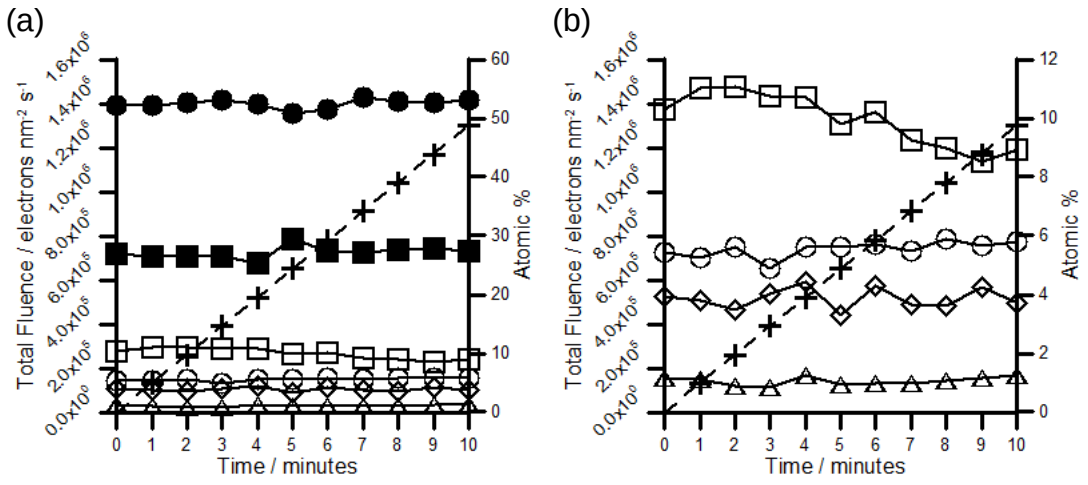

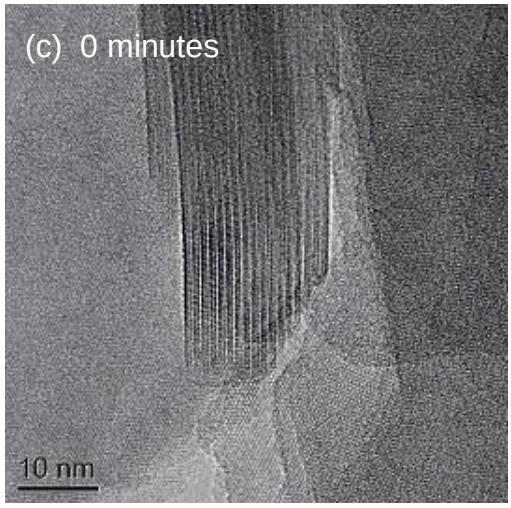
(c) 0 minutes
10 nm

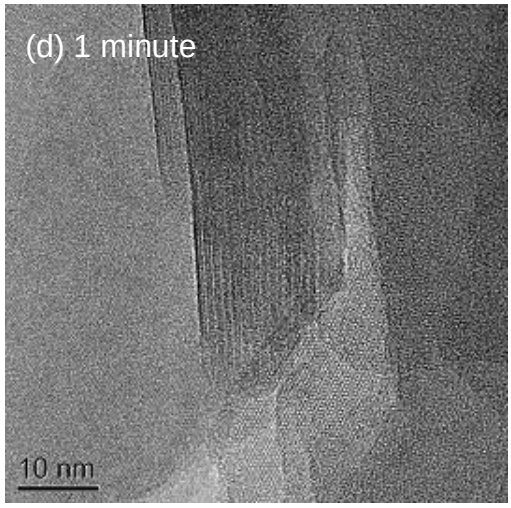
(d) 1 minute
10 nm

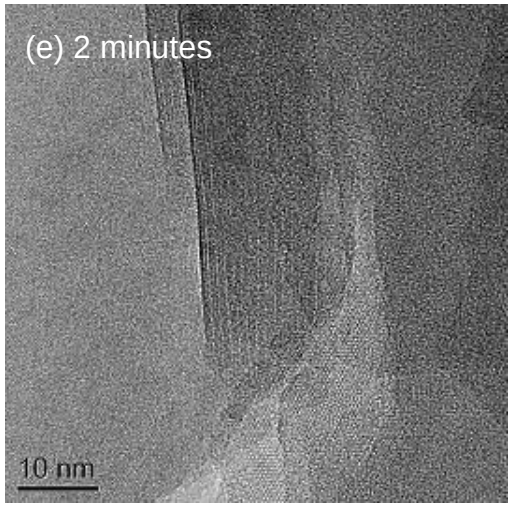
(e) 2 minutes
10 nm

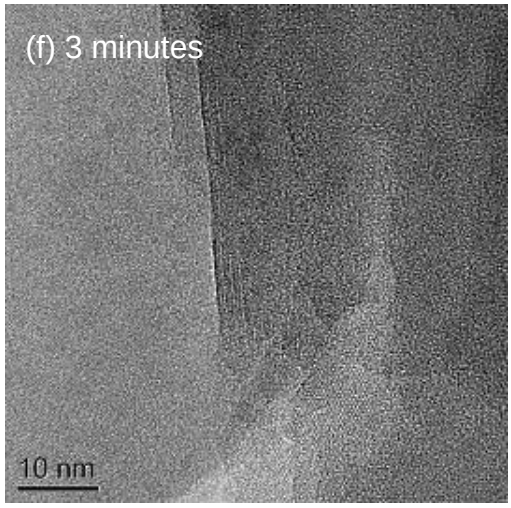
(f) 3 minutes
10 nm

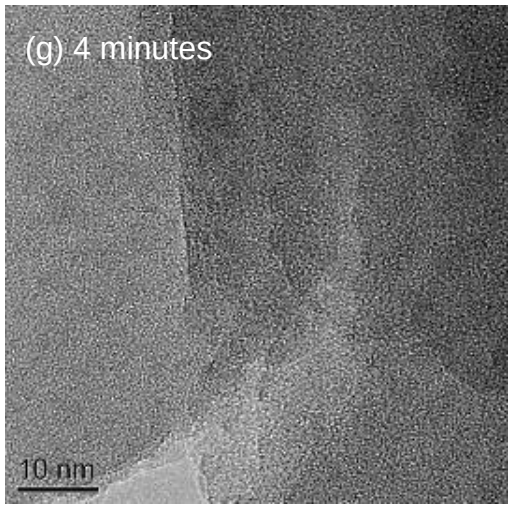
(g) 4 minutes
10 nm

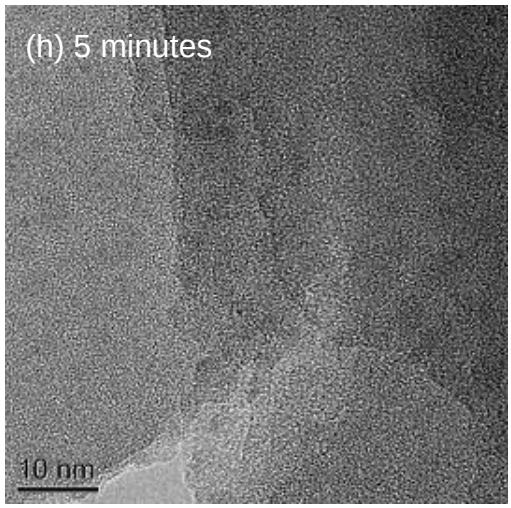
(h) 5 minutes
10 nm

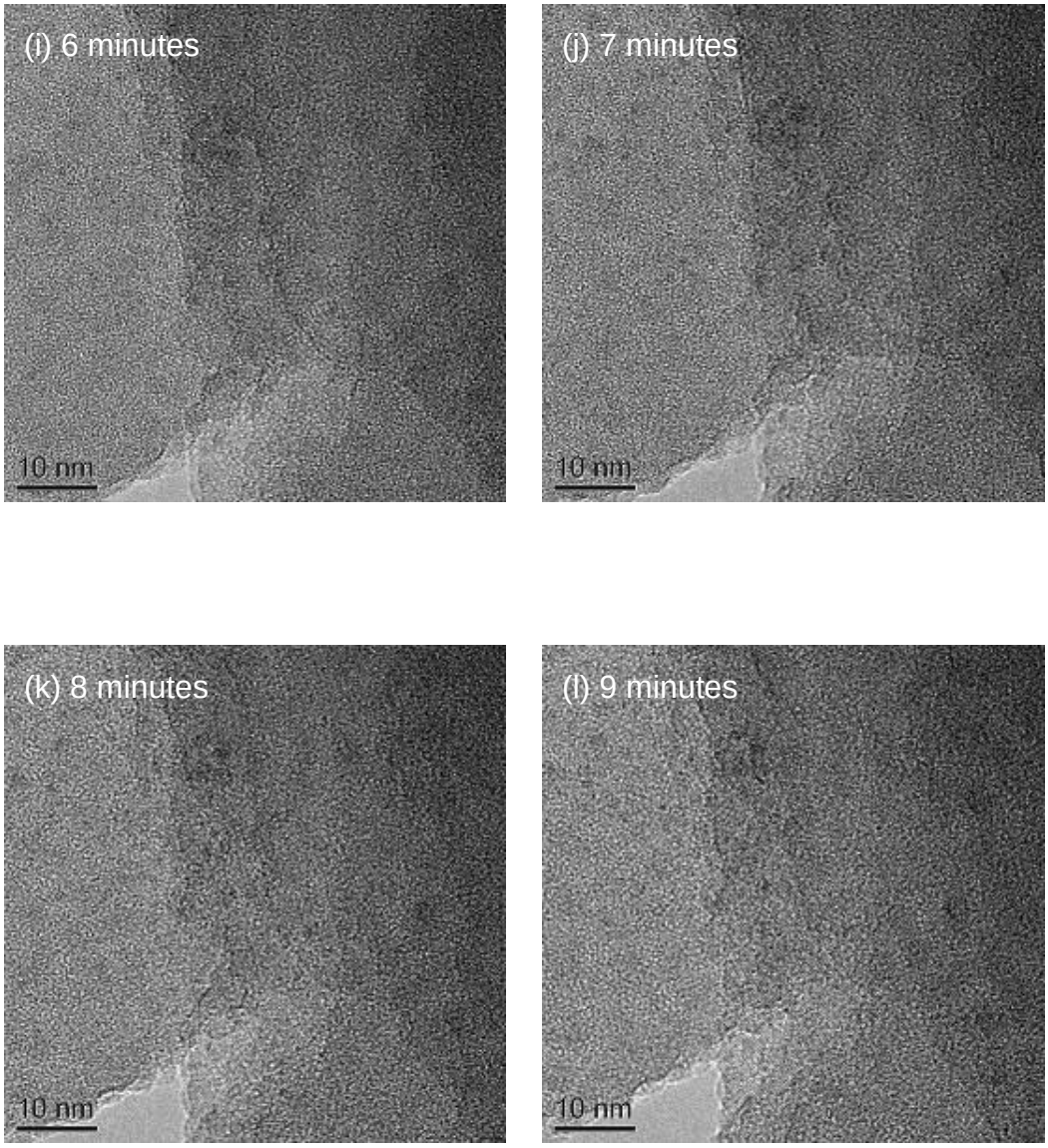


**Figure 6.4** Time series of illite damage by the electron beam when imaged at -190°C. The graph (a) shows the reduction in relative atomic % of key atoms in the sample as a product of increasing electron fluence. Symbols show % of Si (solid circles) Al (solid squares), K (hollow squares), Fe (hollow circles), Mg (hollow diamonds) and Cs (hollow traingles). Graph (b) shows an expanded region of graph (a) with Si and Al removed. Image (c) shows the sample at the beginning of the imaging period and images (d-l) were taken every minute for a further 9 minutes to show loss of sample crystallinity

### 6.3.3 Caesium sorption experiments

To investigate the proposed (Comans et al., 1991, Comans and Hockley, 1992) two-stage sorption process both short term cation-exchange and long term incorporation experiments were conducted. All of the investigations focused on sorption to the illite interlayer sites (rather than edge hydroxyl groups or permanent charge basal plane sites) as these are thought to control long term Cs behaviour. Understanding the mechanism of Cs incorporation requires direct imaging of the induced changes in the clay mineral structure. Transmission electron microscopy is able to directly visualise the illite layers and hence reveal structural changes associated with formation of the expanded (frayed) edge and sorption of Cs therein (Figure 6.5).

#### 6.3.3.1 Expansion and collapse of the illite frayed edges

In the original material all the imaged crystals were found to have a constant 1.0 nm layer thickness (i.e. 2:1 layer + interlayer) along their full length (Figure 6.5 a). Saturating the illite with Ca resulted in an expansion of the interlayer edge, increasing the layer thickness from 1.0 to 1.4 nm (Figure 6.5 b). The presence of Ca in this sample was confirmed by chemical analysis using energy dispersive x-ray (EDX) spectroscopy (Figure 6.6 b). This shows the well documented mechanism of illite weathering which liberates the interlayer K ions (Jackson and During, 1979, Moritsuka et al., 2004, Sparks and Huang, 1985). The 1.4 nm spacing is only possible if the Ca remains in hydrated outer-sphere complexes, where it is easily exchanged (Nakao et al., 2008, Jackson et al., 1952, Jackson, 1968, Comans et al., 1991). Suspending this Ca saturated material in a Cs solution resulted in the

Ca being exchanged with the Cs. As Cs is less strongly hydrated (Rosso et al., 2001) this caused the ‘frayed edges’ to dehydrate and collapse, giving a 1.0 nm spacing at the edge (Figure 6.5 c). Again the reduction in Ca concentration and presence of Cs in the structure was confirmed by EDX spectroscopy (Figure 6.6 c). This mechanism of expansion and collapse has been proposed for many decades in both the radiochemistry and mineral weathering literature (Jackson, 1968, Jackson et al., 1952, Sawhney, 1967). However, here we present direct evidence for this process occurring with Cs. These images demonstrate conclusively that the ‘frayed edge sites’ are simply an expanded region of the interlayer, where large hydrated cations (e.g. Ca) have exchanged K. To investigate the reversibility of this Cs sorption, we attempted to re-expand the Cs-interlayers with Ca. However after this attempt no Ca sorption was observed from EDX chemical analysis (Figure 6.6 d) and Figure 6.5 d shows that the structure remained unexpanded at 1.0 nm. This un-expandable nature of the Cs interlayer explains why Cs cannot be easily desorbed from the illite frayed edge sites.

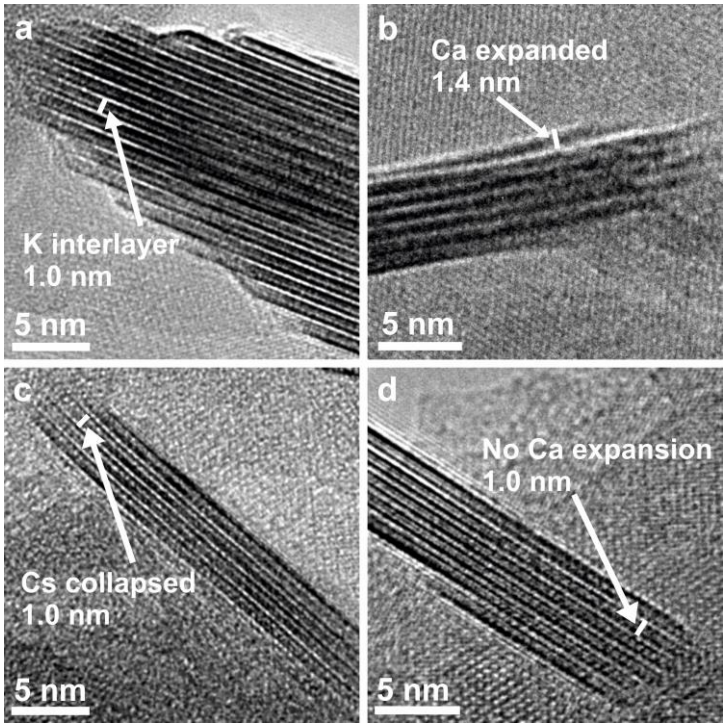


**Figure 6.5** Interlayer expansion and collapse. (a) The initial illite material shows a stable 1.0nm structure, (b) This expands to 1.4nm upon sorption of Ca at the edge of the crystal, (c) Exchange of the edge sorbed Ca for Cs causes a dehydration and re-collapse of the interlayer (d) Cs held in this collapsed interlayer was not exchanged by Ca and the structure did not re-expand

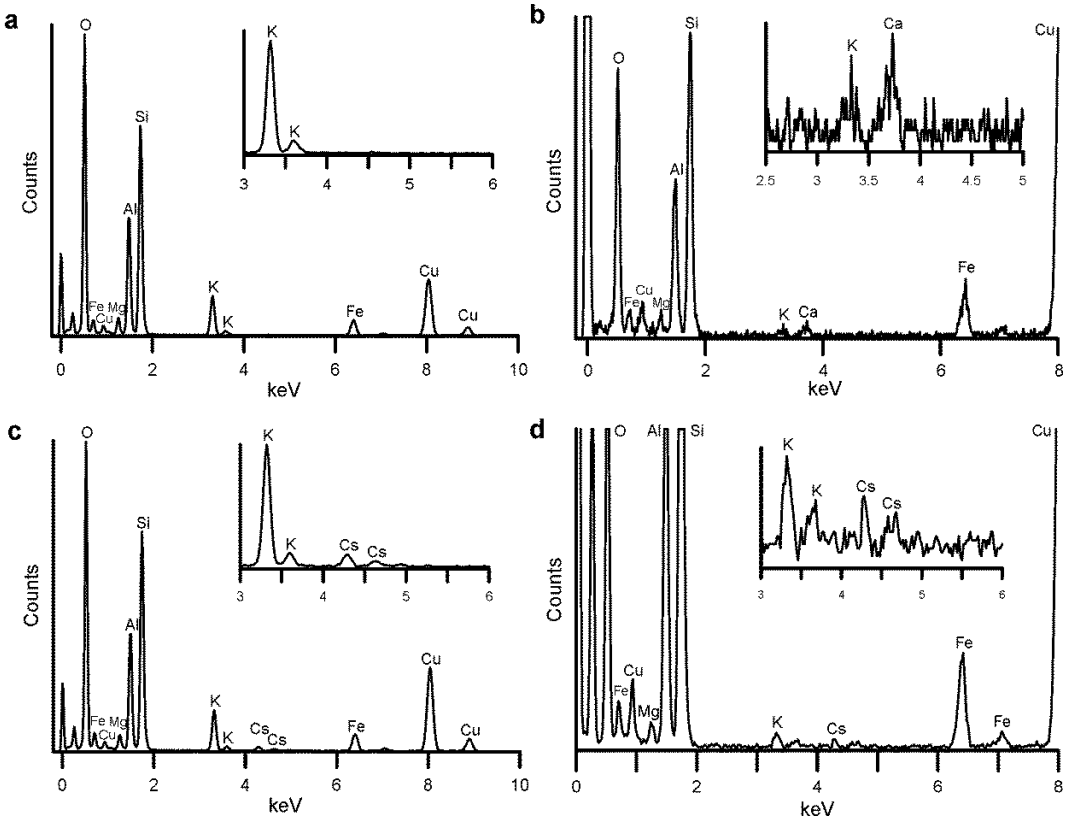


**Figure 6.6** EDX spectra associated with the Ca/Cs illite series (Fig 5.5). (a) Starting illite material, for which no Ca $K_\alpha$ peak at 3.7 keV or Cs $L_\alpha$ peak at 4.3 keV are observed to be present, (insert shows enlargement of relevant region between 3 and 6 keV), (b) Ca illite showing Ca peak at 3.7 keV, insert shows an enhancement of the region with the Ca peak, (c) Cs exchanged Ca-illite shows loss of Ca peak and presence of Cs $L_\alpha$ peak at 4.3 keV, showing that Cs has exchanged for Ca in the illite structure and (d) Interlayer remains Cs filled and shows no Ca present, even after suspension in 0.1 mol $L^{-1}$ CaCl.

#### 6.3.3.2 Cs interlayer incorporation

It is important for management of contaminated land to understand the long term fate of Cs in the interlayer region. Cs sorption can take over a year to reach equilibrium (Poinssot et al., 1999, Sawhney, 1966, Comans et al., 1991, Comans and Hockley, 1992, Konoplev et al., 1996) so it is crucial to study the progress of illite incorporation over this timescale. To investigate this the illite was suspended in CsCl for up to one year. Samples were then taken at 4, 7 and 12 months exposure for high angle annular dark field (HAADF) STEM imaging and EDX elemental mapping. Figure 6.7 presents micrographs of illite viewed along the clay layers at different stages during the process of Cs sorption. The intensity of the HAADF image is proportional to the square of the mean atomic number; allowing layers with different compositions within the clay structure to be identified.

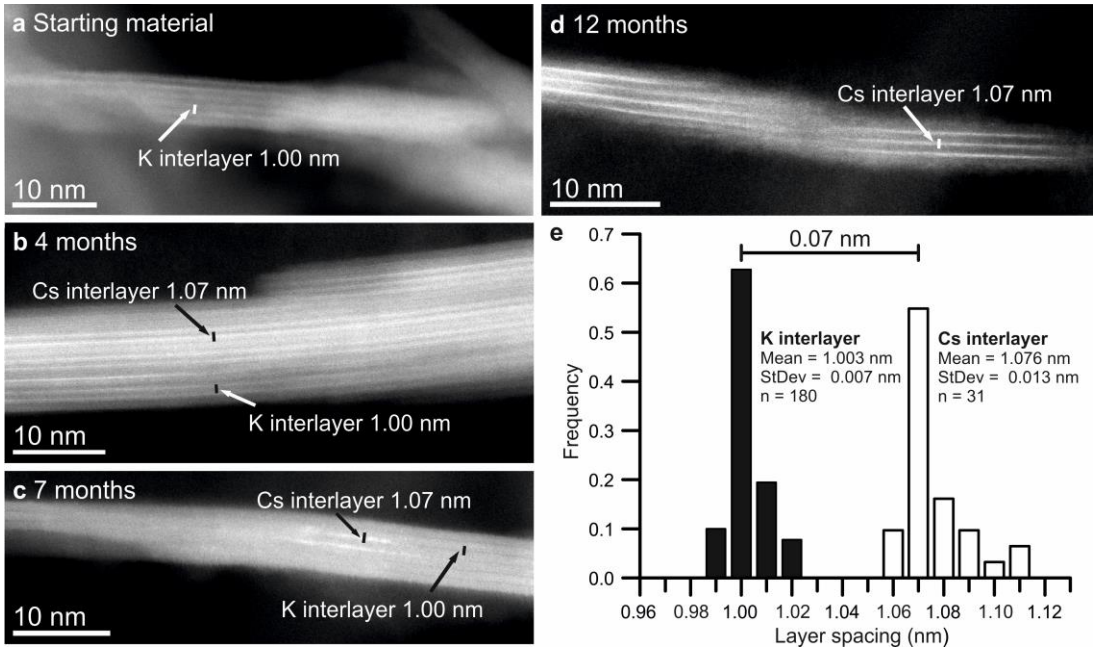


**Figure 6.7** HAADF imaging of Cs interlayer incorporation. (a) Starting illite shows planes with uniform brightness and a constant interlayer spacing of 1.00 nm suggesting the material has a constant composition throughout the structure. (b) After 4 months and (c) 7 months Cs exposure some of the illite interlayer planes are brighter than others, indicating local interlayer regions with a higher atomic number. (d) In illite exposed to Cs for 12 months all of the interlayers are again of uniform intensity but now with an expanded interlayer spacing of 1.07 nm suggesting all interlayers are Cs filled. (e) The interlayer spacing measured from the dark K interlayers (black bars) and bright Cs interlayers (white bars)

These HAADF imaging showed that before being exposed to Cs the starting illite (Figure 6.7 a) shows a layered structure with an average thickness of 1.0 nm (Figure 6.7 e). This value is consistent with the layer thickness determined by density functional theory for an illite with a K filled interlayer (Table 6.1). The wider brighter layers in the image are likely the 2:1 structure and the thinner darker layers are the K filled interlayers. The atomic

composition of this starting material was confirmed by EDX (Figure 6.8 a) and matched the reported formula for this reference illite (Hower and Mowatt, 1966). In contrast, HAADF images of the samples exposed to Cs for 4 or 7 months showed interlayer regions that varied in intensity, even within a single crystal (Figure 6.7 b and c). This indicates that in these samples the interlayer contains regions where the mean atomic number (Z) is greater. Caesium (Z = 55) will give higher intensity than K (Z = 19) in a HAADF image, suggesting that these bright interlayers contain Cs. This is consistent with the observations and contrast simulations of Okumura et al. (2014) for Cs incorporation into phlogopite, strongly suggesting the same incorporation is occurring in these illite samples. The presence of Cs in both of these samples was also confirmed by EDX (Figure 6.8 b). We measured a large number of both dark (n= 180) and bright (n=31) interlayers to determine the average change in layer spacing associated with Cs incorporation. Figure 6.7 e shows the range and frequency of measured layer spacings. From these results it was determined that the total layer thickness of those regions with brighter interlayers was found to be consistently 0.07 nm larger than the less bright interlayers (Figure 6.7 e), showing a significant expansion (Mann Whitney U; $p << 0.001$). This agrees with our density functional theory model for the expected increase in interlayer separation produced by the exchange of interlayer K for Cs (Table 6.1). This change in layer-spacing has been previously proposed to occur when Cs incorporates into aluminosilicates (Kogure et al., 2012, Tamura et al., 2014), supporting the validity of our measurements. These results demonstrate that at 4 and 7 months a number of the interlayers have become filled with Cs. By 12 months, the majority of the interlayers in the imaged sample appear to be bright with a mean layer

spacing of 1.07 nm, consistent with the majority of the interlayers being Cs filled (Figure 6.7 d). An EDX analysis of this region shows significant concentrations of Cs in the structure (Figure 6.8 d and Table 6.2).

**Table 6.1** Lattice parameters for a K and Cs interlayer substituted illite based on both the local density and generalised gradient approximations. In both cases lattice parameters for two different configurations of isomorphic substitution are given.

**Local Density Approximation**

| **Cation** | **Cell length** | | | **Cell angle** | | | |
|---|---|---|---|---|---|---|---|
| **K** | **a (Å)** | **b (Å)** | **c (Å)** | **α (°)** | **β (°)** | **γ (°)** | **Layer spacing (Å)** |
| Iso Sub 1 | 10.32 | 8.906 | 9.969 | 89.504 | 102.094 | 89.823 | 9.747 |
| Iso Sub 2 | 10.319 | 8.912 | 9.965 | 89.508 | 102.167 | 89.85 | 9.741 |

| **Cation** | **Cell length** | | | **Cell angle** | | | |
|---|---|---|---|---|---|---|---|
| **Cs** | **a (Å)** | **b (Å)** | **c (Å)** | **α (°)** | **β (°)** | **γ (°)** | **Layer spacing (Å)** |
| Iso Sub 1 | 10.402 | 8.979 | 10.585 | 89.784 | 101.317 | 89.82 | 10.379 |
| Iso Sub 2 | 10.392 | 8.978 | 10.59 | 89.832 | 101.35 | 89.859 | 10.383 |

**Generalised Gradient Approximation**

| **Cation** | **Cell length** | | | **Cell angle** | | | |
|---|---|---|---|---|---|---|---|
| **K** | **a (Å)** | **b (Å)** | **c (Å)** | **α (°)** | **β (°)** | **γ (°)** | **Layer spacing (Å)** |
| Iso Sub 1 | 10.58 | 9.141 | 10.542 | 89.379 | 102.78 | 89.691 | 10.281 |
| Iso Sub 2 | 10.598 | 9.127 | 10.519 | 89.321 | 102.527 | 89.718 | 10.268 |

| **Cation** | **Cell length** | | | **Cell angle** | | | |
|---|---|---|---|---|---|---|---|
| **Cs** | **a (Å)** | **b (Å)** | **c (Å)** | **α (°)** | **β (°)** | **γ (°)** | **Layer spacing (Å)** |
| Iso Sub 1 | 10.626 | 9.174 | 11.199 | 89.599 | 101.261 | 89.86 | 10.984 |
| Iso Sub 2 | 10.635 | 9.167 | 11.197 | 89.637 | 101.203 | 89.788 | 10.983 |

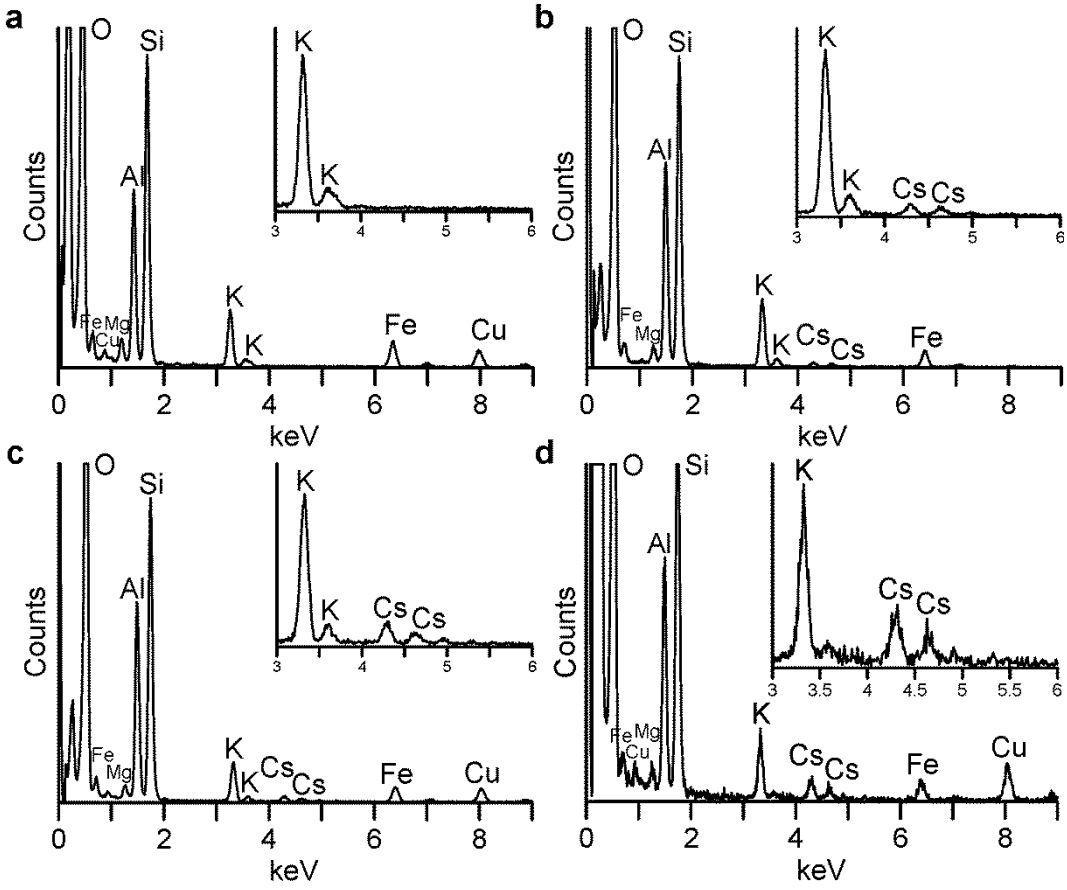


**Figure 6.8** EDX spectral composition of (a) illite starting material, before Cs exposure (b) illite suspended in Cs for 4 months (c) illite suspended in Cs for 7 months and (d) illite after 1 year of Cs exposure

**Table 6.2** Atomic percentage composition of the different elements in the illite after suspension in Cs for up to 1 year; measured through semi-quantitative analysis of the EDX spectra presented in Figure 6.8

| Elements | Starting illite / atomic % | 4 months / atomic % | 7 months / atomic % | 12 months / atomic % |
|---|---|---|---|---|
| **O** | 58 | 52 | 54 | 49 |
| **Si** | 21 | 23 | 23 | 24 |
| **Al** | 11 | 14 | 14 | 13 |
| **Cs** | 0 | 2 | 2 | 6 |
| **K** | 5 | 6 | 4 | 5 |
| **Fe** | 3 | 3 | 2 | 3 |
| **Mg** | 1 | 1 | 1 | 1 |
| **Na** | 0 | 0 | 0 | 0 |

We used extended x-ray absorption fine structure spectroscopy (EXAFS) to further confirm that the Cs present in the 12 month sample was located in the interlayer region. Figure 6.9 a shows the EXAFS data with the calculated fit (dotted line). The fit to the EXAFS data was based on the Cs local environment determined from our DFT calculations for Cs filled illite, shown in Figure 6.9 b (Table 6.1). From the DFT it was determined that the Cs should be coordinated by 12 oxygen atoms at 3.0-3.4 Å and 12 silicon atoms at 4.0Å (coordinating atoms and interatomic distances shown in Figure 6.9 b). The refined EXAFS fit yielded parameters which matched these distances and coordination numbers (within error) (Table 6.3). Therefore after 12 months the majority of the Cs in the sample must be present in the illite interlayer. This confirms the HAADF images and EDX data. Our refined EXAFS fit differs from those previously proposed by Bostick et al. (2002) and Fan et al. (2014). Specifically we found much shorter bond lengths for both the O and Si (Al) shells. This suggests that the interlayers of our sample were more dehydrated than previous studies, likely due to high Cs loadings within the interlayer of our sample (caused by the high concentration and long exposure time).

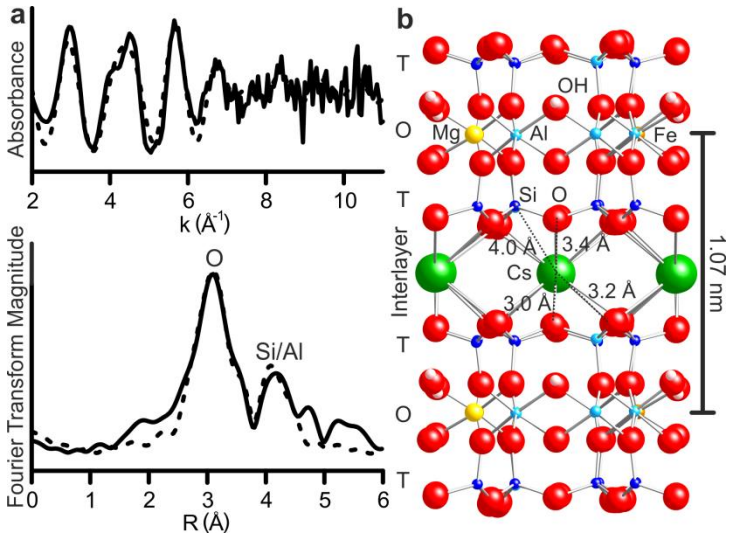


**Figure 6.9** Structural coordination of Cs in the illite interlayer (a) k-space EXAFS spectra and Fourier transform of the EXAFS (solid line) with the refined fit (dotted lines) for 12 oxygen atoms at 3.0-3.3Å and 12 silicon atoms at 4.0Å (b) Crystallographic model of the Cs substituted illite determined by DFT calculations. Atoms and interatomic distances used to fit the EXAFS data are annotated

**Table 6.3** Model fitting parameters for Cs K-edge EXAFS: n, site occupancy; r, inter-atomic bond distance; σ2, Debye-Waller factor. Reduced Chi squared for this fit = 116, R-Factor = 0.020 S02 = 1.05, E0= 6.4 eV

| Shell | n | r (Å) | $\sigma^2$ |
|---|---|---|---|
| **O** | 2 | 3.00 (± 0.03) | 0.0062 (± 0.04) |
| **O** | 4 | 3.16 (± 0.02) | 0.0062 (± 0.04) |
| **O** | 6 | 3.34 (± 0.03) | 0.0131 (± 0.04) |
| **Si/Al** | 12 | 3.99 (± 0.03) | 0.0320 (± 0.04) |

EDX maps were also gathered to determine whether Cs was diffusing along the interlayer into the illite crystals, rather than only being present at the edge. Figure 6.10 shows a HAADF image and accompanying EDX maps looking down onto two illite crystals (i.e. perpendicular to the layers). The maps clearly show that both Cs and K are homogenously distributed

throughout the crystals at the length scale imaged. There is no evidence for any enhancement in Cs concentration at the edge, with Cs detected up to ≈100 nm into the core of the crystal. In EDX maps signal intensity is related to atomic abundance and sample thickness (Fitting et al., 1977). Normalisation of the EDX spectra from the two crystals shown reveals they have an identical Cs/K ratio (Figure 6.10 f). Therefore, the difference in HAADF intensity observed is ascribed to thickness effects. The Cs signal varies with thickness proportionally to the other elements (Figure 6.11) suggesting that the Cs must be structurally incorporated as Cs present solely on the surface would have an EDX intensity unrelated to crystal thickness.

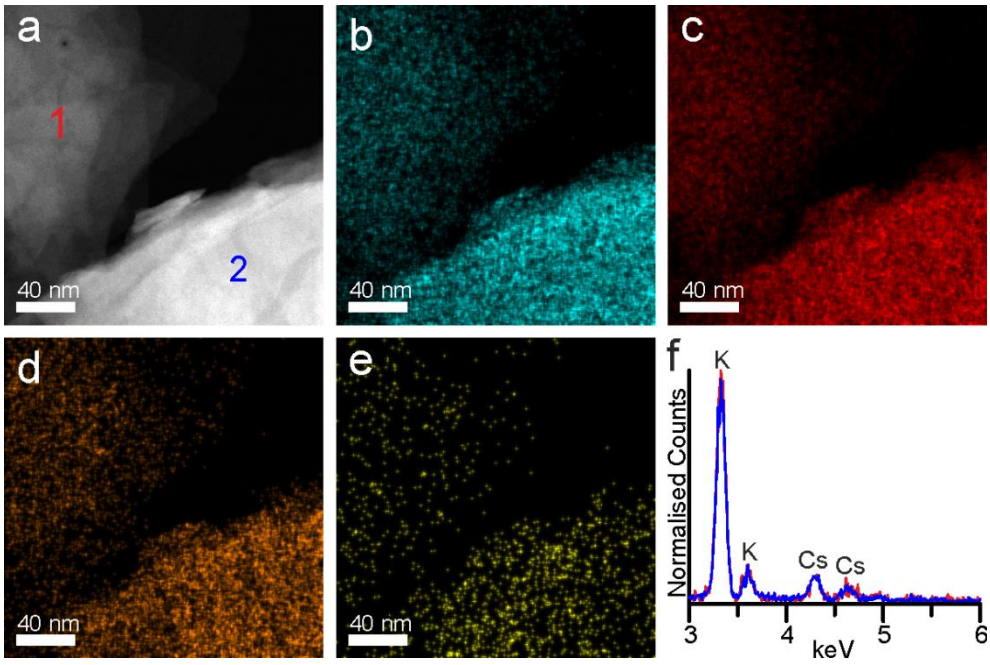


**Figure 6.10** EDX map of the 12 month sample (a) HAADF image of planar surface of one thicker (brighter)and one thinner (darker) illite crystal (b) EDX map of the Al signal, stronger signal from the lower crystal is due to its greater thickness (c) Si EDX map (d) K EDX map (e) Cs EDX map (f) EDX spectra from the whole imaged area showing presence of K and Cs in the structure

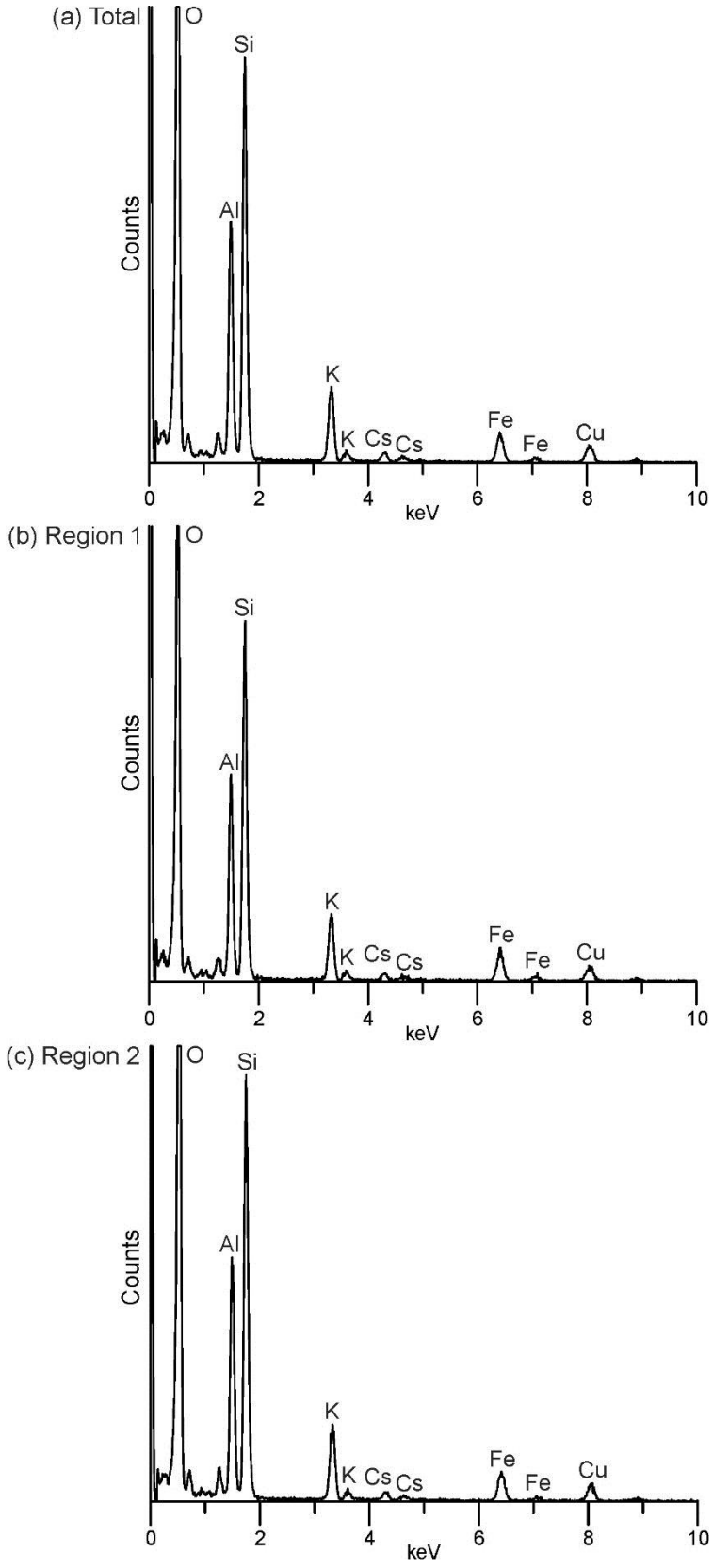


**Figure 6.11** EDX spectral composition of 12 month sample taken from the EDX maps (Fig. 5.10 ) (a) Total imaged area (b) Crystal 1 (c) Crystal 2

Previous authors have shown by lower resolution electron microprobe the presence of a Cs enriched region around the edge of a mica crystal, and from this they argued that Cs would fill all of the edges rather than diffusing into the interlayers (Le Roux et al., 1970, Zachara et al., 2002). However, we found no evidence for Cs being confined to the crystal edges. Instead we propose that Cs initially sorbs to edges where the layer charge is lower and the K ions are less strongly held. We observe many cases where an interlayer plane is entirely filled while nearby layers are unfilled (Figure 6.7 b and c). The reason for this heterogeneous distribution of Cs between layers is unclear but may be due to variation in layer charge on the aluminosilicate 2:1 layers leading to a difference in Cs/K exchange rates. Once exchange has begun the interlayer provides a fast diffusion path meaning it is then possible for the Cs ions to diffuse into and exchange the whole interlayer plane to attain the energetically more favourable Cs substituted structure (Rosso et al., 2001).

## 6.4 Conclusions

Overall, we show that Cs initially sorbs to and becomes irreversibly trapped in the illite interlayers due to collapse of the frayed edge sites. Therefore we can robustly say that Cs held in these specific sites will not be mobile or bio-available in contaminated environments. Over the longer term we observe the diffusion of Cs from these edge sites into the illite interlayer. This interlayer incorporation is the likely long term sink for Cs in contaminated soils. Caesium cannot be easily remobilised from this interlayer region; therefore any effective remediation measures must either separate or

degrade the illite clay fraction. This must be accounted for when considering any potential strategies for management and potential remediation of sites contaminated with radiocaesium.

## 6.5 References

Agar, A. W., Alderson, R. H. & Chescoe, D. 1974. *Practical Methods in Electron Microscopy Volume 2: Principles and Practice of Electron Microscope Operation,* Amsterdam, North-Holland Publishing Company.

Blöchl, P. E. 1994. Projector augmented-wave method. *Physical Review B,* 50**,** 17963-17979

Bostick, B. C., Vairavamurthy, M. A., Karthikeyan, K. G. & Chorover, J. 2002. Cesium adsorption on clay minerals: An EXAFS spectroscopic investigation. *Environmental Science & Technology,* 36**,** 2670-2676.

Bradbury, M. H. & Baeyens, B. 2000. A generalised sorption model for the concentration dependent uptake of caesium by argillaceous rocks. *Journal of Contaminant Hydrology,* 42**,** 141-163.

Champness, P. E. 2001. *Electron Diffraction in the Transmission Electron Microscope,* Oxford, BIOS.

Chen, C. C. & Hayes, K. F. 1999. X-ray absorption spectroscopy investigation of aqueous Co(II) and Sr(II) sorption at clay-water interfaces. *Geochimica Et Cosmochimica Acta,* 63**,** 3205-3215.

Chen, C. C., Hayes, K. F. & Papelis, C. 1997. In-situ EXAFS study on aqueous cobalt(II) and strontium(II) sorption at clay-water interfaces as a function of various solution conditions. *Abstracts of Papers of the American Chemical Society,* 214**,** 48-GEOC.

Chi, M., FitzGerald, J. D., Eggleton, R. A. & Llewellyn, D. J. 1998. Analytical electron microscopy in clays and other phyllosilicates: loss of elements from a 9-nm stationary beam of 300-keV electrons. *Clays and Clay Minerals,* 46**,** 301-316.

Comans, R. N. J., Haller, M. & Depreter, P. 1991. Sorption of cesium on illite: None-equilibrium behaviour and reversibility. *Geochimica Et Cosmochimica Acta,* 55**,** 433-440.

Comans, R. N. J. & Hockley, D. E. 1992. Kinetics of cesium sorption on illite. *Geochimica Et Cosmochimica Acta,* 56**,** 1157-1164.

Cornell, R. 1993. Adsorption of cesium on minerals: A review. *Journal of Radioanalytical and Nuclear Chemistry,* 171**,** 483-500.

Cosslett, V. E. 1969. High-Voltage Electron Microscopy. *Quarterly Reviews of Biophysics,* 2**,** 95-133.

de Koning, A. & Comans, R. N. J. 2004. Reversibility of radiocaesium sorption on illite. *Geochimica Et Cosmochimica Acta,* 68**,** 2815-2823.

Egerton, R. F. 2013. Control of radiation damage in the TEM. *Ultramicroscopy,* 127**,** 100-108.

Egerton, R. F., McLeod, R., Wang, F. & Malac, M. 2010. Basic questions related to electron-induced sputtering in the TEM. *Ultramicroscopy,* 110**,** 991-997.

Fan, Q. H., Tanaka, M., Tanaka, K., Sakaguchi, A. & Takahashi, Y. 2014. An EXAFS study on the effects of natural organic matter and the expandability of clay minerals on cesium adsorption and mobility. *Geochimica et Cosmochimica Acta,* 135**,** 49-65.

Fitting, H. J., Glaefeke, H. & Wild, W. 1977. Electron Penetration and Energy Transfer in Solid Targets. *Physica Status Solidi (A) Applied Research,* 43**,** 185-190.

Fuller, A. J., Shaw, S., Peacock, C. L., Trivedi, D., Small, J. S., Abrahamsen, L. G. & Burke, I. T. 2014. Ionic strength and pH dependent multi-site sorption of Cs onto a micaceous aquifer sediment. *Applied Geochemistry,* 40**,** 32-42.

Hird, A. B., Rimmer, D. L. & Livens, F. R. 1996. Factors affecting the sorption and fixation of caesium in acid organic soil. *European Journal of Soil Science,* 47**,** 97-104.

Hower, J. & Mowatt, T. C. 1966. The mineralogy of illites and mixed-layerillite/montmorillonites. *American Mineralogist,* 51**,** 825-854.

Jackson, B. L. J. & During, C. 1979. Studies of slowly available potassium in soils of New Zealand - I. Effects of leaching, temperature and potassium depletion on the equilibrium concentration of potassium in solution. *Plant and Soil,* 51**,** 197-204.

Jackson, M. L. 1968. Weathering of Primary and Seondary Minerals in Soils. *9th International Congress of Soil Science.* Adelaide, Australia: The International Society of Soil Science and Angus & Robertson Ltd.

Jackson, M. L., Hseung, Y., Corey, R. B., Evans, E. J. & Heuvel, R. C. V. 1952. Weathering Sequence of Clay-size Minerals in Soils and Sediments: II. Chemical Weathering of Layer Silicates. *Soil Science Society of America Proceedings,* 16**,** 3-6.

Jacob, P., Fesenko, S., Bogdevitch, I., Kashparov, V., Sanzharova, N., Grebenshikova, N., Isamov, N., Lazarev, N., Panov, A., Ulanovsky,

A., Zhuchenko, Y. & Zhurba, M. 2009. Rural areas affected by the Chernobyl accident: Radiation exposure and remediation strategies. *Science of the Total Environment,* 408**,** 14-25.

Jacobs, D. G. & Tamura, T. 1960. The Mechanism of Ion Fixation using Radio-isotope Techniques. *7th Internation Congress of Soil Science.* Madison, Wisconsin, USA: The International Society of Soil Science.

Kim, Y., Kirkpatrick, R. J. & Cygan, R. T. 1996. Cs-133 NMR study of cesium on the surfaces of kaolinite and illite. *Geochimica Et Cosmochimica Acta,* 60**,** 4059-4074.

Kinoshita, N., Sueki, K., Sasa, K., Kitagawa, J.-i., Ikarashi, S., Nishimura, T., Wong, Y.-S., Satou, Y., Handa, K., Takahashi, T., Sato, M. & Yamagata, T. 2011. Assessment of individual radionuclide distributions from the Fukushima nuclear accident covering central-east Japan. *Proceedings of the National Academy of Sciences of the United States of America,* 108**,** 19526-19529.

Kogure, T. 2002. Investigations of Micas Using Advanced Transmission Electron Microscopy. *In:* MOTTANA, A., PAOLO SASSI, F., THOMPSON JR, J. B. & GUGGENHEIM, S. (eds.) *Micas: Crystal Chemistry and Metamorphic Petrology.* Mineralogical Society of America.

Kogure, T., Morimoto, K., Tamura, K., Sato, H. & Yamagishi, A. 2012. XRD and HRTEM evidence for fixation of cesium ions in vermiculite clay. *Chemistry Letters,* 41**,** 380-382.

Konoplev, A. V., Bulgakov, A. A., Popov, V. E., Hilton, J. & Comans, R. N. J. 1996. Long-term investigation of Cs-137 fixation by soils. *Radiation Protection Dosimetry,* 64**,** 15-18.

Kresse, G. & Furthmüller, J. 1996a. Efficiency of ab-initio total energy calculations for metals and semiconductors using a plane-wave basis set. *Computational Materials Science,* 6**,** 15-50.

Kresse, G. & Furthmüller, J. 1996b. Efficient iterative schemes for ab initio total-energy calculations using a plane-wave basis set. *Physical Review B,* 54**,** 11169-11186.

Kresse, G. & Joubert, D. 1999. From ultrasoft pseudopotentials to the projector augmented-wave method. *Physical Review B,* 59**,** 1758-1775.

Le Roux, J., Rich, C. I. & Ribbe, P. H. 1970. Ion selectivity by weathered micas as determined by electron microprobe analysis. *Clays and Clay Minerals,* 18**,** 333-338.

McKinley, J. P., Zachara, J. M., Heald, S. M., Dohnalkova, A., Newville, M. G. & Sutton, S. R. 2004. Microscale distribution of cesium sorbed to biotite and muscovite. *Environmental Science & Technology,* 38**,** 1017-1023.

Militzer, B., Wenk, H. R., Stackhouse, S. & Stixrude, L. 2011. First-principles calculation of the elastic moduli of sheet silicates and their application to shale anisotropy. *American Mineralogist,* 96**,** 125-137.

Moritsuka, N., Yanai, J. & Kosaki, T. 2004. Possible processes releasing nonexchangeable potassium from the rhizosphere of maize. *Plant and Soil,* 258**,** 261-268.

Nakao, A., Thiry, Y., Funakawa, S. & Kosaki, T. 2008. Characterization of the frayed edge site of micaceous minerals in soil clays influenced by different pedogenetic conditions in Japan and northern Thailand. *Soil Science & Plant Nutrition,* 54**,** 479-489.

Okumura, T., Tamura, K., Fujii, E., Yamada, H. & Kogure, T. 2014. Direct observation of cesium at the interlayer region in phlogopite mica. *Microscopy,* 63**,** 65-72.

Perdew, J. P., Burke, K. & Ernzerhof, M. 1996. Generalized gradient approximation made simple. *Physical Review Letters,* 77**,** 3865-3868.

Perdew, J. P. & Zunger, A. 1981. Self-interaction correction to density-functional approximations for many electron systems. *Physical Review A,* 23.

Poinssot, C., Baeyens, B. & Bradbury, M. H. 1999. Experimental and modelling studies of caesium sorption on illite. *Geochimica Et Cosmochimica Acta,* 63**,** 3217-3227.

Ravel, B. & Newville, M. 2005. ATHENA, ARTEMIS, HEPHAESTUS: data analysis for X-ray absorption spectroscopy using IFEFFIT. *Journal of Synchrotron Radiation,* 12**,** 537-541.

Rehr, J. J. & Albers, R. C. 2000. Theoretical approaches to x-ray absorption fine structure. *Reviews of Modern Physics,* 72**,** 621-654.

Rosso, K. M., Rustad, J. R. & Bylaska, E. J. 2001. The Cs/K exchange in muscovite interlayers: An AB initio treatment. *Clays and Clay Minerals,* 49**,** 500-513.

Sawhney, B. L. 1965. Sorption of cesium from dilute solutions. *Soil Science Society of America Proceedings,* 29**,** 25-28.

Sawhney, B. L. 1966. Unusual Sorption on Caesium by Vermiculite. *Nature,* 211**,** 893-894.

Sawhney, B. L. 1967. Cesium Sorption in Relation to Lattice Spadcing and Cation Exchange Capacity of Biotite. *Soil Science Society of America Proceedings,* 31**,** 181-183.

Sawhney, B. L. 1972. Selective Sorption and Fixation of Cations by Clay-Minerals - Review. *Clays and Clay Minerals,* 20**,** 93-100.

Sparks, D. L. & Huang, P. M. 1985. Physical Chemisty of Soil Potassium. *In:* MUNSON, R. D. (ed.) *Potassium in Agriculture.* Madison: American Society of Agronomy.

Steefel, C. I., Carroll, S., Zhao, P. & Roberts, S. 2003. Cesium migration in Hanford sediment: a multisite cation exchange model based on laboratory transport experiments. *Journal of Contaminant Hydrology,* 67**,** 219-246.

Tamura, K., Kogure, T., Watanabe, Y., Nagai, C. & Yamada, H. 2014. Uptake of Cesium and Strontium Ions by Artificially Altered Phlogopite. *Environmental Science & Technology,* 48**,** 5808-5815.

Zachara, J. M., Smith, S. C., Liu, C. X., McKinley, J. P., Serne, R. J. & Gassman, P. L. 2002. Sorption of Cs+ to micaceous subsurface sediments from the Hanford site, USA. *Geochimica Et Cosmochimica Acta,* 66**,** 193-211.

# Chapter 7 – An EXAFS study of Sr sorption to illite, goethite and chlorite under hyper-alkaline conditions

This final data chapter presents an investigation of the sorption of Sr to illite, chlorite, iron oxide and a mixed sediment containing all three of these minerals. Sorption was investigated over a large pH range (9-14) using batch sorption experiments. Changes in sorption environment were then investigated using extended x-ray absorption fine structure spectroscopy (EXAFS).

## 7.1 Introduction

The widespread use of nuclear power over roughly the last 50 years has left a large volume of radioactive nuclear waste. This waste is present in many forms, both solid and liquid, and contains a wide range of both actinides (e.g. $^{238}U$, $^{240}Pu$) and fission products (e.g. $^{90}Sr$, $^{137}Cs$, $^{99}Tc$). This chapter focuses specifically on $^{90}Sr$ which is produced in high yield by nuclear fission and is present in large concentrations in nuclear waste. With a half-life of 29 years, $^{90}Sr$ is classified as a medium-lived radionuclide and decays via β-emission to $^{90}Y$, which is also a high energy beta emitter. Historic leaks and authorised discharge from nuclear facilities have released $^{90}Sr$ (and other radionuclides) into the geosphere. This poses a potential risk to the environment and to human health. Therefore it is essential to understand and be able to predict the behaviour of Sr in the surface environment.

Under normal environmental conditions $^{90}Sr$ is present as the aqueous $Sr^{2+}$ cation. The mobility of $Sr^{2+}$ in the environment is chiefly controlled by sorption to the charged surfaces of minerals. Sorption of $Sr^{2+}$ to common mineral phases in soils under moderate environmental conditions (low IS, pH 4-10) is well understood. Strontium primarily sorbs to those minerals with large surface area and cation exchange capacity, chiefly clays and iron oxides (Dyer et al., 2000, Balek et al., 1996, Carroll et al., 2008, Karasyova et al., 1999). Sorption is known to occur at circumneutral pH though charge compensating cation exchange with the $Sr^{2+}$ cation exchanging with other mono and divalent cations in outer-sphere surface complexes (Axe et al., 1998, Carroll et al., 2008, Chen and Hayes, 1999, Parkman et al., 1998, Chen et al., 2006, Sahai et al., 2000). This outer-sphere sorption occurs in competition with other mono and divalent cations and is therefore strongly controlled by the ionic strength of the solution phase (Torstenfelt et al., 1982, Bilgin et al., 2001). Sr sorption is significantly reduced in high ionic strength solutions as the other ions present (such as $Na^{+}$) out-compete $Sr^{2+}$ for the sorption sites (Khan et al., 1995).

Due to use of alkaline liquours in waste treatments (such as at Hanford and Sellafield) significant quantities of the Sr bearing wastes have a hyper-alkaline pH and a high ionic strength (SellafieldLtd, 2009, Ahearne, 1997). Additionally, the use of cementitious materials is widely proposed in geological disposal facilities (both for waste encapsulation and as a backfill) (Savage, 2011). The long term interaction of groundwater with cement is known to lead to the development of high pH, high ionic strength plumes,

rich in Ca. It is therefore also important to understand the sorption of Sr, and other alkali-earths, under these hyper-alkaline conditions. It is well established that the long term interaction of high pH liquors with silicate minerals leads to their dissolution and reprecipitation as neoformed zeolite phases and calcium-silicate-hydrates (Fernández et al., 2009, Tits et al., 2004, Zhao et al., 2004, Tits et al., 2006). Strontium readily incorporates into these phases, leading to its long-term immobilisation (Chorover et al., 2008, Choi et al., 2006). These transformation and incorporation reactions take long time periods under surface pressure and temperature conditions (Chorover et al., 2003). However, Wallace et al. (2013) observed that Sr sorption is also enhanced in high pH solutions over the short term, before these new phases can form. They proposed that Sr sorption at high pH was unaffected by cationic competition at high ionic strength due to formation of an inner-sphere surface complex. Collins et al. (1998) also observed the formation of a Sr-Fe inner-sphere complex on goethite at pH10.

This work aims to build on these discoveries and fully determine the sorption mechanism accounting for enhanced Sr sorption over the short term. Here the sorption of Sr to illite, goethtite and chlorite was investigated across a range of pH and ionic strength conditions. The experiments were run for 48 hours to allow sorption equilibration but to minimise any mineral alteration. The work aimed to determine by EXAFS analysis which minerals sorbed Sr into inner-sphere complexes and at which pH this sorption occurred. A mechanistic explanation of this complexation process and its implications for the behaviour of other alkali-earths is then offered.

## 7.2 Materials and methods

### 7.2.1 Materials preparation

A sample of illite IMT-1 was obtained from the Clay Minerals Society Source Clay Repository. A sample of chlorite was purchased from Ward's Natural Science Establishment. Goethite was synthesised in the lab following the method of Schwertmann and Cornell (2000). The purity of the minerals was confirmed by XRD. The sediment was collected in August 2009 from the Calder Valley, Cumbria. It's mineralogical composition was previously determined by Wallace et al. (2012) and Law et al. (2010) and is known to contain illite, chlorite and iron oxides. All materials were then crushed to <63µm (verified by sieving). To remove any carbonate present the samples were washed in 0.001 mol $L^{-1}$ HCl for two hours on a rotary shaking table in beakers open to the atmosphere (to allow evacuation of $CO_2$). Solid solution separation was achieved by centrifugation at 6,000*g* for 5 minutes. The supernatant was then discarded and the solids rinsed three times with deionised water (repeating the centrifugation procedure each time). Finally the samples were oven dried at 40°C until excess water had evaporated.

### 7.2.2 Batch sorption reactions

As Sr is known to readily precipitate as $SrCO_3$ at high pH great care was taken to exclude carbonate from the system. Solutions of degassed ($CO_2$ and $O_2$ free) NaCl and NaOH at concentrations ranging from $10^{-5}$ to 1 mol $L^{-1}$ were prepared in glass Schott bottles. For this deionsed water was degassed for 30 minutes $L^{-1}$ by bubbling with $N_2$ whilst constantly stirring at 90°C on a hot plate. Following the initial degassing period the relevant mass

of NaOH or NaCl was added to the deionised water while degassing continued. Additionally, 2.5 $x10^{-4}$ mol $L^{-1}$ of Ca (as $CaCl_2.2H_2O$) was added to all solutions to precipitate any carbonate which was not removed as $CO_2$ by the degassing procedure. The solutions were then degassed for another 30 minutes $L^{-1}$ before being transferred to a coy cabinet anaerobic chamber (with average $CO_2$ concentrations <40ppm). Both a 0.005 mol $L^{-1}$ and a 0.02 mol $L^{-1}$ solution of Sr (as $SrCl_2.6H_2O$) were also prepared by the same degassing procedure but Ca was not added.

All sample handling was then performed inside the anaerobic chamber. The minerals were suspended in NaOH and NaCl at a solid solution ratio of 0.8 g 35 $ml^{-1}$ in 40 mL oak ridge centrifuge tubes. Solutions were filtered through a 0.45 µm filter before addition to the solids. This was to ensure removal of any $CaCO_3$ which may have precipitated during the solution preparation. The samples were then spiked with a hundred fold dilution of the 0.005 mol $L^{-1}$ $SrCl_2.6H_2O$ solution (0.35 mL) to yield 3.9 $x10^{-4}$ mol $L^{-1}$ in the following samples: Illite, all NaCl samples; chlorite all NaCl samples, $10^{-3}$ mol $L^{-1}$ NaOH and $10^{-5}$ mol $L^{-1}$ NaOH; goethite, all NaCl samples and $10^{-5}$ mol $L^{-1}$ NaOH; sediment $10^{-5}$ mol $L^{-1}$ NaOH and $10^{-1}$ mol $L^{-1}$ NaOH. All other samples contained a hundred fold dilution of the 0.02 mol $L^{-1}$ $SrCl_2.6H_2O$ solution to yield 1.1 $x10^{-3}$ mol $L^{-1}$ of Sr in solution. Samples were then sealed and equilibrated for 48 hours on a rotary shaker. During equilibration samples remained in the $CO_2$ free atmosphere to prevent any carbonate formation. Following the equilibration period the samples were transferred

unopened from the chamber to a -80°C freezer and frozen to suspend the sorption reaction.

### 7.2.3 EXAFS spectra collection

The Frozen samples were transported to the synchrotron in a $N_2$ purged air tight Kilner jar to minimise any $CO_2$ ingress and with ice packs to prevent defrosting. During the beam time all samples were stored in a freezer and defrosted as needed prior to sample preparation.

Before mounting the samples the tubes were defrosted, centrifuged and the supernatant was decanted. Supernatant pH was determined using a glass bulb electrode calibrated to pH 7 and 10 and 12 with standard calibration solutions. The solutions were then refrozen to minimise $CO_2$ ingress prior to analysis. The wet paste was then mounted in a Perspex sample holder and sealed with Kapton tape windows. The sample was then immediately frozen by immersion in liquid nitrogen. To minimise exposure to atmospheric $CO_2$ during mounting the material was kept under a constant flow of $N_2$ until it was frozen.

The Sr EXAFS data presented here were gathered from three distinct beamline sessions. Spectral data for the chlorite samples with $10^{-5}$, $10^{-2}$ and $10^{-1}$ mol $L^{-1}$ NaOH and the Sediment exposed to $10^{-1}$ mol $L^{-1}$ NaOH were gathered at beamline B18 at the Diamond Light Source. Here the incident beam has a typical operating voltage of 3GeV and a current of 300 mA. The x-rays at B18 are generated from a bending magnet source. The beam is

vertically collimated by a Si mirror before passing through a double crystal Si monochromator. It was then focused onto the sample to give a spot size of 200 x 250 µm. The Sr K edge (16105 keV) EXAFS spectra were gathered from fluorescence x-rays using a 9 element Ge solid state detector. The sample was held at 80 K in a liquid nitrogen cryostat during data collection to improve the signal to noise ratio. The EXAFS data for samples of chlorite, goethite, sediment and illite in a 1 mol $L^{-1}$ NaOH background and the chlorite sample in $10^{-5}$ mol $L^{-1}$ NaOH were gathered at the Dutch Belgian Beamline (DUBBLE) at the European Synchrotron Radiation Facility (ESRF). This has an incident beam voltage of 6.04 GeV and a current of 200 mA. DUBBLE uses a bending magnet source which is vertically collimated by a Si mirror. The correct beam energy is then selected using a double crystal Si monochromator. The final incident beam has a spot size of 400 x 350 µm. Again at the ESRF a 9 element Ge detector was used to gather Sr K-edge fluorescence spectra. Data collection was also performed at 80K in a liquid nitrogen cooled cryostat. Finally Sr K-edge EXAFS data from samples of Illite in $10^{-3}$ and $10^{-1}$ mol L NaOH and Goethite in $10^{-5}$, $10^{-3}$ and $10^{-1}$ mol L NaOH were gathered at beamline I20 at the Diamond light source. Here the x-ray source is derived from a wiggler insertion device. The energy of the collimated beam is then selected by a unique 4 crystal monochromator which yields beam with very high energy stability. The monochromated beam is then focused to give a final spot size of 400 x 350 µm. Sr K-edge fluorescence spectra were gathered using a 64 element solid state Ge detector and samples were held in a liquid nitrogen cryostat at 80 K.

### 7.2.4 EXAFS data analysis and fitting

Multiple XAS scans from each sample were summed and averaged using Athena v 0.8.056 (Ravel and Newville, 2005) to maximise the signal/noise ratio. The background subtraction of the Sr EXAFS was then performed using PySpline v1.1 (Tenderholt et al., 2007). The EXAFS spectra were then fitted in k-space using DLexcurv v1.0 (Tomic et al., 2005) following full curved wave theory (Gunman et al., 1984). *Ab initio* calculations of the phaseshifts were performed using the Hedin-Lundqvist potentials and assuming the von-Barth ground states for all atoms (Binsted, 1998). Shell-by-shell fitting was then performed by estimating initial parameters for shells of backscattering atoms and then interactively refining these parameters. Specifically fits were determined by refining number of atoms (± 25%), interatomic distances (± 0.02 Å in the first shell and ± 0.05 Å in subsequent shells), Fermi energy and Debye-Waller factor ($2\sigma^2$, ± 25%). This procedure was performed initially with a single shell and subsequent shells of surrounding atoms were then added. Additional shells were then accepted where they improved the overall fit quality by greater than 5% (determined by reduction of the least squared residual, R-factor).

### 7.2.5 ICP-OES

The concentration of Sr sorbed to the solid phase was determined as initial $[Sr]_{aq}$ – final $[Sr]_{aq}$. The final concentration of Sr in solution after the 48 hr sorption period was determined by ICP-OES. The frozen solutions were defrosted in the anaerobic chamber and diluted into 10% $HNO_3$ to acidify them. Dilution was necessary due to the high ionic strength of the background Na electrolyte. The concentration of Sr in the diluted solutions

was then measured and the final aqueous concentration in the sample calculated.

### 7.2.6 Solution speciation modelling

Speciation of the alkali earth ions as a function of pH was modelled using PHREEQC (Parkhurst and Appelo, 1999). In all cases a simple model was used with 45 ppm of the relevant element (Ca, Sr, Ba, Ra) at a pH range of 9-14. No other solid or solution phases were included. The activity of the different species was then determined using the Debye-Hückel equation. For Ca, Sr and Ba the modelling was performed using the PHREEQC thermodynamic database. However no thermodynamic data for Ra is provided in this database so Ra modelling was performed using the HATCHES18 database (Bond et al., 1997).

## 7.3 Results

### 7.3.1 Solution

Figure 7.1 shows the total sorption of Sr onto the 4 minerals (a, illite; b, chlorite; c, goethite; d, sediment) after equilibration for 48 hours. In all cases the square data points show sorption of Sr from a background of NaCl and triangles show sorption of Sr from a background of NaOH. Data is presented in terms of percentage sorption with increasing ionic strength. The average pH of the NaCl system (with all minerals) was pH 9.1 ± 0.2. The pH varied greatly with changing NaOH concentration; in this case the pH of each datum point is annotated on the figure. In all mineral systems increasing

ionic strength of NaCl caused a decrease in % sorption of strontium onto the surface. However, the results for sorption in the NaOH system are very different. Here there was no trend towards decreasing Sr sorption with increasing ionic strength.

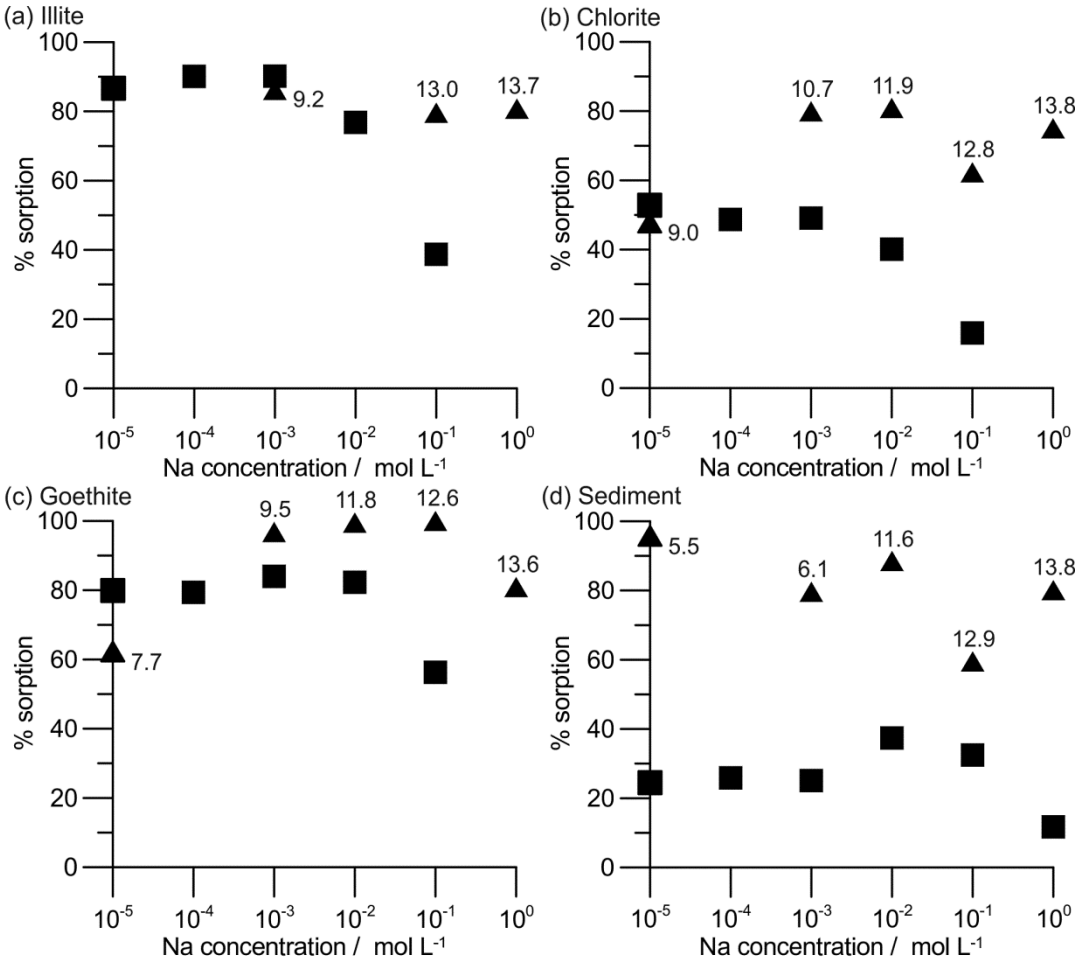


**Figure 7.1** Sorption of Sr to (a) Illite (b) chlorite (c) goethite and (d) sediment as a function of Na concentration in a background of NaCl (squares) and NaOH (triangles).

#### 7.3.1.1 Illite

In the illite system (Figure 7.1 a) near total sorption of the Sr is seen in both the NaCl and NaOH system up to a total ionic strength of $10^{-3}$ mol $L^{-1}$.

However above this the effect of pH on Sr sorption is clear. In the NaCl system the pH remained constant around 9.3 (±0.07). Here the increasing ionic strength caused a large reduction in total Sr sorption from 90% at $10^{-3}$ mol $L^{-1}$ to 77% at $10^{-2}$ mol $L^{-1}$ and 39% at $10^{-1}$ mol $L^{-1}$ NaCl. Comparatively in the NaOH system the pH greatly increased with increasing NaOH concentration and the sorption of Sr remained high. Specifically, 80% of the Sr sorbed to the sediment at $10^{-1}$ mol $L^{-1}$ NaOH (pH 13). This is much more (40%) than in the NaCl background at the same overall ionic strength. Even in the 1 mol $L^{-1}$ NaOH system 80% of the Sr was sorbed to the illite.

#### 7.3.1.2 Chlorite

The chlorite system showed more complex sorption behaviour (Figure 7.1 b). Here significantly more Sr was sorbed to the sediment in the NaOH system than in the NaCl system above an ionic strength of $10^{-4}$ mol $L^{-1}$. In the NaCl system the Sr sorption was reduced to 40% at $10^{-2}$ mol $L^{-1}$ and to 15% at $10^{-1}$ mol $L^{-1}$ NaCl. The pH in the NaCl system was constant at 9.1 ± 0.07. Comparatively in the NaOH system the pH increased greatly with increasing ionic strength, and Sr sorption remained high. At $10^{-3}$ mol $L^{-1}$ NaOH (pH 10.7) around 80% of the Sr was sorbed to the sediment compared to 50% at $10^{-5}$ mol $L^{-1}$ NaOH (pH 9.0). This high Sr sorption was apparent even at $10^{-1}$ mol $L^{-1}$ (pH 12.8) NaOH where 62% of the Sr was sorbed. This is much greater than the Sr sorption from the same ionic strength solution at pH 9.2. The sorption of Sr at 1 mol $L^{-1}$ NaOH (pH 13.7) was even greater than at $10^{-1}$ mol $L^{-1}$, namely 75%.

#### 7.3.1.3 Goethite

In the goethite system (Figure 7.1 c) around 80% of the Sr was sorbed from the NaCl at system up to and including $10^{-2}$ mol $L^{-1}$. The sorption of Sr decreased to 56% in a $10^{-1}$ mol $L^{-1}$ NaCl background. The average pH of the goethite NaCl system was 9.0 ± 0.32 across the concentration range. Comparatively the pH of the NaOH system greatly increased with increasing concentration. Here the sorbed percentage of Sr sorbed to the sediment remained constant at 98.8 ± 1.7 % between $10^{-3}$ mol $L^{-1}$ (pH 9.5) and $10^{-1}$ mol $L^{-1}$ NaOH (pH 12.6). This was much greater than in the comparative concentration of NaCl at pH 9. The total sorption of Sr decreased slightly at 1 mol $L^{-1}$ NaOH (pH 13.6) to 81%.

#### 7.3.1.4 Sediment

The sediment system showed a significant pH buffering effect. Here it was found that all solutions with < $10^{-3}$ mol $L^{-1}$ of NaOH buffered down to below pH 6.0. Wallace et al. (2012) found that below pH 6.0 Sr sorption to the sediment was rapidly reduced. Therefore any reported sorption data from below this pH sorption edge is likely to be affected by pH as well as ionic strength. The Sr sorption data to the sediment reported in Figure 7.1 d was collected at pH 4.8 ± 0.27. Here the maximum Sr sorption percentage was 26% at $10^{-4}$ mol $L^{-1}$ NaCl. This reduced concentration is likely due to the low pH rather than ionic strength. However the effect of ionic strength was still evident with total Sr sorption reducing to 12% at $10^{-1}$ mol $L^{-1}$ NaCl. Sorption the NaOH system was much greater and was unaffected by solution ionic strength. Here again the pH of the system greatly increased as the concentration of NaOH increased. At $10^{-3}$ mol $L^{-1}$ NaOH (pH 6.1) 80% of the

Sr was sorbed to the sediment. This increased to 89% at $10^{-2}$ mol $L^{-1}$ NaOH (pH 11.6) but decreased to 60% at $10^{-1}$ mol $L^{-1}$ NaOH. The total Sr sorption however then increased back to 80% at 1 mol $L^{-1}$ NaOH (pH 13.8).

## 7.3.2 EXAFS

### 7.3.2.1 Illite

EXAFS spectra were gathered for the illite system from samples exposed to a NaOH background at $10^{-5}$ mol $L^{-1}$ (pH 8.9), $10^{-3}$ mol $L^{-1}$ (pH 9.2), $10^{-1}$ mol L (pH 13) and 1 mol $L^{-1}$ (pH 13.7). The resulting spectra and their Fourier transforms are shown in Figure 7.2, where the dotted line represents the best shell by shell fit. The fit parameters are then shown in Table 7.1. The spectrum collected from the sample equilibrated in $10^{-5}$ mol $L^{-1}$ NaOH (pH 8.9) was best fit by a single oxygen shell at 2.6 Å (Figure 7.2 a). Again the spectrum from the $10^{-3}$ mol $L^{-1}$ NaOH background (pH 9.2) sample was best fit with a single O shell at 2.6 Å (Figure 7.2 b). The $10^{-1}$ mol L NaOH background (pH 13) sample was also best fit with a single O shell, again at 2.6 Å (Figure 7.2 c). In this case an attempt was made to fit a Si/Al shell at 3.4 Å; however this yielded no significant improvement in the fit (Table 7.1) and was therefore rejected. Note that it is not possible to differentiate between Si and Al backscatters in EXAFS. As both are present in the structure at this distance the shell is referred to as having either atom present (though Si was included in excurv in all cases). Finally we performed shell by shell fitting for the 1 mol $L^{-1}$ NaOH background system (pH 13.7). In this case a best fit was given by an O shell at 2.7 Å a Si/Al shell at 3.4 Å and a K shell at 5.0 Å (Figure 7.2 d). In this case only one acceptable

crystallographic site was known which satisfied these bond lengths, that is the illite interlayer. Therefore the number of atoms in each shell was fixed (based on the crystallographic structure of the interlayer) and the shell filling improved be refinement of the Debye-Waller factor alone (Table 7.1).

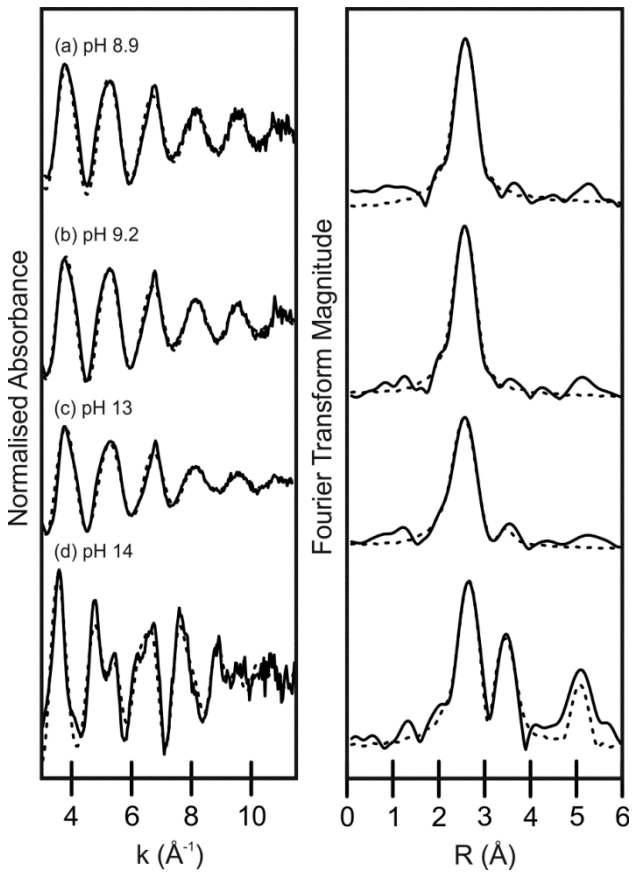


**Figure 7.2** Sr k-space EXAFS and accompanying Fourier transform of Sr sorbed to ilite at (a) pH 8.9, (b) pH 9.2 (c) pH 13.0 and (d) pH 14.0. Solid lines are background subtracted data and dashed lines are refined model fits.

**Table 7.1** EXAFS fitting parameters for Sr sorbed to illite under different pH conditions. n, shell occupancy (± 25 %); r, interatomic distance (± 0.02 Å for first shell and ± 0.05 Å for subsequent shells); $2\sigma^2$, Debye-Waller factor (± 25 %); R, least squared residual. Final accepted (and plotted) fits are marked with an asterisk (*).

| Sample | Shell | n | r (Å) | $2\sigma^2$ (Å$^2$) | R |
|---|---|---|---|---|---|
| **Illite pH 8.9*** | O | 9 | 2.61 | 0.021 | 25.6 |
| **Illite pH 8.9** | O | 8.6 | 2.611 | 0.02 | 24.95 |
| | Si | 0.7 | 3.391 | 0.031 | |
| **Illite pH 9.2*** | O | 9.2 | 2.609 | 0.022 | 19.25 |
| **Illite pH 9.2** | O | 8.9 | 2.61 | 0.022 | 18.9 |
| | Si | 0.6 | 3.34 | 0.041 | |
| **Illite pH13** | O | 9 | 2.604 | 0.03 | 24.63 |
| **IllitepH13*** | O | 8.4 | 2.607 | 0.027 | 22.39 |
| | Si | 1 | 3.331 | 0.024 | |
| **Illite pH 14** | O | 12 | 2.697 | 0.024 | 58.61 |
| **Illite pH 14** | O | 12 | 2.716 | 0.023 | 49.25 |
| | Si | 12 | 3.388 | 0.035 | |
| **Illite pH 14*** | O | 12 | 2.725 | 0.023 | 38.61 |
| | Si | 12 | 3.396 | 0.033 | |
| | K | 6 | 5.038 | 0.014 | |

### 7.3.2.2 Chlorite

Sr K-edge EXAFS spectra were gathered from the chlorite system at 4 different concentrations of NaOH. Specifically these were $10^{-5}$ mol $L^{-1}$ (pH 9.0), $10^{-3}$ mol $L^{-1}$ (pH 10.7), $10^{-1}$ mol $L^{-1}$ (pH 12.9) and 1 mol $L^{-1}$ (pH13.8) NaOH background. Figure 7.3 shows the background subtracted $k^3$ weight EXAFS and their accompanying Fourier Transforms. Here the solid lines represent the recorded data and the dotted lines are the best fits discovered from shell by shell fitting. The accompanying fit parameters for the chlorite system are shown in Table 7.2. The EXAFS spectrum for Sr sorbed to chlorite from the $10^{-5}$ mol $L^{-1}$ NaOH system (pH 9.0) was best fitted with a single oxygen shell at 2.6 Å (Figure 7.3 a). Again in the $10^{-3}$ mol $L^{-1}$ NaOH

background the Sr EXAFS spectrum was best fitted with a single oxygen shell at 2.6 Å (Figure 7.3 b). For the $10^{-1}$ mol $L^{-1}$ NaOH background system (pH 12.9) a single oxygen shell failed to provide the best fit to the recorded spectrum (see Table 7.2). The fit was significantly improved by adding an additional Si/Al shell at 3.8 Å and this is shown in Figure 7.3 d. Finally in the 1 mol $L^{-1}$ (pH13.8) NaOH background the spectrum was fit with the same 2 shell model as the pH 12.9 sample. In this case the addition of a Si/Al shell at 3.8 Å gave minimal improvement in the overall quality of the fit (Table 7.2). However, there was a trend within the sample for increasing shell number with increasing pH. This correlates with the formation of an inner sphere complex and selective sorption at high pH (see Figure 7.1 b). Therefore it is consistent with other results from the chlorite system for Sr to fit with two shells at this pH.

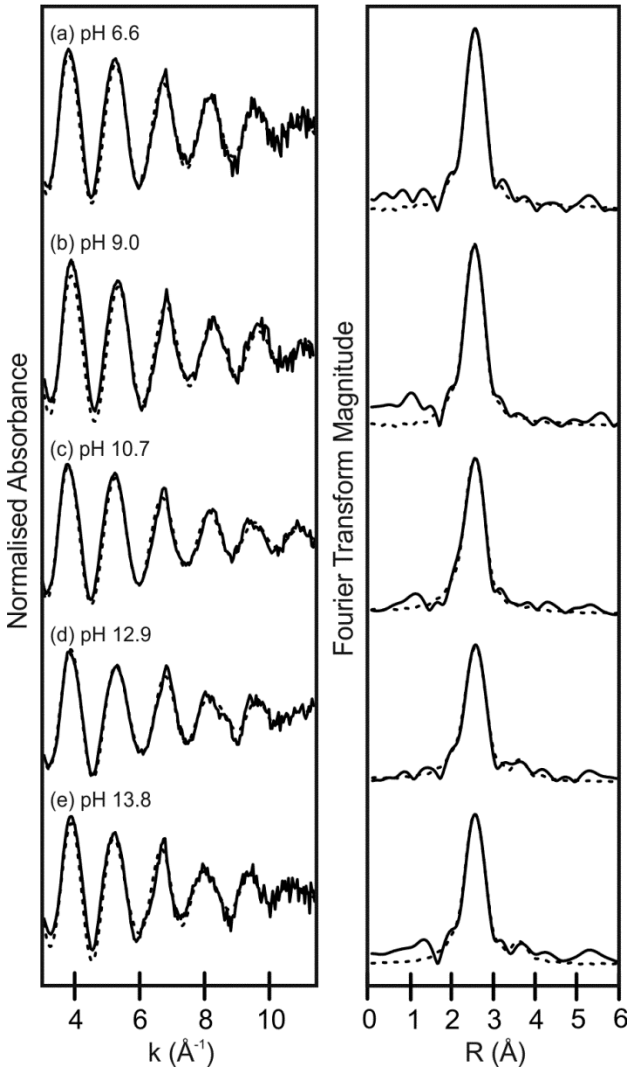


**Figure 7.3** Sr k-space EXAFS and accompanying Fourier transform of Sr sorbed to chlorite at (a) pH 6.6, (b) pH 9.0, (c) pH 10.7, (d) pH 12.9 and (e) pH 13.8. Solid lines are background subtracted data and dashed lines are refined model fits.

**Table 7.2** EXAFS fitting parameters for Sr sorbed to chlorite under different pH conditions. n, shell occupancy (± 25 %); r, interatomic distance (± 0.02 Å for first shell and ± 0.05 Å for subsequent shells); 2σ2, Debye-Waller factor (± 25 %); R, least squared residual. Final accepted (and plotted) fits are marked with an asterisk (*).

| Sample | Shell | n | r (Å) | $2\sigma^2$ (Å$^2$) | R |
|---|---|---|---|---|---|
| **Chlorite pH 6.6** | O | 9.1 | 2.602 | 0.018 | 22.35 |
| **Chlorite pH9** | O | 9 | 2.591 | 0.019 | 27.41 |
| **Chlorite pH10.7** | O | 9.2 | 2.607 | 0.022 | 15.56 |
| **ChloritepH12.9** | O | 8.7 | 2.599 | 0.025 | 20.74 |
| **ChloritepH12.9*** | O | 8.4 | 2.604 | 0.024 | 15.3 |
| | Si | 1.2 | 3.783 | 0.012 | |
| **ChloritepH13.8** | O | 8.8 | 2.626 | 0.021 | 30.86 |
| **ChloritepH13.8*** | O | 9.1 | 2.624 | 0.022 | 30.03 |
| | Si | 2 | 3.805 | 0.021 | |

### 7.3.2.3 Goethite

For goethite, as with the previous minerals representative samples were selected from the NaOH system and Sr EXAFS spectra collected to determine the bonding environment. Figure 7.4 shows the Sr EXAFS spectra and the Fourier transforms with their associated fits for the goethite system. The fit parameters for the shell by shell fits are shown in Table 7.3. Figure 7.4 a shows the spectra obtained for Sr sorption to goethite in a background of $10^{-5}$ mol $L^{-1}$ (pH 7.7). Here the best modelled fit was obtained with a single O shell at 2.6 Å. The spectrum for Sr sorption to goethite in $10^{-1}$ mol $L^{-1}$ NaOH is shown in Figure 7.4 b. In this case an O shell at 2.6 Å and a Fe shell at 3.6Å provided the simplest best fit to the spectra (Figure 7.4 b). Evidence from the Fourier transform supports a second Fe shell at 4.5 Å however the addition of the backscatterer did not significantly improve the overall fit validity (Table 7.3). Finally for the $10^{-1}$ NaOH background (pH 14)

the best fit was given by an O shell at 2.6 Å and single Fe shell at 3.6 Å (Figure 7.4 c). There was no evidence of a second Fe shell.

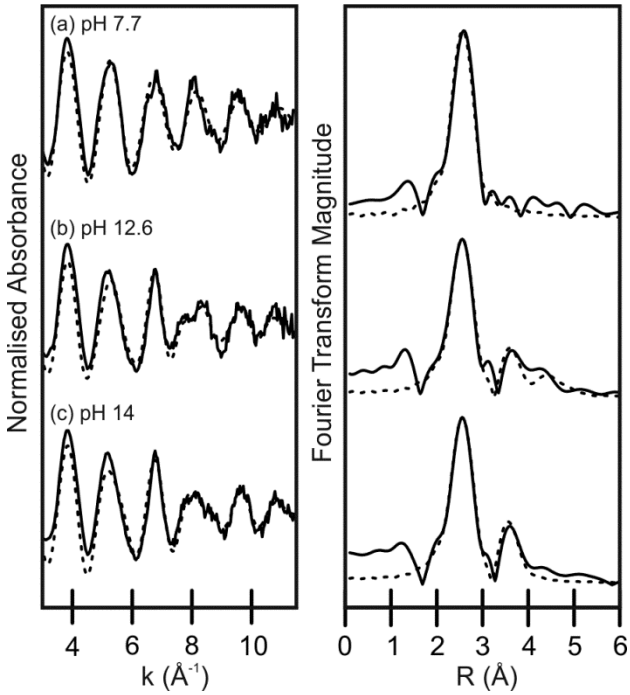


**Figure 7.4** Sr k-space EXAFS and accompanying Fourier transform of Sr sorbed to goethite at (a) pH 7.7, (b) pH 12.6 and (c) pH 14.0. Solid lines are background subtracted data and dashed lines are refined model fits.

**Table 7.3** EXAFS fitting parameters for Sr sorbed to goethite under different pH conditions. n, shell occupancy (± 25 %); r, interatomic distance (± 0.02 Å for first shell and ± 0.05 Å for subsequent shells); 2σ2, Debye-Waller factor (± 25 %); R, least squared residual. Final accepted (and plotted) fits are marked with an asterisk (*).

| Sample | Shell | n | r (Å) | $2\sigma^2$ ($Å^2$) | R |
|---|---|---|---|---|---|
| **Goethite pH7.7*** | O | 9 | 2.602 | 0.019 | 32.57 |
| **Goethite pH12.6** | O | 8.9 | 2.596 | 0.027 | 48.74 |
| **GoethitepH12.6** | O | 9 | 2.601 | 0.024 | 42.91 |
| | Fe | 3.2 | 3.596 | 0.028 | |
| **GoethitepH12.6*** | O | 8.1 | 2.599 | 0.021 | 38.68 |
| | Fe | 2.9 | 3.598 | 0.027 | |
| | Fe | 3.3 | 4.479 | 0.029 | |
| **Goethite pH 13.8*** | O | 8.6 | 2.602 | 0.021 | 38.32 |
| | Fe | 3.5 | 3.563 | 0.027 | |

### 7.3.2.4 Sediment

Finally, Sr K edge EXAFS were gathered for the $10^{-1}$ (pH 13) and 1 mol $L^{-1}$ (pH 13.8) sediment samples. The EXAFS spectra and associated Fourier transforms are shown in Figure 7.5. In both cases both a single and double shell fit was tried. For the $10^{-1}$ mol $L^{-1}$ sample a single oxygen shell was fitted at 2.6 Å with a resulting Debye-Waller factor of 0.031. In this sample the addition of a Si/Al shell at 3.8 Å significantly improved the overall fit quality; it is this final 2 shell fit which is displayed in Figure 7.5 a. The fit parameters for both the one shell and two shell fit are shown in Table 7.4. Again in the case of the 1 mol $L^{-1}$ sediment sample (Figure 7.5 b) the best fit was obtained with two shells. An oxygen shell was fitted at 2.6 Å and a Si/Al shell, again at 3.8 Å. Again in this case the addition of a Si/Al shell significantly improved the overall fit (Table 7.4).

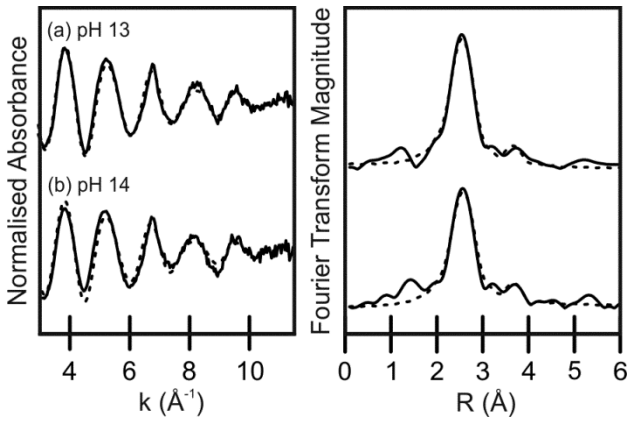


**Figure 7.5** Sr k-space EXAFS and accompanying Fourier transform of Sr sorbed to a mixed phase sediment at (a) pH 13.0 and (b) pH 14.0. Solid lines are background subtracted data and dashed lines are refined model fits.

**Table 7.4** EXAFS fitting parameters for Sr sorbed to the mixed phase sediment under different pH conditions. n, shell occupancy (± 25 %); r, interatomic distance (± 0.02 Å for first shell and ± 0.05 Å for subsequent shells); 2σ2, Debye-Waller factor (± 25 %); R, least squared residual. Final accepted (and plotted) fits are marked with an asterisk (*).

| Sample | Shell | n | r (Å) | $2\sigma^2$ (Å$^2$) | R |
|---|---|---|---|---|---|
| **Sediment pH13** | O | 9.1 | 2.603 | 0.031 | 21.84 |
| **Sediment pH13*** | O | 8 | 2.599 | 0.026 | 16.42 |
| | Si | 1.4 | 3.81 | 0.016 | |
| **Sediment pH14** | O | 8.1 | 2.616 | 0.029 | 34.18 |
| **Sediment pH14*** | O | 7.5 | 2.613 | 0.026 | 32.96 |
| | Si | 1.4 | 3.816 | 0.017 | |

## 7.4 Discussion

### 7.4.1 Effect of pH on Sr sorption

The solution sorption data (Figure 7.1) indicates that in a NaCl solution at a slightly alkaline pH Sr sorbs through classical cation exchange. In this system both the Na and Sr ions are competing for the same charged surface sites on all the minerals. The sorption is non selective and controlled only by equilibrium reactions of both ions between the surface and solution. Therefore when the ionic strength of Na in solution increases the equilibrium reaction is shifted to increase Na sorption to the mineral surface. Therefore Na out-competes Sr and the total Sr surface concentration decreases (resulting in a decrease in % sorption). However in the NaOH system the increasing concentration of Na is accompanied by an increase in the solution pH. Here, as the Na concentration increases it does not compete with Sr and the Sr sorption remains as high as in the low ionic strength experiments. This phenomenon was observed in all the mineral systems indicating that it is likely to be caused by the chemistry of the solution, rather than any nature of the sorption site.

### 7.4.2 EXAFS analysis of Sr sorption environment

The specific sorption of Sr onto the minerals at high pH suggests there was a change in the sorption mechanism and that Sr was no longer sorbing via classical cation exchange in competition with Na. To investigate this, EXAFS spectra were collected for Sr across the pH range and onto each of the 3 minerals (and the mixed sediment). The measured EXAFS spectra and Fourier transforms for the 4 minerals systems are shown in Figures 7.2 – 7.5

and the EXAFS fit parameters in Tables 7.1 – 7.4. The first thing that is apparent from the fits is that below pH 12.5-13 the Sr is sorbing to all the minerals with a single oxygen shell. This is identical to the solution species (Sahai et al., 2000, O'Day et al., 2000) and indicative of the formation an outer-sphere surface complex, via classical cation exchange. Strontium held in these outer-sphere complexes is in thermodynamic equilibrium with the solution and any competing ions in solution. This therefore explains why increasing ionic strength (in the NaCl system) at this moderate pH led to a reduction in strontium sorption. This process of outer-sphere sorption has been widely observed and discussed by other authors and is thought to account for Sr mobility in the environment (Axe et al., 1998, Carroll et al., 2008, Parkman et al., 1998)

The novelty of this work becomes apparent in those EXAFS spectra obtained from Sr sorbed at extremely high pH and ionic strength. Here the sorption mechanism for Sr changes from showing a single oxygen shell to multiple coordination shells. These multiple shells are indicative of the formation of an inner-sphere complex (Tits et al., 2006, Collins et al., 1998). This change in sorption mechanism was seen in all three of the mineral systems, however the nature of the surface site was noticeably different.

#### 7.4.2.1 Illite

Firstly, Sr showed two distinct inner-sphere sorption environments on illite at pH 13 (Figure 7.2 c) and pH 14 (Figure 7.2 d). Specifically at pH 13 the best fit for the EXAFS was obtained with both an oxygen shell at 2.6 Å and Si (Al)

shell at 3.3 Å. Although, the improvement in fit by adding a second shell was quite small (~9%) compared to the one shell model (Table 7.1). The percentage sorption in the pH 13 NaOH experiment is greater (~80% versus ~40%) than the NaCl experiment (pH 9) at the same ionic strength (Figure 7.1 a). Therefore including the possibility of inner sphere sorption must be considered even though the EXAFS evidence for an inner sphere coordination environment is weak. This is consistent with the inner-sphere surface complex observed by Wallace et al. (2013) for Sr adsorption to a mixed sediment from a KOH dominated high pH solution. Therefore it is proposed that the high pH of this system has altered the sorption mechanism of Sr. Rather than sorbing via cation exchange, it has become specifically sorbed to the surface.

At pH 14 the EXAFS data shows that strontium is sorbed to illite via a different incorporation mechanism. The EXAFS spectrum collected from this sample (Figure 7.2 d) was best fitted by three coordination shells, specifically a shell of 12 oxygen at 2.7 Å, a Si/Al shell at 3.4 Å and an additional K shell at 5.0 Å. Based on the crystallographic structure of illite the only place where strontium could be held in this coordination environment is within the illite interlayer. Therefore, in this system Sr is becoming incorporated into the interlayer structure of the illite mineral. This mechanism has been previously observed for monovalent alkali ions (such as K and Cs) (Chorover et al., 2008, Dyer et al., 2000, Poinssot et al., 1999, Bostick et al., 2002) but was not previously known to occur for divalent alkaline-earths. It has previously been thought that the large hydration energy of the alkaline

earths (such as $Sr^{2+}$ and $Ca^{2+}$) meant they would only enter into the interlayer while remaining hydrated in outer-sphere complexes (as was seen at pH 9; Figure 7.2 a) (Jackson and During, 1979, Jackson, 1968, Sparks and Huang, 1985). However this new result indicates that at high pH Sr can shed its hydration shell and become incorporated into the illite interlayer.

#### 7.4.2.2 Chlorite

The EXAFS spectra indicated that Sr sorption to chlorite showed a very similar trend to illite. This is understandable as they are both aluminosilicate clay minerals. Again at pH 12.9 (Figure 7.3 d) the inclusion of a Si/Al shell at 3.7 Å significantly improved the model fit (Table 7.2). This coordination environment was best described by the same inner-sphere surface complex. This same 2 shell fit also proved the best fit for Sr sorbed to Chlorite at pH 13.8 (Figure 7.3 e). This difference from the illite system is due to the mineralogical variation between illite and chlorite. Chlorite does not have an ion filled interlayer, but instead has its 2:1 layers separated by a brucite-like layer (Weaver and Pollard, 1973, Grim, 1968). Therefore the interlayer incorporation of Sr seen in illite at pH 14 was not possible as these sorption sites are not present on chlorite. Therefore the Sr was likely sorbing via inner-sphere surface complexation onto the basal surface. This ion-specific incorporation again explains why the Sr sorption percentage was so high, even in a high ionic strength background solution.

#### 7.4.2.3 Goethite

The goethite system showed a change in the sorption coordination environment at both pH 12.6 and 14 (Figure 7.4 c and d). At pH 12.6 the Sr is coordinated by a double Fe shell (at 2.9 Å and 3.3 Å) indicative of an inner-sphere complex. This is not present at pH 7.7 where Sr is present in an outer-sphere complex. At pH 14 the Sr again appears to be coordinated in an inner-sphere complex but with a single close Fe shell (at 3.6 Å). This suggests that the Sr is forming an alternative inner-sphere complex at a different reactive site on the goethite surface to that formed at pH 12.6. This inner-sphere surface complexation on goethite was previously observed by Collins et al. (1998) at pH 10.2 but fitted by a single Fe shell at 4.3 Å. Therefore, it appears that the Sr atom migrates into a closer complex as the pH of the background solution increases.

#### 7.4.2.4 Sediment

Finally the coordination environment of Sr onto sediment at hyper-alkaline pH was tested as a real world analogue. The sediment investigated was the same as that used by Wallace et al. (2013) and is analogous to that underlying the UK Sellafield site. Although the sediment is known to contain all the minerals investigated here (Wallace et al., 2012, Law et al., 2010, Thorpe et al., 2012), chlorite dominates the reactive surface area (Wallace et al., 2013). The EXAFS spectra for the pH 13 and 14 samples (Figure 7.5) shows that in both cases Sr was held in an inner-sphere surface complex coordinated by a O shell at 2.6 Å and a Si/Al shell at 3.8 Å. This most closely matches the bonding environment found for Sr on the surface of chlorite and

therefore suggests that chlorite is the dominant phase controlling Sr sorption in these sediments (at hyper alkaline pH).

### 7.4.3 Sorption mechanism

It has already been shown from the illite EXAFS that at hyper-alkaline pH Sr appears to behave as a monovalent rather than a divalent cation. Strontium is known to exist in the aqueous phase as two species. The divalent $Sr^{2+}$ ion is dominant under most pH conditions. However, at hyper alkaline pH Sr is known to form the monovalent $SrOH^{+}$ species in solution (Takeno, 2005). The presence of $SrOH^{+}$ as the dominant species in solution could offer a mechanistic explanation for the formation of inner-sphere surface complexes in these hyper-alkaline systems. Additionally, if the other alkali-earth ions show the same solution speciation behaviour it is possible that they would also sorb via the same mechanism as Sr.

To test this hypothesis PHREEQC was used to model the speciation of 4 important alkaline earth ions, namely Ca, Sr, Ba and Ra. Sr was chosen as it is investigated in this study. The decision was taken to also investigate Ca, Ba and Ra as these are important elements that are relevant to the disposal of nuclear wastes (Ca is the dominant ion in many types of cement leachate; Ra is an important long lived radionuclide and Ba is often used as an analogue for Ra) (De Windt et al., 2004, Fernández et al., 2009). The modelling results (Figure 7.6) showed that Ca, Sr and Ba all formed a hydroxide species within the pH range investigated, but that Ra was only present as $Ra^{2+}$. However the pH at which the hydroxyl species became

dominant varied between the different elements. Strontium began to speciate as $SrOH^+$ above pH 11.5 and became the dominant solution species above pH 13.7 (Figure 7.6 b). The EXAFS investigations showed that the inner-sphere complexes did not form at pH's below 11 (e.g. Figure 7.2 c) but were readily apparent above 12.5. This strongly suggests that the speciation of Sr from a 2+ to a 1+ cation allows it to form inner-sphere surface complexes. All of the tested minerals have hydroxyl groups present on their surfaces. Therefore we would propose that at elevated pH the Sr is likely sorbing into inner sphere complexes via ligand exchange of its aqueous OH group for the $OH^-$ present on the surface of the minerals. Interestingly we also noted that the $SrOH^+$ is only incorporated into illite when it is the dominant solution species. It has been widely reported that $Cs^+$ and other monovalent alkali cations are selectively incorporated into inner-sphere complexes in the illite interlayer (Bostick et al., 2002, Sawhney, 1972, Eberl, 1980). Cs is known to be selectively retained in this interlayer site (see chapter 5 and appendix A). Therefore it would be valuable to investigate whether, once incorporated, Sr was also retained in the illite interlayer across a range of pH and IS conditions.

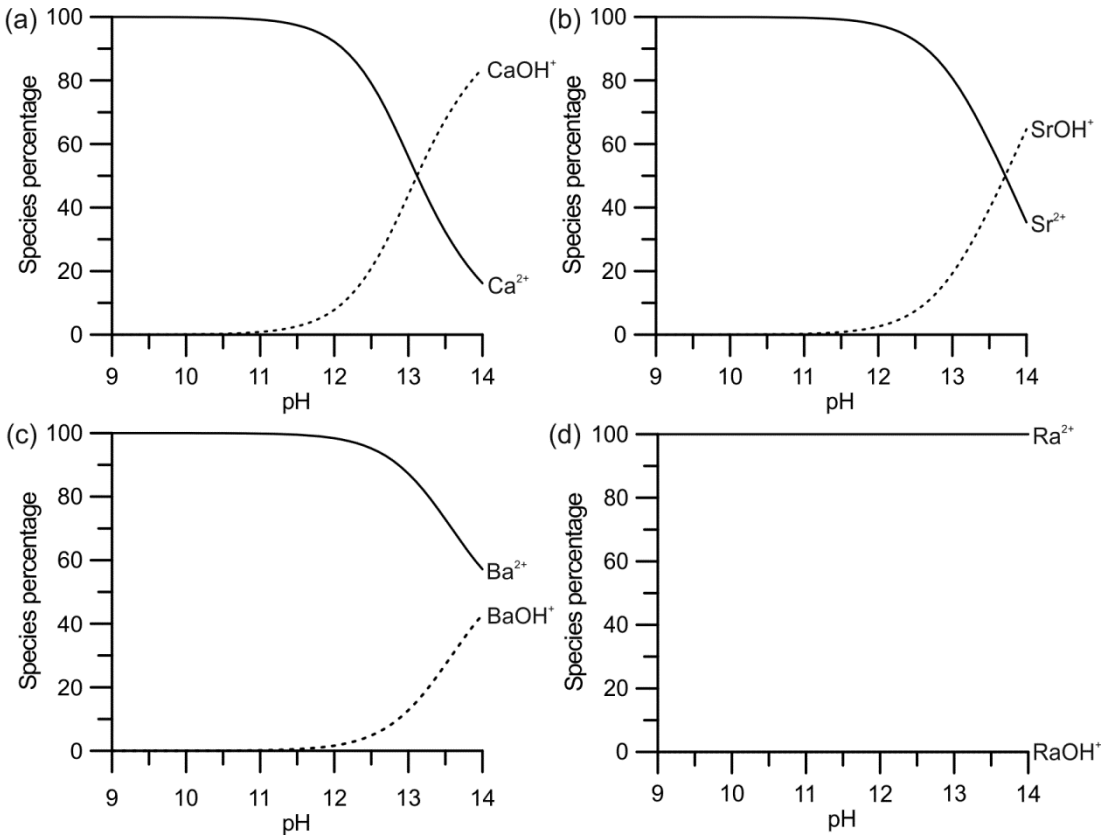


**Figure 7.6** Speciation of four alkali earth elements as a function of pH determine by PHREEQC modelling (a) $Ca^{2+}$ and $CaOH^{+}$ (b) $Sr^{2+}$ and $SrOH^{+}$ (c) $Ba^{2+}$ and $BaOH^{+}$ (d) $Ra^{2+}$ and $RaOH^{+}$

### 7.4.4 Implications for radionuclide behaviour

The conclusion that it is the speciation of Sr into the $SrOH^{+}$ species that is responsible for its inner-sphere incorporation and retention has important implications for the behaviour of the other ions modelled. Both Ca and Ra are expected to be present in solutions at cementitious geological disposal facilities for radioactive waste. Ra as a long lived radionuclide is present in the waste and Ca is abundant when leached from the cementitious backfill. The interaction of this backfill with groundwater is expected to yield high pH high ionic strength solution, known as young cement water (Wallace et al., 2013, Fernández et al., 2009). Therefore it is essential to understand the

sorption behaviour of these important elements in high pH and IS environments. Due to the high radiotoxicity of Ra, Ba is often used as a non-toxic analogue in experiments (Jones et al., 2011). The modelling results show two important points. Firstly, in this high pH and high IS environment the $CaOH^+$ species will dominate. Our EXAFS data has shown that (for $SrOH^+$) these monovalent hydroxyl species can sorb in inner-sphere complexes. If $CaOH^+$ can form inner sphere complexes in the same way as $SrOH^+$ significant concentrations of Ca may be sorbed onto mineral surfaces at high pH. This would reduce the total concentration of Ca in solution. Current predictions of radionuclide migration assume a given concentration of Ca (NDA, 2010b, NDA, 2010a). Our result show that sorption of $CaOH^+$ may reduce the total solution concentration and may have implications for precipitation of U and Ra bearing carbonate phases (Jones et al., 2011, NDA, 2010b). Secondly the modelling shows that while Ba forms a $BaOH^+$ species, which may also sorb via inner-sphere complexation; Ra remains as $Ra^{2+}$ which would only be bound via cation exchange. Therefore the sorption of Ba in high IS, high pH systems may be greater than for Ra and analogue experiments using Ba may underestimate the concentration of Ra remaining mobile in the aqueous phase.

## 7.5 Conclusions

Here it has been shown from batch sorption experiments and EXAFS spectroscopy that under conditions of high ionic strength and high pH, Sr is selectively retained on charged surfaces of minerals. Under low pH conditions Sr speciates as the divalent $Sr^{2+}$ cation which sobs in outer-

sphere complexes. This occurs in competition with other monovalent and divalent cations and is strongly controlled by solution ionic strength with Sr sorption reducing with increasing ionic strength. At high pH however the monovalent $SrOH^+$ ion dominates in solution. This Sr species adsorbs via inner-sphere surface complexation and allows the retention of Sr on charged surface sites even when high concentrations of competing ions are present.

## 7.6 References

Ahearne, J. F. 1997. Radioactive waste: The size of the problem. *Physics Today,* 50**,** 24-29.

Axe, L., Bunker, G. B., Anderson, P. R. & Tyson, T. A. 1998. An XAFS analysis of strontium at the hydrous ferric oxide surface. *Journal of Colloid and Interface Science,* 199**,** 44-52.

Balek, V., Málek, Z., Šubrt, J. & Ždimera, A. 1996. Characterization of iron(III) oxide and oxide-hydroxide as Sr-sorbent. *Journal of Radioanalytical and Nuclear Chemistry,* 212**,** 321-331.

Bilgin, B., Atun, G. & Keceli, G. 2001. Adsorption of strontium on illite. *Journal of Radioanalytical and Nuclear Chemistry,* 250**,** 323-328.

Binsted, N. 1998. *EXCURV98: CLRC Daresbury Laboratory computer program,* Warrington, CLRC Daresbury.

Bond, K. A., Heath, T. G. & Tweed, C. J. 1997. HATCHES: A Reference Thermodynamic Database for Chemical Equilibrium Studies. NDA.

Bostick, B. C., Vairavamurthy, M. A., Karthikeyan, K. G. & Chorover, J. 2002. Cesium adsorption on clay minerals: An EXAFS spectroscopic investigation. *Environmental Science & Technology,* 36**,** 2670-2676.

Carroll, S. A., Roberts, S. K., Criscenti, L. J. & O'Day, P. A. 2008. Surface complexation model for strontium sorption to amorphous silica and goethite. *Geochemical Transactions,* 9.

Chen, C. C., Coleman, M. L. & Katz, L. E. 2006. Bridging the gap between macroscopic and spectroscopic studies of metal ion sorption at the oxide/water interface: Sr(II), Co(II), and Pb(II) sorption to quartz. *Environmental Science and Technology,* 40**,** 142-148.

Chen, C. C. & Hayes, K. F. 1999. X-ray absorption spectroscopy investigation of aqueous Co(II) and Sr(II) sorption at clay-water interfaces. *Geochimica Et Cosmochimica Acta,* 63**,** 3205-3215.

Choi, S., O'Day, P. A., Rivera, N. A., Mueller, K. T., Vairavamurthy, M. A., Seraphin, S. & Chorover, J. 2006. Strontium speciation during reaction of kaolinite with simulated tank-waste leachate: Bulk and microfocused EXAFS analysis. *Environmental Science & Technology,* 40**,** 2608-2614.

Chorover, J., Choi, S., Amistadi, M. K., Karthikeyan, K. G., Crosson, G. & Mueller, K. T. 2003. Linking cesium and strontium uptake to kaolinite weathering in simulated tank waste leachate. *Environmental Science and Technology,* 37**,** 2200-2208.

Chorover, J., Choi, S., Rotenberg, P., Serne, R. J., Rivera, N., Strepka, C., Thompson, A., Mueller, K. T. & O'Day, P. A. 2008. Silicon control of strontium and cesium partitioning in hydroxide-weathered sediments. *Geochimica Et Cosmochimica Acta,* 72**,** 2024-2047.

Collins, C. R., Sherman, D. M. & Ragnarsdottir, K. V. 1998. The adsorption mechanism of Sr2+ on the surface of goethite. *Radiochimica Acta,* 81**,** 201-206.

De Windt, L., Pellegrini, D. & Van Der Lee, J. 2004. Coupled modeling of cement/claystone interactions and radionuclide migration. *Journal of Contaminant Hydrology,* 68**,** 165-182.

Dyer, A., Chow, J. K. K. & Umar, I. M. 2000. The uptake of caesium and strontium radioisotopes onto clays. *Journal of Materials Chemistry,* 10**,** 2734-2740.

Eberl, D. D. 1980. Alkali cation selectivity and fixation by clay minerals. *Clays and Clay Minerals,* 28**,** 161-172.

Fernández, R., Mäder, U. K., Rodríguez, M., De La Villa, R. V. & Cuevas, J. 2009. Alteration of compacted bentonite by diffusion of highly alkaline solutions. *European Journal of Mineralogy,* 21**,** 725-735.

Grim, R. E. 1968. *Clay Mineralogy,* New York, McGraw-Hill.

Gunman, S. J., Binsted, N. & Ross, I. 1984. A rapid, exact curved-wave theory for EXAFS calculations. *Journal of Physics C: Solid State Physics,* 17**,** 143-151.

Jackson, B. L. J. & During, C. 1979. Studies of slowly available potassium in soils of New Zealand - I. Effects of leaching, temperature and potassium depletion on the equilibrium concentration of potassium in solution. *Plant and Soil,* 51**,** 197-204.

Jackson, M. L. 1968. Weathering of Primary and Seondary Minerals in Soils. *9th International Congress of Soil Science.* Adelaide, Australia: The International Society of Soil Science and Angus & Robertson Ltd.

Jones, M. J., Butchins, L. J., Charnock, J. M., Pattrick, R. A. D., Small, J. S., Vaughan, D. J., Wincott, P. L. & Livens, F. R. 2011. Reactions of radium and barium with the surfaces of carbonate minerals. *Applied Geochemistry,* 26**,** 1231-1238.

Karasyova, O. N., Ivanova, L. I., Lakshtanov, L. Z. & Lövgren, L. 1999. Strontium Sorption on Hematite at Elevated Temperatures. *Journal of Colloid and Interface Science,* 220**,** 419-428.

Khan, S. A., RiazurRehman & Khan, M. A. 1995. Sorption of strontium on bentonite. *Waste Management,* 15**,** 641-650.

Law, G. T. W., Geissler, A., Boothman, C., Burke, I. T., Livens, F. R., Lloyd, J. R. & Morris, K. 2010. Role of Nitrate in Conditioning Aquifer Sediments for Technetium Bioreduction. *Environmental Science & Technology,* 44**,** 150-155.

NDA 2010a. The 2010 UK Radioactive Waste Inventory.

NDA 2010b. Geological Disposal: Radionuclide Behaviour Status Report. Nuclear Decommissioning Authority.

O'Day, P. A., Newville, M., Neuhoff, P. S., Sahai, N. & Carroll, S. A. 2000. X-ray absorption spectroscopy of strontium(II) coordination. I. Static and thermal disorder in crystalline, hydrated, and precipitated solids and in aqueous solution. *Journal of Colloid and Interface Science,* 222**,** 184-197.

Parkhurst, D. L. & Appelo, C. A. J. 1999. *User's guide to PHREEQC (version 2),* Denver, US Geological Survey.

Parkman, R. H., Charnock, J. M., Livens, F. R. & Vaughan, D. J. 1998. A study of the interaction of strontium ions in aqueous solution with the surfaces of calcite and kaolinite. *Geochimica Et Cosmochimica Acta,* 62**,** 1481-1492.

Poinssot, C., Baeyens, B. & Bradbury, M. H. 1999. Experimental and modelling studies of caesium sorption on illite. *Geochimica Et Cosmochimica Acta,* 63**,** 3217-3227.

Ravel, B. & Newville, M. 2005. ATHENA, ARTEMIS, HEPHAESTUS: data analysis for X-ray absorption spectroscopy using IFEFFIT. *Journal of Synchrotron Radiation,* 12**,** 537-541.

Sahai, N., Carroll, S. A., Roberts, S. & O'Day, P. A. 2000. X-ray absorption spectroscopy of strontium(II) coordination - II. Sorption and precipitation at kaolinite, amorphous silica, and goethite surfaces. *Journal of Colloid and Interface Science,* 222**,** 198-212.

Savage, D. 2011. A review of analogues of alkaline alteration with regard to long-term barrier performance. *Mineralogical Magazine,* 75**,** 2401-2418.

Sawhney, B. L. 1972. Selective Sorption and Fixation of Cations by Clay-Minerals - Review. *Clays and Clay Minerals,* 20**,** 93-100.

Schwertmann , U. & Cornell, R. M. 2000. *Iron Oxides in the Laboratory: Preparation and Characterisation,* Weinheim, Wiley-VCH.

SellafieldLtd 2009. Generic Basics for Inventory Challenge - Legacy Alkaline Sludge Systems. Cumbria, UK: Sellafield Ltd.

Sparks, D. L. & Huang, P. M. 1985. Physical Chemisty of Soil Potassium. *In:* MUNSON, R. D. (ed.) *Potassium in Agriculture.* Madison: American Society of Agronomy.

Takeno, N. 2005. Atlas of Eh-pH diagrams: Intercomparison of thermodynamics databases. National Institute of Advanced Industrial Science and Technology.

Tenderholt, A., Hedman, B. & Hodgson, K. O. 2007. Pyspline: A modern, cross-platform program for the processing of raw averaged XAS edge and EXAFS data. *AIP Conference Proceedings,* 882**,** 105-107.

Thorpe, C. L., Lloyd, J. R., Law, G. T. W., Burke, I. T., Shaw, S., Bryan, N. D. & Morris, K. 2012. Strontium sorption and precipitation behaviour during bioreduction in nitrate impacted sediments. *Chemical Geology,* 306-307**,** 114-122.

Tits, J., Wieland, E., Dobler, J. P. & Kunz, D. The uptake of strontium by calcium silicate hydrates under high pH conditions: An experimental approach to distinguish adsorption from Co-precipitation processes. *In:* OVERSBY, V. M. & WERME, L. O., eds., 2004 Kalmar. 689-694.

Tits, J., Wieland, E., Müller, C. J., Landesman, C. & Bradbury, M. H. 2006. Strontium binding by calcium silicate hydrates. *Journal of Colloid and Interface Science,* 300**,** 78-87.

Tomic, S., Searle, B. G., Wander, A., Harrison, N. M., Dent, A., Mosselmans, J. F. W. & Inglesfield, J. E. 2005. New Tools for the Analysis of EXAFS: The DL_EXCURV Package. *CCLRC Technical Report DL-TR-2005-00.*

Torstenfelt, B., Andersson, K. & Allard, B. 1982. Sorption of Strontium and Cesium on Rocks and Minerals. *Chemical Geology,* 36**,** 123-137.

Wallace, S. H., Shaw, S., Morris, K., Small, J. S. & Burke, I. T. 2013. Alteration of sediments by hyperalkaline k-rich cement leachate: Implications for strontium adsorption and incorporation. *Environmental Science and Technology,* 47**,** 3694-3700.

Wallace, S. H., Shaw, S., Morris, K., Small, J. S., Fuller, A. J. & Burke, I. T. 2012. Effect of groundwater pH and ionic strength on strontium sorption in aquifer sediments: Implications for 90Sr mobility at contaminated nuclear sites. *Applied Geochemistry,* 27**,** 1482-1491.

Weaver, C. E. & Pollard, L. D. 1973. *The chemistry of clay minerals,* Amsterdam, Elsevier.

Zhao, H., Deng, Y., Harsh, J. B., Flury, M. & Boyle, J. S. 2004. Alteration of kaolinite to Cancrinite and sodalite by simulated Hanford tank waste and its impact on cesium retention. *Clays and Clay Minerals,* 52**,** 1-13.

# Chapter 8 – Conclusions

This chapter presents a summary of the overall findings of the thesis. The key results from each data chapter are summarised. It closes with concluding remarks on the implications of the results in the thesis and suggestions for future research.

## 8.1 Summary of results

The radioactive isotopes of Cs (chiefly $^{137}Cs$) and Sr (mainly $^{90}Sr$) are major legacy contaminants present at a number of highly contaminated sites world-wide. For management and remediation of these sites to be effective it is extremely important to have a detailed scientific understanding of the processes governing contaminant behaviour. To this end this thesis has presented a detailed investigation of the mechanistic processes governing the behaviour of Cs and Sr in the surface environment. As both Cs and Sr have simple redox chemistry (Söderlund et al., 2011, Carroll et al., 2008) their environmental behaviour is chiefly controlled by sorption to charged surface sites within the soil matrix. This thesis investigated the sorption of Cs and Sr to both the permanent and variable charge sites on clay minerals and iron hydroxides, both in isolation and within a mixed phase sediment.

Chapter 5 presented the first results of this thesis and focused on the sorption of $^{137}Cs$ onto a micaceous aquifer sediment under a wide range of solution conditions. This work used batch sorption experiments and a refined

cation exchange model to determine the influence of solution pH and ionic strength on the sorption of Cs across a wide concentration range. The results showed firstly that Cs was able to sorb to multiple sites within the sediment and that the dominance of each site was controlled chiefly by the concentration of Cs in solution. At very low concentrations Cs sorbed to a highly selective site, thought to be located at the frayed interlayer edge of illite. Sorption of Cs to these so called ‘frayed edge sites’ occurred independently of solution pH and ionic strength (NaCl and KCl). As the concentration of Cs increased the frayed edge sites became saturated and excess Cs was sorbed to other parts of the sediment. Here pH and ionic strength were important as H, K and Na cations were able to compete with Cs for these non-specific sites. The key new result of this work was that at low pH, sorption of Cs to the non-specific sites is greatly reduced. This process has not been previously observed and may explain enhanced mobility of Cs under acidic conditions.

Chapter 6 investigated at the atomistic scale the nature of illite frayed edge sites and the sorption of Cs therein. Atomic scale scanning transmission electron microscopy was used to image expansion of the illite interlayer by Ca incorporation and its subsequent collapse when Ca was exchanged for Cs. This is the first direct mechanistic explanation for the selective sorption and retention of Cs in illite. Elemental mapping (by spatially resolved energy dispersive x-ray spectroscopy) showed that over the long term Cs migrated into the interlayer forming a Cs-illite. The bonding environment of Cs in this

interlayer was then confirmed by extended x-ray absorption fine structure spectroscopy, coupled to a density functional theory model.

Finally Chapter 7 focused on the sorption of Sr from hyper-alkaline solutions onto the surface of illite, chlorite and goethite. It was shown that under near-neutral pH conditions $Sr^{2+}$ sorbed into outer-sphere complexes in competition with other cations. Therefore increasing ionic strength (NaCl) caused a reduction in Sr sorption. However under hyper-alkaline pH conditions (>pH 12.5) Sr speciated as $SrOH^{+}$ and was able to form inner-sphere surface complexes. This allowed Sr to absorb to the mineral surfaces even under extremely high ionic strength conditions (1 mol $L^{-1}$ Na, as $NaOH^{+}$). Of particular note, it was observed that at pH 14, $SrOH^{+}$ dominated solution speciation, and EXAFS evidence confirmed that Sr was incorporated into the interlayer of illite, just as was previously observed to occur for Cs.

## 8.2 Implications

The results presented in this thesis represent a significant advance in understanding of the fundamental sorption processes governing the long term mobility of two key radionuclides, $^{137}Cs$ and $^{90}Sr$.

Chapters 5 and 6 present new insights into Cs sorption that will have important implications for the management of nuclear sites contaminated with this radionuclide. Specifically the importance of solution pH on Cs

sorption has been clearly shown. Previous work had not investigated the effect of pH on sorption of Cs at relatively high concentration, and $H^+$ competition has not previously been incorporated into predictive models (Bradbury and Baeyens, 2000). Therefore the modified predictive models presented in this thesis should allow a far more accurate prediction of Cs sorption behaviour (and therefore mobility) under low pH conditions. Additionally the long term sorption experiments in chapter 6 established that the Cs selective sorption capacity of illite increased over time. It was shown that as Cs migrated into the illite interlayer more Cs could be incorporated into the structure and removed from solution. This shows that over long time scales the amount of Cs irreversibly incorporated into illite will increase, reducing any potential long term mobility.

The investigations of Sr sorption at hyper-alkaline pH have significant implications for the management of Sr at sites where it is present in the surface under hyper-alkaline conditions (such as at Sellafield and Hanford (Chorover et al., 2008, Babad et al., 1993, McKenzie et al., 2011)). It has been previously well establish that over the long term, Sr from hyper-alkaline liquors becomes immobilised in neoformed zeolite phases and calcium-silicate-hydrates via dissolution and reprecipitation of silicate minerals (Fernández et al., 2009, Tits et al., 2004). However results from this thesis show that before this process can occur Sr is immobilised by incorporation into inner-sphere surface complexes. This likely prevents the short term migration of Sr and explains the low mobility observed under hyper alkaline conditions.

## 8.3 Future research

A number of potentially fruitful avenues of future research have been revealed as a result of this thesis. Firstly the modelling done in chapter 5 relied on simple equilibrium constants due to a lack of information on the Cs sorption environment. However this mechanistic and atomistic understanding of Cs incorporation into the interlayer has been established in chapter 6. Therefore it would prove extremely valuable to incorporate this new knowledge into detailed surface-complexation models of Cs sorption. These are far more scientifically robust than simple cation-exchange models currently employed. As well as improving the understanding of sorption this atomistic understanding of Cs incorporation should prove useful in focusing research into removing Cs from these interlayer sites. This proves an important yet elusive goal for remediation of Cs contaminated soils. Previous attempts have relied on cation exchange which proved unfruitful (e.g. appendix 1). It is hoped that the improved understanding of Cs' coordination environment in the interlayer yielded by this thesis may allow the effective targeting of any future research into its removal.

Finally, it was postulated in chapter 7 that Ca, Ba and Ra may exhibit the same inner-sphere complexation behaviour as Sr under high pH conditions. Ca is a common groundwater cation and an important component of high pH cement leachates and Ra is an important radionuclide in repository scenarios (De Windt et al., 2004, Fernández et al., 2009). Therefore it may prove valuable to investigate the sorption mechanism of these elements at high pH. Also $Ba^{2+}$ is used as a proxy for $Ra^{2+}$ in many studies (Jones et al.,

2011) – however the modelling presented here suggests that at high pH sorption behaviour may not be equivalent; therefore care must be taken when extrapolating results from Ba studies to predict Ra behaviour.

Overall, this thesis has significantly improved current understanding of Cs and Sr behaviour in the environment. However, many fruitful avenues of research still remain.

## 8.4 References

Babad, H., Cash, R. J., Deichman, J. L. & Johnson, G. D. 1993. High-priority Hanford Site radioactive waste storage tank safety issues: An overview. *Journal of Hazardous Materials,* 35**,** 427-441.

Bradbury, M. H. & Baeyens, B. 2000. A generalised sorption model for the concentration dependent uptake of caesium by argillaceous rocks. *Journal of Contaminant Hydrology,* 42**,** 141-163.

Carroll, S. A., Roberts, S. K., Criscenti, L. J. & O'Day, P. A. 2008. Surface complexation model for strontium sorption to amorphous silica and goethite. *Geochemical Transactions,* 9.

Chorover, J., Choi, S., Rotenberg, P., Serne, R. J., Rivera, N., Strepka, C., Thompson, A., Mueller, K. T. & O'Day, P. A. 2008. Silicon control of strontium and cesium partitioning in hydroxide-weathered sediments. *Geochimica Et Cosmochimica Acta,* 72**,** 2024-2047.

De Windt, L., Pellegrini, D. & Van Der Lee, J. 2004. Coupled modeling of cement/claystone interactions and radionuclide migration. *Journal of Contaminant Hydrology,* 68**,** 165-182.

Fernández, R., Mäder, U. K., Rodríguez, M., De La Villa, R. V. & Cuevas, J. 2009. Alteration of compacted bentonite by diffusion of highly alkaline solutions. *European Journal of Mineralogy,* 21**,** 725-735.

Jones, M. J., Butchins, L. J., Charnock, J. M., Pattrick, R. A. D., Small, J. S., Vaughan, D. J., Wincott, P. L. & Livens, F. R. 2011. Reactions of radium and barium with the surfaces of carbonate minerals. *Applied Geochemistry,* 26**,** 1231-1238.

McKenzie, H. M., Coughlin, D., Laws, F. & Stampler, A. 2011. Groundwater Annual Report 2011. Sellafield Ltd.

Söderlund, M., Lusa, M., Lehto, J., Hakanen, M., Vaaramaa, K. & Lahdenperä, A.-M. 2011. Sorption of Iodine, Chlorine, Technetium, and Cesium in Soil. Eurajoki, Finland: Posiva.

Tits, J., Wieland, E., Dobler, J. P. & Kunz, D. The uptake of strontium by calcium silicate hydrates under high pH conditions: An experimental approach to distinguish adsorption from Co-precipitation processes. *In:* OVERSBY, V. M. & WERME, L. O., eds., 2004 Kalmar. 689-694.

# Appendix A – Caesium desorption trials

The first appendix presents results from trials performed to investigate desorption of trace concentrations of Cs from the mixed sediment (chapter 5).

## A.1 Desorption by Cation exchange

Chapter 5 of this thesis presented a study of Cs sorption onto a micaceous sediment representative of the alluvial sediment underlying the Sellafield site. As part of this work some trials were performed to determine the reversibility of Cs sorption by simple cation exchange with both Na and K ions. The isotopic exchange of $^{137}Cs$ by $^{133}Cs$ was also tested.

Initially the sediment was equilibrated for 48 hours with $10^{-11}$ mol $L^{-1}$ Cs (as a 45 Bq $ml^{-1}$ spike of $^{137}Cs$). The concentration of Cs sorbed to the sediment was then determined by liquid scintillation counting. After the sorption period was over the solution was decanted and separated samples of the sediment were resuspended in 1 mol $L^{-1}$ solutions of NaCl, KCl and CsCl at the same solid/ solution ratio (100 g $L^{-1}$). The samples were then shaken for a further 48 hour period of desorption before analysis of final Cs solution concentration by liquid scintillation counting. All the desorption experiments were performed over a pH range of 2-7.

The results (Figure A.1) show that large amounts of the sorbed caesium are not readily available for exchange by any of the tested exchangers. In the same way that the sediments selectively adsorbed caesium in preference to competing K and Na ions (see chapter 5) they appear to selectively retain it. The fact that potassium ions were able to desorb around 30% of the caesium where sodium achieved no significant desorption suggests that the sediments may have two distinct sorption sites; a high affinity site which specifically retains Cs only and a second site available for both Cs and K, but not Na. The pH of the desorbing solution had no effect.

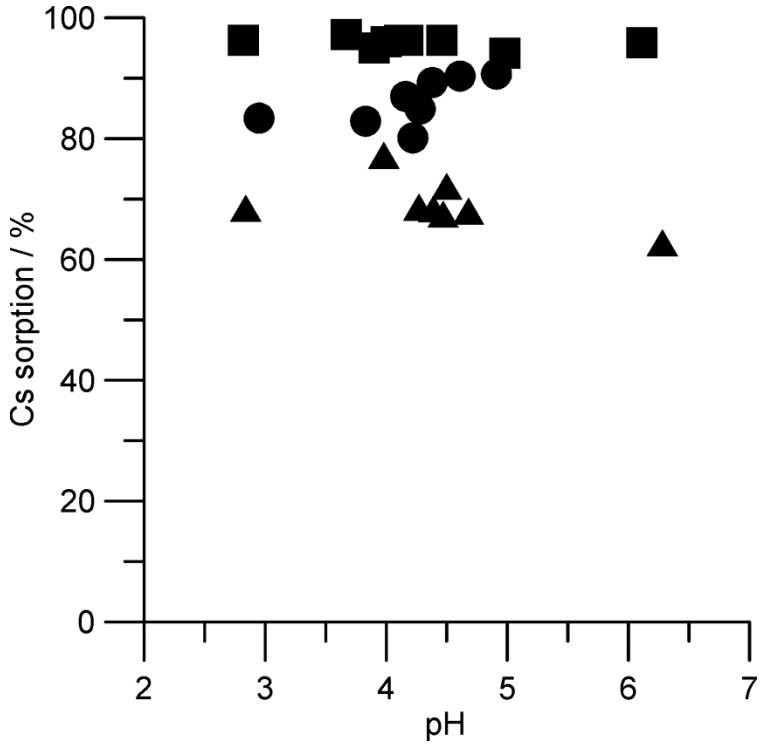


**Figure A.1** Retention of sorbed Cs after cation exchange with: K, triangles; Na (squares) and Cs (circles).

## A.2 Desorption with Sodium Tetraphenylboron

As it was found that cation exchange was unsuccessful in liberating trace concentrations of Cs from the high affinity sorption sites other methods were sought. It has been well established from results in this thesis that Cs is selectively sorbed into the collapsed interlayers of illite (chapter 6). The high affinity site present in the mixed sediment described in chapter 5 is likely to be these collapsed illite interlayers.

Illite interlayers are naturally filled with K ions (Grim, 1968). The large organic molecule sodium tetraphenylboron is widely used in agriculture and soil science to determine non-exchangeable K in soils, which is held in the interlayer (Cox and Joern, 1997, Cox et al., 1996, Darunsontaya et al., 2010, Wang et al., 2010). Therefore it was hypothesised that it may be possible to use sodium tetraphenylboron to exchange Cs out the interlayer sites and desorb it back into solution.

To test this, trace concentrations of Cs ($10^{-11}$ mol $L^{-1}$ as 45 Bq $ml^{-1}$ $^{137}Cs$) were sorbed to the mixed sediment used in chapters 5 and 7 (and for the previous desorption experiments). A sediment sample was equilibrated for 48 hours. The supernatant from the sample was then removed and it was resuspended in 0.1 mol $L^{-1}$ sodium tetraphenylboron solution at the same solid: solution ratio (100 g $L^{-1}$). The sample was then shaken for 48 hours and desorbed Cs concentration analysed by liquid scintillation counting.

Results (Table A.1) showed that the sodium tetraphenylboron treatment failed to desorb any Cs from the interlayer sites in the allotted time. The likely explanation is that Cs was more strongly retained than K in the interlayer and could not be mobilised. Alternatively desorption of Cs from the interlayers may be kinetically controlled and the experiments were not run for a sufficient time period for Cs to be removed.

**Table A.1** Percentage Cs desorbed by exchange with sodium tetraphenylboron

| Sorption | | Desorption | | |
|---|---|---|---|---|
| pH | Cs Sorbed / % | pH | Cs Sorbed / % | Cs Desorbed / % |
| 9.29 | 99.9 | 9.86 | 99.9 | 0 |

## A.3 References

Cox, A. E. & Joern, B. C. 1997. Release kinetics of nonexchangeable potassium in soils using sodium tetraphenylboron. *Soil Science,* 162**,** 588-598.

Cox, A. E., Joern, B. C. & Roth, C. B. 1996. Nonexchangeable ammonium and potassium determination in soils with a modified sodium tetraphenylboron method. *Soil Science Society of America Journal,* 60**,** 114-120.

Darunsontaya, T., Suddhiprakarn, A., Kheoruenromne, I. & Gilkes, R. J. 2010. The kinetics of potassium release to sodium tetraphenylboron solution from the clay fraction of highly weathered soils. *Applied Clay Science,* 50**,** 376-385.

Grim, R. E. 1968. *Clay Mineralogy,* New York, McGraw-Hill.

Wang, H. Y., Sun, H. X., Zhou, J. M., Cheng, W., Du, C. W. & Chen, X. Q. 2010. Evaluating Plant-Available Potassium in Different Soils Using a Modified Sodium Tetraphenylboron Method. *Soil Science,* 175**,** 544-551.

# Appendix B - PHREEQC modelling code

## B.1 Notes for users

The following input file can be copy and pasted to PHREEQC (Parkhurst and Appelo, 1999). The model, when run with the wateq4f.dat thermodynamic database (Ball and Nordstrom, 1991) will then output the results presented in the Na contour plot (see Figure 5.7). Other modelling outputs presented in this paper can be modelled by changing the composition of the solution terms (e.g. changing to K instead of Na will give the K contour plot).

## B.2 PHREEQC code

```
Title Initial solution

Solution 1
pH 7
Units g/l
K       0.035
Cl      0.0692
Mg      0.0404
S       0.0260
O(0)    0.1000
Na        0.0349
Si      0.0191
N       0.0045

save solution 1

end
```

```
TITLE Caesium Sorption experiment
use solution 1

EXCHANGE_MASTER_SPECIES
    X    X-
    Y    Y-
    Z    Z-

EXCHANGE_SPECIES
    Y- = Y-
    log_k  0.0

    Z- = Z-
    log_k  0.0

    X- = X-
    log_k   0.0

    H+ + X- = HX
    log_k     2.5

    K+ + X- = KX
    log_k      0.5

    Na+ + X- = NaX
    log_k           0.0

    Na+ + Y- = NaY
    log_k          0.0

    K+ + Y- = KY
    log_k         0.6

    H+ + Y- = HY          # Set as equal to Cs
```

```
        log_k           3.6

        Ca+2 + 2Y- = CaY2
        log_k           0.8

        Mg+2 + 2Y- = MgY2
        log_k           0.6

        Na+ + Z- = NaZ
        log_k           0.0

        K+ + Z- = KZ
        log_k           1.5

        H+ + Z- = HZ
        log_k           1.75    # Poinsot, et al 1999

        Ca+2 + 2Z- = CaZ2
        log_k           0.8

        Mg+2 + 2Z- = MgZ2
        log_k           0.6

EXCHANGE 1
X       6.5e-3
Y       1.6e-4
Z       4.0e-6
-equilibrate solution 1

save exchange 1

end
TITLE Sorption of caesium
```

```
EXCHANGE_SPECIES
        Cs+ + X- = CsX      #planar
        log_k 1.2

        Cs+ + Y- = CsY      #TypeII
        log_k 3.6

        Cs+ + Z- = CsZ      #FES
        log_k 7.0

PHASES
Fix_H+
        H+ = H+
        log_k 0.0

SELECTED_OUTPUT
      -file [file name]
      -m Cs+ CsX CsY CsZ
      -t Cs
USE EXCHANGE 1
use solution 1

solution 2
ph 7
units moles/l
Na 1.0e-1
Cs 1.0e-9

solution 3
ph 7
units moles/l
Na 1.0e-1
Cs 5.0e-9
```

```
solution 4
ph 7
units moles/l
Na 1.0e-1
Cs 1.0e-8

solution 5
ph 7
units moles/l
Na 1.0e-1
Cs 5.0e-8

solution 6
pH 7
units moles/l
Na 1.0e-1
Cs 1.0e-7

solution 7
ph 7
units moles/l
Na 1.0e-1
Cs 5.0e-7

solution 8
ph 7
units moles/l
Na 1.0e-1
Cs 1.0e-6

solution 9
ph 7
units moles/l
Na 1.0e-1
```

```
Cs 5.0e-6

solution 10
ph 7
units moles/l
Na 1.0e-1
Cs 1.0e-5

solution 11
ph 7
units moles/l
Na 1.0e-1
Cs 5.0e-5

solution 12
ph 7
units moles/l
Na 1.0e-1
Cs 1.0e-4

solution 13
ph 7
units moles/l
Na 1.0e-1
Cs 5.0e-4

solution 14
ph 7
units moles/l
Na 1.0e-1
Cs 1.0e-3

solution 15
ph 7
```

```
units moles/l
Na 1.0e-1
Cs 5.0e-3

solution 16
ph 7
units moles/l
Na 1.0e-1
Cs 1.0e-2

solution 17
ph 7
units moles/l
Na 1.0e-1
Cs 5.0e-2

solution 18
ph 7
units moles/l
Na 1.0e-1
Cs 1.0e-1

end


USE EXCHANGE 1
use solution 2
EQUILIBRIUM_PHASES 1; Fix_H+  -7.0  NaOH 10.0
end

USE EXCHANGE 1
use solution 3
EQUILIBRIUM_PHASES 1; Fix_H+  -7.0  NaOH 10.0
end
```

```
USE EXCHANGE 1
use solution 4
EQUILIBRIUM_PHASES 1; Fix_H+  -7.0  NaOH 10.0
end

USE EXCHANGE 1
use solution 5
EQUILIBRIUM_PHASES 1; Fix_H+  -7.0  NaOH 10.0
end

USE EXCHANGE 1
use solution 6
EQUILIBRIUM_PHASES 1; Fix_H+  -7.0  NaOH 10.0
end

USE EXCHANGE 1
use solution 7
EQUILIBRIUM_PHASES 1; Fix_H+  -7.0  NaOH 10.0
end

USE EXCHANGE 1
use solution 8
EQUILIBRIUM_PHASES 1; Fix_H+  -7.0  NaOH 10.0
end

USE EXCHANGE 1
use solution 9
EQUILIBRIUM_PHASES 1; Fix_H+  -7.0  NaOH 10.0
end

USE EXCHANGE 1
use solution 10
EQUILIBRIUM_PHASES 1; Fix_H+  -7.0  NaOH 10.0
```

```
end

USE EXCHANGE 1
use solution 11
EQUILIBRIUM_PHASES 1; Fix_H+  -7.0  NaOH 10.0
end

USE EXCHANGE 1
use solution 12
EQUILIBRIUM_PHASES 1; Fix_H+  -7.0  NaOH 10.0
end

USE EXCHANGE 1
use solution 13
EQUILIBRIUM_PHASES 1; Fix_H+  -7.0  NaOH 10.0
end

USE EXCHANGE 1
use solution 14
EQUILIBRIUM_PHASES 1; Fix_H+  -7.0  NaOH 10.0
end

USE EXCHANGE 1
use solution 15
EQUILIBRIUM_PHASES 1; Fix_H+  -7.0  NaOH 10.0
end

USE EXCHANGE 1
use solution 16
EQUILIBRIUM_PHASES 1; Fix_H+  -7.0  NaOH 10.0
end

USE EXCHANGE 1
use solution 17
```

```
EQUILIBRIUM_PHASES 1; Fix_H+  -7.0  NaOH 10.0
end

USE EXCHANGE 1
use solution 18
EQUILIBRIUM_PHASES 1; Fix_H+  -7.0  NaOH 10.0
end
```

## B.3 References

Ball, J. W. & Nordstrom, D. K. 1991. User's manual for WATEQ4F with revised thermodynamic database and test cases for calculating speciation of major, trace and redox elements in natural waters.

Parkhurst, D. L. & Appelo, C. A. J. 1999. *User's guide to PHREEQC (version 2),* Denver, US Geological Survey.

# Appendix C - Presentations and Awards

This appendix gives a summary of all presentations given and prizes and grants awarded to the candidate during the tenure of the PhD (2010-2014)

## C.1 Presentations

### C.1.1 Invited lectures

**Fuller, A.J.,** Shaw, S., Ward, M.B., Haigh, S., Mosselmans, J.F.W., Peacock, C.L., Stackhouse, S., Dent, A., Trivedi, D., and Burke, I.T. (2014) The long term environmental behaviour of radioactive caesium after nuclear accidents, *Yorkshire Contaminated Land Forum,* Sheffield, UK

**Fuller, A.J.,** Shaw, S., Ward, M.B., Haigh, S., Mosselmans, J.F.W., Peacock, C.L., Stackhouse, S., Dent, A., Trivedi, D., and Burke, I.T. (2013) The long term fate of radioactive caesium in soil after nuclear accidents and implications for Fukushima, Japan, *Leeds Geological Association public lecture series,* Leeds, UK

**Fuller, A.J.**, Shaw S., Peacock, C.L., Trivedi, D., Small, J.S., Abrahamsen, L.G. and Burke, I.T. (2013) Multi-site sorption of $^{137}Cs$ on a micaceous sediment: the importance of pH and competing ions, *ESSI Seminar Series, School of Earth and Environment,* Leeds, UK

### C.1.2 Conference oral presentations

**Fuller, A.J.,** Shaw, S., Ward, M.B., Haigh, S., Mosselmans, J.F.W., Peacock, C.L., Stackhouse, S., Dent, A., Trivedi, D., and Burke, I.T. (2014) Nano-scale TEM imaging of caesium incorporation into illite interlayers, *24$^{th}$ V.M Goldschmidt meeting (Goldschmidt 2014)*, Sacramento, California, USA

**Fuller, A.J.,** Shaw, S., Ward, M.B., Haigh, S. Peacock, C.L., Trivedi, D. and Burke, I.T. (2013) High resolution ChemiSTEM observations of Cs absorption into illite, *Mineralogical Society Environmental Mineralogy Group - Research in Progress,* Sheffield, UK

**Fuller, A.J.**, Shaw S., Peacock, C.L., Trivedi, D. and Burke, I.T. (2012) Solution chemistry controls multi-site sorption of $^{137}$Cs on micaceous soils, *22$^{nd}$ V.M. Goldschmidt (Goldschmidt 2012),* Montréal, Québec, Canada

**Fuller, A.J.**, Shaw S., Peacock, C.L., Trivedi, D. and Burke, I.T. (2012) Solution chemistry controls multi-site sorption of $^{137}$Cs on micaceous soils, *Mineralogical Society Environmental Mineralogy Group - Research in Progress,* Reading, UK

**Fuller, A.J.**, Shaw S., Peacock, C.L., Trivedi, D. and Burke, I.T. (2011) Developing effective remediation of radionuclides in contaminated ground, *COGER*, Stirling, UK

### C.1.3 Conference poster presentations

**Fuller, A.J.**, Shaw, S., Peacock, C.L., Ward, M., Haigh, S., Trivedi, D., Small, J.S., Abrahamsen, L., Stackhouse, S. and Burke. I.T. (2013) A nano to macro scale investigation of caesium sorption to illite and sediment, *14$^{th}$ International Conference on the Chemistry and Migration Behaviour of Actinides and Fission Products in the Geosphere (Migration 2013)*, Brighton, UK

**Fuller, A.J.**, Shaw S., Peacock, C.L., Trivedi, D. and Burke, I.T. (2011) Geochemical influences on caesium adsorption onto Sellafield sediment, *Mineralogical Society Environmental Mineralogy Group - Research in Progress,* Edinburgh, UK

## C.2 Prizes and grants

***April 2014:*** Letter of commendation – School of Earth and Environment postgraduate research student publication prize

***Sept 2013:*** Migration 2013 best poster prize - US$500

***June 2012:*** Goldschmidt 2012 student travel grant - CAD$1000

***May 2012:*** Royal Society of Chemistry Radiochemistry Group young researchers fund - £300